Ultrafast dynamics of photo-doped Mott antiferromagnets

Thesis by
Omar Mehio

In Partial Fulfillment of the Requirements for the
Degree of
Doctor of Philosophy

CALIFORNIA INSTITUTE OF TECHNOLOGY
Pasadena, California

2023
Defended May 15, 2023

Omar Mehio
ORCID: 0000-0001-7923-2178

ACKNOWLEDGEMENTS

During my time at Caltech, I was blessed to make countless friends, collaborators, and connections that not only enabled the completion of the work in this thesis, but will likely impact me for the rest of my life. It was truly one of the most beautiful times of my life, despite the difficulty of the PhD itself, mostly owing to these relationships. I know that I will look back at my time in Pasadena fondly, with a bit of sadness that it has come to a close, and a bit of excitement for what is to come. In these acknowledgments, I hope to impart the feeling of gratitude towards those who made this experience possible.

I start by thanking my advisor Professor David Hsieh. The impacts of Dave's mentorship are readily visible in every aspect of my work. His caring and empathetic advising style fosters a vibrant atmosphere that made it possible for me to thrive during my time at Caltech. Much of the work presented in this thesis departs quite significantly from the established research directions of our group; it was only possible because of Dave's continued trust in me and the independence that he gave me as a student and researcher. Dave is very generous with his time and resources, and is always ready to support our work in any way possible. I cannot thank Dave enough for the guidance he provided over the previous years, and for helping me grow to be the scientist I am today.

The ideas that underlie the presented results were almost all borne out of close collaborations rich with stimulating discussions and passionate debates. I now thank those that made these collaboartions possible, beginning with Hoglie Ning. I learned how to be a scientist alongside Honlgie, as we were partners from the start of my time in Dave's group. Working alongside each other on almost every project, we learned everything from assembling optics and ordering parts to writing manuscripts and pushing works towards publication. I still remember the early days of our PhD when we were still scrapping to get our experiments going, and we would end the long days in the lab with a feast of delicious food and tea. It was an honor to work with him for all these years, and to develop the strong friendship that continues to flourish.

Just like a super hero, Xinwei Li joined the group right when I needed him the most. He helped me solve some of the most challenging issues I faced in building the THz setup and analyzing the data collected. I still remember the day that Xinwei and I

decided to begin our collaboration in the lab during the winter holiday of 2018, and I am still thankful for that decision. It has been an inspiration to watch Xinwei work, as his dedication towards his craft is almost unparalleled. Working with him on the projects in this thesis has been a pleasure, and I would not be the same scientist today without this collaboration.

As soon as I met Yuchen Han when she was a prospective student, I knew that I would love working with her. She has become one of my closest friends during our time collaborating. Yuchen has seen me go through one of the most difficult times of my PhD from a perspective that few others have, and she has always handled it with such grace during our collaboration. I want to sincerely thank her for her empathy and support in these moments. She has also been there for the happiest of times as well, and it is always a pleasure to share a cup of coffee or bowl of noodles with her or to talk about the most recent anime releases and her recent experiences travelling. Aside from her wonderful character, Yuchen is a brilliant scientist who quickly surpassed me as the THz expert in the group and I am so excited to see what her future holds. I will truly miss working with her.

I also want to thank my other lab mates. Chen Li and I joined Caltech at the same time, and she has become a great friend over the past six years. I will miss her company. I want to thank Nicholas Laurita for teaching me about the fundamentals of THz spectroscopy and for helping me set up the original experiment. It was a sad day when Alberto de la Torre left the lab; he had become a great friend and mentor during his time at Caltech, and I look forward to crossing paths again in the future. Finally, I would like to thank all the other group members that accompanied my time at Caltech: Junyi Shan, Kyle Seyler, Mingyao Guo, Daniel Van Beveren, Alon Ron, Preston Zhou, Ryo Noguchi, Youngjoon Han, Carina Belvin, Tejas Deshpande, and Hoon Kim. One of the best aspects of Dave's group is the culture, and my discussions with each of these valued group members were invaluable to the success of my PhD.

Many collaborations from around the world enabled the work presented in this thesis. I thank Zala Lenarčič, whose theoretical work has been crucial to understanding many of the ideas presented in this thesis. I also thank Michael Buchhold for discussing these results with me, and for providing fresh perspectives on my results. My experiments would not have been possible without the samples grown by Zach Porter and Stephen Wilson; I am indebted to them for their efforts. Finally, I want to thank Leon Balents, Mengxing Ye, Rick Averitt, Patrick Lee, Matteo Mitrano,

Michele Buzzi, Scott K. Cushing, and Victor Galitski for useful discussions about my work.

I hope that the friendships I made at Catelch will last a lifetime. I was blessed to make many companions during this time, all of whom I will miss and hope to keep in touch with: Sunghyuk Park, Hesham Zaini, Hamza Raniwala, Eray Atay, Sammmy Shaker, Basel Mostafa, Sina Booeshaghi, Albert Wandui, Varun Raj, Alexander Dalzell, Alexander Moss, Tom Naragon, Benjamin Riviere, and many others. A special note goes out to Aidan Fenwick. He has become my brother during this period of my life, which would not have been the same without him. There is nobody else that I would have shared these formative years with. I will honestly and sincerely miss his company.

Finally, I want to thank my family. Nada Mehio is not only my sister, but my friend and my mentor. My PhD was always much easier becuase I watched my sister go through hers, and becuase of her unconditional and unwavering support. No matter what I was going through, I knew that I could go to Nada for comfort and advice. The daily (hourly) pictures of my nephew Abraham that she sends to the family chat really have gotten me through some tough moments. I am so blessed to have Nada in my life, and I hope that I play a similar role in hers.

I met my wife Lina Demis right as I was starting my final year of my PhD. I feel as though I have lived two lives: a life before meeting her, and a new life after. Her support was so important and critical to me during this year that I am honestly unsure how I was able to complete the first five years.

My most sincere thanks is extended to my parents Mohamad Mehio and Rola Mehio. My parents have truly seen me at my lowest, and have supported me unconditionally through every single moment. This PhD is as much yours as it is mine.

ABSTRACT

Strong coupling between spin and charge degrees of freedom in two-dimensional spin-1/2 Mott antiferromagnets (AFMs) creates a rich platform to study quantum many-body physics. For decades, the consequences of these interactions have been intensely studied in thermal equilibrium, where the introduction of charge carriers through chemical doping has been shown to generate a vibrant phase diagram rich with unconventional types of charge, spin, and orbital ordering. In recent years, however, attention has grown to include the study of these materials as they are driven far from equilibrium using intense pulses of light produced by femtosecond laser sources. In addition to fundamental interest in the resultant dynamics, recent experimental and theoretical studies have suggested that driven Mott insulators can host states of matter that cannot be accessed in thermal equilibrium.

While many driving protocols have been developed—spanning from the selective excitation of bosonic modes to photon-dressing via coherent time-periodic driving—the simplest conceptual approach to engineering Mott insulators with light is known as photo-doping. In this procedure, the material is impulsively driven resonantly with a transition from a filled band to an empty band, transiently producing charge carriers. Given the impact of chemical doping in thermal equilibrium, photo-doping has garnered interest as an important tool in the study of driven Mott insulators. Early successes in the study of photo-doped Mott AFMs include the observation of ultrafast demagnetization and the prediction of non-thermal magnetic states, charge density waves, and superconductivity. Photo-doping thus holds promise to generate an out-of-equilibrium phase diagram that is equally rich to that found in equilibrium.

Yet, many open questions about the basic properties of photo-doped Mott insulators remain unresolved. Whether charge instabilities exist as a result of interactions between the photo-dopants has yet to be examined. Moreover, while theoretical studies have suggested that antiferromagnetic correlations can enhance attractive interactions between photo-dopants, evidence of the resultant bound states remain elusive. Even the light-matter interactions that generate the photo-dopants are in need of investigation, as the fate of a Mott insulator driven by strong electric fields remains a fundamental open theoretical and experimental problem.

In this thesis, I present a series of experiments designed to answer each of these questions. After describing the properties of Mott insulators in Chapter 1, I present

the experimental details of the tools that enable these studies in Chapter 2. Taking a multi-messenger approach to ultrafast spectroscopy, a suite of ultrafast probes simultaneously track the spin and charge degrees of freedom to paint a holistic picture of the out-of-equilibrium state. In Chapter 3, I use ultrafast THz conductivity to establish the existence of an insulating photo-excited fluid of Hubbard excitons (HEs), which are bound states that are thought to form as a result of attractive spin-mediated interactions. This magnetic binding mechanism is studied in more detail in Chapter 4 by examining the properties of these HEs in the magnetic critical region of several materials that lie in different magnetic universality classes. In Chapter 5, I study the effects of HE formation on the ultrafast demagnetization that is known to occur following photo-doping. Finally, I turn my attention towards the photo-dopant generation mechanism in Chapter 6, exploring the effects of strong electric field driving in Mott insulators. I find signatures of the so-called Keldysh crossover from a multiphoton-absorption- to a quantum-tunneling-dominated pair production regime. Altogether, this work establishes photo-doped Mott insulators as a rich playground to engineer non-equilibrium phases of matter and study quantum many-body dynamics.

PUBLISHED CONTENT AND CONTRIBUTIONS

[1] Xinwei Li, Honglie Ning, Omar Mehio, Hengdi Zhao, Min-Cheol Lee, Kyung-wan Kim, Fumihiko Nakamura, Yoshiteru Maeno, Gang Cao, and David Hsieh. Keldysh Space Control of Charge Dynamics in a Strongly Driven Mott Insulator. *Physical Review Letters*, 128(18):187402, May 2022. doi: 10.1103/PhysRevLett.128.187402.
O.M. contributed to the experimental effort and analyzed the data.

TABLE OF CONTENTS

LIST OF FIGURES

Chapter 1

INTRODUCTION

At a conference in Bristol in 1937, Jan Hendrick de Boer and Evert Verwey presented a perplexing issue to their peers [165, 166]. They found that many materials, especially transition metal oxides, demonstrate insulating behavior when they were theoretically predicted to be metals. This observation was astounding because it was the first reported violation of the band theory of solids, which is hailed as one of the great early successes of quantum mechanics. Band theory predicts that electrons in crystalline materials lie in energy windows known as bands, which host a continuum of states for the electrons to occupy. Because these bands are separated by energy gaps, they create a clear criterion to distinguish between metals and insulators. In the former, the highest occupied electron state lies within a band, allowing for infinitesimal excitation of the electrons. In the latter, the highest occupied band is full, so its excitation is blocked by the energy gap separating the next band. By these considerations, the transition metal oxides studied by Verwey and de Boer should in principle be metals, because a simple counting of the electrons per unit cell demonstrates that the valence band should only be partially occupied.

It was quickly pointed out by Rudolf Peierls that correlations between electrons must be the reason behind these anomalous insulating behaviors [165, 166]. Band theory relies on models that consider the electrons to be nearly free, only interacting with each other indirectly through screening. Indeed, in each of the materials that band theory describes successfully—such as the noble metals or semiconductors—correlations between electrons can be ignored, ensuring the validity of the predictions. When electron-electron interactions are no longer negligible, however, these models break down, and so do the predictions of band theory. Subsequent work by Sir Nevill Mott [163, 164, 166], John Hubbard [95–97], Martin Gutzwiller [85], Junjiro Kanamori [107], and others showed that these transition metal oxides were insulating because of an interaction-driven metal-to-insulator transition: electrons in the system localize one another due to the intense Coulomb repulsion between them. Since then, these types of insulators have been known as Mott insulators.

While the source of the insulating state was unraveled, the properties of Mott insulators continue to confound and fascinate physicists to this day. Aside from the strong

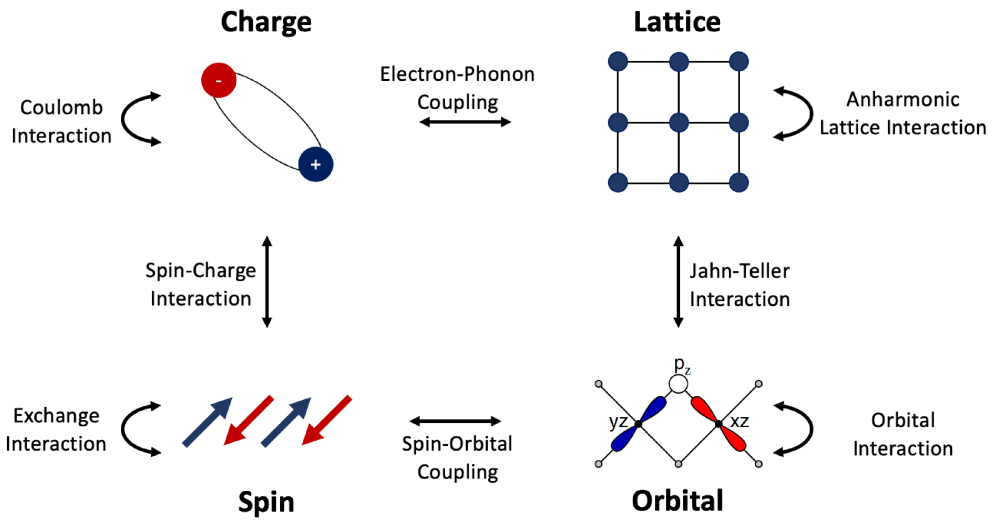

Figure 1.1: Diagram showing the interactions that exist between the charge, spin, orbital and lattice degrees of freedom in Mott insulators and other strongly correlated electron systems. Image of the orbitals was adapted from Reference [101].

Coulomb interaction, a myriad of different interactions between different degrees of freedom—charge, spin, orbital and lattice—have been identified in Mott insulators (Figure 1.1). The interplay between these interactions gives rise to a vast range of collective phenomena, the most striking of which are revealed when these materials are doped with charge carriers [126]. If electrons or holes are added to the system, typically through chemical substitution, the Mott insulating state quickly collapses and from its remains emerge a series of exotic phases. Most importantly, it was discovered in 1986 that copper-oxide Mott antiferromagnets exhibit superconductivity at extraordinarily high temperatures [21], surpassing liquid Nitrogen temperatures [243]. The community quickly realized that the physics of strong correlations must be invoked to understand this observation, inspiring an ongoing decades-long effort to understand how the coupling of spin and charge degrees of freedom can drive the formation of bound states of charge carriers. Aside from superconductivity, a wealth of other phases litter the rich temperature-doping phase diagram, spanning charge density wave orders to strange metallic phases to pseudogap phenomena (Figure 1.2) [18, 49, 126].

Traditionally, searches for these phases of matter have focused on the ground state of materials in thermal equilibrium. This approach relies on the iterative—and often serendipitous—process synthesizing chemically stable compounds and spectroscopically characterizing them to determine whether they demonstrate the desired

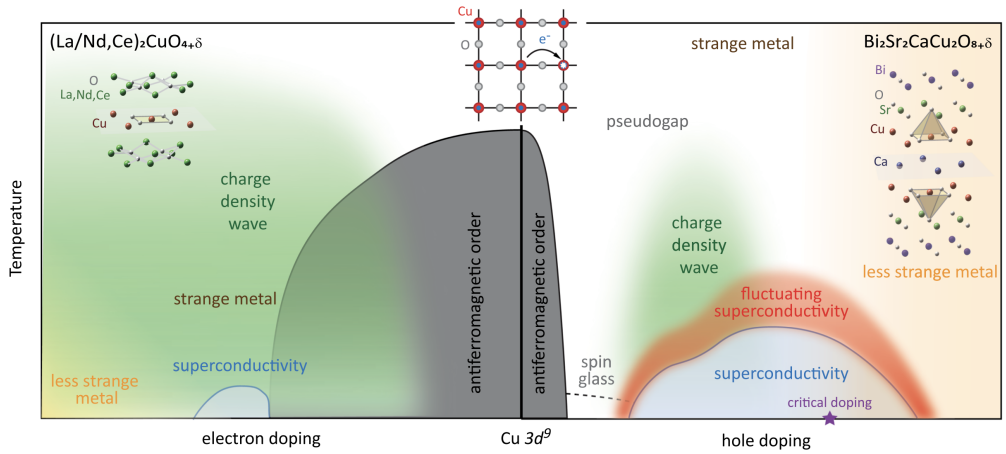

Figure 1.2: Schematic temperature-doping phase diagram of the electron- and hole-doped cuprate superconductors. From Reference [206].

physics. While this method has successfully allowed us to survey the quantum phases that nature has made available to us, it leaves little control in the hands of the researcher in what those phases are and the emergent properties they possess. For this reason, efforts in condensed matter physics and materials science have increasingly focused on the development of experimental protocols that allow for the intentional design of quantum phases [19].

The external driving of materials with light has become a promising tool in this endeavor [27, 53]. The rich phase space of light-matter interactions can be exploited to directly modify the microscopic degrees of freedom that generate the phases of interest, and have been shown to induce long-lived non-equilibrium states. Several theoretical and experimental breakthroughs have been made in the past decade. While these examples are plentiful, highlights include putative superconductivity induced by resonant driving of optical phonons [32, 36, 40, 67, 139, 158], topological phases of matter generated with photon-dressed states [151], and ultrafast switching into thermally inaccessible states [213]. Each of these examples demonstrate that light creates novel pathways towards inherently non-equilibrium phenomena.

A light-based engineering protocol that is quite relevant to the case of Mott insulators is photo-doping, which involves exciting the material resonantly with a transition from a filled band to an empty band. This technique is thought to simulate chemical doping in the sense that it introduces or removes charges from the bands involved with the photo-excitation process. These charge carriers create a metastable out-of-equilibrium state since their immediate recombination is inhibited by the presence

of the charge gap [60, 129, 157, 198, 211], requiring the transfer of the excess energy to external degrees of freedom. Given that charge doping has such profound effects on the behavior of Mott insulators in equilibrium, photo-doping is a promising avenue for electronic property control in these materials. However, a flurry of recent work has suggested that photo-doping should not be viewed simply as an ultrafast and reversible alternative to chemical doping. Led primarily by theoretical predictions [7, 62, 62, 75–77, 108, 133, 154, 168, 237, 239], studies have revealed that photo-doping can potentially generate novel phases and phenomena that are not accessible in thermal equilibrium. Examples of the proposed phenomena include metal-to-insulator transitions [193], bad metallic behavior [61], nonthermal antiferromagnetic states [15, 238], ferromagnetism [168], charge orders [25, 143, 168], the formation of excitons [26, 46, 78, 84, 129, 130, 202, 223, 224], s-wave [25, 168], d-wave [215, 234], spin-triplet [240], and η-paired [64, 110, 111, 132, 136, 168, 222] superconducting states, hidden spin-orbital ordered phases [133, 135], and transient trapping into metastable states [214]. Altogether, these predictions suggest the tantalizing possibility that photo-doping can generate a non-equilibrium phase diagram just as rich as its equilibrium counterpart.

On the other hand, progress on the experimental front is far more nascent. Despite several pioneering results—which have primarily focused on excitation and relaxation dynamics [48, 92, 142, 159, 172, 173, 183, 185, 186], photo-induced melting of ordered phases [2, 54, 55, 123, 146, 147, 150, 182], and transient metallicity [14, 39, 140, 141, 179, 180, 217, 247, 247]—the vast majority of the predicted phenomena have yet to be discovered, and many fundamental questions about the photo-excited state remain unresolved. The primary experimental challenge that hinders progress is the difficulty in spectroscopically probing the out-of-equilibrium state. Due to the strong coupling between different microscopic degrees of freedom in Mott insulators, it is crucial to probe multiple material properties simultaneously in order to reconstruct a complete picture of the transient state of matter. Moreover, strong correlations often make spectral features a challenge to interpret [18, 126]. Conventional models used to interpret optical, scattering, and photo-emission scattering spectra often break down in the presence of strong correlations, leading to multiple competing theories. In some cases, certain phenomena are hidden from detection altogether, further inhibiting characterization of the transient state of matter. These complications—paired with the requirement of ultrafast time resolution—have made the experimental characterization of photo-doped Mott systems a great challenge that is starting to be overcome by advances in ultrafast science.

This uncertainty can be contrasted against weakly correlated rigid-band insulators, where photo-doping has been extensively studied and is well-understood. In these materials, the photo-doping process generates holes and electrons in the valence and conduction bands, respectively. Since intra-band relaxation is much faster than electron-hole recombination, a quasi-equilibrium population of photo-dopants can be maintained [10, 114]. Much of the phenomenology thereafter is centered around the formation of bound electron-hole pairs known as excitons [41, 89, 120, 204, 232]. The presence of excitons has many important consequences on the non-equilibrium state. Not only do they determine the recombination properties of the material [105, 188, 249], but interactions between them results in the formation of a many-body phase diagram rich with phenomena such as Mott metal-to-insulator transitions [10, 98, 105, 114, 249] and Bose-Einstein condensation [33, 35, 162, 184, 205]. Whether the photo-doped Mott insulator is also well-described by the formation of excitons is still a critical open question. Unlike semiconductors, photo-doping in a Mott insulator generates local many-body states described by empty or doubly occupied sites in the material's lattice, known as holons and doublons respectively [168]. While a quasi-equilibrium population of these quasiparaticles will also form [129, 157, 198, 211], their subsequent dynamics are starkly different than their counterparts in rigid band insulators, which are described by single-particle theories. In weakly correlated materials, many body interactions can be reduced to screening effects and the photo-doped electrons and holes are nearly free, interacting with one another only through the Coulomb interaction. On the other hand, holons and doublons interact heavily with their environments, especially with magnetic degrees of freedom [68]. These interactions are predicted create novel pathways for exciton formation that are unavailable in rigid band insulators [46, 84, 129, 130, 221]. However, the existence and stability of these excitons is still an open question, with some evidence against their formation [168, 202] and some supporting it [4, 46, 84, 129, 221, 227, 242]. As such, an understanding of their properties has been largely limited to the theoretical domain.

The presence of excitons in photo-doped Mott antiferromagnets will have profound ramifications on the character of the out-of-equilibrium state of matter and the resultant phase diagram. Whether excitons in Mott insulators can form excitonic phases of matter—such as excitonic fluids—is not yet known owing to uncertainty with regards to their metastability [202]. Aside from this possibility, exciton formation will also have important consequences on charge and magnetic dynamics. With regards to the former, excitons are predicted to recombine through multi-magnon

emission processes that explain the ultrafast (∼1 ps) charge relaxation times observed in Mott antiferromagnets [129, 130]. From the point of view of the magnetic properties, excitons are less destructive to the long-range antiferromagnetic order than free holons and doublons [46, 84, 221, 242]. However, the impact of excitons on the photo-doped magnetic phase diagram has yet to be considered, precluding a complete understanding of the observed magnetic dynamics.

Finally, while these questions have been centered around the dynamics of photo-dopants after they have been introduced into the system, it is equally important to understand the mechanisms by which holons and doublons are generated. The most straightforward method to generating a holon-doublon (HD) pair is through photo-excitation resonant with an optically-active transition from a filled band to an empty band. However, by driving the material below its band gap where no electronic transitions exist, alternative nonlinear pathways to HD generation become available [175, 226]. These can be parameterized with the so-called Keldysh adiabicity parameter, which describes whether light with a given wavelength and intensity will generate HD pairs through a quantum tunneling mechanism or a multiphoton absorption mechanism [175, 226]. The point at which one mechanism dominates over the other in the space of photon energy to electric field strength is known as the Keldysh crossover, a predicted hallmark of which is a change in width of the nonthermal distribution of HD pairs in momentum space [175]. Thus, by controlling the experimental parameters of the pump pulse, the distribution of photo-excited carriers in the material's band structure can be tuned. This possibility creates a novel tuning knob in the design of photo-doped phases that has yet to be explored owing to a lack of experimental study of Mott insulators in the Keldysh crossover regime.

The starting point for understanding each of these aspects of photo-doping is to consider the basic properties of a Mott insulator and the expected behavior of a single charge dopant introduced into the system. From that point, different complications—such as bound pair formation and magnetic order parameter dynamics—can be considered to reconstruct an overall picture of the photo-induced state. This discussion begins with the Hubbard model, which is the simplest theoretical description of a Mott insulator. In this thesis, we specifically focus on the case of two-dimensional spin-1/2 systems, as these ingredients are thought to be essential to the phenomenology described above [23, 126].

1.1 The Hubbard Model

The Hubbard model is designed to capture the essential features of Mott insulators using minimal number of free parameters and interactions. This tight binding model considers a square lattice in which each site can host up to two electrons. These electrons can hop from one site to another, and they interact with one another through the Coulomb interaction. Despite this simplicity, the Hubbard model and its various extensions are still actively studied until this day and are thought to capture a vast extent of the phenomenology of Mott insulators. Its success underscores the importance of local interactions in Mott systems. Our discussion will closely follow that of Reference [68], with additional details obtained from Reference [71] and Reference [166].

We begin by considering the assumptions that underlie the development of this model. First, we assume that only one band is present near the Fermi energy (ε_F) and that all other bands are far away energetically. This assumption is justified because bands far above and far below ε_F should be minimally affected by the presence of electron-electron interactions since the electron-ion interaction will dominate. Using this assumption, if a Bloch state of energy ε_p, momentum $\vec{p}$, and band index α has a wave function $\Psi_{\vec{p},\alpha}$, then a series of Wannier states can be constructed:

$$\Psi_\alpha(\vec{r}_i) = \frac{1}{\sqrt{N}} \sum_{\vec{p}\in \mathrm{BZ}} e^{i\vec{p}\cdot\vec{r}_i} \Psi_{\vec{p},\alpha}(\vec{r}_i) \tag{1.1}$$

where $\vec{r}_i$ is the location of the ith electron and $\vec{p} \in \mathrm{BZ}$ means all momenta included within the Brillouin Zone. Since the first assumption is that only one band is physically relevant, we can drop the index α.

Using these states, we can write the full extent of the Coulomb interaction matrix elements as:

$$U_{ij,i'j'} = \int d^3r_1 d^3r_2 \Psi_i^*(\vec{r}_1)\Psi_j^*(\vec{r}_2)\tilde{V}(\vec{r}_1-\vec{r}_2)\Psi_{i'}(\vec{r}_1)\Psi_{j'}(\vec{r}_2). \tag{1.2}$$

Here, $\tilde{V}$ is the screened Coulomb interaction. The second assumption of the Hubbard model is that only the maximal "on-site" matrix element is relevant, $U_{ii,ii} \equiv U$. We can make this assumption for two reasons. First, the overlap between Wannier states decreases exponentially with the distance, and so we should expect that the matrix elements $U_{i,j,i',j'}$ should decrease rapidly with the distance $|\vec{r}_1 - \vec{r}_2|$. Second, $\tilde{V}$ itself falls off with distance, as expected for a Coulomb potential.

We are now ready to assemble the Hamiltonian. Since this is a tight binding model with tunneling between sites and the Coulomb interaction, we only have two terms:

$$\begin{aligned} H = &- \sum_{\substack{\vec{r}_i,\vec{r}_j \\ \sigma=\uparrow,\downarrow}} \left(c^\dagger_\sigma(\vec{r}_i) t_{ij} c_\sigma(\vec{r}_j) + c^\dagger_\sigma(\vec{r}_j) t_{ij} c_\sigma(\vec{r}_i) \right) \\ &+ \frac{1}{2} \sum_{\substack{i,j,i',j' \\ \sigma,\sigma'=\uparrow,\downarrow}} U_{ij,i'j'} c^\dagger_\sigma(\vec{r}_i) c^\dagger_{\sigma'}(\vec{r}_j) c_{\sigma'}(\vec{r}_{j'}) c_\sigma(\vec{r}_{i'}). \end{aligned} \tag{1.3}$$

In this second-quantized notation, $c^\dagger_\sigma(\vec{r}_j)$ creates an electron at site $\vec{r}$ with spin σ. These creation operators satisfy the following:

$$\begin{aligned} \{c_\sigma(\vec{r}), c^\dagger_{\sigma'}(\vec{r}')\} &= \delta_{\sigma,\sigma'} \delta_{\vec{r},\vec{r}'} \\ \{c_\sigma(\vec{r}), c_{\sigma'}(\vec{r}')\} &= 0. \end{aligned} \tag{1.4}$$

The first term represents tunneling from one site to another. In the simplest form of the Hubbard model, this tunneling is restricted to nearest-neighbor hopping such that $t_{i,j} \equiv t$ if i and j are nearest neighbor, and zero otherwise. The second term, which accounts for the Coulomb interaction can also be simplified using our assumption that only the on-site Coulomb interaction is present, giving

$$U_{ij,i'j'} = U \delta_{ij} \delta_{i'j'} \delta_{ii'}. \tag{1.5}$$

With these considerations, we are left with the following Hamiltonian known as the Hubbard model:

$$H = -t \sum_{\substack{\langle \vec{r},\vec{r}' \rangle \\ \sigma=\uparrow,\downarrow}} \left(c^\dagger_\sigma(\vec{r}) c_\sigma(\vec{r}') + \text{h.c.} \right) + U \sum_{\vec{r}} n_\uparrow(\vec{r}) n_\downarrow(\vec{r}) \tag{1.6}$$

where the notation $\langle \vec{r}, \vec{r}' \rangle$ indicates that $\vec{r}$ and $\vec{r}'$ are on nearest-neighboring sites. $n_\sigma(\vec{r}) = c^\dagger_\sigma(\vec{r}) c_\sigma(\vec{r})$ is the counting operator. Since each site can host up to two electrons, they must be of opposite spin due to the Pauli exclusion principle. Thus, the $n_\sigma(\vec{r})$ will only return 0 or 1, and the Hilbert space is the tensor product of the following four states per site: $|0\rangle, |\uparrow\rangle, |\downarrow\rangle, |\uparrow\downarrow\rangle$. The empty site $|0\rangle$ is commonly known as a holon, while a doubly-occupied site $|\uparrow\downarrow\rangle$ is commonly known as a doublon. Both of these states are spin singlets, meaning their total spin is $S = 0$.

1.1.1 The strong-coupling limit

This model cannot be solved exactly in dimensions greater than one. However, we can consider its properties in certain limits relevant to Mott insulating systems. To do this, we begin by defining certain operators to re-cast the Hamiltonian into a more convenient form. First, we define operators to count the charge and spin on each site. For the former, we can count the total number of electrons each site:

$$en(\vec{r}) = e\sum_{\sigma} n_{\sigma}(\vec{r}) = e\sum_{\sigma} c^{\dagger}_{\sigma}(\vec{r})c_{\sigma}(\vec{r}) \equiv ec^{\dagger}_{\sigma}(\vec{r})1_{\sigma\sigma'}c_{\sigma'}(\vec{r}). \tag{1.7}$$

The following expression can be used to calculate the total charge:

$$Q = e\sum_{\vec{r}} n(\vec{r}) \equiv eN_e. \tag{1.8}$$

In the last step, the Einstein summation convention is used. To determine the spin at each site, the following operator can be used:

$$\vec{S}(\vec{r}) = \frac{\hbar}{2}c^{\dagger}_{\sigma}(\vec{r})\vec{\tau}_{\sigma\sigma'}c_{\sigma'}(\vec{r}) \tag{1.9}$$

where $\vec{\tau}$ is a vector of the three Pauli matrices:

$$\tau_1 = \begin{pmatrix} 0 & 1 \\ 1 & 0 \end{pmatrix} \qquad \tau_2 = \begin{pmatrix} 0 & -i \\ i & 0 \end{pmatrix} \qquad \tau_3 = \begin{pmatrix} 1 & 0 \\ 0 & -1 \end{pmatrix}. \tag{1.10}$$

This operator can be used to re-write the Coulomb interaction term of the Hubbard model Hamiltonian. Consider the following operator

$$\sum_{\vec{r}} \left(\vec{S}(\vec{r})\right)^2 = \sum_{\substack{\vec{r} \\ a=1,2,3}} S^a(\vec{r})S^a(\vec{r}). \tag{1.11}$$

By expanding the components, and making use of the following identity

$$\sum_{a=1,2,3} \tau^a_{\alpha\beta}\tau^a_{\gamma\delta} = 2\delta_{\alpha\delta}\delta_{\beta\gamma} - \delta_{\alpha\beta}\delta_{\gamma\delta} \tag{1.12}$$

we can re-write this operator as

$$\sum_{\vec{r}} \left(\vec{S}(\vec{r})\right)^2 = \sum_{\vec{r}} \left(\frac{3}{4} n(\vec{r}) - \frac{3}{2} n_{\uparrow}(\vec{r}) n_{\downarrow}(\vec{r})\right). \tag{1.13}$$

The first term gives a constant of $\frac{N_e U}{2}$, which can be dropped. Thus, the Coulomb interaction term of the Hamiltonian can be re-written as

$$H_{int} = U \sum_{\vec{r}} n_{\uparrow}(\vec{r}) n_{\downarrow}(\vec{r}) = -\frac{2}{3} U \sum_{\vec{r}} \left(\vec{S}(\vec{r})\right)^2. \tag{1.14}$$

This form allows us to easily study the properties of the Hubbard model under two constraints. The first constraint is that the system is at half filling. Since each site can host two electrons, this constraint means that the total number of electrons N_e is equal to the total number of sites in the lattice N. The half-filled case is an important starting point for the understanding of the Hubbard model and Mott insulators. Deviations from half-filling will be considered thereafter.

Second, we will consider the strong-coupling limit of the Hubbard model, in which $U \to \infty$. In this case, the interaction term will completely dominate the Hamiltonian, allowing the hopping term to be neglected. From Equation 1.14, it is apparent that when U is infinite the total spin $\vec{S}(\vec{r})$ on each site should be maximized and doubly-occupied sites are forbidden. Thus, because the system is at half-filling each site will be occupied by one electron that will be either a $|\uparrow\rangle$ state or a $|\downarrow\rangle$ state. With this, we have arrived at the origin of the Mott insulating state: when the Coulomb interaction dominates over the hopping strength, the electrons are localized onto each site as hopping in the lattice will create double occupied sites, which are forbidden. As a result, a charge gap on the order of U will open in the conduction band. The newly created valence and conduction bands are known as the lower Hubbard band (LHB) and the upper Hubbard band (UHB), respectively. A hole-like excitation in the LHB corresponds to an empty site in the Hubbard lattice known as a holon, while an electron-like excitation in the UHB corresponds to a doubly-occupied site known as doublon.

1.1.2 Magnetism in the strong-coupling limit

Aside from encompassing the physics of the Mott insulating state, the Hubbard model in the strong-coupling limit is also naturally captures the magnetic present in these systems. To see this, we start by noting that when only H_{int} is present in the Hamiltonian, the resulting insulating state is massively degenerate, as any

spin configuration is allowed. The degeneracy can be lifted by allowing for virtual exchange processes enabled by fluctuations of the hopping term, which leads to an expansion of the order t/U. If the system is originally in some spin configuration with every site occupied by one electron, the perturbative term will create intermediate states in which an electron is transferred from one site to another, creating one site is doubly occupied and one site that is empty. This state is U above the ground state energetically and its matrix element is t^2. Thus, we should expect that the energetic parameter of the effective Hamiltonian describing this process should be $2t^2/U$, where the factor of 2 comes from the fact that this process can be performed in two different ways. When the electron returns to its original position, the final spin configuration will either be the same as the original state, or differ by one spin exchange. An explicit calculation of this degenerate perturbation theory expansion will confirm that the effective Hamiltonian is the quantum Heisenberg magnet, giving the following Hamiltonian:

$$H_{Heisenberg} = J \sum_{\langle \vec{r}, \vec{r}' \rangle} \vec{S}(\vec{r}) \cdot \vec{S}(\vec{r}'). \tag{1.15}$$

J is a factor known as the spin exchange interaction and is equal to $2t^2/|U|$. This result is valid for any dimension and any lattice. From this result, it is apparent that the Hubbard model at half filling and in the strong-coupling limit naturally produces magnetic interaction. J in most Mott insulators is negative, meaning that most of these materials host antiferromagnetic correlations and form long-range order below some critical temperature.

1.2 The single hole problem

In the previous section, the Hubbard model was derived and its properties were explored at half-filling in the strong-coupling limit. In particular, we found that the Mott insulating state occurs when double occupancy becomes prohibitively expensive, and that quantum Heisenberg interactions naturally emerge from this model when fluctuations are considered. We are now ready to consider how the properties of this model are affected as we leave half filling through charge doping. As a starting point, we consider the case where a single electron is removed from the system, creating an empty site—a holon—in the lattice ($|0\rangle$). This scenario, which is commonly referred to as single-hole problem captures the essence of the strong spin-charge interactions that drive much of the interesting phenomenology of Mott insulators and their doped variants.

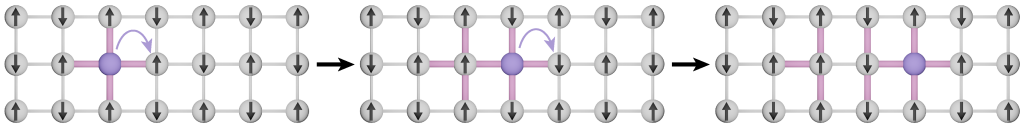

Figure 1.3: Schematic of a free holon (purple) moving through a square lattice with AFM interactions. With each hopping action away from its starting position (left panel), the length of the string will increase (middle and right panels). Excited bonds are shown in magenta.

Once the holon is added to the system, a new term in the Hamiltonian must be included to capture the kinetic energy associated with the motion of the holon. Using a hopping term similar to that written in Equation 1.6, since a holon hopping from one site to another is equivalent to a spin hopping into the site of the holon [68]. The total Hamiltonian can be written as

$$H_{t-J} = -t \sum_{\substack{\langle \vec{r},\vec{r}' \rangle \\ \sigma=\uparrow,\downarrow}} \left(c^{\dagger}_{\sigma}(\vec{r}) c_{\sigma}(\vec{r}') + \text{h.c.} \right) + J \sum_{\langle \vec{r},\vec{r}' \rangle} \vec{S}(\vec{r}) \cdot \vec{S}(\vec{r}') \tag{1.16}$$

where J is still equal to $2t^2/U$. Equation 1.16 is known as the $t-J$ model and often serves as the starting point for any discussion of a doped Mott insulator in the strong coupling limit. The key to its relevance is that it captures the competition between the kinetic energy of the holon and the antiferromagnetic correlations of the spins.

To visualize this competition, consider a holon in an antiferromagnetic Mott insulator (Figure 1.3). The presence of the holon creates a defect in the antiferromagnetic motif, as a single spin will be removed from the lattice to accommodate it. When the holon hops to a nearest neighboring site, it does so by trading places with the spin at that site. Since neighboring sites are on opposite sublattices of the antiferromagnetic motif, the newly spaced spin will now be oppositely aligned to its new neighbors creating an energy cost in the spin sector. As the holon continues to travel, it will continue to flip spins, leaving in its wake a string of magnetic excitations. From this, it is apparent that the kinetic energy of the holon and energy of the spins cannot be simultaneously minimized. This competition underlies much of the phenomenology unique to doped two-dimensional spin-1/2 Mott insulators and has many important consequences that must be considered when studying photo-doped materials.

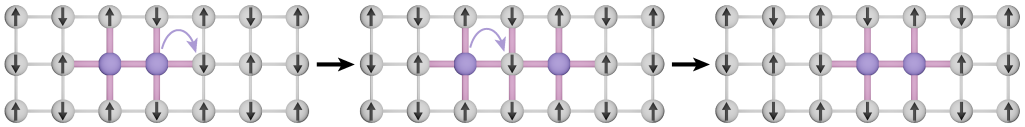

Figure 1.4: Schematic of a bound holon pair moving in a square lattice with AFM interactions. Holons are depicted as purple spheres. When one holon hops away from the other (middle panel), it will increase the length of the string of magnetic excitations compared to its original position (left panel). However, if the second holon coherently follows the first (right panel), it will repair the spin excitations, maintaining the overall cost to the spin sector. Excited bonds are shown in magenta.

In the Ising limit, the holon will become infinitely massive because the string serves as a linear confining potential that binds it to its original position. When the perpendicular components of the Heisenberg spin exchange are included, however, pairs of spins can be flipped spontaneously because they are no longer eigenstates of the new Hamiltonian [68]. In other words, these quantum fluctuations will eventually heal the spin excitations along the path, thereby relaxing the tension of the string [29, 68, 109, 145, 195]. This healing process mobilizes the holon. Due to this healing process, the holon essentially pulls a finite-length string along with it as it travels through this lattice. One can think of the string and the holon as a composite entity known as a polaron. Polarons were first studied in the mid-20th century to understand the effect of excess charge carriers in a polarizable material [69]. The electron or holon locally deforms the ions around it, creating a potential well that it can become trapped in. The resulting composite quantum object—the charge carrier and the deformed lattice—can be considered as a quasiparticle consisting of a charge carrier dressed by a cloud of lattice excitations. This concept lends itself naturally to the situation of Mott insulators, where instead of a deformations of the crystal lattice, the holon produces a deformation of the antiferromagnetic spin background. This spin background in turn induces a localizing potential that enhances the mass of the holon. Thus, we consider the holon to be dressed by a cloud of spin excitations and call this composite quasiparticle a spin polaron. The properties of these spin polarons have been extensively studied theoretically and experimentally and have been reviewed elsewhere [126].

1.3 Bound state formation in Mott AFMs

An important outcome of doping a Mott insulator is the emergence of superconductivity. In the cuprate family of Mott antiferromagnets, superconductivity seems to be driven by mechanisms that depart from the traditional Bardeen-Copper-Schrieffer theory for superconductivity [126]. Since the strongest energy scales in these systems are the on-site Coulomb interaction U ($\sim$ 1 eV) and the antiferromagnetic exchange interaction J ($\sim$ .1 eV) [5, 126], many theories have emerged describing possible spin-mediated mechanisms for the formation of Cooper pairs, along with a prodigious list of spectroscopic characterizations in an attempt to quantitatively falsify or verify these theories [126].

While the specific mechanism that drives the hole pairing of a cuprate superconductor still remains up to debate, we can arrive at a simple picture of how pairing of charge carriers can occur in a doped Mott insulator by building upon the discussion of polaron formation in the case of as single holon. As discussed, a polaron forms because the charge carrier is dressed by the spin excitations that its motion generates. This spin-dressing dramatically enhances the mass of the holon, thereby greatly reducing its mobility it to some extent. An intuitive way to think about this is to consider that the holon auto-localizes itself because the string serves as a confining linear potential. If—instead of the single hole problem—we consider the presence of two charge carriers, a novel situation can arise in which the mobility of the charge carriers is re-established. Suppose the two carriers are originally on neighboring sites. If one carrier travels away from the other, a string will be formed creating a confining potential that connect the two [28, 46, 84, 94, 129, 130, 202, 242]. Now, the second carrier coherently has the opportunity to coherently follow the first, tracing its path. In doing so, it will repair the spin excitations that he first charge carrier left in its wake. This spin-flip restoration process allows for the charge carriers to be mobile while simultaneously preserving the spin-exchange energy since the extent of spin excitations will always be limited only to the distance between the two carriers, unlike the individual carrier whose motion leads to a continuous increase in magnetic cost. The correlated motion of the pair—which can also be seen as the bound state of two spin polarons [242]—represents the formation of a bound state driven by the interplay between the kinetic energy of the charge carriers and the potential energy of the spin background.

Recently, the viability of string-mediated pairing has been suggested both experimentally and theoretically. Quantum gas microscopes designed to simulate the

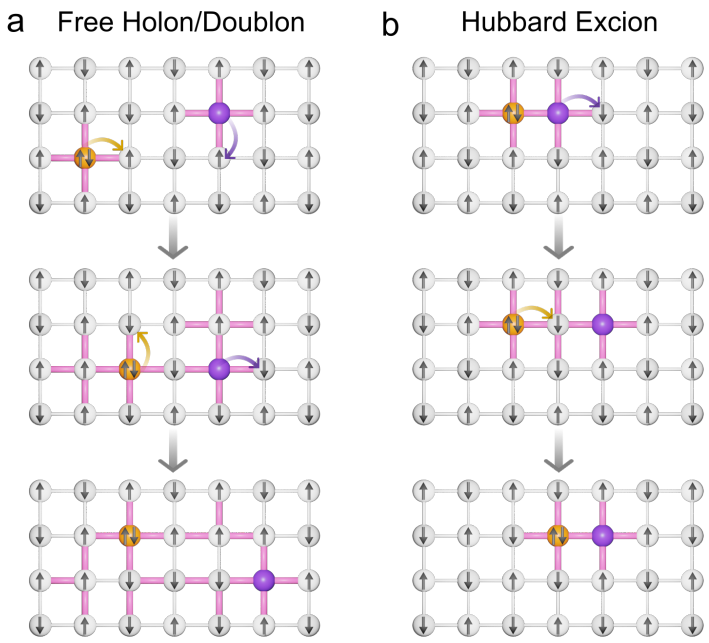

Figure 1.5: Schematic of Hubbard exciton formation. **a** Schematic of a free holon (purple) and a free doublon (orange) moving through a square lattice with AFM interactions. With each hopping action away from its starting position (top panel), the length of the string will increase (middle and bottom panels). Excited bonds are shown in magenta. **b** Schematic of a HE moving in a square lattice with AFM interactions. When the holon (purple) hops away from the doublon (orange) (middle panel), it will increase the length of the string of magnetic excitations compared to its original position (top panel). However, if the doublon coherently follows the holon (bottom panel), it will repair the spin excitations, maintaining the overall cost to the spin sector. Excited bonds are shown in magenta.

Hubbard model [83] have directly visualized both the formation of spin polarons [102, 121] as well as the formation of geometric strings [43]. These efforts have been expanded to explicitly demonstrate the magnetically-mediated formation of two-holon bound states [91]. Theoretical calculations have supported these results, demonstrating that charge carriers indeed gain energy by coherently following one another in antiferromagnetic Hubbard systems [28, 84].

1.3.1 Hubbard excitons

These notions of magnetically mediated pair formation were initially motivated to explain the presence superconductivity in chemically doped Mott antiferromagnets [84]. However, they have also been invoked to predict the presence of bound carriers that are unique to photo-doped antiferromagnetic Mott insulators [28, 46, 84, 94,

129, 130, 202, 242]. When a photo-excitation is resonant with the Mott gap, a holon and a doublon are simultaneously created. These two charge carriers can interact with one another via the same string-binding mechanism since—just like holons—doublons also generate strings as they travel through the lattice (Figure 1.5a). The bound state that results from this interaction between a holon and a doublon is known as a Hubbard exciton (HE) (Figure 1.5b). Unlike conventional excitons in weakly correlated rigid-band semiconductors—which are purely bound through Coulomb interaction—the properties of HEs are theoretically predicted to depend sensitively on the magnetic degrees of freedom that bind them [28, 46, 84, 94, 129, 130, 202, 242]. Numerical studies have revealed that excitons should host rich internal structures [129, 130], which spectra and binding energies that are dependent on J [94, 242]. The excited levels in these spectra have been shown to be vibrational and rotational modes of the string that connects the holon and doublon [84]. Moreover, the dynamics of HEs have been predicted to be intimately related to the magnetic degrees of freedom as well [129, 130]. Unlike Coulombic excitons—which tend to recombine radiatively or through exciton-exciton interactions—HEs are thought to recombine through multi-magnon emission, reflecting the strong spin-charge coupling in these systems. The radii and masses of HEs are also predicted to be correlated with the strength of the magnetic interactions in the system [94].

Experimentally, however, many basic questions about HEs remain unresolved. The reason for his experimental uncertainty is the lack of clear spectral probes of HEs in real compounds. Traditionally, excitons are detected in the optical spectra of materials as a series of peaks below the optical band gap—known as the free particle continuum—which marks the energy at which free electrons and holes are generated by light [113, 232]. The excitonic peaks are often sharp and well-separated from the continuum, indicating that they are stable against decay intro free carriers. Observations of these excitonic states are quite ubiquitous within the study of weakly correlated rigid band insulators [11, 12, 16, 17, 59, 74, 112, 113, 152, 156, 160, 190, 220, 246], ranging III-V semiconductors to transition-metal dichalcogenides to molecular systems. On the other hand, spectral fingerprints of HEs have only been observed in a small handful of compounds [4, 80, 86, 142, 172, 221, 233], and demonstrate characteristics that have called into question as to whether they are stable quasiparticles. Most importantly, peaks in equilibrium optical spectra that have been interpreted as HE states are not well-separated from the free holon-doublon continuum [80, 86, 202, 233], implying that the excitons are unstable against decay into free carriers [202].

The uncertainty with regards to Hubbard excitonic stability poses several important open questions, and creates experimental challenges that must be overcome. First, it is unclear what role HEs play in the photo-excited state and dynamics of Mott antiferromagnets. In photo-doped semiconducting systems, the free carriers initially generated by the pulse of light will begin to decay towards the band edge through intra-band relaxation processes [105, 249]. However, the return to equilibrium—marked by the recombination of all photo-excited holes and electrons—is bottlenecked by the large amount of energy that must be emitted to overcome the charge gap. In the interim, excitons form to lower the total energy, creating a photo-excited insulating state [105, 106, 249]. In the case of Mott insulators, however, it is unknown whether excitons will form during the evolution of the photo-excited state owing to their proximity to the holon-doublon continuum. This question is not only important to understanding the recombination pathways of photo-excited Mott systems, but has important implications on the dynamics of the magnetic subsystem as will be discussed in the following chapters. Second, while theoretically predicted, the spin-binding mechanism has not been experimentally confirmed to drive the formation of HEs. Since holons and doublons are oppositely charged, they should also be prone to forming bound states due to the Coulomb interaction. Thus, it is unclear to what extent the magnetic interaction is responsible for exciton formation in real Mott insulators.

1.4 Current progress in photo-doped Mott antiferromagnets

We conclude this introduction with a brief overview of current progress in photo-doped antiferromagnetic Mott insulators. Specifically, our attention will be focused on the parent phases of the copper-oxide family of Mott insulators that demonstrate high-T_c superconductivity, as well as the material Sr_2IrO_4 which demonstrates much of the same phenomenology upon chemical doping. While the cuprates have been studied somewhat extensively using out-of-equilibrium optical techniques, the vast majority of the efforts have focused on the dynamics of materials that have already been chemically doped out of the Mott insulating state and into the superconducting regime. Instead, the efforts of this thesis are focused on understanding the effects of photo-doping on the Mott insulating state, which is relatively under-studied.

To this end, we organize the section as follows. First, we will introduce the material Sr_2IrO_4 as a model Hubbard system. We focus our discussion on Sr_2IrO_4 because it is the primary platform upon which the work presented this thesis was performed. A more exhaustive review can be found in Reference [23]. The cuprate phenomenology

has been reviewed extensively elsewhere [18, 49, 126]. Second, results pertaining primarily to charge degrees of freedom after photo-doping will be presented. Finally, we will conclude by examining the evolution of the magnetic properties in these systems following the photo-doping process.

1.4.1 Sr_2IrO_4 as a model Hubbard system

Historically, $5d$ transition metal oxides were not considered to be candidates for Mott insulating physics. The large spatial extent of the valence electron wave functions in these systems increase sufficiently increase the overlap between neighboring sites—and ultimately the electronic bandwidth—such that the strong-coupling regime cannot be reached. However, unlike the more localized $3d$ transition metal oxides that traditionally host Mott insulating phases, the heavy atomic weights in $5d$ systems like the Iridates generate strong spin-orbital coupling (SOC) that has profound impacts on the electronic structure. Importantly, they can reduce the bandwidth of the valence band enough such that a moderate value of U can induce a Mott instability.

To understand this SOC-driven Mott transition, we begin with a description of the microscopic structure of Sr_2IrO_4. This d^5 material has a K_2NiF_4 structure, isostructural to La_2CuO_4 [37]. As such, it hosts a quasi-2D structure, with Ir-O planes separated Sr atoms. The Ir-O planes are composed of a square lattice of Ir atoms, each of which are surrounded by an octahedral cage of O atoms which form a corner-shared network. Due to the crystal fields of the octahedral cage, lifts the five degenerate d orbitals of the Ir atoms into three lower orbitals with t_{2g} symmetry and two higher orbitals with e_g symmetry separated by the crystal field energy $10Dq$ [1]. Since the crystal field splitting is large, the system organizes into the low-spin configuration in accordance with the Aufbau principle. Thus, two of the t_{2g} orbitals are filled and one is half filled, while both e_g orbitals remain empty [1, 115]. The bandwidth of the valence band formed from the partially-filled t_{2g} orbitals is much too large (~ 1 eV) for the moderate on-site Coulomb interaction of ~ 2 eV to induce a Mott transition [115].

The orbital angular momentum L in the t_{2g} states is partially quenched owing to a relation known as the $T-P$ equivalence [209], which shows that the matrix elements of $L = 2$ the t_{2g} states can be mapped onto the p states of free atoms with $L = 1$ character. Thus, the t_{2g} form an effective angular momentum $L_{eff} = 1$ subsystem with $L_{z,eff} = -1, 0, 1$. Since there are five electrons in the low-spin configuration.

Including the effects of SOC, which is quite strong in this system ($\sim$ 0.5 eV), the t_{2g} orbitals will further split into a lower $J_{eff} = 3/2$ quartet and a $J_{eff} = 1/2$ Kramers doublet [1, 115]. The former is completely filled, while the latter hosts one electron and is half-filled. Note that, though Hund's rules seem to be broken by the fact that the $J_{eff} = 1/2$ orbital is higher in energy than the $J_{eff} = 3/2$ orbitals, its true (non-effective) angular momentum is actually $J = 5/2$, while the true angular momentum of the $J_{eff} = 3/2$ quartet is still $J = 3/2$ [115]. Importantly, the bandwidth of this new $J_{eff} = 1/2$ valence band is greatly reduced ($\sim$0.5 eV) as compared to that of the original t_{2g} bands, allowing for the moderate U to induce a Mott transition. Thus, the $J_{eff} = 1/2$ splits into a filled LHB and an empty UHB. The resultant density of states and corresponding optical conductivity of Sr_2IrO_4 is shown in Figures 1.6a and b, respectively. Two broad peaks appear in the optical conductivity at $\sim$ 0.5 eV and $\sim$ 1.0 eV [115, 161, 199, 244]. The former, known as the α peak, represents the transition from the $J_{eff} = 1/2$ LHB to the $J_{eff} = 1/2$ UHB. The latter, known as the β peak is predominantly formed by transitions from the $J_{eff} = 3/2$ band to the $J_{eff} = 1/2$ UHB [115, 244].

An important consequence of the SOC-mediated Mott transition is that each Ir site hosts a localized moment with $J_{eff} = 1/2$ character [1, 23, 115, 116]. These moments are formed even in the absence of long-range magnetic order, as is typical for a Mott insulator. Importantly, they serve the same role as the $S = 1/2$ moments in the cuprates, and we refer to them as the pseudospin hereafter. They interact with one another via superexchange through the O sites, endowing them with the usual antiferromagnetic Heisenberg interactions [101]. Indeed, as measured through resonant inelastic x-ray scattering (RIXS), Sr_2IrO_4 demonstrates pseudospin dynamics that are remarkably similar to that of La_2CuO_4 [117], which is known to be a nearly ideal Heisenberg antiferromagnet. However, strong SOC and tetragonal slightly affect the low-energy pseudospin dynamics [23], with the most significant impact being a large out-of-plane spin wave gap that reflects a moderate XY anisotropy present in this system [229]. Nevertheless, it is remarkable that the in-plane spectrum Sr_2IrO_4 is so well-described by the Heisenberg model [70, 117] despite the fact that its SOC is orders of magnitude larger than in the cuprates, and it is clear that strong-coupling theories accurately describe the pseudospin dynamics. Altogether, it is well-established that Sr_2IrO_4 is a SOC-driven, quasi-2D Mott insulator pseudospin-1/2 moments that demonstrate strong Heisenberg-like interactions. Moreover, unlike the cuprates which are actually charge-transfer insulators, Sr_2IrO_4 is a true manifestation of the single-band Hubbard model and thus serves as an

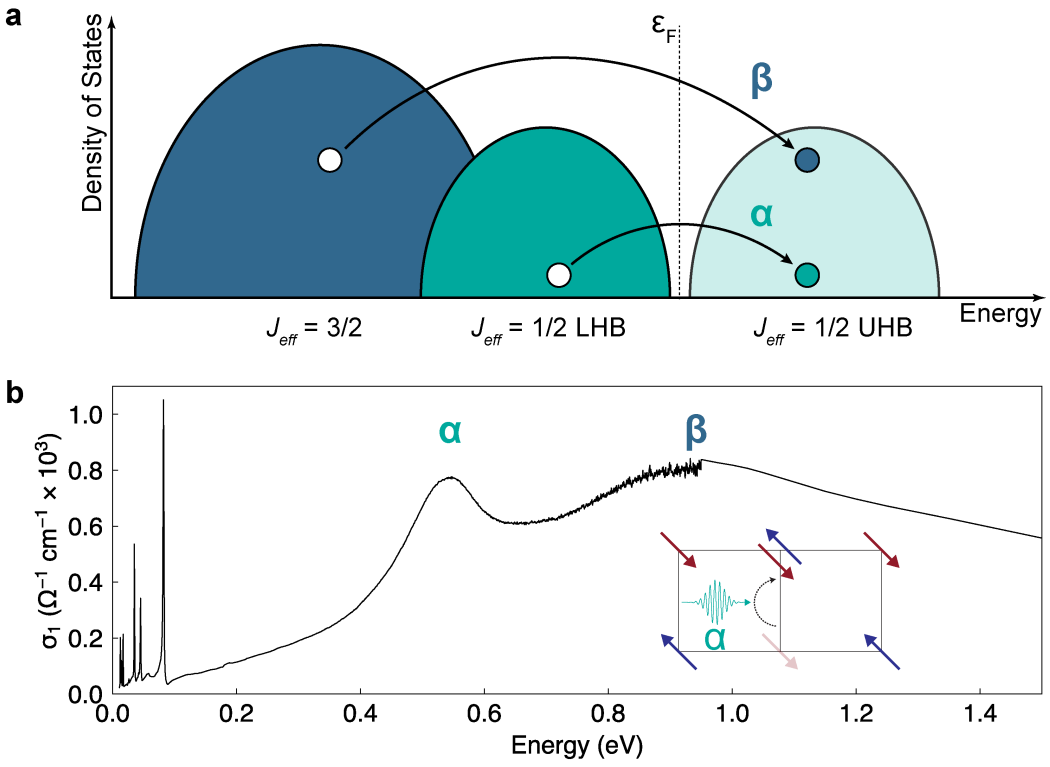

Figure 1.6: Electronic structure of Sr_2IrO_4. **a** Electronic density of states of Sr_2IrO_4. The $J_{eff} = 1/2$ LHB $\rightarrow J_{eff} = 1/2$ UHB (α) and $J_{eff} = 3/2 \rightarrow J_{eff} = 1/2$ UHB (β) transitions are shown as arrows and labeled. **b** Optical conductivity of Sr_2IrO_4 [199]. Peaks corresponding to the α and β transitions are labeled. Inset: Real-space depiction of a photo-excitation resonant with α. A doubly occupied site (doublon) and an empty site (holon) are simultaneously created.

excellent starting point for the study of photo-doping effects.

1.4.2 Electronic dynamics

Pioneering work was performed by Matsuda *et al.* in 1994 [148], who were the first to study the femtosecond scale photo-doping dynamics in insulating cuprates. They used a time-resolved white light spectroscopy technique in the transmission geometry to study the evolution of the charge-transfer peak—which marks the transition from the copper bands into the oxygen bands—following the injection of holons and doublons using an above-gap driving pulse. They found that the transmission rapidly drops following the photo-excitation process, indicating the formation of transient metallic behavior. Interestingly, they saw that the relaxation back towards equilibrium occurred on a rapid timescale, with the initial decay of the photo-induced signal occurring between 0.6 to 0.9 ps. This ultrafast decay could not be explained by the

typical radiative recombination observed in semiconducting compounds. Instead, they conjectured that it could be explained by the ultrastrong coupling between spin and charge in these compound: the photo-excited holons and doublons recombined by emitting their excess energy into the magnon bath.

This result was the first glimpse of a recurring theme in the study of photo-doped Mott insulators. Namely, these systems nearly universally demonstrate ultrafast dynamics that can only be explained by invoking the physics of strong coupling between the spin and charge degrees of freedom. Building upon this seminal work, Okamoto *et al.* [178, 180] published a series of results in which they analyzed the photo-induced spectra of La_2CuO_4 and Nd_2CuO_4 under varying pumping conditions, probing conditions, and with much faster time resolutions (40 fs) than the earlier work. Several important outcomes of the photo-doping process were identified. First, they found that not only was the decay time of the photo-induced signal fast, but so was the rise time. The system entered its photo-induced metallic state on time scales much faster than the instrumental time resolution of 40 fs. Second, by comparing the photo-induced spectrum against that of a chemically doped sample, they deduced that the photo-dopants were inducing a Mott insulator-to-metal transition. The metallic phase decays rapidly, within 40 fs, owing to intraband relaxation effects. Finally, following the relaxation of the photo-induced metallic state, they identified the formation of two mid-gap peaks, which they assigned to polaronic origins. They examine the dynamics of these peaks in each material and relate them to the electron-phonon coupling strengths.

From these works, we can draw several conclusions. First, the photo-doping process will induce a transient metallic response in the material owing to the injection of photo-dopants. There are some signatures that this metallic response replicates that of chemical doping, but that the photo-doped system will rapidly evolve thereafter as the carriers localize via intra-band relaxation processes. The subsequent recombination dynamics of these carriers must be understood in terms of strong coupling with the phononic and magnonic baths. It turns out that this general phenomenology is rather ubiquitous within the study of Mott insulators. Similar dynamics have been demonstrated in Sr_2IrO_4. Piovera *et al.* [186] studies the photo-dopant dynamics of this compound using photo-emission techniques. Similar to the cuprates, they found that a metallic state was generated immediately following the pump pulse, and rapidly decayed into in-gap states near the chemical potential. However, unlike the cuprates, Hsieh *et al.* [92] found that the ultrafast decay times depend sensitively

on the presence of antiferromagnetic order. This behavior was interpreted in light of the intermediate coupling character of Sr_2IrO_4.

1.4.3 Magnetic dynamics

When discussing the single hole problem, we noted that the motion of a holon scrambles the antiferromagnetic motif by creating spin excitations. One can imagine that beyond a certain threshold of dopants, long-range order can no longer be supported as the spin configuration will be sufficiently disrupted. This phenomenology is rather apparent in chemically doped compounds, as the magnetic ordering temperature is suppressed immediately upon the introduction of dopants. Beyond a critical doping value, long-range order melts and the system is paramagnetic at all temperatures. Interestingly, however, short-range correlations remain persistent in this paramagnetic regime in both the cuprates and Sr_2IrO_4, as denoted by the continued presence of a magnetic excitation spectrum.

Aspects of this phenomenology are reproduced in the photo-doped case. Dean *et al.* [55] used resonant x-ray scattering techniques to study the magnetic dynamics in Sr_2IrO_4 following a drive resonant with the Mott gap (0.6 eV pump photon energy). By first tracking the evolution of the magnetic Bragg peak, they found that the long-range magnetic order is suppressed and fully melts beyond a critical fluence of ~ 5 mJ/cm^2. Moreover, they measure the scattered photons as a function of momentum transfer, energy loss, and time to track the evolution of the entire magnon spectrum, thereby elucidating the behavior of the short-range magnetic correlations following the drive. Similar to the chemical doped system, the magnetic excitation spectrum survives even in the photo-induced paramagnetic regime.

Similar results were produced with ultrafast optical probes. de la Torre *et al.* [54] used time resolved second harmonic generation polarimetry to track the evolution of the magnetic order parameter following a photo-doping drive (1.0 eV pump photon energy). This technique will be discussed in Chapter 2. They found that, similar to the work by Dean *et al.*, the magnetic order parameter disappears. However, they found that this occurs beyond a critical fluence of 0.9 mJ/cm^2. Afanasiev *et al.* [2] were able to observe the demagnetization using the magneto-optical Kerr effect and studied the relationship between the charge dynamics and the demagnetization dynamics as a function of temperature.

Finally, an important point to note from these three studies is that the value of the critical fluence is different in each report. This fact is likely due to the use of different

pump photon energies for each experiment. As a result, each experiment creates transitions between different bands, and likely produces different photo-induced states. This notion showcases a unique opportunity of photo-doping, as chemical doping can only affect the valence and conduction bands. As of now, however, the microscopic mechanisms that drive these differences are not yet understood.

1.5 Overview of the results

In this introduction, we have laid out many open questions surrounding the properties of photo-doped Mott insulators. We summarize these questions here:

- **Charge instabilities in the photo-doped state:** Unlike chemical doping, the photo-doping process simultaneously creates a hole-like and electron-like excitation. It is currently unknown whether interactions between the two can result in the formation of excitons or other charge instabilities, and if so, how these excitons affect the dynamics of the photo-induced states.

- **Properties of spin-bound excitons:** In two-dimensional spin-1/2 antiferromagnetic Mott insulators, excitons are theoretically predicted to be bound through the antiferromagnetic spin-exchange interaction. Many open questions about these HEs remain experimentally unresolved. In particular, it is unknown whether they are stable bound states, and to what extent the spin-exchange interaction is necessary for their formation.

- **Dynamics of antiferromagnetic order:** A central topic of investigation in photo-doped Mott antiferromagnets is the evolution of the long-range magnetic order. While ultrafast demagnetization has been theoretically predicted experimentally observed predicted, a full picture of the non-equilibrium dynamics remains unclear. Particularly important questions are how bound states would affect the transient magnetic properties, and the effects of photo-doping from different bands.

- **Nonlinear holon-doublon generation mechanisms:** Nonlinear holon-doublon generation is possible through intense subgap driving with an AC electric field. Direct experimental tests of the resultant photo-carrier dynamics and momentum space distributions remain elusive. A detailed ultrafast spectroscopic study of Mott insulators subject to intense electric fields is thus an important question in the field of photo-doping and the general research area of light-matter interactions in strongly correlated electron systems.

In the remaining chapters of this thesis, we present results from a series of experiments designed to answer each of these questions. In Chapter 2, we present the experimental details of the ultrafast spectroscopic tools that enable these studies. In Chapter 3, we report the transient formation of a Hubbard excitonic fluid in Sr_2IrO_4

using ultrafast terahertz conductivity. This result establishes not only the metastability of HEs, but reveals the role that they play in the evolution of photo-doped state. In Chapter 4, we build upon these results to establish that magnetic correlations are critical to the existence of HEs in the Ruddlesden-Popper series iridates $Sr_{n+1}Ir_nO_{3n+1}$. We do this by leveraging the differences in the magnetic universality classes of the different elements in the series, which endow them with distinct magnetic critical properties. The attention is turned towards the effects of photo-doping on antiferromagnetic order in Chapter 5. By using time-resolved second harmonic polarimetry as a probe of the magnetic order parameter, we establish that photo-doping from different bands will melt the magnetic order at different rates. We attribute this effect to the fact that different photo-doping processes will create different ratios of holons, doublons, and HEs, each of which impacts the AFM motif differently. Finally, in Chapter 6, we move away from resonant excitation to explore the effects of subgap driving on Mott insulators and their photo-excited properties. We find signatures of the so-called Keldysh crossover from a multiphoton-absorption- to quantum-tunneling-dominated pair production regime, and demonstrate that the momentum space distribution of the charge carriers can be controlled using this criterion. We also find signatures of ultrafast bandwidth renormalization.

Chapter 2

ULTRAFAST SPECTROSCOPY OF MOTT INSULATORS

Experimentally, photo-doping is enabled by femtosecond laser technologies. While the energy of a continuous-wave (CW) laser is distributed over all time, the energy in these pulsed sources is compressed into femtosecond bursts of light. As a result, the peak electric field within each of these pulses is much higher than what can be achieved in a CW source, while simultaneously benefiting from significantly lower average heating. This unique set of properties creates the opportunity to drive materials using strong electric fields while preventing the sample from being destroyed by heat. The myriad light-matter interactions that emerge as a result can be leveraged to engineer materials.

While the photo-doping process is conceptually quite simple, probing the resulting state of matter is a much more complicated affair. When a correlated electron system is driven with an intense pulse of light, many microscopic degrees of freedom will simultaneously be affected either through the light itself or through interactions with one another. Probing this highly non-equilibrium state is a challenge because different reporters for each of the affected degrees of freedom is needed. Indeed, a serious effort has been undertaken in the past decades to develop a vast portfolio of ultrafast spectroscopic tools to monitor the evolution of the photo-induced phase of matter, each of which is sensitive to different material properties. Similar to the astronomical principle of multi-messenger spectroscopy—in which the details of an astronomical event are pieced together through various reporters spanning from light to neutrinos to gravitational waves—simultaneously probing several degrees of freedom in a driven solid state system allows us to paint a picture of the dynamical light-induced phase.

With regards to our specific task of photo-doping Mott systems, the relevant degrees of freedom are charge and spin. As such, we employ a suite of techniques sensitive to both of these degrees of freedom. For the former, we employ a combination of time-resolved time-domain THz spectroscopy (tr-TDTS) and transient reflectivity. These tools allow us to probe changes in the optical conductivity following the photo-doping drive across a broad range of frequencies spanning from the THz to the visible. Both techniques also boast the ability to detect and track bosonic

excitations of different ordered subsystems in the material. To track the magnetic subsystem, we utilize time-resolved second harmonic polarimetry, which can detect the presence of long-range order through its impact on the material's nonlinear optical susceptibility tensors.

In the following, we introduce the principles of ultrafast optics by providing an overview of the laser system used in this thesis. We then describe the optical properties of strongly correlated electron systems and the various features that one can expect in optical spectra. Finally, we provide a detailed description of each of the probes utilized in the results reported in the remaining chapters. However, before delving into the details of ultrafast experiments, we begin by introducing the principles of second order nonlinear optics. This subject is crucial to understanding many of the physical principles that underpin the techniques used in this thesis.

2.1 Prelude: Second-order nonlinear optics

Nonlinear optics is a class of light-matter interactions that describes situations in which materials respond nonlinearly to the application of light. These effects are usually only observable for high electric field strengths, making them especially relevant when dealing with amplified femtosecond pulses. We are especially interested in second-order nonlinearity, which gives rise to a wealth of phenomena that enable the functionality of our laser systems, the driving protocols used to create the out-of-equilibrium states, and the probing techniques used to monitor them. Usually, the material property of interest is the optical polarization, and so we begin our treatment with a definition of this quantity. Our treatment will closely follow the discussion in Reference [6].

The electric flux density $\mathbf{D}$ is defined as

$$\mathbf{D} = \varepsilon_0 \mathbf{E} + \mathbf{P} \tag{2.1}$$

where ε_0 is the permittivity of free space, $\mathbf{E}$ is the electric field of the light and $\mathbf{P}$ is the optical polarization in the material. In the linear response regime, $\mathbf{P}$ is directly proportional to the electric applied electric field:

$$P = \varepsilon_0 \chi_e E. \tag{2.2}$$

Here, χ_e is the electric susceptibility of the material. In the linear response, the susceptibility is a scalar. For now, we also assume that the polarization and the

electric field are scalars for simplicity. Moving beyond the linear regime, we can write the polarization as

$$P = \varepsilon_0 \left[\chi^{(1)} E + \chi^{(2)} E^2 + \chi^{(3)} E^3 + \cdots \right]. \tag{2.3}$$

Here, $\chi^{(1)}E$ represents the linear term, while the terms proportional to multiple factors of E are the nonlinear terms. Their coefficients $\chi^{(n)}$ are tensors known as the n-th order susceptibilities.

We now narrow our focus towards the second-order linearity, featuring the second-order susceptibility $\chi^{(2)}$ and two input electric fields. In the general case, these electric field can have different frequencies ω_2 and ω_2, giving

$$E = \frac{1}{2} \left[\tilde{E}(\omega_1) e^{i\omega_1 t} + \tilde{E}(\omega_2) e^{i\omega_2 t} + \text{c.c.} \right]. \tag{2.4}$$

Expanding the nonlinear polarization given from the second-order term gives

$$\begin{aligned} P^{(2)}_{NL} = & \frac{\varepsilon_0}{4} \{ \chi^{(2)}(2\omega_1 : \omega_1, \omega_1) \tilde{E}^2(\omega_1) e^{i2\omega_1 t} + \chi^{(2)}(2\omega_2 : \omega_2, \omega_2) \tilde{E}^2(\omega_2) e^{i2\omega_2 t} \\ & + 2\chi^{(2)}(\omega_1 + \omega_2 : \omega_1, \omega_2) \tilde{E}(\omega_1) \tilde{E}(\omega_2) e^{i(\omega_1+\omega_2)t} \\ & + 2\chi^{(2)}(\omega_1 - \omega_2 : \omega_1, -\omega_2) \tilde{E}(\omega_1) \tilde{E}^*(\omega_2) e^{i(\omega_1-\omega_2)t} \\ & + \chi^{(2)}(0 : \omega_1, -\omega_1) \tilde{E}(\omega_1) \tilde{E}^*(\omega_1) + \chi^{(2)}(0 : \omega_2, -\omega_2) \tilde{E}(\omega_2) \tilde{E}^*(\omega_2) \} \\ & + \text{c.c.} \end{aligned} \tag{2.5}$$

It is clear that the second-order nonlinearity mixes the input fields, resulting in several terms. The parenthetical notation following the instances of $\chi^{(2)}$ in Equation 2.5 indicates which fields are being mixed, and the resultant frequency of the output field. For example, $\chi^{(2)}(\omega_1 + \omega_2 : \omega_1, \omega_2)$ indicates that the two input fields have frequencies ω_1 and ω_2, while the output field has frequency $\omega_1 + \omega_2$. Four different frequency mixing effects can be seen in Equation 2.5, which we have organized by line. The $2\omega_1$ and $2\omega_2$ terms are known as second harmonic generation, the $\omega_1 + \omega_2$ and $\omega_1 - \omega_2$ are known as sum and difference frequency generation, respectively, and the zero frequency terms are known as optical rectification. Each of these terms will play an important role in this thesis: sum and difference frequency generation enable the photo-doping driving protocols, optical rectification underpins the generation of

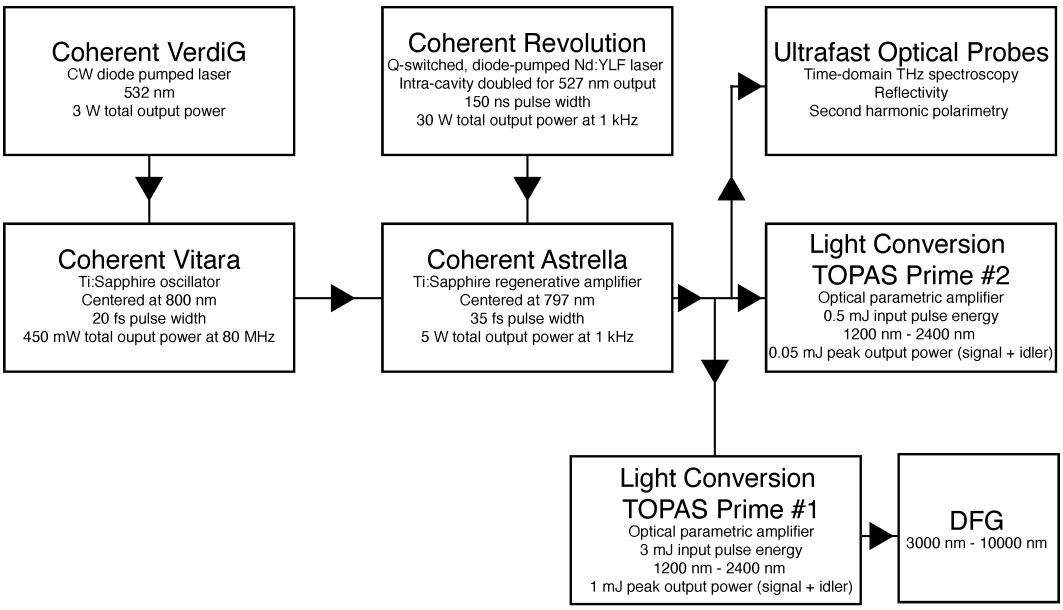

Figure 2.1: A schematic depicting the various elements that comprise the amplified femtosecond laser system used in this thesis.

the THz frequencies with which we will probe low-energy electronic dynamics, and second harmonic generation enables the second harmonic polarimetry technique with which we will detect changes to the magnetic order parameter. Accordingly, each of these second-order nonlinearities will be discussed in more depth as we approach each of these experimental techniques later in this chapter.

2.2 A brief introduction to ultrafast optics

A femtosecond laser source is comprised of a series of lasers that work in tandem to produce the final intense ultrafast pulse train. A schematic of the specific laser system used in the majority of this thesis is shown in Figure 2.1. Our specific model is the Coherent Astrella. This system is a Ti:Sapphire-based regenerative amplifier that produces 1 kHz pulse train of 35 fs pulses centered at 800 nm with 5 W of total output power. However, while we will describe the specifics of our laser setup, the general structure of this apparatus is quite general and applies to most commercial femtosecond laser sources in use today, as do the physical principles that its operation is based on. Our discussion will closely follow that of Reference [6], within which much more detail can be found about each of the presented subjects.

2.2.1 Generating femtosecond pulses: The oscillator

The journey begins with the Coherent Verdi-G, which is a CW diode-pumped green laser centered at 532 nm. This source pumps the gain medium in a Ti:Sapphire laser oscillator system that is capable of producing femtosecond pulses. Our specific model is the Coherent Vitara, which produces pulses with a 70 nm bandwidth. The method by which the oscillator system produces a femtosecond pulse train is known as mode locking.

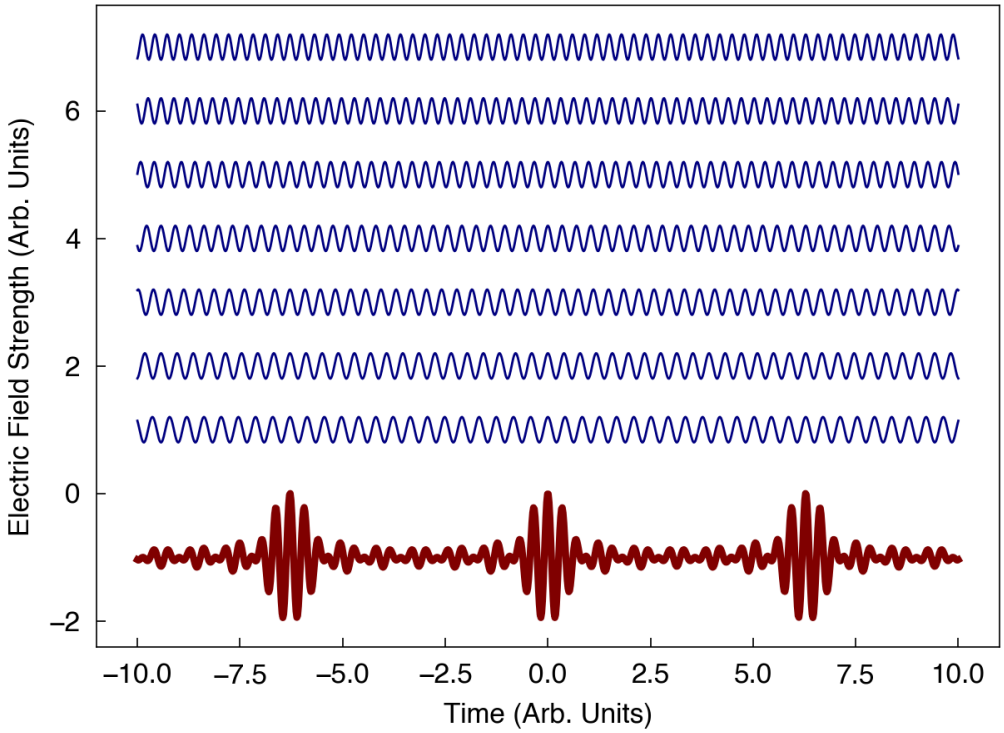

Figure 2.2: A depiction of the principle of mode locking. Seven oscillations (blue) of different but equally separated frequencies constructively interfere when phase-locked to produce a train of short pulses (red).

To understand mode locking, we must first understand the factors that determine the frequency content of a laser. The first determining factor is the geometry of the laser cavity. To be specific, here we consider the simplest case known as the Fabry-Pérot cavity which consists of two mirrors facing each other. Such a cavity is capable of only hosting certain, discrete frequencies of light due to constraints on the phase of the light as it makes a round trip through the cavity. These frequencies are given by

$$f_m = \frac{mc}{2l} \tag{2.6}$$

where m is an integer, c is the speed of light, and l is the length of the cavity (the distance between the two mirrors). These are known as the longitudinal modes of the laser cavity. The spacing between each mode is given by

$$\Delta f = f_{m+1} - f_m = \frac{c}{2l}. \tag{2.7}$$

The second factor that determines the frequency output of the laser is the frequency bandwidth of the gain medium. If the bandwidth is broad enough, several longitudinal modes will be included in the output spectrum of the laser. We denote the total number of modes included in the bandwidth as N. When these modes have no fixed phase relationship with one another, they can be treated as a series of independent emitters and their collective output intensity will fluctuate randomly over a characteristic timescale of $1/N\Delta f$. However, if an optical element is introduced to fix the phase of each emitter, then they will constructively interfere to produce an intensity profile consisting of a periodic series of short pulses (Figure 2.2). The period of this pulse train will be $1/\Delta f$, while the duration of each pulse is approximately $1/N\Delta f$. The Coherent Vitara used in our laboratory has a period of 12.5 ns between pulses, corresponding to a frequency spacing of 80 MHz. Since Ti:Sapphire has a bandwidth of roughly 10^{14} Hz, more than 10^6 longitudinal modes can potentially be supported. Thus, the minimum pulse width that can be achieved is $\sim$10 fs. In typical systems, however, oftentimes the full bandwidth of the Ti:Sapphire crystal is not achieved in the final pulse, reducing the total number of modes. For example, the factory specifications for our Vitara quote a bandwidth of 70 nm and a pulse width of < 20 fs.

Having conceptually described the principle of mode locking, we are now ready to address how is practically accomplished within the oscillator. To fix and stabilize the phase between the longitudinal modes, an optical element must be included in the cavity that will modulate the light as a function of time. The simplest method to accomplish this is known as active mode locking, in which an external electrical signal is used to drive a modulator, such as an amplitude modulator. If the amplitude modulator is driven to act as a shutter that "opens" once per round trip within the cavity τ, allowing just a single pulse to pass back and forth within the cavity. In the frequency domain, this driving serves to generate side bands of the longitudinal modes at $f_m \pm n\tau$ where n is an integer. Since all the side-bands are generated by the same driving pulse—hence are driven in phase—each mode f_m will be locked with

its adjacent modes. A major drawback of active mode locking is that its response time is too slow, preventing its use from generating ultrafast pulses.

This drawback can be overcome with passive mode locking. In this technique, a nonlinear optical element is used to modulate the light instead of an externally driven modulator. Due to the nonlinear optical properties of this element, which is known as a saturable absorber, its absorption decreases as the intensity of the light passing through it increases. In this way, the light in the cavity itself can generate the periodic modulation needed to induce mode locking through its interaction with the saturable absorber. In the time domain, the saturable absorber will allow intense spikes of intensity within the cavity to pass while attenuating the CW light that exists outside of these spikes. As the light continues to make round trips through the cavity, these spikes will continue to sharpen and as they interact with the absorber they serve as the time-periodic modulator.

In the Vitara, as well as most commercial Ti:Sapphire lasers with $\sim$ 10 fs pulse widths, a special type of passive mode locking is known as Kerr lens mode locking is used. The optical Kerr effect is a nonlinear optical process in which refractive index of the medium is dependent on the applied field strength:

$$n = n_0 + n_2 I(t) \tag{2.8}$$

where n is the total index of refraction of the material, n_0 is the un-pumped index of refraction, and n_2 is the nonlinear index of refraction. $I(t)$ is the intensity of the light, which is proportional to the modulus squared of the electric field. Since the spatial distribution of the light in the cavity has a Gaussian power distribution, the field is much more intense at the center of the beam. Thus, the light passing through the Kerr medium will create a spatially varying index of refraction, which serves as a lens that focuses the light. In this way, the high intensity modes are focused more tightly within the Kerr medium than the low intensity modes. In the so-called soft aperture operation of a Kerr lens mode locked laser, the gain medium (i.e., the Ti:Sapphire rod) itself acts as the Kerr medium. Thus, the light that is focused more tightly has a better cross section with the pump light in the gain medium—in our case the green light from the Verdi G. As a result, the more tightly focused light is amplified much more strongly than the less tightly focused light. Thus, similar to the saturable absorber, continued round trips will lead to selective amplification of the spikes and serve as a time-periodic modulator of the intensity in the cavity,

leading to mode locking. The benefit of Kerr lens mode locking are the fast response times of the optical Kerr effect (estimated to be 1 or 2 fs) allowing incredibly short pulses to be achieved. Moreover, since the gain medium itself acts as the modulating element, the full bandwidth of the gain medium can be preserved since no additional optical elements must be introduced such as driven optical modulators or saturable absorbers, each of which will have their own bandwidths.

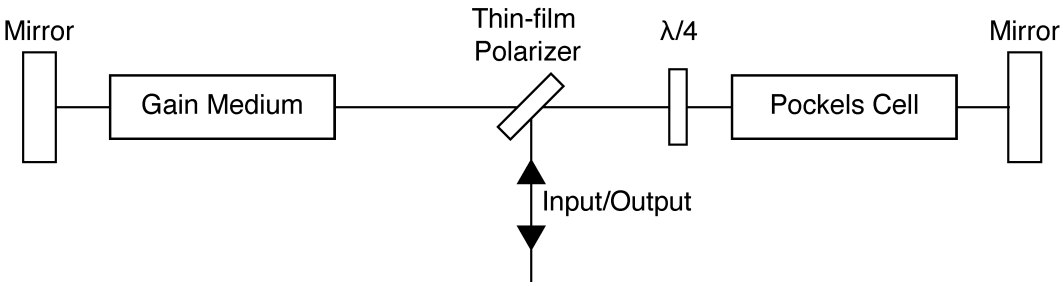

Figure 2.3: Schematic of a cavity in a regenerative amplifier. Adapted from Reference [6].

2.2.2 Amplifying femtosecond pulses: The regenerative amplifier

While the oscillator is able to produce a stable femtosecond pulse train through mode locking, these pulses are quite weak with typical pulse energies on the order of 1 nJ. For the experiments performed in this thesis, pulse energies on the order of 1 mJ are needed to achieve both the requisite pumping conditions and seed the spectroscopic probes. This amplification factor of 10^6 can be achieved in an apparatus known as a regenerative amplifier. The specific model used in the experiments reported in this thesis is the Coherent Astrella. A simple schematic of a generic regenerative amplifier is shown in Figure 2.3. The key elements of the regenerative amplifier cavity are the seed pulse that will be amplified, the gain medium and the laser that pumps it, a polarizing element (P) that reflects light of a certain polarization and transmits the perpendicular polarization, a quarter waveplate ($\lambda/4$), and an electro-optic Pockels cell. A Pockels cell is an optical device whose polarizing properties depend on the voltage applied across it. In the regenerative amplifier, it will either be set for zero retardation, or it will be set to serve as a quarter waveplate.

Regenerative amplification involves three distinct steps designed to first charge the gain medium, then trap the seed pulse within the cavity to enable amplification, and finally to release the amplified pulse [6]:

1. **Charging stage:** The objective of this stage is to allow the gain medium accumulate energy from the pump laser. Any spontaneous emission by the gain medium is first polarized by the polarizer, then is rotated by 90° as it makes a double-pass through the quarter waveplate, and is reflected out of the cavity as it reaches the polarizer again. At this point, the Pockels cell is set to zero retardation.

2. **Amplification stage:** A pulse from the oscillator is directed into the polarizer using a pulse picker. Its polarization is set such that it reflects into the cavity. At this point, the Pockels cell is still set to zero retardation, so when the pulse makes its double-pass through the quarter waveplate its polarization has rotated by 90° so it now transmits through the polarizer towards the gain medium to be amplified. During the time that it the pulse makes its double-pass through the gain medium, before it again reaches the Pockels cell, the retardation is set such that the Pockels cell serves as a quarter waveplate. Now, as the pulse does its double-pass through the quarter waveplate and the Pockels cell, which collectively serve as a half waveplate, its polarization will be unchanged and it will continue to pass through the polarizer. At this point, the pulse is trapped within the regenerative amplifier and will continue to make round trips through the gain medium.

3. **Output stage:** After the desired number of round trips have been performed, the Pockels cell is deactivated before the pulse reaches it. Accordingly, the next double-pass through the waveplate will rotate the polarization of the pulse by 90°, allowing it to reflect off the polarizer and out of the regenerative amplifier.

This regenerative amplification scheme is technically achieved through a process known as chirped pulse amplification. During the amplification process, a challenge arises in that the pulse becomes so strong that it will eventually start to catastrophically damage the optical elements of the amplifier. To overcome this challenge, the pulse is first stretched in time—often up to hundreds of picoseconds—before it enters the regenerative amplifier. In doing so, the overall pulse energy remains the same, but the peak electric field is reduced drastically. This less intense pulse can now be safely amplified. As it exits the amplifier, it is compressed in time again to its original temporal width, resulting in an intense, femtosecond-width pulse. To stretch the pulse, a grating or prism pair is used to separate the different colors within

the broadband pulse. Each color is then sent along a different path, such that longer wavelengths have a shorter path length than the shorter wavelengths. Then, all the colors spatially recombined via a second pass through the grating or prism pair. The resultant pulse—known as a chirped pulse—is now much longer in time since the shorter wavelengths are lagging behind the longer wavelengths. The pulse is compressed by passing through the same prism or grating apparatus but in reverse.

Finally, a note on the gain medium and pumping laser. The gain medium in our amplifier is another Ti:Sapphire crystal. Similar to the oscillator, the gain medium is pumped by a green laser. In the case of the Astrella, the pump laser used in the regenerative amplification cavity is also another pulsed laser in order to maximize the energy stored in the gain medium. This laser is the Coherent Revolution, which is a Q-switched, diode-pumped, intra-cavity doubled Nd:YLF laser with a central output frequency of 527 nm.

2.2.3 Generating different frequencies: The optical parametric amplifier

The amplified pulse that escapes the regenerative amplifier is the starting point for all experimentation in our lab. It not only can be used to drive materials into an non-equilibrium state for us to investigate, but it also serves as the seed for the probes we use for that investigation. However, a limitation of the amplified pulse is that its frequency is fixed by the Ti:Sapphire gain medium at ~800 nm. For many experiments, it is crucial to obtain light at different frequencies in order to be resonant with different features within a material's optical spectrum. For example, when photo-doping, tuning the photon energies allows for control over which bands are being driven. For Mott insulators, relevant energies are often in the infrared and visible regimes. Conveniently, it is possible to generate these energies using the amplified 800 nm pulse via a frequency conversion process known as optical parametric amplification.

The resulting apparatus is known as an optical parametric amplifier (OPA). In our lab, we have two commercial Light Conversion TOPAS Prime OPAs, both of which are capable of producing pulses between 1200 nm and 2400 nm. The first (dubbed OPA 1) receives a 3.5 mJ pulse from the Astrella as an input, generating a peak converted wavelength output of 1 mJ. This OPA is primarily used for driving the samples into an out of equilibrium state, as the pulses are quite energetic. The second OPA (OPA 2) receives a 0.5 mJ pulse from the Astrella, generating a peak output of 0.05 mJ. As such OPA 2 is primarily used to probe the near-infrared

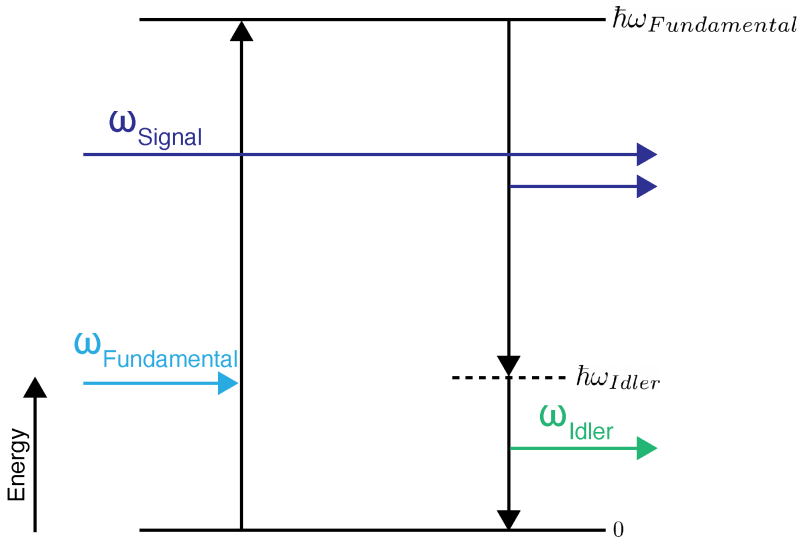

Figure 2.4: Diagram of the optical parametric amplification process.

transient reflectivity response at various photon energies.

The working principle of the OPA is optical parametric frequency conversion, which is a consequence of the second-order nonlinear effects described in Section 2.1. Consider the following relation:

$$\omega_0 = \omega_s + \omega_i. \tag{2.9}$$

This process describes the down-conversion of an incoming photon ω_0 with some energy—known as the fundamental energy—into two other photons ω_s and ω_i—known as the signal and idler, respectively—with lower photon energies that sum to that of the fundamental. As a matter of convention, we denote the output beam with the higher photon energy as the signal that with the lower photon energy as the idler. In practice, parametric amplification is performed by sending photons of two energies—the fundamental and the signal—into a nonlinear crystal. There, the crystal will mediate an interaction that results into the conversion of fundamental photons into two photons with the signal wavelength and the idler wavelength (Figure 2.4. In this way, the signal is effectively amplified. The energy of the signal—and hence that of the idler—can be changed by tuning elements in the optical path of the OPA, as will be seen shortly.

Technically, the OPA is composed of three beams split from the input pulse, which will serve as the fundamental in the parametric amplification. We use the parameters from OPA 1 for concreteness. The first contains 4% of the total input

power is focused tightly onto a piece of sapphire to generate a broadband pulse via supercontinuum generation, a nonlinear optical process in which an intense femtosecond pulse generates an ultra-broadband spectrum of energy running from the near infrared through visible. Importantly, it contains within its bandwidth the signal wavelength. The second section (16% of the power) of the fundamental is directed onto a nonlinear crystal along with the white light pulse at a non-collinear angle. Before they reach the crystal, one pulse is delayed with respect to the other. This is done in order to tune which portion of the supercontinuum pulse—which is chirped—interacts with the fundamental, thereby selecting the signal wavelength. This selection can be buttressed by tuning the polar rotation angle of the nonlinear crystal which affects the phase-matching between the two wavelengths. Since the two pulses are non-collinearly incident onto the crystal, they can be spatially separated after the amplification process. The residual fundamental and idler are blocked. The signal proceeds to a second nonlinear crystal for a second amplification stage with the remaining 80% of the fundamental power. Again, the efficiency of the parametric amplification process can be controlled via the temporal delay between the signal and the fundamental and the angle of the nonlinear crystal. Following the second amplification stage, which is performed in the co-linear geometry, the residual fundamental is blocked with a filter and the signal and idler are separated with a wavelength separator.

Both the signal and the idler can directly be used in the experiments. However, it is possible to reach even longer wavelengths using a differential frequency generation (DFG) apparatus. Performed outside of the OPA, this is done by directing both the signal and the idler onto another nonlinear crystal, where their frequencies are mixed to give their difference $\omega_{DFG} = \omega_s - \omega_i$. The DFG in our lab technically allows us to access wavelengths up to 10 μm, but the power becomes quite weak above 5 or 6 μm, preventing use of these longer wavelengths in most experiments.

2.3 Interlude: Optical spectroscopy of solids

Optical spectroscopy is an essential tool in the study of condensed matter. Its frequency resolution is unparalleled, even reaching 5 neV in some cases. Moreover, current laser technology can generate photons in the 1 meV to 10 eV range in a laboratory setting. This broad spectral range covers the fundamental energy scales of the microscopic interactions in these systems—and accordingly, the physical phenomena that they produce. Each of these features will impart a unique spectral fingerprint onto the optical spectra in these materials, creating a macroscopic

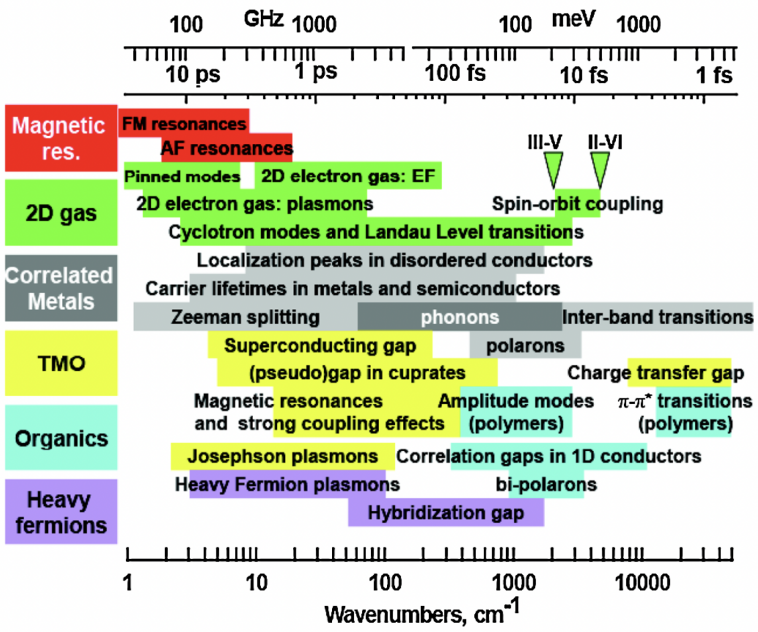

Figure 2.5: A depiction of various processes in correlated electron systems and their typical time and energy scales. Each one of these phenomena has a unique spectral fingerprint that will appear in a material's optical conductivity. From Reference [18].

window to peer into their microscopic nature. These processes include a variety of interband transitions, structural and magnetic bosonic excitations, electronic resonances, excitons, and many more fundamental features of condensed matter systems (Figure 2.5). Optical probes rely on a wealth of different light-matter interactions, each of which are mediated by different degrees of freedom in the material. As a result, by building different probes, different degrees of freedom can be monitored to enable the multi-messenger approach of experimentation. From a practical perspective, several different optical apparatuses can be comfortably built from a single laser system, facilitating this sort of study. This superb energy selectivity and experimental flexibility allows for a careful exploration of the energetic landscape of materials, and has led to significant contributions to our understanding of weakly correlated and strongly correlated electron systems alike.

For the specific use case scenario of photo-doping Mott insulators, optical spectroscopies satisfy the demanding requirements of probing the quantum many-body out-of-equilibrium state. Aside from their sensitivity to both the charge and magnetic degrees of freedom, these techniques can be constructed to resolve the evolution of the photo-doped system as a function of time. By using a pulsed laser source, such

as those described in Section 2.2 and introducing a variable delay between a strong driving pulse—commonly known as the pump—and a weaker probing pulse, the transient response of the material can be stroboscopically recorded. This so-called "pump-probe" scheme of measurement is nearly universally employed in all ultrafast spectroscopic techniques.

2.3.1 A description of optical responses

The primary objective of optical techniques is to leverage the material's electrodynamic response to extract their response functions. A particularly important example is that of the optical conductivity $\tilde{\sigma}(\omega)$ which is the linear response function that describes the current $j(\omega)$ generated by an applied electric field [8]:

$$\tilde{j}(\omega) = \tilde{\sigma}(\omega)\tilde{E}(\omega). \tag{2.10}$$

$\tilde{\sigma}(\omega)$ is a complex quantity, and the real and imaginary parts are referred to as σ_1 and σ_2, respectively. Each of the various excitations generated in solids will have absorption properties that will affect the functional form of $\tilde{\sigma}(\omega)$. To calculate these functional forms, the most commonly implemented method is the Kubo-Greenwood model [8]:

$$\sigma_1(\omega) = \frac{e^2}{(2\pi m)^2\omega}|\langle f|p|i\rangle|^2 D_{fi}(\hbar\omega). \tag{2.11}$$

We see that the conductivity depends on two physical quantities: the dipole matrix element $\langle f|p|i\rangle$ and the joint density of states (DOS) $D_{fi}(\hbar\omega)$. The former considers dipole-active optical transitions from an initial state $|i\rangle$ to a final state $|f\rangle$, and incorporates the effects of symmetry constraints and selection rules into $\sigma_1(\omega)$. The latter accounts for the fact that for an optical transition to occur, there must be a finite density of occupied states at the initial energy, and a finite density of unoccupied states the final energy. Thus, the joint DOS reflects how many optical transitions are available to occur at a given energy, and is determined by the electronic band structure and the carrier distribution.

The imaginary part can be found through the Kramers-Kronig relation [8]:

$$\sigma_2(\omega) = -\frac{2\omega}{\pi}\int_0^\infty d\omega' \frac{\sigma_1(\omega')}{\omega'^2 - \omega^2}. \tag{2.12}$$

Similarly, $\sigma_1(\omega)$ can be found using $\sigma_2(\omega)$:

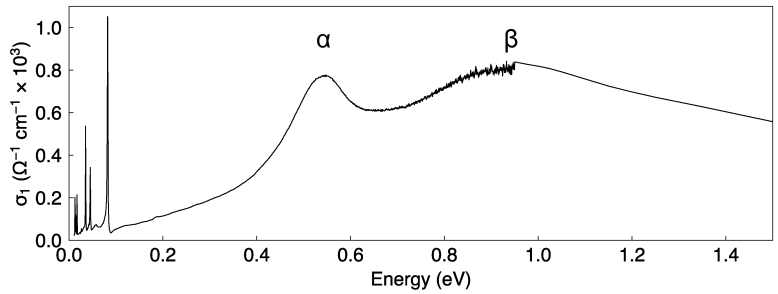

Figure 2.6: Optical conductivity of Sr_2IrO_4 [199]. The $J_{eff} = 1/2$ LHB $\rightarrow$ $J_{eff} = 1/2$ UHB (α) and $J_{eff} = 3/2 \rightarrow J_{eff} = 1/2$ UHB (β) transitions are labeled.

$$\sigma_1(\omega) = \frac{2}{\pi}\int_0^\infty d\omega' \frac{\omega'\sigma_2(\omega')}{\omega'^2 - \omega^2}. \tag{2.13}$$

These Kramers-Kronig relations arise from constraints on the real and imaginary parts of the $\tilde{\sigma}(\omega)$ stemming from the principle of causality. In fact, they apply to any causal response function—including the dielectric function and the index of refraction. Later in this thesis, we will use Kramers-Kronig relations to extract the amplitude and phase of the complex reflectivity form the absolute reflectance. Using $\tilde{\sigma}(\omega)$, we can extract other optical constants. The dielectric function, for example, is given by $\tilde{\varepsilon}(\omega) = \frac{i\tilde{\sigma}(\omega)}{\varepsilon_0\omega}$ [8, 18]. In turn, the index of refraction is given by $\tilde{n}(\omega) = \sqrt{\tilde{\varepsilon}(\omega)}$.

$\tilde{\sigma}(\omega)$ can be measured in multiple ways. For certain frequency regimes, it is possible to perform a phase-resolved measurement of the electric field in the time domain after it reflects or transmits through the sample. By comparing this data to an absolute reference, both the real and imaginary parts of $\tilde{n}(\omega)$, and hence the real and imaginary parts of $\tilde{\sigma}(\omega)$, can be directly extracted without resorting to Kramers-Kronig relations. Technological limitations prevent this sort of phase-resolved detection in the majority of frequency regimes, and is limited to mid- and far-infrared frequencies. For the near-infrared, visible, and ultraviolet regimes, the most common tool is to measure $R_{s/p}(\omega)$ for as broad of a frequency range as possible and to perform a Kramers-Kronig analysis to extract the reflected phase, allowing one to reconstruct the real and imaginary parts of $\tilde{n}(\omega)$ and eventually $\tilde{\sigma}(\omega)$.

2.3.2 Basic features of an optical spectrum

Having understood the physical mechanisms that generate an optical spectrum, we are now in a position to interpret these spectra. In Figure 2.6, we plot the optical conductivity of Sr_2IrO_4 as an example of the spectrum of a prototypical Mott insulator (reproduced from Figure 1.6b). Since the material is an insulator, there is minimal low-energy spectral weight. The sharp peaks below 100 meV are attributed to absorption from infrared-active phonon modes, while the broader higher energy α and β peaks at ~0.5 eV and ~1.0 eV, respectively, are attributed to inter-band transitions. Each of these absorptions is well-described by a Lorentzian line shape [8]:

$$\sigma(\omega) = \frac{Ne^2}{m} \frac{\omega}{i(\omega_0^2 - \omega^2) + \omega/\tau} \tag{2.14}$$

where ω_0 is the central frequency of the resonance and τ is the relaxation rate of the absorption, and is inversely proportional to the width of the peak. The constants N, e, and m are the electron density, charge, and mass, respectively.

Metals, on the other hand, feature low-energy spectral weight that peaks at $\omega = 0$, giving the dc value of conductivity. This is usually modelled with the Drude formula, which is the $\omega \to 0$ limit of Equation 2.14:

$$\sigma(\omega) = \frac{Ne^2\tau}{m} \frac{1}{1 - i\omega/\tau}. \tag{2.15}$$

Interestingly, in addition to a more rigorous calculation using the Kubo formalism, these results can be obtained through classical arguments describing the motion of a charge subjected to external forces from the driving field and internal restoring forces. They are exceptionally successful at describing the general absorption features of materials, especially those that are weakly correlated. While still effective in strongly correlated systems such as Mott insulators, these materials will often feature strong deviations from these models. For example, the extended-Drude model accounts for a frequency-dependent m and τ and is used to explain the heavy, strongly-interacting nature of electrons in correlated systems. In reality, interpretation of optical conductivity can be an arduous, and oftentimes messy, affair reflecting the fact that strongly interacting degrees of freedom will each leave their unique fingerprint on the spectrum. However, it is precisely this fact that has allowed for optical spectroscopy to lead to such great advancements in our

understanding of correlated electron systems, as each wiggle and peak is indicative of an underlying process that can be studied.

2.4 Time-resolved time-domain THz spectroscopy

In solid state systems, the fundamental energy scales for a vast range of phenomena often fall within the region spanning 0.1 meV to 100 meV. As a result, this energy window is rich with spectroscopic features that arise from these low-energy phenomena, including carrier lifetimes, bosonic excitations, superconducting and hybridization gaps, cyclotron resonances, plasmons, localization peaks, intra-excitonic transitions, and so on (Figure 2.5). Indeed, nearly every degree of freedom renders some sort of spectroscopic manifestation within this frequency range, colloquially known as the THz regime (.1 - 20 THz). Probing within this energy window thus grants access to a wealth of information about the material.

Though interesting from a condensed matter physics perspective, access to this energy window is challenging as much of it lies within the so-called THz gap in which there are very few technologies to emit and detect radiation. However, the use of femtosecond laser technologies helps to overcome this challenge as we can leverage the high electric field strengths associated with the ultrashort pulses. As alluded to in Section 2.1, nonlinear optical processes can be used for photon energy conversion through frequency mixing. These effects scale quadratically with the electric field, making them a viable pathway to extend the experimentally accessible wavelengths into the THz gap. In the following, we will discuss the methods behind generating, detecting, and analyzing THz-frequency light. The resulting technique that uses this THz radiation to analyze the electrodynamic properties of materials is known as time-domain THz spectroscopy (TDTS). We start with a method to generate light via optical rectification in pumped nonlinear crystals.

2.4.1 Optical rectification

In Equation 2.5, the two zero-frequency terms describe a process known as optical rectification, in which the electric field produces a polarization with the form [6]:

$$P_{NL}(t) \sim |\tilde{E}(t)|^2. \tag{2.16}$$

In other words, the nonlinear polarization will follow the optical intensity of the input pulse. Note that the current associated with the motion of bound charge carriers in the nonlinear crystal is equal to the time derivative of the polarization

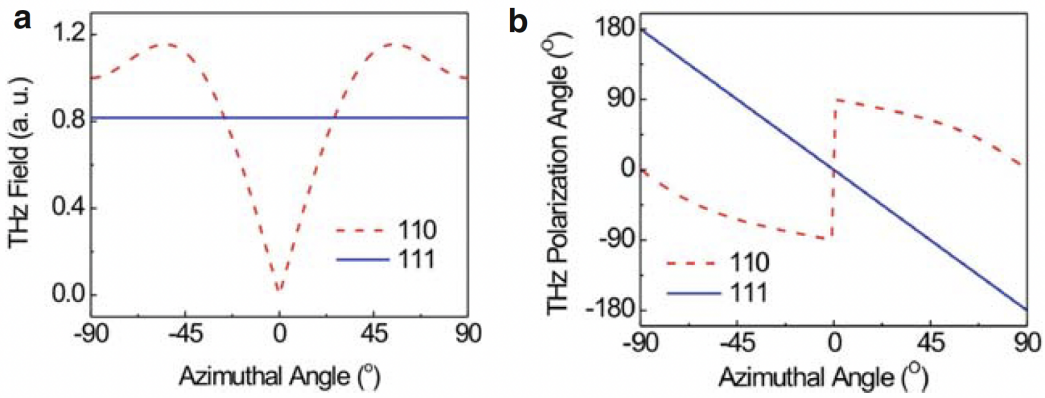

Figure 2.7: The THz electric field amplitude (**a**) and polarization (**b**) as a function of the azimuthal angle of the nonlinear crystal within which optical rectification is achieved. The azimuthal angle is defined as the angle between the [001] axis of the crystal and the polarization of the optical pulse. From Reference [250].

$\partial P/\partial t$. Accordingly, just how time varying currents of free charges will generate radiation, so too will the motion of these bound charges. The time varying nonlinear polarization thus produces a radiated field with the following form [6]:

$$E_{\text{rad}} \sim \frac{\partial^2 P_{NL}}{\partial t^2}. \tag{2.17}$$

As with most nonlinear processes that originate from bound-charge motion, optical rectification is likely exceptionally fast. As a result, the bandwidth of the emitted THz pulse is only limited by the frequency components contained within the input optical pulse that drives the nonlinear crystal in the ideal case. From the frequency-domain perspective, optical rectification can be seen as difference frequency mixing of the frequencies contained within the bandwidth of the input pulse. This point of view helps to further understand how the input pulse width limits the bandwidth of the output THz pulse. The shorter the optical pulse is in time, the broader it is in the frequency domain, resulting in a larger breadth of frequency differences.

In reality, the crystal itself will also impose its own bandwidth constraints on the emitted THz pulse, stemming from the presence of optical phonons THz regime and the difference in refractive index between the optical pulse and the emitted THz pulse. In the case of the former, THz-frequency phonons in the nonlinear crystal will strongly absorb any radiation, thereby preventing their emission. In the case of the latter, the refractive index differences will cause the optical pulse to travel at a different speed than the THz radiation inside the nonlinear crystal. A large

mismatch between these two will prevent the generation of THz radiation. More specifically, since the shape of the THz field is determined by the envelope function of the optical pulse, phase matching requires that the group velocity of the optical pule is matched with the phase velocity of the THz pulse [169]:

$$\frac{k(\omega_{\mathrm{THz}})}{\omega_{\mathrm{THz}}} \approx \left(\frac{\partial k}{\partial \omega}\right)_{\mathrm{opt}}. \tag{2.18}$$

This phase matching condition can be used to determine the maximum distance over which THz generation will still occur in the crystal, which is known as the coherence length [169]. Crystals should be chosen such that their thickness is less than or equal to the coherence length. In general, there is an inverse relationship between THz bandwidth and crystal thickness owing to the phonons and the phase matching constraints effects.

The most popular materials for THz generation via optical rectification are (110)-oriented ZnTe and GaP crystals. They both have long coherence lengths at the 800 nm wavelength pertinent to Ti:Sapphire lasers, and they have relatively large nonlinear optical coefficients. Typical bandwidths are 0.3 THz—2.5 THz for the former and 0.5 THz—6 THz for the latter. While GaP boasts a much larger bandwidth, it is nearly 4.5 times less efficient in THz field generation and detection [38]. Both of these crystals have a zincblende structure with a $\bar{4}3m$ point group symmetry [38, 187, 250]. To simultaneously achieve maximal phase matching and to fix the polarization of the emitted THz pulse, the relationship between the crystal axes and the polarization of the optical pulse must be fixed with respect to one another. For crystals with the same structure as GaP and ZnTe, the relationship between the emitted THz field and the THz polarization can be found in Figure 2.7 [250]. The azimuthal angle is defined as the angle between the [001] axis of the crystal and the polarization of the optical pulse.

2.4.2 Electro-optic sampling

The THz electric field is detected through a technique known as electro-optic sampling (EOS). EOS leverages yet another second-order nonlinear effect with a susceptibility of the form $\chi^{(2)}(\omega;\omega,0)$. Essentially, a low-frequency electric field (i.e., the THz pulse) and an optical field (i.e., an 800 nm pulse from the amplifier) interact to form a second-order polarization at the optical frequency. During this process, known as the Pockels effect, the THz electric field generates a birefringence in the crystal proportional to its field strength [6, 169, 187]. The polarization of the optical

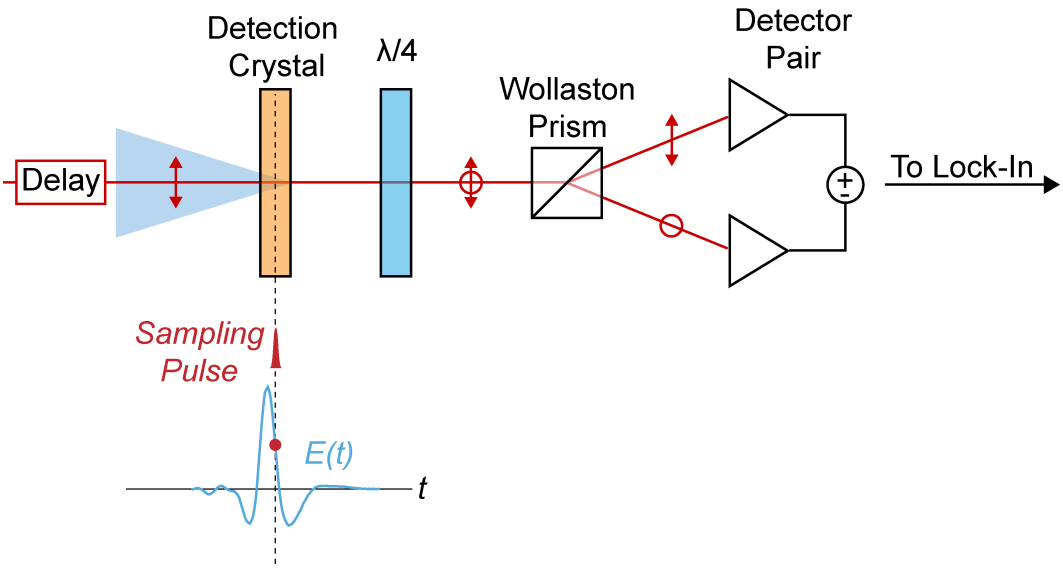

Figure 2.8: A schematic of a typical electro-optic sampling setup. The THz radiation is in light blue while the sampling pulse is shown in red.

pulse will rotate due to this birefringence. Thus, by detecting that polarization rotation of the optical pulse, the THz electric field strength can be determined. In practice, this technique is enabled by the fact that the optical pulse—known as the sampling pulse—has a much shorter duration (35 fs) than the THz pulse (~1 ps). As a result, the sampling pulse can be temporally delayed with respect to the THz pulse to sample different portions of the electric field profile. Through iterative measurement, the entire THz pulse can be resolved as a function of time, granting access to its full spectrum through a fast Fourier transform.

A schematic of an EOS optical path is shown in Figure 2.8. The THz pulse and the sampling pulse are each focused onto an electro-optic crystal. They are collinear to maintain spatial overlap through the entire crystal length. The sampling pulse then passes through a half- or quarter-waveplate before a Wollaston prism spatially separates the *s*- and *p*-polarized components of the pulse. Each polarization is then detected in the pair of sensors on a balanced photodiode. These signals are subtracted from one another, and the difference is the ultimate measured quantity. The waveplate is used to set this difference to be zero in the absence of THz pulse, allowing any rotation caused by the THz to be measured without a constant background. This differential "balanced detection" scheme is known to facilitate low-noise measurements of the THz pulse that are often limited by the shot-noise

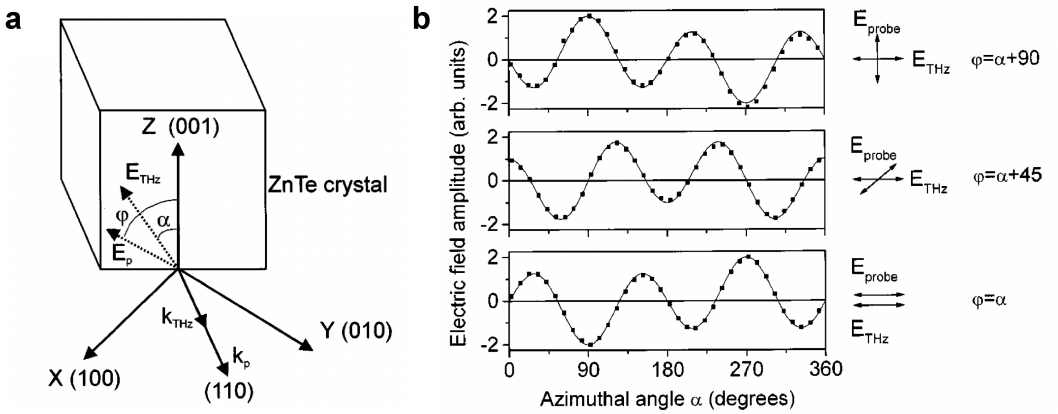

Figure 2.9: Relative orientation of THz polarization, sampling pulse polarization, crystal axes in the electro-optic sampling scheme. **a** Definition of the relative angles between the of THz electric field polarization, the sampling pulse polarization, and the nonlinear crystal axes in the electro-optic sampling scheme. **b** Dependence of the detected THz electric field for various polarization configurations as a function of the crystalline azimuthal angle. From Reference [187].

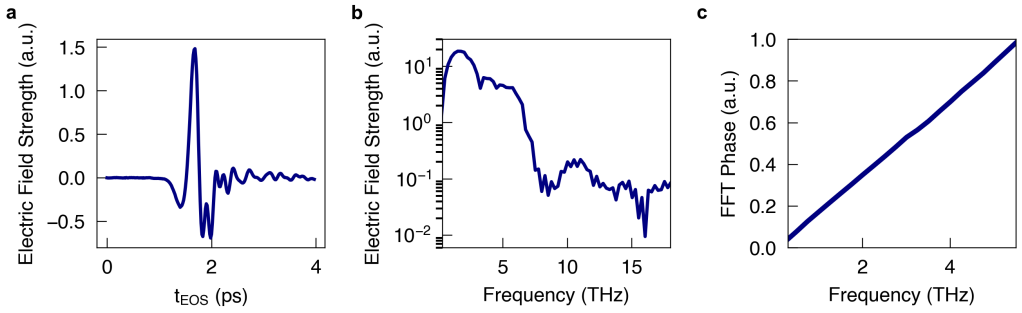

Figure 2.10: Example of a THz electric field obtained with electro-optic sampling. **a** Time-domain THz electric field transient $E(t)$ obtained with electro-optic sampling. **b,c** The corresponding frequency-domain amplitude (**b**) and phase (**c**) obtained through a FFT.

of the laser.

To maximize the detection efficiency, a particular relationship between the THz pulse polarization, the sampling pulse polarization, and the electro-optic crystal orientation must be achieved [187]. These angles are defined in Figure 2.9a for the particular case of (110)-oriented ZnTe crystal, which is a common electro-optic detector along with GaP. The measured dependence on the detected THz electric field and these angles is shown in Figure 2.9b.

An example of a pulse obtained with EOS is shown in Figure 2.10a. This field was

generated via optical rectification with a 1 mm thick ZnTe crystal pumped by a 0.6 mJ 800 nm pulse with a width of 35 fs. It was detected in a 1 mm thick ZnTe crystal using an 800 nm 35 fs sampling pulse with 0.01 mJ of pulse energy. Since the full electric field profile of the THz pulse is being resolved as a function of time, we have access to both the amplitude (Figure 2.10b) and the phase (Figure 2.10c) of the spectrum, which can be accessed through a fast Fourier transform (FFT). This information allows us to calculate complex material parameters such as the index of refraction and the optical conductivity without resorting to Kramers-Kronig transformations.

2.4.3 Introducing time resolution

To study the effects of photo-doping, time resolution must be introduced into the EOS measurement scheme. This task can be achieved through the introduction of a driving pulse that is delayed with respect to the THz pulse and the sampling pulse. There are now two time axes to keep track of. The first is the axis along which the sampling pulse is delayed with respect to the THz pulse for the EOS measurement scheme. We denote this THz pulse measurement axis as t_{EOS}. Since the electric field profile is mapped out along t_{EOS}, it is the Fourier conjugate to the THz frequency ω. The second is the delay t between the pump pulse that drives the sample and the sampling pulse, which is a measure of the time elapsed since photo-excitation. The definition of $t = 0$ is somewhat arbitrary, but here we define it as the time at which the pump first reaches the sample, as will be seen in the following sections.

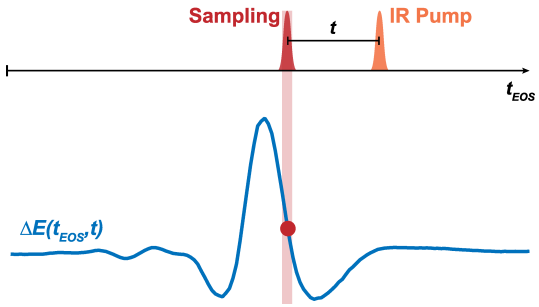

Figure 2.11: Schematic representation of the time-resolved time-domain THz measurement scheme. The relationship between the THz electric field, the sampling pulse, and the pump pulse in time is shown.

A schematic of the relationship between the three pulses is shown in Figure 2.11. Note that the THz pulse is much longer than both the pump and the sampling pulses. The time resolution is not set by the THz pulse duration, however, due to the advantages of the EOS sampling scheme [47, 99]. To measure the transient

spectrum at a given pump-probe time delay t, the relative delay between the pump pulse and the sampling pulse is fixed, and both are swept together along the t_{EOS} axis to measure the pump-induced THz electric field profile. In this way, each part of the THz electric field profile only records the response of the sample only at the time delay t. In a conventional spectrally-resolved pump probe experiment, such as white-light spectroscopy, the delay between the pump and probe would be fixed, then the spectrum would be measured after both fields have interacted with the sample. In our case, measuring the spectrum corresponds to the Fourier transform of the electric field profile in the time-domain, and so the EOS measurement axis can be measured for an arbitrarily long time without sacrificing the time resolution.

2.4.4 The time-domain THz spectrometer

Figures 2.12 and 2.13 displays schematics of the specific time-domain THz spectrometers used to collect the data presented in this thesis. Each of the setups is built within an environment purged with N_2 gas in order to minimize atmospheric absorption of the THz radiation. All of the photo-induced spectra were collected in the reflection geometry using the time-resolved time-domain THz spectrometer shown in Figure 2.12a. This setup was seeded by 800 nm, 35 fs pulses produced by a Ti:sapphire amplifier operating at 1 kHz, which was split into three arms. The first arm (3.5 mJ pulse energy) was sent into an optical parametric amplifier (OPA) that served as the tunable near-infrared (NIR) pump source. The second arm (0.6 mJ pulse energy) was used to generate the broadband THz-frequency probe through optical rectification of the 800 nm pulses. The third arm (1 μJ pulse energy) was reserved for the electro-optic sampling (EOS) sampling pulse used to measure the THz electric field $E(t_{\mathrm{EOS}})$. The temporal delay t_{EOS} between the 800 nm EOS sampling pules and the THz probe was controlled with a motorized delay stage. The optical path of the NIR pump pulse also included a motorized delay stage that was used to control the temporal delay t relative to the sampling pulse. The THz pulse was fixed in time. Each of these three paths was carefully measured during the construction of the apparatus in order to ensure that they all had the same length, guaranteeing that there was temporal overlap between them.

The THz generation path begins with pumping a nonlinear optical crystal using the 0.6 mJ 800 nm pulse, such as ZnTe or GaP. A Teflon filter was used as a low-pass filter to block the residual 800 nm radiation while transmitting the THz radiation. The THz pulse was then sent into a 1:3 telescope constructed of two 90 $^\circ$ off axis parabolic mirrors to expand the THz beam, allowing for a tighter focus

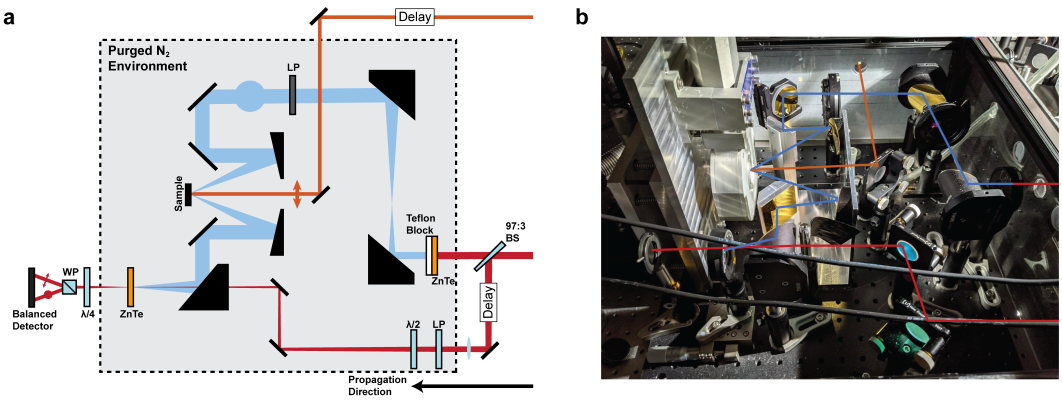

Figure 2.12: Schematic of a reflection geometry time-domain THz spectrometer. **a** Schematic of the reflection-based tr-TDTS used in this thesis. The light blue path is the THz radiation, the red paths represent the 800 nm THz generation pulse and the 800 nm EOS probe pulse, respectively, and the orange path is the tunable NIR pump. **b** An image of the setup in the lab with lines depicting the optical paths of the sampling, THz, and NIR pump pulses. Color coding is the same as in a.

at the sample position. The expanded beam is then passes through a wire-grid polarizer (InfraSpecs model P01) before being directed into an alignment apparatus that contains two flat mirrors and two 30° off-axis parabolic mirrors (Figure 2.12b). This alignment tool facilitates the challenging task of guiding the THz pulse into the 30° off-axis parabolic mirrors that focus the THz pulse onto the sample surface and collect its reflection. It was built such that the cryostat could fit between the two flat mirrors, as closely as possible to the parabolic mirrors, in order to minimize the working distance. After the collimated beam leaves the sample alignment apparatus, it enters one final 90° off-axis parabolic mirror and is focused onto the EOS detection crystal. The final parabolic mirror has a small hole drilled through it to pass the sampling pulse.

The sampling pulse is split from the 0.6 mJ 800 nm pulse using a wedged beam sampler. It then passes into a retro-reflector mounted atop a motorized delay stage, which introduces the temporal control needed for the EOS measurement scheme. The pulse then passes through a long focal length lens positioned such that the focus is on the nonlinear detector crystal. Before it reaches the crystal, the beam first passes through a linear polarizer and a half-waveplate to control the power and polarization of the pulse. The half-waveplate is placed after the polarizer in order to keep the power constant as the polarization is rotated. The beam then passes through the hole into the final off-axis parabolic mirror in the THz path before reaching the detector crystal. It then passes into the EOS apparatus described in Figure 2.8.

The path of the NIR pump pulse is relatively simple compared to the THz and sampling paths. After exiting the OPA, the pump pulse is directed towards the THz setup. Before reaching the sample, it passes into a retro-reflector mounted atop a motorized delay stage, which introduces the temporal control needed to introduce time resolution. It is then guided between the two 30° off-axis parabolic mirrors in the THz path before striking the sample at normal incidence. Because the THz spot size is quite large ($\sim$ 1 mm), the entire sample is often pumped in order to ensure complete spatial overlap between the pump beam and the THz beam. For this reason, the pump pulse is left collimated when it reaches the sample. The spot size can be controlled via an upstream telescope if needed (not shown).

An important consideration is that the pump pulse can scatter into the THz detection path after it arrives to the sample. This can be detrimental to the measurement because the scattered light can interact with the sampling pulse in the detector crystal, creating spurious signals that interfere with the desired measurement. As such, a filter must be placed between the sample and the detector to block pump scatter. Strangely enough, we found that black garbage bags worked rather well for this purpose. They completely blocked the pump scatter while fully transmitting the THz pulse, unlike more traditional low-pass filters such as Teflon and silicon. However, it can only be used in an extremely low-power situation such as the case of the scattered pump light, otherwise it has the tendency to burn. It is for this reason that we do not use it to block the residual 800 nm light that pumps the THz generation crystal.

Two different configurations of detection and generation crystals were used in these measurements. The first utilized a 0.2 mm thick <110> GaP crystal for generating the THz pulse and a 0.2 mm thick <110> GaP crystal mounted on 1 mm thick <100> GaP for EOS detection, yielding a bandwidth of 0.5 THz to 6 THz. The second utilized 1.0 mm thick <110> ZnTe crystals for both generation and EOS detection, yielding a bandwidth of 0.35 THz to 2 THz.

The spectrometer constructed in the transmission geometry shown in Figure 2.13 was used to measure equilibrium optical properties. This setup is similar to the reflection-based spectrometer. The main difference the THz radiation is focused onto the sample surface at normal incidence using a 90° off-axis parabolic mirror. The transmitted light is then collected for detection with a second 90° off-axis parabolic mirror following its transmission through the sample. The EOS path is essentially the same between the two setups.

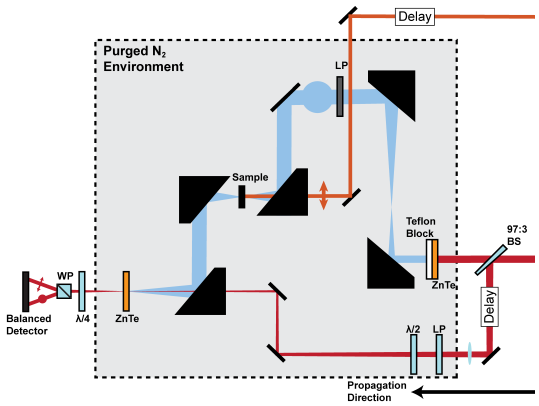

Figure 2.13: Schematic of the transmission-based tr-TDTS used in this thesis. The light blue path is the THz radiation, the red paths represent the 800 nm THz generation pulse and the 800 nm EOS probe pulse, and the orange path is the tunable NIR pump.

2.4.5 Detection protocols

Measurement of both the equilibrium THz electric field profile $E(t_{\mathrm{EOS}})$ and its pump induced changes $\Delta E\left(t_{\mathrm{EOS}}, t\right) = E_{Pumped}\left(t_{\mathrm{EOS}}, t\right) - E\left(t_{\mathrm{EOS}}\right)$ at a fixed time delay t are enabled through differential lock-in detection. To measure the former, a mechanical chopper is placed in the THz path and is set to rotate at half the repetition rate of the laser, thereby allowing only every other THz pulse to transmit. The sampling pulse is kept at the laser repetition rate. Accordingly, the polarization of only every other sampling pulse is modified by the THz pulse. The balanced detection scheme will then produce a signal at half the repetition rate of the laser. The mechanical chopper serves as the reference trigger for a lock-in amplifier, which filters the EOS signal from a balanced photodiode. Such a detection technique yields a "THz-on" minus "THz-off" detection of the THz electric field. The signal from the lock-in amplifier is then fed to a computer which iteratively varies t_{EOS} and records the differential signal, thereby yielding $E(t_{EOS})$.

To measure $\Delta E\left(t_{\mathrm{EOS}}, t\right)$, two different protocols can be used. In the first, only one chopper is utilized to chop the NIR pulse at half the repetition rate of the laser. As a result, only half of the THz pulses will reflect off of a photo-excited sample, while the other half will reflect off of the equilibrium sample. Accordingly, the probe pulses will successively detect the effects of $E(t_{EOS})$ and $E_{Pumped}(t_{EOS}, t)$. The mechanical chopper again serves as the reference trigger for a lock-in amplifier, which filters the EOS signal from a balanced photodiode. Now, the signal will yield the difference of $E_{Pumped}(t_{EOS}, t)$ and $E(t_{EOS})$, producing $\Delta E(t_{EOS}, t)$.

The second protocol utilizes two choppers and two lock-in amplifiers. The first chopper chops the THz pulse at half the repetition rate of the laser, and is used to reference the first lock-in. The second chopper chops the NIR pump pulse at half the repetition rate of the THz pulse (one fourth the repetition rate of the laser) and is used as a reference for the second lock-in. When this is done, the $E(t_{EOS})$ can be detected simultaneously with $\Delta E(t_{EOS}, t)$, ensuring that any spectral artifacts due to long-term drift are eliminated. The cost is a reduction in the signal-to-noise ratio by half owing to the reduction in the duty cycle of the measurement. We utilized both detection protocols in our experiments depending on the strength of the signal; both yielded identical results. When the single-chopper method was used, the static THz electric field and its transient changes were measured sequentially at each t to ensure that there were no spectral artifacts owing to long-term drift of the laser system.

Finally, in some cases it is desirable to measure $\Delta E\ (t_{\text{fixed}}, t)$, in which the photo-induced THz electric field is measured at a fixed point t_{fixed} in the t_{EOS} axis. Sweeping t allows us to measure the time-evolution of this fixed point. While these "pump-probe" traces do not yield a frequency-resolved response, they provide frequency-integrated information about the dynamics when t_{fixed} is anchored to the peak of $E(t_{\text{EOS}})$ [188]. Importantly, these traces are over 100 times faster to acquire than the full mapping of $\Delta E(t_{\text{EOS}}, t)$.

2.4.6 Characterizing performance

We use two different metrics to characterize the response of our system. The first is the dynamic range of the spectrum. We define this quantity as the ratio of the peak in the spectrum divided by the average value of the noise. For the ZnTe-based experiment, a dynamic range of 1000-2000 is consistently achieved (Figure 2.14a). On the other hand, when GaP crystals are used for generation and detection, our dynamic range drops to roughly 500 (Figure 2.14b). This reduction stems from the fact that GaP is a less efficient THz emitter and detector than ZnTe. Moreover, our GaP crystals are 5 times thinner than the ZnTe crystals in order achieve a broader bandwidth.

The second metric we use serves as a frequency-resolved measure of the noise and allows us to define our bandwidth. We begin by taking three identical scans of $E(t_{EOS})$ consecutively (Figures 2.14a and b). Then, we transform each scan to the frequency domain, and divide the spectra with one another. An example of the

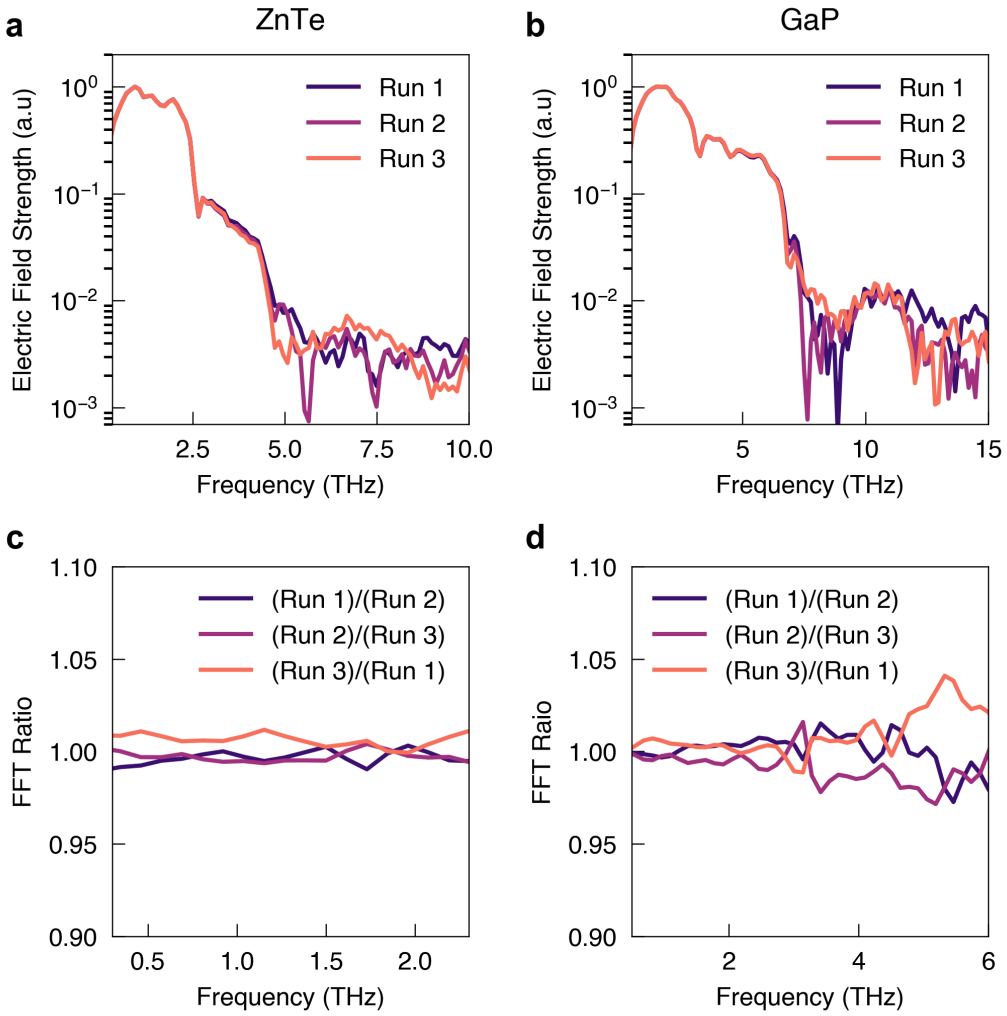

Figure 2.14: Performance characteristics of the time-domain THz spectrometer. **a,b** THz electric field spectra $E(\omega)$ obtained through FFT of time-domain spectra captured with the EOS measurement scheme for ZnTe- (a) and GaP-based (b) setups. The three measurement runs were taken back-to-back. In the ZnTe-based setup, the (110)-oriented generation and detection crystals were both 1 mm thick. In the GaP-based setup, the (110)-oriented generation crystal was 0.2 mm thick while the 0.2 mm thick (110)-oriented detection crystal was mounted on a (100)-oriented 1 mm thick crystal. **c,d** Ratios of the three runs taken for ZnTe (c) and GaP (d).

resulting curves are plotted in Figure 2.14c for ZnTe and Figure 2.14d for GaP. It is apparent that for some region in frequency space, the three curves hover closely to 1, and deviate dramatically beyond a certain point. We define the flat region close to 1 as our bandwidth, as the THz electric field has enough strength at these frequencies to allow for reproducible measurement. Outside of this flat region, the

noise begins to dominate, resulting in the large deviations from 1. Usually, our maximum deviation from 1 within the flat range is less than 1% for ZnTe across the whole bandwidth. For GaP, the deviation was less than 1% between 0.5 THz and 3 THz, and less than 3% between 3 THz and 6 THz.

2.4.7 Sample preparation, sample mounting, and cryogenics

We now discuss how the sample is introduced into the spectrometer. More often than not, the samples must be cooled to cryogenic temperatures in order to access different electronic phases of the material. To do this, we use a continuous flow microscopy cryostat (CryoIndustries RC102). For the window, we mostly use a polymer material known as TPX because of its ability to transmit most of the GaP THz bandwidth and much of the OPA frequency range. For normal incidence experiments, we can also use z-cut quartz. However, its birefringent properties prevent its use in experiments in which the THz pulse is obliquely incident onto the sample surface. For the reflection geometry, the cryostat is fixed onto a mount that allows us to tip and tilt it through a series of spring-loaded knobs, thereby controlling the direction of the reflected pulse. This mount is then attached onto a series of translation stages that are in turn mounted onto the table, allowing us to move the sample in space. For the transmission geometry, a T-slot construction is used to fix a steel plate on top of the spectrometer. A hole is cut out of this steel plate for the cryostat to hang through, thereby exposing both sides of the cryostat to allow for transmission of the THz pulse. For this geometry, the translation stages are also fixed onto the steel plate using tapped holes that are machined into the plate. The cryostat is attached to the translation stages using an L-shaped bracket.

To mount the sample into the cryostat, we use different sample holders for each spectrometer. For the reflection geometry, the sample is mounted onto the tip of a copper cone (Figure 2.15a). This sample holder was designed to accommodate samples that are smaller than the THz spot size to ensure that reflections from the sample holder do not enter the detection path. For the transmission geometry, we use a copper sample holder that has two apertures on it (Figure 2.15b). We mount the sample over one of the apertures, while leaving the other aperture exposed for referencing. The cryostat is translated laterally to access each of the aperture. Before the sample is mounted, scans are taken through each aperture to ensure that they are identical.

When attaching these sample holders to the cryostat, Apiezon N Grease is used

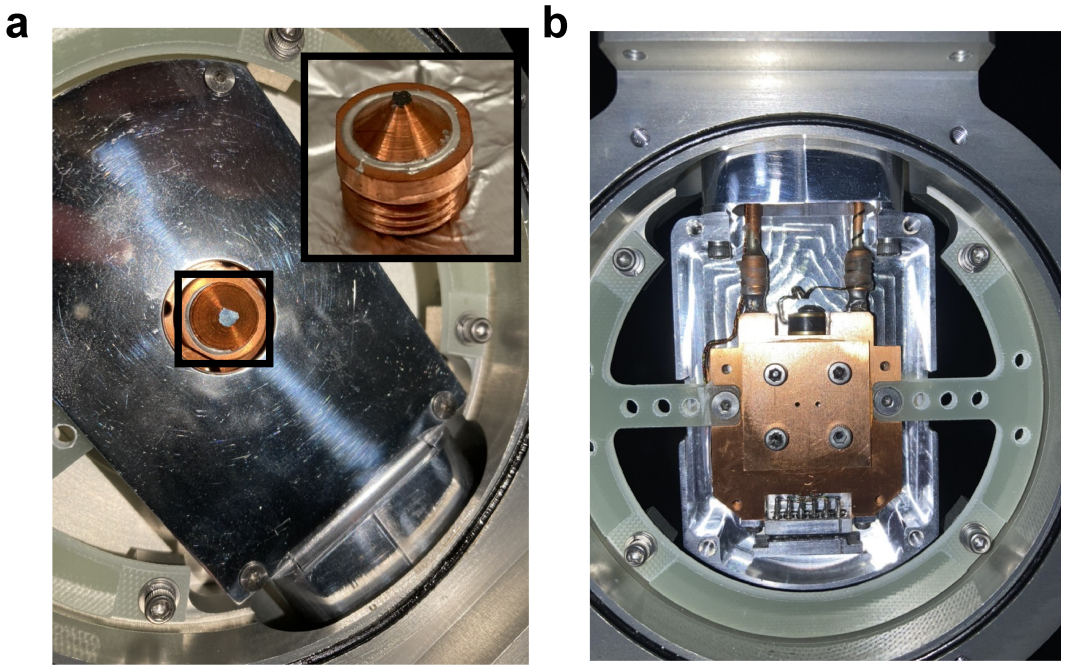

Figure 2.15: Sample holders used in the time-domain THz spectrometers. **a** Sample holder used in the reflection-based tr-TDTS mounted in the cryostat. The inset shows the side-view of the sample holder outside of the cryostat. **b** Sample holder used in the transmission geometry tr-TDTS mounted in the cryostat. In a, the radiation shield is attached to the cryostat, while in b it is removed to better show the full extent of the sample holder.

to ensure good thermal contact. The samples are attached to the sample holder using either conductive silver epoxy (EPO-TEK H2OE), conductive silver paint (e.g., PELCO Conductive Silver Paint, 30g), or Apiezon N Grease depending on the application. For the THz measurements, the sample surfaces were polished to a mirror finish using diamond lapping paper with a grit size of 1 μm.

2.4.8 Extracting equilibrium optical properties

The goal of TDTS is to experimentally determine the complex index of refraction $\tilde{n}(\omega)$ of a material. The first step is to measure the complex transmission $\tilde{t}(\omega)$ of the sample. To do this, the THz electric field was first measured after transmission through the sample, which was sitting over an aperture in the sample holder. Then, immediately after, the sample holder is translated such that the THz pulse instead transmits through a bare aperture that is identical to the one used to measure the sample. An example sample holder with the two apertures can be seen in Figure 2.15b. All other parameters are kept fixed. These two field transients were divided

in the frequency domain to obtain the experimental complex transmission $\tilde{t}_{Exp.}(\omega)$.

To extract $\tilde{n}(\omega)$ from this data, $\tilde{t}_{Exp.}(\omega)$ is compared against the expected theoretical response $\tilde{t}_{Th.}(\omega)$. $\tilde{t}_{Th.}$ can be found by considering the process of a plane wave of frequency ω transmitting through a slab of thickness d and index of refraction $\tilde{n}(\omega)$ [174]. We assume that the plane wave is normally incident onto the first face of the slab. Assuming that the index of refraction outside of the slab is equal to 1, the radiation will experience the following transmission coefficient:

$$\frac{2\tilde{n}(\omega)}{\tilde{n}(\omega)+1}. \tag{2.19}$$

Inside the sample, the wave will accumulate a phase given by:

$$\exp\left(i\frac{\omega d}{c}\tilde{n}(\omega)\right). \tag{2.20}$$

Finally, as the light exits the sample, it will incur a second transmission coefficient given by:

$$\frac{2}{\tilde{n}(\omega)+1}. \tag{2.21}$$

Thus, the total transmission through the sample is given by:

$$\tilde{t}_{sample}(\omega) = \frac{4\tilde{n}(\omega)}{(\tilde{n}(\omega)+1)^2}\exp\left(i\frac{\omega d}{c}\tilde{n}(\omega)\right). \tag{2.22}$$

On the other hand, as the light passes through the aperture, it will only require a phase as there are no interfaces through which it must transmit:

$$\tilde{t}_{aperture}(\omega) = \exp\left(i\frac{\omega d}{c}\right). \tag{2.23}$$

Dividing $\tilde{t}_{sample}(\omega)$ and $\tilde{t}_{aperture}(\omega)$ yields the $\tilde{t}_{Th.}(\omega)$:

$$\tilde{t}_{Th.}(\omega) = \frac{4\tilde{n}(\omega)}{(\tilde{n}(\omega)+1)^2}\exp\left(i\frac{\omega d}{c}(\tilde{n}(\omega)-1)\right). \tag{2.24}$$

$\tilde{n}(\omega)$ can now be quantitatively extracted by minimizing the difference between $\tilde{t}_{Exp.}(\omega)$ and $\tilde{t}_{Th..}(\omega)$ using a least-squares algorithm at each ω with $\tilde{n}(\omega)$ as the

variable of interest. Once $\tilde{n}(\omega)$ is determined, all other optical constants including the complex optical conductivity $\tilde{\sigma}(\omega)$ and the complex dielectric constant $\tilde{\varepsilon}(\omega)$.

Note that this process can in principle be done in the reflection geometry also by measuring the absolute reflection $\tilde{r}_{Exp.}(\omega)$ from the sample and comparing against the theoretical expectation $\tilde{r}_{Th.}(\omega)$. This task is challenging to accomplish experimentally, however. The difficulty lies in identifying a proper way to reference the electric field from the sample. In the transmission geometry, the electric transmitted through the sample can be referenced to obtain the absolute transmission $\tilde{t}_{\omega}$ by simply removing the sample from the system and measuring the electric field again (i.e., measuring the bare aperture). In the reflection geometry, a nearly perfect reflector, such as gold, would need to be put in place of the sample. The challenge is that the position of the reflector would need to be identical to that of the sample in order to maintain the phase of the electric field transient. While this perfect placement can often not be achieved, an alternative is to evaporate a thin layer of gold onto the sample surface *in situ*. However, this method would require an evaporator to be within the cryogenic environment in order to access the sample surface, which is not possible with most optical cryostats. In addition, the gold evaporation can permanently damage the sample surface.

2.4.9 Extracting transient optical properties

Time-resolved (tr-) TDTS can be used measure photo-induced changes to the optical constants of a driven material. The experimental value that is measured is the pump-induced change of the electric field reflected from the sample normalized by its equilibrium value $\frac{\Delta\tilde{E}(\omega,t)}{\tilde{E}(\omega)}$. This quantity is equal to $\frac{\Delta\tilde{r}(\omega,t)}{\tilde{r}(\omega)} = \frac{\tilde{r}'(\omega,t)-\tilde{r}(\omega)}{\tilde{r}(\omega)}$ where $\tilde{r}(\omega)$ and $\tilde{r}'(\omega,t)$ are the equilibrium and photo-induced complex reflectivity of the sample, respectively [99]. Similarly to how we found the equilibrium index of refraction $\tilde{n}(\omega)$ in the previous section, we can calculate the theoretically expected value of $\frac{\Delta\tilde{r}(\omega,t)}{\tilde{r}(\omega)}$ and minimize its difference from the experimental quantity $\frac{\Delta\tilde{E}(\omega,t)}{\tilde{E}(\omega)}$ to extract the optical constants of the photo-induced state. This process is facilitated by the fact that $\tilde{r}(\omega)$ is a known quantity that can be calculated from $\tilde{n}(\omega)$, which can be experimentally found through an equilibrium TDTS measurement. Thus the only unknown quantity is the photo-induced complex index of refraction $\tilde{n}'(\omega,t)$, which will appear in $\tilde{r}'(\omega,t)$.

We are now left with the task of determining the theoretical value of $\frac{\Delta\tilde{r}(\omega,t)}{\tilde{r}(\omega)}$. An important consideration in tr-TDTS experiments is the penetration depth mismatch

between the pump pulse and the THz probe pulse. Since the photo-induced optical constant will only exist within the regions of the sample that are influenced by the pump, the THz probe may be sensitive to both pumped and un-pumped portions of the material if its penetration depth is longer than the pump. Thus, depending on the level of mismatch, different models will need to be used to determine the optical response of the material.

The first scenario we will consider is when the THz pulse penetrates much deeper into the sample than the pump pulse. In this case, the pumped region can be considered as a thin film atop an unperturbed bulk. The film will have a thickness equal to the penetration depth of the pump d, and the THz electric is taken to be a constant within the film. This situation can be analytically solved by considering the boundary conditions of the electromagnetic field between the vacuum and the unperturbed bulk, which includes a contribution from the surface current density $j_s = \Delta\tilde{\sigma}(\omega)\tilde{E}(\omega)$ where $\Delta\tilde{\sigma}(\omega)$ is the pump-induced change to the optical conductivity. An analysis of this situation yields an analytic solution for $\Delta\tilde{\sigma}(\omega)$ [99]:

$$\Delta\tilde{\sigma}(\omega) = \left(\frac{1}{377 \times d}\right) \frac{\frac{\Delta\tilde{E}(\omega)}{\tilde{E}(\omega)}\left(\tilde{n}^2(\omega) - 1\right)}{\frac{\Delta\tilde{E}(\omega)}{\tilde{E}(\omega)}\left[\cos(\theta_0) - \sqrt{\tilde{n}^2(\omega) - \sin^2(\theta_0)}\right] + 2\cos(\theta_0)} \tag{2.25}$$

where d is the penetration depth of the pump pulse and θ_0 is the angle of incidence.

In situations where the penetration depth mismatch is not so extreme, we can instead model the system using the so-called stratified medium approach. This model assumes the pump decays exponentially inside the sample with a characteristic length-scale equal to the penetration depth. We break this exponential profile into N layers. Then, we assume that each layer has a unique photo-induced index of refraction that approaches the bulk index of refraction as the layers go deeper into the sample:

$$\tilde{n}'(z, \omega) = \tilde{n}(\omega) + \Delta\tilde{n}(\omega)\, e^{-\alpha z} \tag{2.26}$$

where ω is the frequency, z is the layer depth into the sample, α is the penetration depth of the pump, $\tilde{n}(\omega)$ is the complex equilibrium index of refraction, and $\Delta\tilde{n}(\omega)$ is the complex photo-induced change to the index of refraction. The reflection from this stratified medium is modeled using a characteristic matrix $M(z)$ that relates the field at some depth in the medium z to the field at $z = 0$ [30, 99]:

$$M(z) = \begin{bmatrix} \cos(k_0\tilde{n}'(z)z\cos\theta) & -\frac{i}{p}\sin(k_0\tilde{n}'(z)z\cos\theta) \\ -ip\sin(k_0\tilde{n}'(z)z\cos\theta) & \cos(k_0\tilde{n}'(z)z\cos\theta) \end{bmatrix} \tag{2.27}$$

where θ is the angle of incidence and $p = \tilde{n}\cos\theta$. Note that the argument ω has been dropped from $\tilde{n}'(z,\omega)$ because this matrix must be calculated for each value of ω.

The total response from all the layers $M(z_N)$ is given by the product of the characteristic matrix $M_j(z_j - z_{j-1})$ that describes each layer $z_j - z_{j-1}$. From this global characteristic matrix, the reflectivity can be calculated as [30, 99]:

$$r' = \frac{(m_{11} + m_{12}p_L)p_1 - (m_{21} + m_{22}p_L)}{(m_{11} + m_{12}p_L)p_1 + (m_{21} + m_{22}p_L)} \tag{2.28}$$

where $p_1 = \cos\theta$ and $p_L = \tilde{n}(L)\cos\theta_L$. $\tilde{n}(L)$ is the index of refraction evaluated at the probe penetration depth L and θ_L is the angle that the electric field would have as it leaves the probed region. θ_L can be found via Snell's law as $\cos\theta_L = \sqrt{1 - (\sin\theta_0/\tilde{n}(L))^2}$.

Having modeled the theoretical expectation for the THz reflectivity from the stratified medium (Equation 2.28), the transient refractive index defined in Equation 2.26 can be determined through a least-squares algorithm that minimizes the difference from $\frac{\Delta\tilde{E}(\omega,t)}{\tilde{E}(\omega)}$. Note that this minimization must be performed for each t and ω, each of which will have a unique characteristic matrix.

Extraction of transient optical conductivity in Sr_2IrO_4

In Chapters 3 and 4, we perform tr-TDTS measurements on Sr_2IrO_4. There, we use the thin-film approximation due to the large penetration depth mismatch between the IR pump (73 nm) [24] and the THz probe, which transmits through the ~100 μm thick sample. To prove that the thin film approximation is accurate, we also extracted the transient optical conductivity using the stratified medium approach. The results are summarized in Figure 2.16. The numerically solved stratified medium solution is nearly identical with the analytical thin film approximation, indicating the validity of the thin-film approximation. Similar arguments can be applied to the case of $Sr_3Ir_2O_7$, which exhibits similar penetration depth mismatches to Sr_2IrO_4 [3].

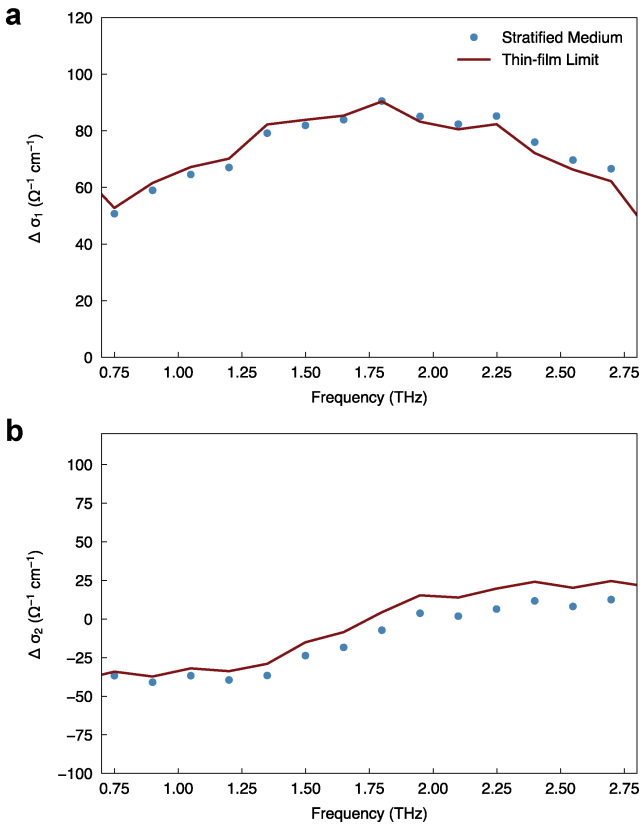

Figure 2.16: Transient optical conductivity in Sr_2IrO_4 obtained with different models. **a**,**b** Comparison of the real (a) and imaginary (b) parts of the optical conductivity obtained with the thin-film approximation and stratified medium approach.

2.5 Time-resolved reflectivity

While TDTS allows for a direct extraction of the complex index of refraction of a material, the technique is limited to a very narrow range of energies. The reason is that the EOS measurement protocol relies on the fact that the THz electric field transient is much slower than the sampling pulse width. When dealing with higher energy probes—ranging from the mid infrared to the visible—this condition no longer holds and the conventional femtosecond pulse can no longer sample the pulse. On the other hand, detector technologies based on photodiodes are readily available in these energy ranges. It is thus possible to measure the intensity $I \propto |\tilde{E}|^2$ of the light. From this, both the phase and magnitude of $\tilde{r}(\omega)$ can be determined via a Kramers-Kronig transformation if it is measured over a broad enough energy range. Doing so allows for $\tilde{n}(\omega)$ and related constants to be determined.

Reflectivity measurements have proven to be particularly useful probe of photo-induced phenomena. In these experiments, the photo-induced change in the reflec-

tivity normalized to its equilibrium value $\Delta R(\omega, t)/R(\omega)$ is measured. These data can be analyzed as follows [18]:

$$\frac{\Delta R}{R}(\omega, t) = \frac{\partial \ln(R(\omega))}{\partial \varepsilon_1(\omega)} \Delta\varepsilon_1(\omega, t) + \frac{\partial \ln(R(\omega))}{\partial \varepsilon_2(\omega)} \Delta\varepsilon_2(\omega, t) \tag{2.29}$$

where ε_1 and ε_2 are the photo-induced changes in the real and imaginary parts of the dielectric function $\Delta\tilde{\varepsilon}(\omega, t)$, respectively. This formula implies that important information about the photo-induced optical properties can be deduced from transient reflectivity spectra. As covered in Section 2.3, the optical conductivity is dependent on the joint density of states and the symmetry properties of the material (i.e., the selection rules associated with a given transition). As such, the photo-induced changes to the reflectivity can be interpreted in light of these considerations. For example, if there is no reason to believe that the selection rules of a transition at a given probe frequency ω will not change following photo-excitation, then $\Delta R(\omega, t)/R(\omega)$ will reflect changes to the joint density of states. These changes can be caused by photo-induced modifications of the band structure or changes in the carrier distribution. Moreover, since different physical processes have different fundamental timescales, the dynamics of $\Delta R(\omega, t)/R(\omega)$ can provide further information about the underlying mechanism driving the photo-induced changes.

Finally, a quick note that transient reflectivity is also sensitive to the excitation of bosonic modes. Most often, these modes are phonons, which are excited through the displacive excitation of coherent phonons or impulsive stimulated Raman scattering mechanisms. Other bosonic excitations, such as magnons and collective charge density wave modes, can also be detected. Each of these modes will appear as oscillations as a function of time in the dynamics of $\Delta R(\omega, t)/R(\omega)$.

2.5.1 Experimental apparatus

A schematic of a transient reflectivity setup is shown in Figure 2.17. In our lab, the apparatus is seeded by the two OPAs described in Section 2.2 (Figure 2.1). The stronger OPA (OPA1) is used for the pump line that photo-excites the sample, while the weaker OPA (OPA2) serves as the probe line to measure $\Delta R/R$. This design provides the flexibility to independently tune the wavelength of both the pump and probe through the entire OPA range of 1200 nm to 2400 nm. Moreover, the use of a second harmonic generation stage allows us to access visible wavelengths also.

In the pump line, the beam first passes through a lens pair that serves as a telescope to control the spot size. Making the collimated beam bigger (smaller) will create a

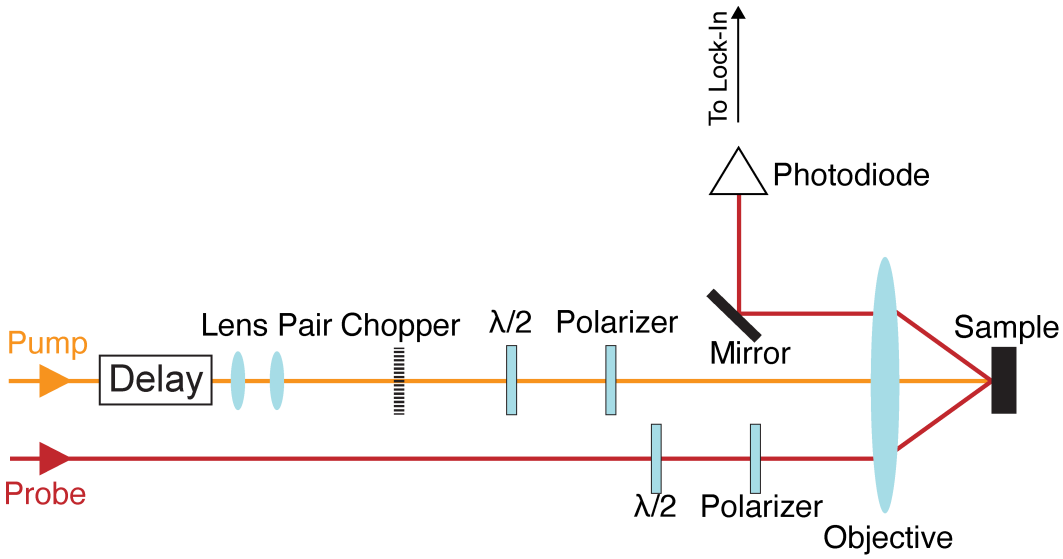

Figure 2.17: Schematic of the transient reflectivity setup used in this thesis.

tighter (wider) focus on the sample surface after the objective lens. The beam then passes through a half-waveplate and a polarizer. The pair allows for independent control over the pump polarization and power. The beam is then directed into a retro-reflector mounted atop a motorized delay stage which generates the tunable temporal delay between the pump and the probe. Finally, the pulse passes through a mechanical chopper that enables the use of a differential lock-in detection scheme, before passing into an objective optic—such as a lens or an off-axis parabolic mirror—that focuses the beam onto the sample surface at normal incidence. The probe beam simply travels through a polarizer and half-waveplate before being focused onto the sample by the objective optic. Unlike the pump, the probe is obliquely-incident onto the sample surface such that the reflection can be collected and passed into a photo-diode, which passes its signal into a lock-in amplifier for detection.

The differential lock-in detection scheme is similar to that used to detect THz-induced polarization rotation of the sampling pulse in Section 2.4. The mechanical chopper in the pump line rotates at half the repetition rate of the laser, such that every other pulse is blocked. As a result, half of the probe pulses are modulated by the pump (i.e., they are reflected from a photo-excited sample), while the other half are not (i.e., they are reflected from the equilibrium sample). Since lock-in amplifier is referenced by the chopper, it will filter the signal from the photo-diode to yield the difference of the pumped and un-pumped signals (ΔR). R can be measured by

blocking the pump and setting the lock-in reference to the laser repetition rate.

2.5.2 Data analysis

A typical signal obtained from a pump-probe style experiment consists of a sharp onset followed by an exponential decay. The former indicates the arrival of the pump. Since transient reflectivity probes electronic degrees of freedom, which respond quickly (~1-10 fs) to the light, this response is often limited by the time resolution of the experimental setup. The term "time zero" refers to the moment that the maximum of the pump pulse arrives at the sample surface. The exponential decay represents the various carrier relaxation processes that occur folowing the photo-excitation process. These can include inter- and intra-band relaxation, coupling to different bosonic baths such as magnons or phonons, radiative processes, or higher order multi-partite recombination processes such as Auger recombination [18]. Most of the time, the signal is well-described by the following phenomenological model [253]:

$$\frac{1}{2}\left[1 + \text{ erf}\left(2\sqrt{2}\ \left(\frac{t-t_0}{t_r}\right)\right)\right] \times \left[\sum_i \left[A_i \exp\left(-\frac{t-t_0}{\tau_i}\right)\right] + b\right] \tag{2.30}$$

where t is the pump-probe time delay, and the fitting parameters t_0, t_r, and A_i and τ_i are time zero, the rise time, and the strength and decay constant of each exponential i, respectively. The pump-induced offset b captures much slower decay processes (~ns) such as heat diffusion out of the pumped region of the sample. The number of exponential is determined by the number of carrier relaxation processes present in the system. The most common forms of Equation 2.30 are single- and double-exponential expressions.

2.6 Time-resolved second harmonic polarimetry

Thus far, our discussion of measurement techniques has focused on probes of a material's optical conductivity. While this is an important quantity to measure, it is only one facet of a material that mainly provides information about its band structure and excitation spectra. An important question that often cannot be directly answered by these probes is whether certain symmetries are present in a material. Much of our understanding of condensed matter systems is based on the notion that ordered phases spontaneously break the symmetries of the un-ordered phase. For

this reason, probes of symmetry are crucial in the study of phase transitions, and have been a cornerstone of the characterization of solids. Traditionally, these efforts have focused on diffraction techniques. However, for the femtosecond-scale investigation of the photo-doped systems studied in this thesis, an optical measurement would be preferable as it can be more easily interfaced with the laser systems that seed the other techniques.

Nonlinear harmonic generation polarimetry techniques have emerged as a viable alternative to diffraction techniques in the study of material symmetries. The most widely adopted variant is that focused on second harmonic generation (SHG). In this measurement, the intensity of SHG light generated by the crystal is recorded as the crystal rotates about its surface normal. Since the SHG process is controlled by nonlinear optical susceptibility tensors such as those described in Section 2.1, the resulting intensity patterns will reflect the symmetries of these tensors. The nonlinear optical susceptibility tensors, in turn, must remain invariant under transformations that respect the symmetry of the crystal, as per Neumann's principle. Therefore, the SHG patterns can be used to deduce the underlying symmetries of the material. SHG polarimetry has been widely adopted to study the symmetry properties of crystalline, magnetic, and other more exotic electronic orders.

2.6.1 Physical principle

We begin by discussing the physical principles that underpin the second-harmonic generation polarimetry, following the discussions in References [225, 252]. Consider an electric field E_i of polarization $i = (x, y, z)$ that is radiated due to the interaction of an incident field with a medium. E_i is determined by the inhomogeneous wave equation:

$$\left(\nabla^2 - \frac{1}{c^2}\frac{\partial^2}{\partial t^2}\right) E_i = S_i \tag{2.31}$$

S_i is the source term induced in the medium by the incident field. When electromagnetic radiation passes through a medium, it will induce electric dipole P_i, magnetic dipole M_i, electric quadrupole $Q_{i,j}$, and higher rank moments all of which can will have their own contributions to the source term. Keeping only P_i, M_i, and Q_{ij}, S_i can be described as:

$$S_i = \mu_0 \frac{\partial^2 P_i}{\partial t^2} + \mu_0 \left(\varepsilon_{ijk} \nabla_j \frac{\partial M_k}{\partial t}\right) - \mu_0 \left(\nabla_j \frac{\partial^2 Q_{ij}}{\partial t^2}\right) \tag{2.32}$$

where μ_0 is the vacuum permeability and ε_{ijk} is the Levi-Civita tensor. Each of the terms within S_i can be expanded in powers of the incident radiation:

$$\begin{aligned} P_i &\propto \chi_{ij}^{PE} E_j + \chi_{ij}^{PM} H_j + \chi_{ijk}^{PEE} E_j E_k + \chi_{ijk}^{PEM} E_j H_k + \chi_{ijk}^{PMM} H_j H_k + \cdots \\ M_i &\propto \chi_{ij}^{ME} E_j + \chi_{ij}^{MM} H_j + \chi_{ijk}^{MEE} E_j E_k + \chi_{ijk}^{MEM} E_j H_k + \chi_{ijk}^{MMM} H_j H_k + \cdots \\ Q_{ij} &\propto \chi_{ijk}^{QE} E_k + \chi_{ijk}^{QM} H_k + \chi_{ijkl}^{QEE} E_k E_l + \chi_{ijkl}^{QEM} E_k H_l + \chi_{ijkl}^{QMM} H_k H_l + \cdots \end{aligned} \tag{2.33}$$

where we have only retained terms up to the second order in the incident electric (E_i) or magnetic fields (H_i). The tensors χ are the susceptibility tensors associated with each of these processes. The superscript can be read as the origin of the induced source, followed by the fields that are involved. Due to Neumann's principle, these tensors will encode the point group symmetries of the medium. In other words, the tensors should remain invariant under transformations that respect the symmetries of the material. As a result, the number of independent, non-zero tensor elements will greatly be reduced since these symmetry transformations will enforce a set of relationships among them.

Note that in Section 2.1, we presented an expression for the nonlinear polarization P_i induced in a material by an electric field in (Equation 2.5). This formula was in fact an expansion of the $\chi_{ijk}^{PEE} E_i E_k$ term—commonly referred to as the ED term—of P_i. Four nonlinear optical processes were identified to originate from this term, including SHG, sum and difference frequency generation, and optical rectification. In actuality, each of the second-order terms in Equation 2.33 will produce these processes. These additional terms were previously neglected because the ED contribution to S_i is orders of magnitude stronger than the second-order magnetic dipole (MD) and electric quadrupolar (EQ) term. In materials that preserve inversion symmetry, however, the ED term vanishes. In these systems, other contributions to the measured SHG intensity must be considered.

Once the appropriate process is determined, the theoretically expected pattern for the radiation must be compared against the experimental data. The experimentally measured quantity is a SHG intensity as the crystal is rotated about its surface normal. Thus far, however, we have only discussed the nonlinear densities P_i, M_i, and Q_{ij}. To convert from these quantities to the emitted electric field E_i, Maxwell's equations and the Fresnel equations must be solved with the correct boundary conditions at the sample-vacuum interface. For terms stemming from P_i the radiated light is

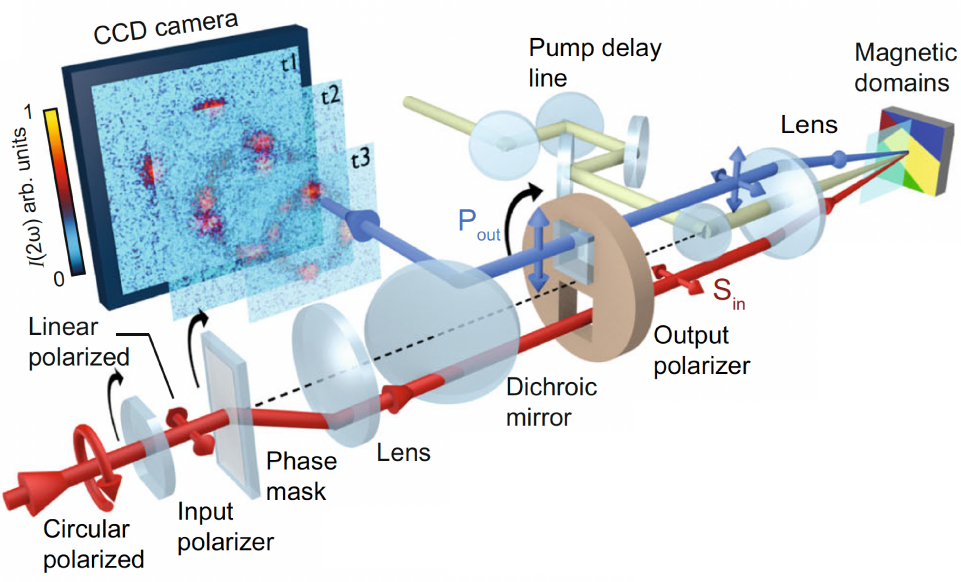

Figure 2.18: Schematic of a time-resolved rotational-anisotropy second harmonic generation setup used in this thesis. The red path tracks the fundamental probe light, the blue path tracks the second-harmonic generated light, and the off-white path tracks the pump light. The black curved arrows indicate the optics that are rotated together to generate the enable the collection of the RA pattern. The CCD camera shows an example of images collected at three different time delays for Sr_2IrO_4. From Reference [54]

proportional the absolute value squared of the term. Specific expressions for the radiated intensity can be derived by considering the polarizations of the incoming and outgoing light. Since each can be either $s-$ or $p-$polarized, there are four unique polarization channels to consider. The experimental data can then be fit with these expressions.

2.6.2 Experimental apparatus

The goal of SHG polarimetry is to measure the SHG intensity as the sample rotates about its surface normal. However, due to our use of cryogenics, the task of rotating the sample is a technical challenge as it is contained within the high vacuum of the cryogenic environment. One avenue to overcome this challenge is to simulate the sample rotation by keeping the sample stationary, but instead to rotate the scattering plane while keeping the polarizations of the incoming and outgoing light locked to the scattering plane. A detailed description of the resulting apparatus can be found in Reference [88].

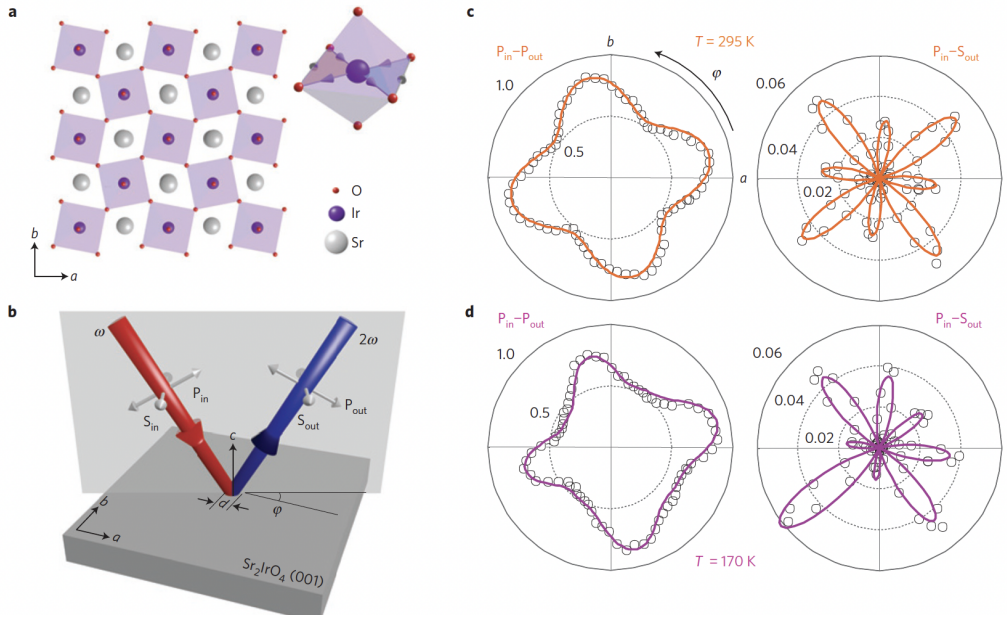

Figure 2.19: Equilibrium second harmonic polarimetry measurements of Sr_2IrO_4. **a** Crystal structure of Sr_2IrO4 as viewed from the (001) orientation. The inset depicts a single Ir atom ensconced in a octahedron of O atoms. **b** A schematic depiction of the RA-SHG measurement. **c** RA-SHG pattern of Sr_2IrO_4 collected at 295 K for both the $P_{in} - P_{out}$ and $P_{in} - S_{out}$ polarization configurations. Solid lines are fits of the RA patterns to the crystalline bulk EQ term. **d** RA-SHG pattern of Sr_2IrO_4 collected at 170 K for both the $P_{in} - P_{out}$ and $P_{in} - S_{out}$ polarization configurations. Solid lines are fits to the RA patterns for a combination of the crystalline bulk EQ term and the C_1 ED term that onsets below T_N. From Reference [251].

A schematic of the specific setup used in this thesis can be found in Figure 2.18 [54]. The experiment is seeded by Ti:sapphire regenerative amplifier producing 100 fs pulses centered at 800 nm at a repetition rate of 100 kHz. The light is first circularly polarized using a quarter wave plate before passing through a linear polarizer that sets the input polarization to be $s-$ or $p-$ polarized. It then passes through a lens pair that serves to telescope the beam size. Near the focus, a fused silica binary phase mask is used to separate the beam into many orders, all of which are blocked except the +1 order. The beam will come out of the phase mask at an angle that deviates from the original optical path. This angle is what enables the rotation of the scattering plane angle: rotating the phase mask will result in a procession of the beam about the original beam path. The processing beam is then passed through a lens that directs the beam to be parallel with the original beam path, allowing it to draw a circle as the phase mask rotates. The beam is then focused onto the sample using an objective lens. The reflected light is collected through the objective and is passed

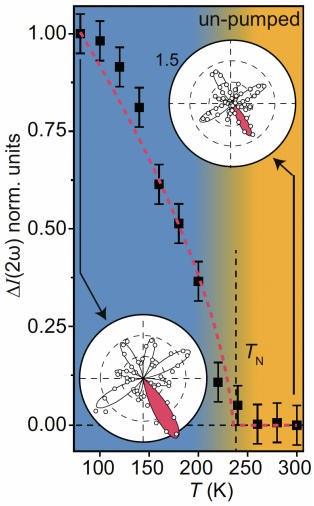

Figure 2.20: SHG intensity measured at the dominant lobe in the $P_{in} - S_{out}$ RA pattern measured as a function of temperature. The insets show the full RA pattern at several temperatures, with the dominant lobe highlighted in red. From Reference [54].

through a second linear polarizer that sets the output polarization to s or p. Note that the input polarizer and the output polarizer both rotate along with the PM to ensure that the polarizations are locked to the scattering plane. The light is then directed through a periscope consisting of dichroic mirrors that filter out the fundamental light, ensuring that only second harmonic light reaches the detector. Finally, the beam passes through another set of filters that further eliminate the fundamental frequency before arriving at an electron-multiplying CCD for detection. On the CCD, a circle will be drawn out as the phase mask rotates. Each position on the circle marks a different scattering plane angle. Thus, but integrating over this circle, the intensity of the SHG as a function of scattering plane angle is recorded and ready to be analyzed using the methods described above.

A pump can be introduced into this setup to study out-of-equilibrium phenomena. The pump beam is sourced from an OPA pumped by the same regenerative amplifier that seeds the SHG setup. Before reaching the sample, the pump beam passes through a retro-reflector mounted on a motorized delay stage that controls the temporal delay with respect to the probe. However, unlike the TDTS and transient reflectivity experiments, it is not possible to implement a differential lock-in technique to measure the pump-induced changes. Instead, the absolute SHG intensity is measured at each time delay on the CCD.

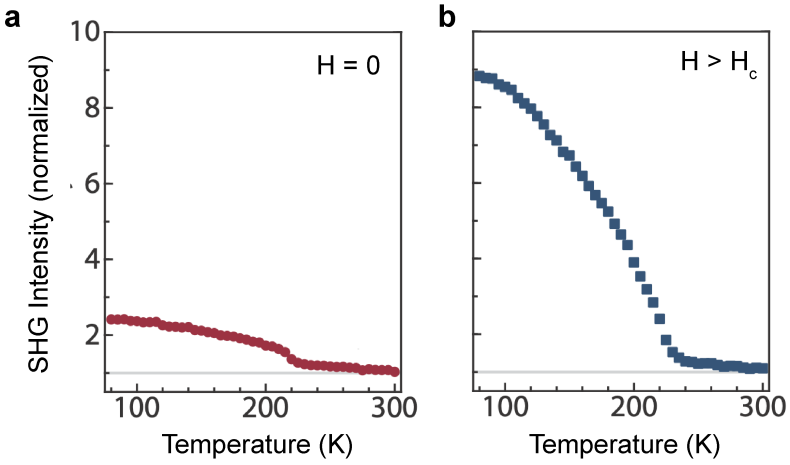

Figure 2.21: Temperature dependence of the SHG intensity in static Sr_2IrO_4 measured as a function of magnetic field. **a,b** SHG intensity measured at the dominant lobe in the $P_{in} - S_{out}$ RA pattern measured as a function of temperature for $H = 0$ (a) and $H = 370$ mT, which is greater than H_c. From Reference [200].

2.6.3 Second harmonic polarimetry of Sr_2IrO_4

We conclude this section by summarizing the work that has been done to study magnetism in Sr_2IrO_4 using SHG polarimetry. This discussion follows the works of Zhao *et al.* [251] in which the connection between SHG and magnetism Sr_2IrO_4 was first discovered, Seyler *et al.* [200] in which the origin of the magnetic signal was elucidated, and de la Torre *et al.* [54] in which the effects of photo-doping on the magnetic order were studied.

The crystal structure and axes of Sr_2IrO_4 are defined in Figure 2.19a. In the paramagnetic phase, the rotational-anisotropy (RA) SHG pattern—that is, the pattern obtained by rotating the scattering plane angle ϕ (Figure 2.19b) and measuring the SHG intensity—exhibits a clear C_4 symmetry (Figure 2.19c) [251]. Since the crystal structure preserves inversion symmetry, the ED contribution $P_i(2\omega) \propto \chi^{PEE}_{ijk} E_j(\omega) E_k(\omega)$ is not allowed. The next leading-order term from the bulk is the electric quadrupolar (EQ) term described by $P_i(2\omega) \propto \chi^{QEE}_{ijkl} E_j(\omega) \nabla_k E_l(\omega)$, which completely accounts for the data (Figure 2.19c). No contribution from the surface, which naturally breaks inversion symmetry, was detected. However, when the material was cooled down to below its Néel temperature ($T_N = 230$ K), the symmetry of the RA pattern was reduced from C_4 to C_1 (Figure 2.19d) [251]. Tracking the intensity of the strongest lobe as a function of temperature, a clear order-parameter-like onset is observed (Figure 2.20) [251]. The reduction the RA symmetry is not compatible with the reported Néel structure. Since the antiferromagnetically-aligned

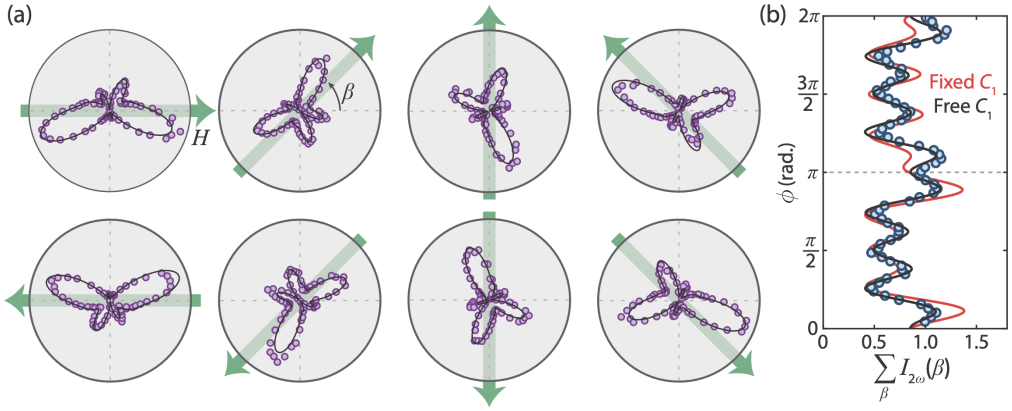

Figure 2.22: Dependence of the RA-SHG pattern in Sr_2IrO_4 as a function of the magnetic field direction. (a) RA-SHG patterns acquired in $P_{in} - S_{out}$ geometry at 80 K for different applied magnetic field angles (β). The magnetic field strength was fixed to 370 mT. Solid black lines are fits to the EQ + MD model. Other than the rotation of β, the susceptibility tensor elements were fixed. (b) Summation of the field-dependent RA data over all β. Solid lines show fits to a model that includes both the bulk EQ + MD terms and the anomalous C_1 term, where the latter either rotates with β (black) or is independent of β (red). From Reference [200].

magnetic moments in Sr_2IrO_4 are canted, a net ferromagnetic moment appears in each layer. These ferromagnetic moments are stacked in a $- + +-$ pattern, which preserves C_2 symmetry. The reduction in symmetry also cannot be accounted for by any structural distortions since there are no reports of a reduction in crystallographic symmetry that onsets below T_N.

Instead, the C_1-symmetric pattern indicates the onset of a new radiation source. Several mechanisms were proposed, including a formation of a magnetoelectric loop-current order that would generate ED radiation [251], laser-based re-arrangement of the ferromagnetic stacking order [57], and enhanced sensitivity to surface magnetic order [57]. Laser-based re-arrangement was ruled out by the fact that the results were unaffected by the intensity of the probe light [200]. To distinguish between the remaining two possibilities, the field dependence of the anomalous C_1 SHG signal was studied [200]. In an in-plane magnetic field, Sr_2IrO_4 undergoes a meta-magnetic transition from the C_2-preserving $- + +-$ ferromagnetic layer stacking to a C_2-breaking $+ + ++$ stacking above a critical field H_c [189]. Whereas the net ferromagnetic moment of this order should rotate rigidly with the magnetic field [189], the magnetoelectric order cannot couple linearly to magnetic field except in the presence of an additional electric field [201].

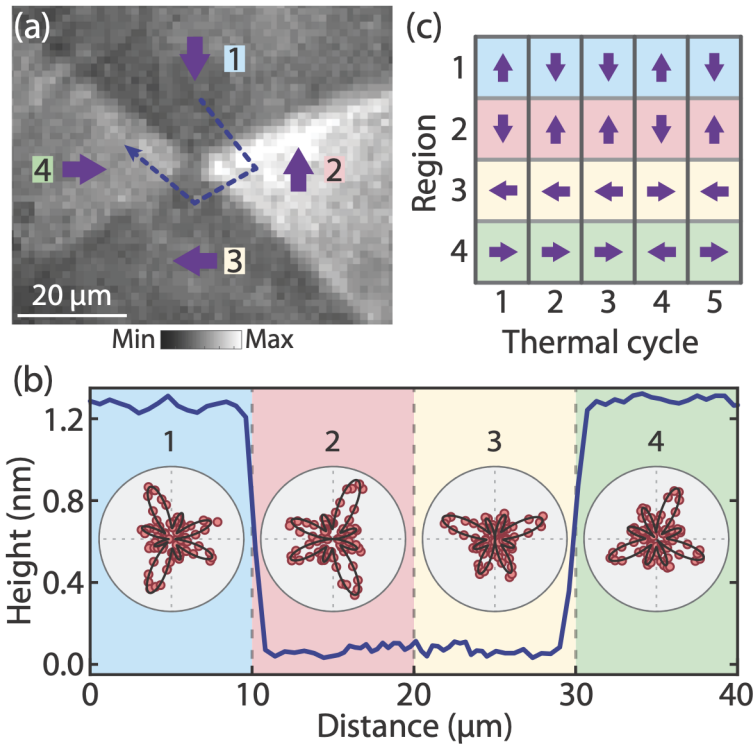

Figure 2.23: Correlated topographic mapping and SHG imaging of Sr_2IrO_4. (a) An SHG image captured in the $P_{in} - P_{out}$ geometry. The temperature was fixed to 80 K, and the RA angle ϕ was fixed to a point in the pattern that would allow for different magnetic domains to be distinguished. The orientations of the C_1 order parameter (purple arrows) were determined by taking full RA SHG scans in each region. (b) Topographic height profile along a line cut shown by the dashed line in (a) obtained with atomic force microscopy. Insets show the local $P_{in} - S_{out}$ RA pattern in each domain. Black lines are fits to the bulk EQ + ED model. (c) Orientation of the C_1 order parameter at 80 K after successive thermal cycles from 80 K to 295 K and back to 80 K in each of the four regions. From Reference [200].

When measured in a field of 370 mT, above H_c, the RA SHG pattern still demonstrates the anomalous C_1 contribution and the crystallographic EQ term [200]. However, an additional bulk-magnetization-dependent term is strongly enhanced in the + + ++ state. As a result, the low-temperature SHG intensity in the + + ++ state is much larger than in the zero-field state (Figure 2.21). To examine how the anomalous C_1 term couples to the field, the field orientation was rotated about the surface normal. The pattern rotates by 180° upon rotation of the field from H to $-H$, implying that both the bulk-magnetization dependent SHG and C_1 SHG processes couple linearly to the field, ruling out the magnetoelectric order scenario (Figure

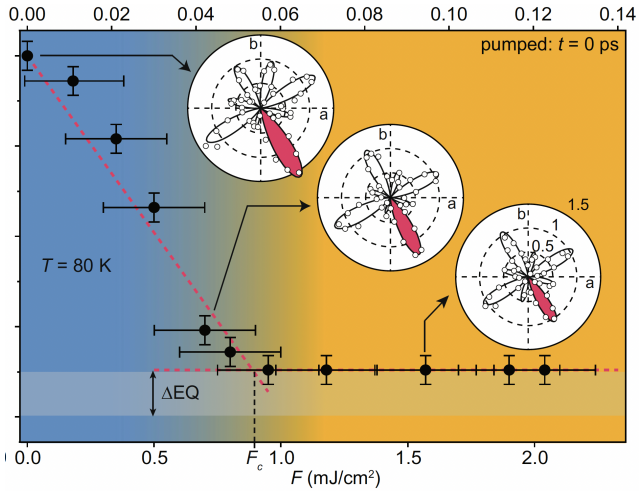

Figure 2.24: SHG intensity measured at the dominant lobe in the $P_{in} - S_{out}$ RA pattern in photo-doped Sr_2IrO_4 measured as a function of fluence. The insets show the full RA pattern at several fluences, with the dominant lobe highlighted in red. From Reference [54].

2.22).

The remaining possibility is that the C_1 term originates from a surface magnetization-induced SHG process. To confirm this scenario, a widefield SHG image of the sample surface was taken in the absence of a magnetic field, revealing the presence of many domains (Figure 2.23a) [200]. Within each domain, the orientation of the RA pattern was rotated by either 90° or 180° from its neighboring domain (Figure 2.23a,b). By comparing the SHG image to a topographic survey of the sample taken with atomic force microscopy, it was found that the domain pairs with a relative 90° rotation were on an atomically-flat region of the sample and are likely caused by crystallographic twin boundaries in which the in-plane a and b axes were interchanged (Figure 2.23b). On the other hand, the 180° rotations only occurred across steps on the sample surface where the height changes by a bilayer (Figure 2.23c). This observation is consistent with surface-magnetization-induced SHG from the established $-++-$ stacking in the zero-field case. This SHG process is of the ED type and can be expressed as $P_i(2\omega) \propto \chi_{ijkl} M_{s,l} E_j(\omega) E_k(\omega)$, where the vector $\mathbf{M}_s$ is the surface magnetization. Since $\mathbf{M}_s$ reverses every two layers in the material from $-++-$ to $+--+$, the SHG pattern will exhibit a 180° rotation across the bilayer.

This understanding can be further confirmed by thermally cycling the sample from 80 K to 295 K and back to 80 K [200]. As can be seen in Figure 2.23c, the patterns

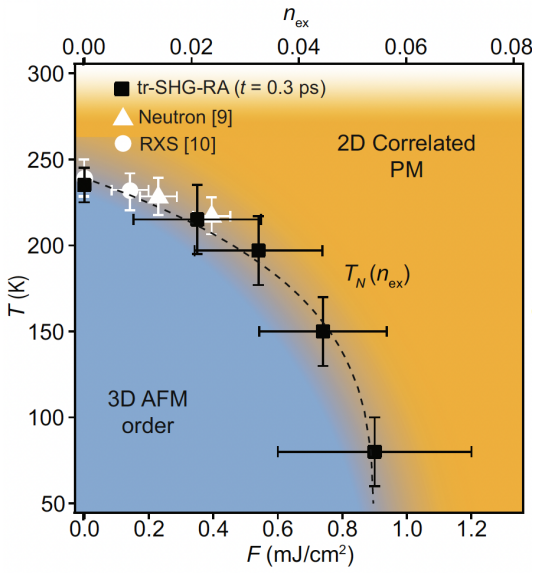

Figure 2.25: Out-of-equilibrium magnetic phase diagram of Sr_2IrO_4 obtained by tracking the critical fluence F_c at which the C_1 order parameter disappears in the RA-SHG patterns at various temperatures. From Reference [54].

in regions that border a step (regions 1 and 2, regions 3 and 4) in the sample are always anti-correlated, while no correlation is observed for regions on a single level (regions 1 and 4, regions 2 and 3). This behavior indicates that regions that border the step are a part of a single magnetic domain, while those on a single level are not. Instead, the differences between regions on the same level result from structural twinning defects.

Building upon these results, SHG was also used to study the evolution of the magnetic order in Sr_2IrO_4 in response to a photo-doping drive [54]. The pump photon energy was tuned to be resonant with the β peak in the optical conductivity that marks transitions from the filled $J_{eff} = 3/2$ band to the empty upper Hubbard band. As the fluence of the pump pulse was increased, the C_1 SHG term was slowly reduced until it vanished beyond a critical fluence F_c of roughly 1.0 mJ/cm^2, corresponding to a photo-dopant density n_{ex} = 0.06 excitations per Ir atom (Figure 2.24). The experiment was repeated as a function of temperature, revealing an out-of-equilibrium phase diagram that closely resembles that obtained with chemical doping (Figure 2.25).

Chapter 3

THE HUBBARD EXCITONIC FLUID

3.1 Excitons in Mott insulators

An important distinction between chemically-doped materials and photo-doped materials is the simultaneous presence of an electron-like excitation and a hole-like excitation. Interactions between the two can lead to excitonic bound states. Excitons have been extensively studied within the realm of weakly correlated rigid band insulators, in which they are bound through the Coulomb interaction. Aside from the impact they have on the opto-electronic properties of these materials [144], excitons also play a critical role in determining their out-of-equilibrium properties. The photo-excitation process can lead to a metastable population of excitons since particle-hole recombination is slowed by the presence of the charge gap. The excitons within this ensemble can interact with one another, forming unique phases of matter including insulating fluids [105, 249], Bose-Einstein condensates [205], density wave orders [34], and electron-hole droplet states [254].

The presence of excitons is also important in determining the recombination dynamics of the photo-doped system. Depending on the symmetries of their host crystal, their spatial and energetic properties, and their coupling to different degrees of freedom in the material, excitons demonstrate a strikingly broad range of lifetimes explained by a myriad of microscopic mechanisms. For example, the spatial separation of the electron and hole that constitute an electron can lead to extremely stable excitons, with lifetimes exceeding 100 ns [103]. On the other hand, ultrafast ($\sim$100 fs) radiative recombination has been observed in excitons that couple strongly to light [188]. Studying excitonic dynamics can thus reveal important aspects of the material and its out of equilibrium properties, including its charge distribution, the presence of microscopic interactions, and the presence of different excitonic phases.

While excitons are routinely studied in driven semiconductors, they have not been extensively considered in the photo-excited properties of Mott antiferromagnets (AFMs). Recently, however, evidence has been emerging that excitons also are also important in the properties of photo-doped Mott insulators. A theoretical study of the photo-excited recombination dynamics in the cuprates, for example, has revealed that the ultrafast ($\sim$1 ps) timescales can be explained by the presence of spin-bound

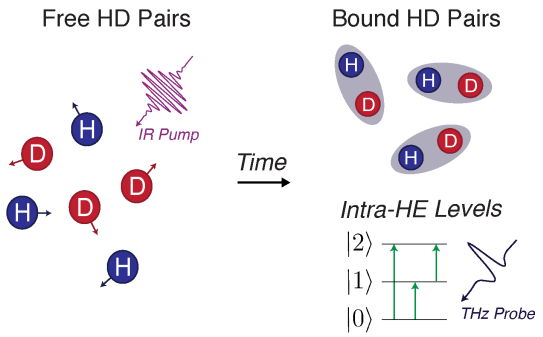

Figure 3.1: A photo-doping induced HD plasma transforms into a fluid of bound HEs as a function of time. Transitions between internal HE levels (green arrows), which are populated upon HD plasma decay, are probed by a THz pulse.

Hubbard excitons (HEs) [129, 130]. Due to their the strong coupling magnetic degrees of freedom, these HEs can efficiently emit magnons, thereby facilitating a rapid recombination across the gap. In addition to the charge dynamics, excitons have also been invoked to explain the magnetic excitation spectra of photo-doped Mott AFMs. Both time-resolved resonant inelastic x-ray scattering and time-resolved Raman scattering have revealed the emergence of low-energy spectral weight below the single- and two-magnon excitation energies. A recent theoretical study has assigned this weight to the presence of HEs that form at the absorption edge [227].

These results suggest that it is crucial to unravel the previously unappreciated role the HEs play in the photo-doped states of Mott AFMs. Progress in this endeavor is currently limited by the lack of a suitable experimental probe of the excitonic states. As discussed in Section 1.3.1, the potential Hubbard excitonic states identified thus far overlap heavily with the Mott gap edge [80, 86, 221], implying that excitons are unstable against decay into the free holon-doublon (HD) continuum [202]. Not only does this fact call into question to what extent HEs survive in the out-of-equilibrium state, but it poses an experimental challenge. Since the HE states and the HD continuum occur at the same energies, it is not possible to distinguish their dynamics when probing at the near-infrared energies associated with these transitions.

This challenge can be overcome by instead looking towards much lower energies. A direct approach to distinguishing between a plasma of unbound HD pairs and a fluid of bound HEs is to exploit their unique spectral features at THz frequencies. Whereas the former exhibits a metallic Drude response, the latter should exhibit an insulating response characterized by finite energy peaks corresponding to transitions

between different excitonic bound states (Figure 3.1), which are predicted to lie in the meV range [46, 105, 242, 249]. Tracking HE dynamics via intra-excitonic peaks, rather than via excitonic resonances in interband optical spectra, is also advantageous because it enables access to optically dark HEs with finite center-of-mass momenta and is not obscured by the effects of photo-doping induced bandgap renormalization and mid-gap state formation, which are pronounced in Mott insulators [180].

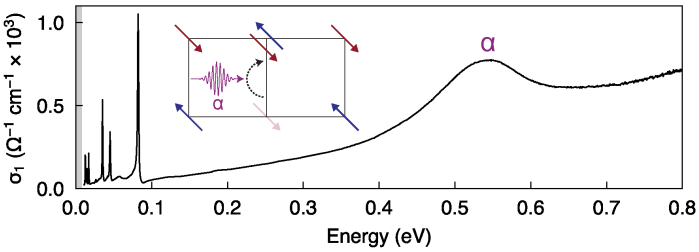

Figure 3.2: Optical conductivity of Sr_2IrO_4 [199]. Inset: Real-space depiction of HD creation via photo-excitation that is resonant with the Mott gap transition α.

3.2 THz Intra-excitonic Spectroscopy of Sr_2IrO_4

Here, we use time-resolved time-domain THz spectroscopy (tr-TDTS) to probe the transient low energy dynamics of photo-doped holons and doublons in the square lattice AFM Mott insulator Sr_2IrO_4. As covered in Section 1.4.1, the low energy electronic structure of Sr_2IrO_4 consists of a completely filled band of spin-orbital entangled pseudospin $J_{eff} = 3/2$ states and a narrow half-filled band of $J_{eff} = 1/2$ states, which splits into a lower Hubbard band (LHB) and an upper Hubbard band (UHB) due to on-site Coulomb repulsion [115]. Optical conductivity measurements show the LHB $\rightarrow$ UHB transition peak (dubbed the α transition) lying just below 0.6 eV (Figure 3.2) [161, 199]. The localized $J_{eff} = 1/2$ moments are coupled through strong Heisenberg-type exchange interactions (J = 60 meV) [117], which is in principle conducive to spin-mediated HD binding, and undergo long-range Néel-type AFM ordering below a temperature T_N = 230 K [37]. Although resonant inelastic x-ray scattering measurements have shown evidence of a spin-orbital resonance inside the HD continuum, associated with an intra-site $J_{eff} = 3/2$ to $J_{eff} = 1/2$ excitation [117], no direct evidence of HEs—generated through inter-site LHB to UHB excitation—has been reported.

Ultrafast tr-TDTS measurements were performed in reflection geometry on (001) single crystals of Sr_2IrO_4. HD pairs are optically generated using a near-infrared

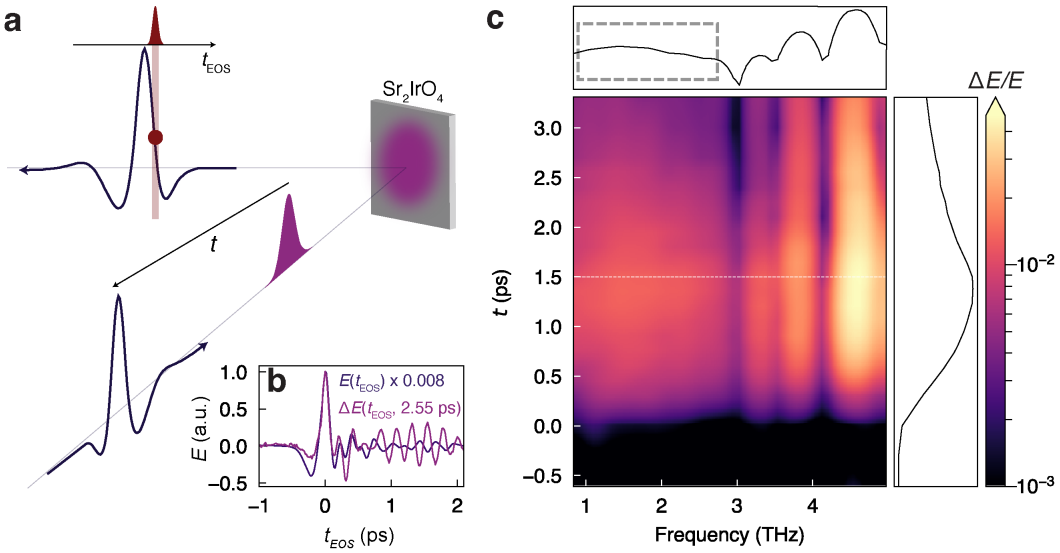

Figure 3.3: Time-resolved THz spectrum of Sr_2IrO_4. **a** Schematic of the tr-TDTS setup. The sample is excited by an intense near-infrared pulse (magenta) resonant with the α transition. The transient response at a fixed time-delay t is then probed by a weak broadband THz pulse (blue). An 800 nm pulse (maroon) measures pump-induced changes of the reflected THz pulse through EOS (see Section 2.4). **b** Equilibrium (blue) THz pulse $E(t_{\mathrm{EOS}})$ and its pump induced change (magenta) $E(t_{\mathrm{EOS}}, t = 2.55$ ps). **c** Differential change in the reflected THz spectrum of Sr_2IrO_4 taken at 80 K in response to α peak-resonant photo-excitation with fluence 2 mJ/cm^2. Top: Spectrum at $t = 1.5$ ps. Gray box highlights the broad peak. Right: Frequency-integrated response as a function of t.

100 fs (FWHM) pump pulse tuned on-resonance with the α transition (0.6 eV). After a variable time delay t, the low energy charge response is probed by a phase-locked broadband (2 $\rightarrow$ 24 meV) THz pulse, whose electric field profile in the time domain is measured by electro-optic sampling (EOS) as a function of the recording time t_{EOS} (Figure 3.3a). Figure 3.3b shows the reflected THz field transient $E(t_{\mathrm{EOS}})$ from the un-pumped crystal overlaid with its pump-induced change $\Delta E(t_{\mathrm{EOS}}, t)$ recorded at a fixed time delay of $t = 2.55$ ps. The predominant features of $\Delta E(t_{\mathrm{EOS}}, t)$ track $E(t_{\mathrm{EOS}})$ with minimal phase offset, indicating that the presence of photo-dopants increases the THz reflectance as expected.

Pump-induced differential THz spectra in the frequency domain are obtained by Fourier transforming the field transients with respect to t_{EOS}. Figure 3.3c shows typical spectra from Sr_2IrO_4 acquired at a temperature $T = 80$ K and a pump fluence of 2 mJ/cm^2 plotted as a function of t. At all frequencies, we observe a fast rise in the reflected field amplitude upon injection of photo-dopants at $t = 0$, followed by a

slower exponential decay over several picoseconds. Four peaks clearly appear in the spectra after pump-excitation. There are three sharp peaks above 3 THz that match the three lowest frequency infrared-active phonon modes in Sr_2IrO_4 [51, 161, 199], as well as one broader peak centered near 1.5 THz, which lies more than 1 THz above the highest energy zone-center magnon mode [13, 55, 117]. Our measurement of the refractive index of un-pumped Sr_2IrO_4 by TDTS in transmission geometry (see Section 2.4) shows no evidence of phonon or magnon peaks in the vicinity of 1.5 THz (Figure 3.4), consistent with previous reports. These results suggest that the broad peak is not an excitation of a structural or magnetic origin, and can potentially be attributed to an excitonic origin.

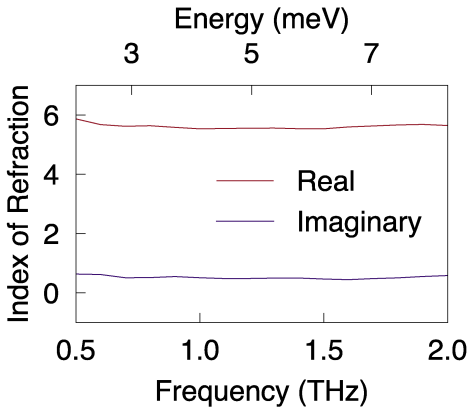

Figure 3.4: Real and imaginary parts of the index of refraction of Sr_2IrO_4 in the THz regime (shaded gray energy window in Figure 3.2).

This conclusion is supported through an analysis of the full dielectric response of the photo-doped state, which is extracted from the differential THz spectra through standard electrodynamical relations using the thin film approximation (Section 2.4.9). Figure 3.5 show the pump-induced change to the real $\Delta\sigma_1(\omega)$ and imaginary $\Delta\sigma_2(\omega)$ parts of the optical conductivity at different t. Immediately upon injection of photo-dopants ($t = 0$) there is a positive increase in both $\Delta\sigma_1(\omega)$ and $\Delta\sigma_2(\omega)$, as is expected from a conducting plasma of unbound holons and doublons [180, 210, 249]. Over the next several hundred femtoseconds, $\Delta\sigma_1(\omega)$ evolves into a peak shape centered around 1.5 THz, while $\Delta\sigma_2(\omega)$ develops a dispersive lineshape with a zero-crossing at the same frequency. These are signatures of a Lorentzian dielectric function, consistent with the absorptive response of a bound Hubbard excitonic state. In fact, this evolution from a Drude-like response into an absorptive Lorentzian response is a hallmark of exciton formation following photo-excitation resonant with the α

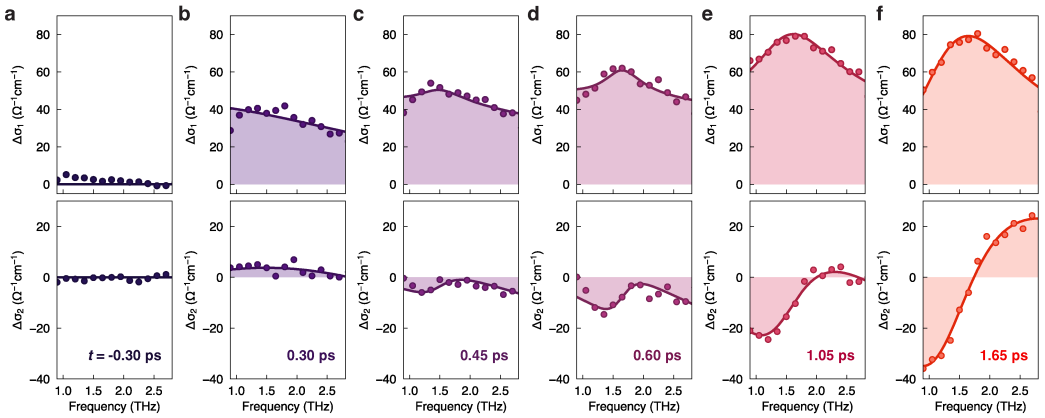

Figure 3.5: Photo-doping induced optical conductivity transients of Sr_2IrO_4. **a-f** $\Delta\sigma_1(\omega)$ (top panels) and $\Delta\sigma_2(\omega)$ (bottom panels) extracted from differential THz spectra at various t. Fits to the Drude-Lorentz model (Equation 3.1) are displayed as solid lines.

transition, with the Lorentzian representing a transition from one internal excitonic level to another [105, 210, 249].

To understand the temporal interplay between free and bound HD states, $\Delta\sigma_1(\omega)$ and $\Delta\sigma_2(\omega)$ were simultaneously fit to a sum of Drude and Lorentz oscillator functions at each t:

$$\frac{D}{2}\left[\frac{1}{\gamma_{\text{Drude}} - i\omega}\right] + \frac{L_{\text{HE}}}{2}\left[\frac{\omega}{i\left({\omega_{\text{HE}}}^2 - \omega^2\right) + \omega\gamma_{\text{HE}}}\right] + \frac{L_{\text{Bgd.}}}{2}\left[\frac{\omega}{i\left({\omega_{\text{Bgd.}}}^2 - \omega^2\right) + \omega\gamma_{\text{Bgd.}}}\right]. \tag{3.1}$$

The first term is a Drude term. The second term is a Lorentzian term representing the HE mode. The final Lorentzian term describes a weak background, likely caused by pump-induced changes of higher energy features such as the phonon transitions. One or two background Lorentzians were used depending on the dataset. The fitting constants D, L_{HE}, and $L_{\text{Bgd.}}$ are the strengths of the Drude, HE, and background terms, respectively. The fitting constants γ_{Drude}, γ_{HE}, and $\gamma_{\text{Bgd.}}$ are the widths of the Drude, HE, and background terms, respectively. The fitting constants ω_{HE} and $\omega_{\text{Bgd.}}$ are the central frequencies of the HE and background terms, respectively. For $t \leq 450$ fs, the value of γ_{Drude} was left as a free parameter, while for later t it was fixed to its average fitted value in order to constrain the number of free parameters

and improve the quality of the fit. In Figure 3.6, a representative dataset is shown along with each of the individual components of the fit.

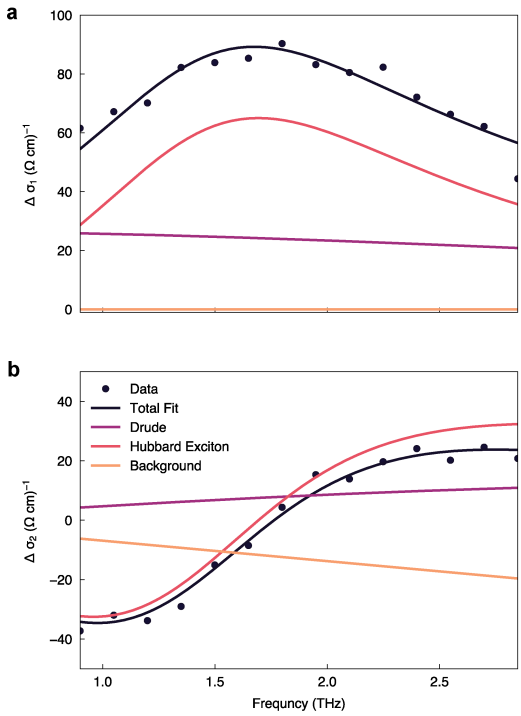

Figure 3.6: Individual components of the Drude-Lorentz fitting of **a** $\Delta\sigma_1(\omega)$ and **b** $\Delta\sigma_2(\omega)$ plotted with the original data at t = 1.5 ps. The pump energy was fixed at 0.6 eV, resonant with the α transition, and set to a fluence of 2 mJ/cm^2. The temperature of the sample was 80 K.

A high quality of fit is achieved at each t as shown in Figure 3.5. The spectral weights (SW) associated with the Drude and intra-excitonic Lorentzian components, defined as the area under the fits to $\Delta\sigma_1(\omega)$, are proportional to the number of free and bound carriers, respectively [106]. As shown in Figure 3.7, the Drude SW increases from zero starting at t = 0 and reaches a maximum ($t \approx$ 0.4 ps) after the pump pulse has been completely absorbed. Previous time-resolved near-infrared reflectivity [55, 92] and angle-resolved photoemission spectroscopy measurements [186] on Sr_2IrO_4 showed that intraband cooling of photo-dopants occurs on an ultrashort timescale of around 60 fs, which is typical for AFM Mott insulators [180]. Therefore, by t = 0.4 ps, the unbound holons and doublons have relaxed near the Hubbard band edges. At these early times, the system exhibits a finite Drude SW with a relatively low scattering rate (3.9 ± 0.1 THz at t = 0.3 ps) compared to 15 % Rh doped metallic Sr_2IrO_4 crystals [244], indicating conducting behavior. Between

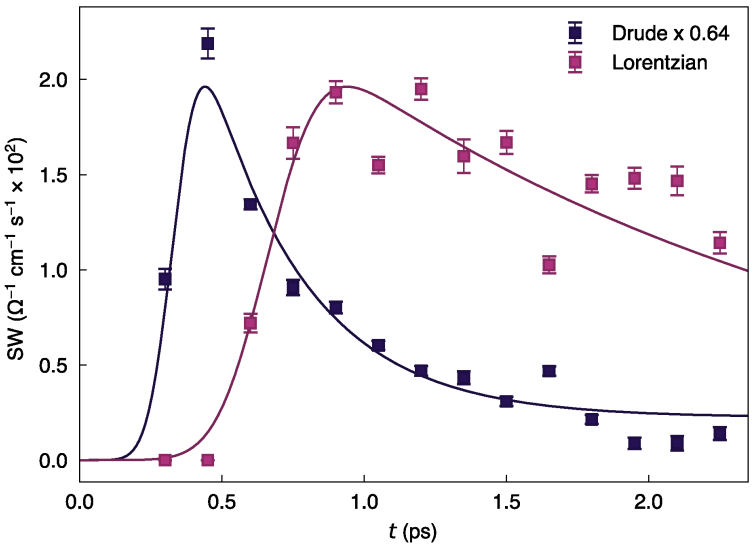

Figure 3.7: SW of the Drude and HE Lorentzian terms versus t obtained by the Drude-Lorentz fitting of the data in Figure 3.5. The solid lines are fits to a single exponential function (Equation 2.30). Error bars are obtained from the standard deviation of the least-squares-fitting algorithm.

t = 0.4 ps and 1 ps, there is a rapid decay of the Drude SW that coincides with a rise in the Lorentzian SW from zero, demonstrating a SW transfer from the former to the latter component. This aligns with our expectation that free holons and doublons can only bind into stable HEs when their kinetic energy falls below a threshold value. At t = 1 ps, the Lorentzian SW reaches a maximum and subsequently decays over a timescale of several picoseconds due to HE recombination. During this decay, there is a time window when the system possesses a finite Lorentzian SW but vanishing Drude SW within our experimental resolution, thus realizing a transient insulating HE fluid. A dynamical crossover from a conducting electron-hole plasma to an insulating excitonic fluid was previously identified in the photo-doped rigid band semiconductor GaAs through analogous features in tr-TDTS data [105, 249]. However, the characteristic timescales for exciton formation and decay in Sr_2IrO_4 are three orders of magnitude shorter.

3.3 Pump photon energy dependence

Thus far, we have performed experiments resonant with the α transition that marks LHB $\rightarrow$ UHB transition. However, another possibility would be to pump the J_{eff} =3/2 $\rightarrow$ UHB transition, known as the β transition. Doing so will initially excite a J_{eff} = 3/2 electron to the J_{eff} = 1/2 upper Hubbard band, leaving behind a hole in

the J_{eff} = 3/2 band [115, 244]. It is well known that in Sr_2IrO_4 the photo-carrier relaxation towards the gap edge occurs on an ultrafast (~10 fs) timescale [92]. Due to this rapid thermalization process, we should expect that some subset of the holes produced in the J_{eff} = 3/2 band should relax into the lower Hubbard band, leaving them available for Hubbard exciton formation with electrons in the upper Hubbard band. However, because some subset of the J_{eff} = 3/2 holes will directly recombine with J_{eff} = 1/2 electrons, the number of excitons generated relative to the total number of photo-excited carriers should be reduced as compared to the case of directly pumping the α transition. Thus, we can compare the fraction of the total photo-carriers that become excitons when pumping the α versus β transitions to provide further evidence for our interpretation of the data.

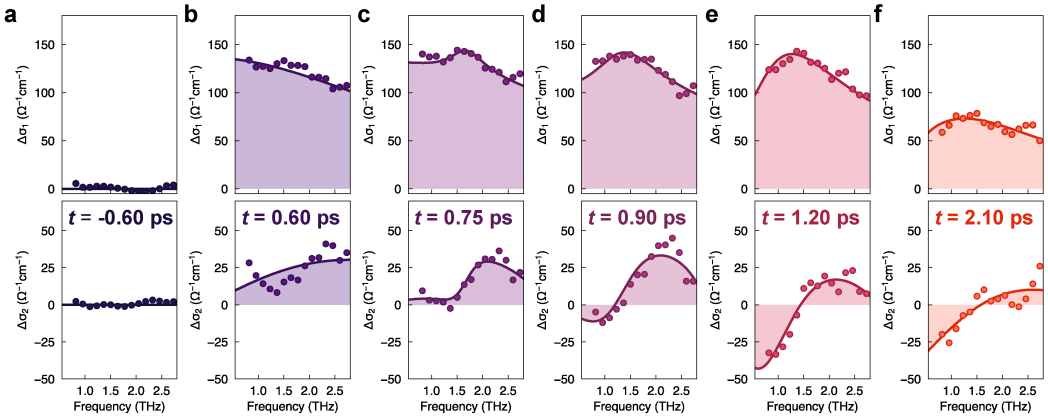

Figure 3.8: **a-f** $\Delta\sigma_1(\omega)$ (top panels) and $\Delta\sigma_2(\omega)$ (bottom panels) extracted from differential THz spectra at various t. The pump was set to 1.0 eV (resonant with the β transition) and the data were taken at 80 K. Fits to the Drude-Lorentz model (Equation 3.1) are displayed as solid lines.

Accordingly, we performed additional experiments at a pump photon energy of 1 eV, which is resonant with the β transition. In line with our expectations, we see the emergence of a Drude response immediately after the arrival of the pump followed by an ultrafast spectral weight transfer into a finite energy peak, similar to pumping the α transition (Figure 3.8). To characterize this spectral weight transfer, we performed the same Drude-Lorentz fitting described in Equation 3.1. In Figure 3.9, we plot the Drude and Lorentzian spectral weights for both the α and β pumping cases. As can be seen, while a Drude-to-Lorentz spectral weight transfer is observed in both cases, the spectral weight ratio between the two terms is not the same for each pumping case. While the α case produces a Lorentz to Drude ratio of roughly 0.64 at their peaks, the β case produces a ratio of 0.23. Since the Drude spectral

weight is indicative of the number of free carriers and the Lorentzian spectral weight is indicative of the number of bound carriers [106], we can conclude that the conversion efficiency from free carriers to bound pairs is significantly reduced in the β case as compared to the α case. This is consistent with the expected result described in the previous paragraph, providing further evidence for our assignment of the Lorentzian component to an excitonic origin.

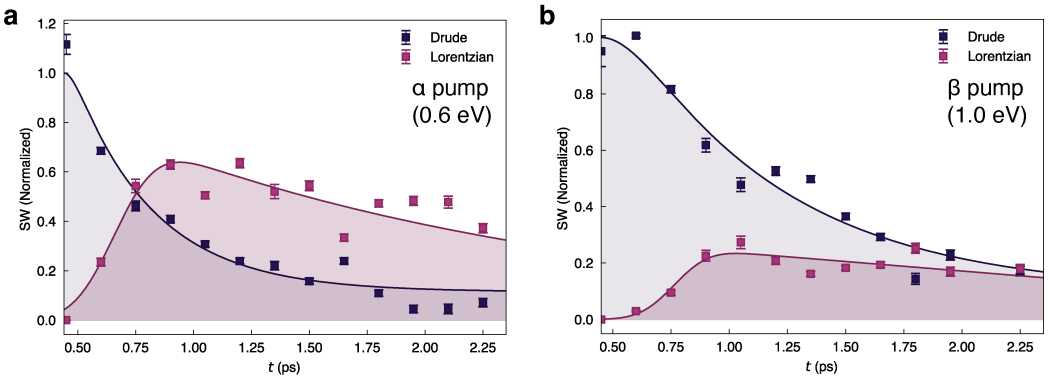

Figure 3.9: Temporal evolution of the spectral weight in α- and β-pumped Sr_2IrO_4. **a**,**b** Spectral weight of the Drude and HE Lorentzian terms versus time delays t for the α pumping case (a) and the β pumping case (b). The data is normalized to the maximum of the Drude spectral weight in each of the panels. The solid lines and shaded regions are guides to the eye. Error bars are obtained from the standard deviation of the least-squares-fitting algorithm.

3.4 Determining the Hubbard excitonic recombination pathway

Since tr-TDTS probes excitons with center-of-mass momenta lying both inside and outside of the light cone [105, 188], it is sensitive to all radiative and non-radiative recombination pathways. In WSe_2, for example, an ultrafast radiative recombination of bright excitons and a slower Auger recombination of dark excitons was clearly manifested through a two-step decay of the $1s$-$2p$ intra-excitonic peak [188]. To uncover the pathway underlying the ultrafast HE recombination in Sr_2IrO_4, we measured the decay dynamics of the total SW about the 1.5 THz mode—obtained by integrating $\Delta\sigma_1(\omega)$ from 0.8 to 2 THz—at a series of temperatures from 80 K to 300 K (Figure 3.10a). The functional form of the decay for $t > 1$ ps, which is dominated by the Lorentzian term (Figure 3.7), is well described by a single exponential at all temperatures (Figure 3.10a), suggesting one predominant exciton recombination pathway. Although sub-picosecond radiative recombination has been reported in semiconductors with large interband dipole moments [188, 210], this

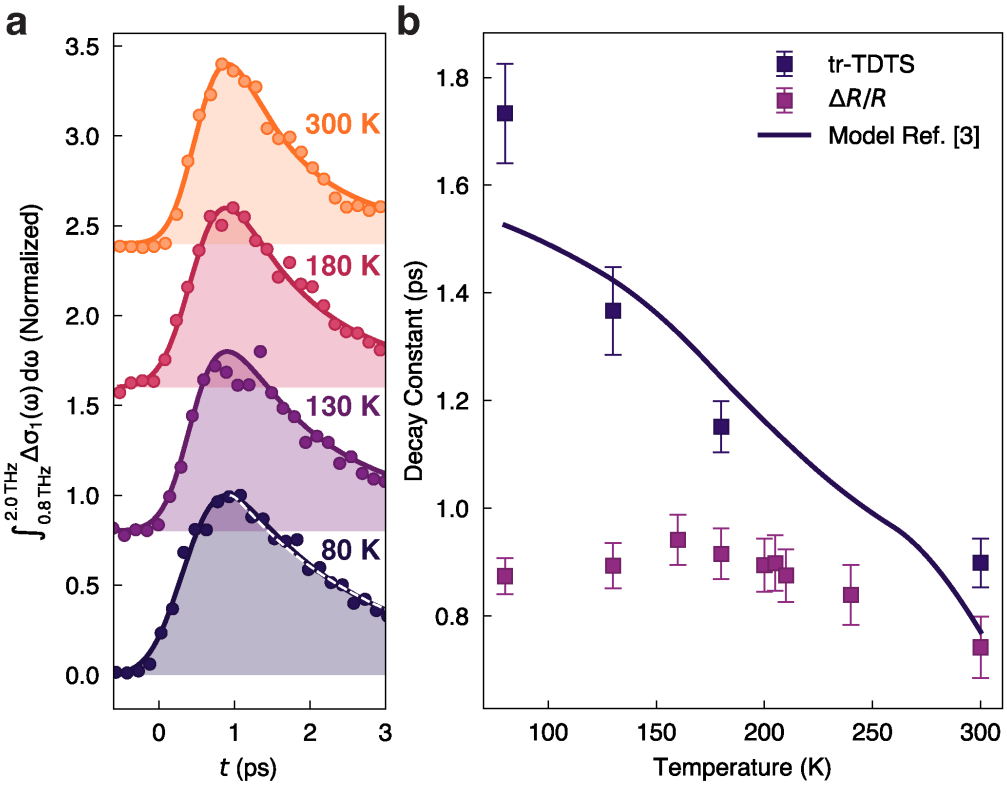

Figure 3.10: Temperature dependence of Hubbard exciton decay properties. **a** Temperature dependence of the photo-induced changes to $\Delta\sigma_1(\omega)$ integrated from 0.8 THz to 2.0 THz. Solid lines are fits to a single exponential function (Equation 2.30). The white dashed line in the 80 K dataset is the exponential fit to the Lorentzian SW shown in Figure 3.7, showing excellent agreement. **b,** Temperature dependence of the exponential decay constants extracted from the data in panel a and from the infrared reflectivity transients ($\Delta R/R$) shown in Figure 3.12. Details of this measurement can be found in Section 2.5. The solid line is a fit to the multi-magnon emission model described in Reference [129]. Error bars are the standard deviation from the least-squares-fitting algorithm.

process is unlikely in Sr_2IrO_4 owing to the *d*-*d* character of the α transition [115] and the complete absence of excitonic peaks in interband optical spectra [161, 199] (Figure 3.2). Auger recombination can also be ruled out because the exponential decay time is fluence independent (Figure 3.11), indicating a monomolecular rather than multi-molecular recombination process.

Given the strong coupling of charges to the pseudospin [117, 161] and lattice [93, 138, 161] degrees of freedom in Sr_2IrO_4, we examine the possible role of collective bosonic excitations in the recombination of HEs. The highest energy

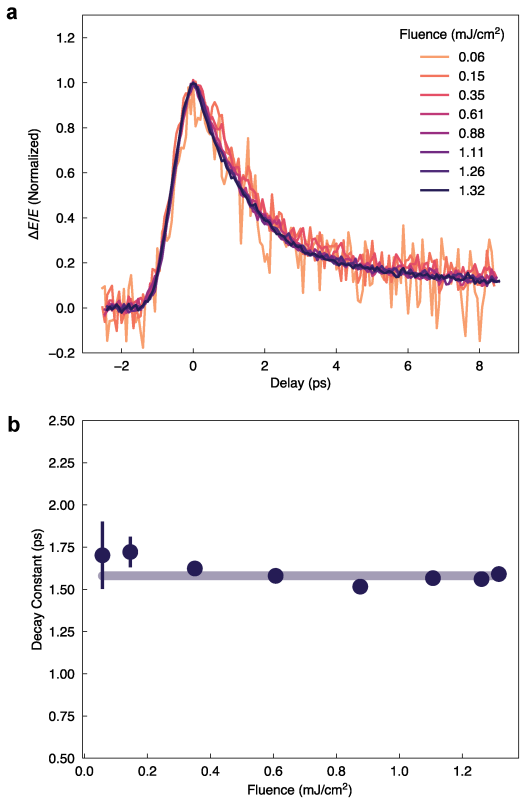

Figure 3.11: Fluence independence of THz frequency decay dynamics. **a** $\Delta E(t_{\mathrm{EOS}}, t)$ traces taken with t_{EOS} fixed to the time where $E(t_{\mathrm{EOS}})$ is maximal (see Section 2.4 for details) plotted as a function of the fluence of the α-resonant (0.6 eV) photo-excitation. Data was collected at a sample temperature of 80 K. **b** Decay constants extracted from an exponential fitting (Equation 2.30) of the traces in panel a. The solid line is a guide to the eye. Error bars are the standard deviation from the least-squares-fitting algorithm.

magnon [117] and phonon [51] modes in Sr_2IrO_4 lie near 200 meV and 90 meV, respectively, well below the Mott gap scale (Figure 3.2). Therefore HEs can in principle recombine through multi-magnon or higher-order multi-phonon emission channels [129–131]. This mechanism naturally explains the strong temperature dependence of the exponential HE decay time τ, which clearly contrasts with the largely temperature independent decay of the infrared charge response (Figure 3.10b, Figure 3.12), for the following reason. Optical conductivity measurements have shown that upon cooling from 300 K to 80 K, the Mott gap $\Delta(T)$ of Sr_2IrO_4 is significantly enhanced [161, 199]. This means that a greater number of bosons must be emitted in order for HEs to relax across the Mott gap, leading to a larger τ [211]. In fact, numerical studies of the 2D square lattice Hubbard model have

predicted that HEs can rapidly recombine through multi-magnon emission on the picosecond timescale with $\tau \propto \exp[\zeta\Delta(T)/J]$, where J is the magnetic exchange energy and ζ is a factor of order unity [129, 130]. Using the experimentally reported values of $\Delta(T)$ [161] and J = 60 meV [117], we find that this equation provides a good fit to the measured temperature dependence of τ (Figure 3.10b), with a fitted value of $\zeta = 0.76(2)$. Such strong coupling of HEs to magnons supports the idea that AFM correlations play a significant role in HD binding. Note that even though 3D long-range AFM order is lost above T_N, individual 2D layers continue to exhibit pronounced AFM correlations with a well-defined magnon spectrum in the paramagnetic phase since the scale of J far exceeds T_N [70, 81, 82]. Since it is in-plane correlations that are critical to the stability of HEs [46, 130, 202, 221], this behavior is consistent with the absence of anomalies in τ near T_N. Further evidence for this recombination process can be obtained through measurements of the bosonic excitation spectra in Sr_2IrO_4 via time-resolved inelastic x-ray scattering [55], time-resolved absorption [13], or time-resolved Raman spectroscopy [81], and is a critical direction of future work.

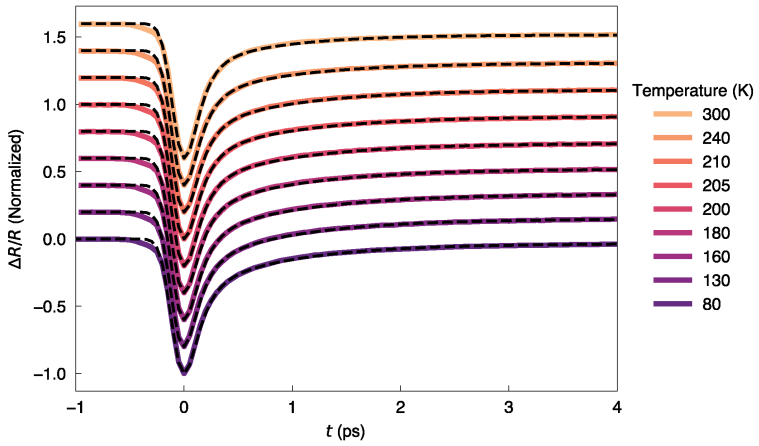

Figure 3.12: $\Delta R/R$ traces taken on Sr_2IrO_4 as a function of temperature. The probe energy was fixed at 1.55 eV. The pump energy was fixed at 0.6 eV, resonant with α, and a fluence near 2 mJ/cm^2 was used. The black dashed lines are fits to a double exponential function (Equation 2.30).

3.5 Microscopic modeling of the excitonic states

To identify the specific intra-excitonic transition responsible for the 1.5 THz peak, we compare our data with many-body model calculations. Sr_2IrO_4 is well-described theoretically by the single-band Hubbard model [115, 231] in the presence of the

nearest-neighbor (NN) Coulomb interaction:

$$H = -t_{NN} \sum_{\langle ij \rangle s} (c^{\dagger}_{js} c_{is} + h.c.) + U \sum_{i} n_{i\uparrow} n_{i\downarrow}, + V \sum_{\langle ij \rangle} n_i n_j. \tag{3.2}$$

The sum runs over NN pairs of sites $\langle ij \rangle$ on the 2D square lattice and c_{js} are the fermionic annihilation operators for the electron with spin $s = \pm\frac{1}{2}$ on site j. Before the arrival of the pump pulse, the half-filled system is in its ground state. The pump pulse excites an electron across the Mott gap, creating a holon in the LHB and a doublon in the UHB. It is known that through intraband cooling, the photo-excited holons and doublons quickly ($\sim$ 60 fs) relax to the band minimum [55, 92, 180, 186]. However, further relaxation via recombination across the Mott gap is bottlenecked by the large amount of energy ($\sim$ 0.5 eV) that needs to be transferred to other bosonic degrees of freedom (spins, phonons) with much smaller energy scales ($\sim$ 1-100 meV), leading to typical timescales exceeding 1 ps [92, 180]. Because intraband relaxation and recombination occur on drastically different timescales, we canonically transform the Hubbard model so as to separate them evidently in different orders of the small $1/U$ parameter [129, 130]. While the exact canonical transformation preserves the model, we drop the terms that appear with parametrically small prefactors ($1/U^n, n > 2$) or are subleading compared to terms already included in lower orders of the $1/U$ expansion. We end up with an effective model $\tilde{H} = H_{tJV} + H_{rc}$, where H_{tJV} captures holon and doublon hopping, on-site and NN Coulomb interaction, and the interaction-mediated spin exchange, while H_{rc} captures the recombination processes that can be treated as a perturbation:

$$\tilde{H} = H_{tJV} + H_{rc} \tag{3.3}$$

$$\begin{aligned} H_{tJV} = t_{\mathrm{NN}} \sum_{\langle ij \rangle, s} (h^{\dagger}_{is} h_{js} - d^{\dagger}_{is} d_{js} + h.c.) + U \sum_{i} n_{di} \\ - V \sum_{\langle ij \rangle} (n_{di} n_{hj} + n_{hi} n_{dj}) + J \sum_{\langle ij \rangle} \left(\mathbf{S}_i \cdot \mathbf{S}_j - \frac{1}{4} \delta_{1, n_i n_j} \right) \end{aligned} \tag{3.4}$$

$$H_{rc} = t_{rc} \sum_{(ijk), ss'} \left(h_{ks} d_{js'} \vec{\sigma}_{s\bar{s}'} \cdot \mathbf{S}_i + h.c. \right), \quad t_{rc} = \frac{2t^2}{U} = \frac{J}{2}. \tag{3.5}$$

We have introduced holon and doublon creation operators, $h^{\dagger}_{is} = c_{is}(1 - n_{i\bar{s}})$, $\quad d^{\dagger}_{is} =$

$c^{\dagger}_{i\bar{s}} n_{is}$, and corresponding density operators $n_{hi} = (1/2)\sum_s h^{\dagger}_{is} h_{is}$, $n_{di} = (1/2)\sum_s d^{\dagger}_{is} d_{is}$. Here $\bar{s} = -s$ is the opposite spin of s and $\vec{\sigma} = \{\sigma^x, \sigma^y, \sigma^z\}$ is a vector of Pauli matrices so that in the above notation $\sigma^a_{s,s'}$ corresponds to the $(\frac{3}{2} - s, \frac{3}{2} - s')$ component of the σ^a matrix. The sum over (ijk) runs over i, j, k, where $j \neq k$ are the NN sites to site i. The values of the nearest-neighbor hopping $t_{\mathrm{NN}} = 0.26$ eV, nearest-neighbor inter-site Coulomb energy $V = 0.39$ eV and exchange $J = 4t^2_{\mathrm{NN}}/U = 0.06$ eV were chosen consistently with reported values for Sr_2IrO_4 [117, 231, 236], with U being the on-site Coulomb energy.

Motivated by the fluence independent tr-TDTS response (Figure 3.11), indicating the irrelevance of exciton-exciton interactions, we assume low densities of photo-excited HD pairs. Having already separated sectors with different number of HD pairs on the level of the Hamiltonian—H_{tJV} conserves the number of HD pairs while H_{rc} perturbatively changes it—we can extract the metastable states at the bottom of the UHB using the Lanczos algorithm for exact diagonalization of H_{tJV} within the sector with one HD pair, while neglecting H_{rc}. These states are ostensibly the terminal point of the intraband relaxation process and, as we will point out with several indicators, correspond to excitonic states of bound HD pairs that lead to the formation of the transient insulating phase. The Lanzcos approach is ideal for this problem because it is suited for the calculation of the lowest eigenstates within the sector with one HD pair. Moreover, the Lanczos approach allows us to treat the system using periodic boundary conditions on $N = 26$ sites, which is larger than what would be possible if we had considered the full exact diagonalization of the Hubbard model directly. We use $N_{Lan} = 160,180$ Lanczos basis vectors for which the lowest eigenstates are well converged.

Eigenstates within the subspace of a single HD pair are calculated via exact diagonalization of H_{tJV} on a 26-site square cluster using the Lanczos algorithm [129, 130]. As shown in Figure 3.13a, the eigenvalue spectrum at zero center-of-mass momentum features four discrete bound HE levels spaced by several THz, separated from a higher energy HD continuum. In order to determine the symmetry of these excitonic states, we calculate the matrix elements $|\langle \psi^{hd}_{\vec{k},m} | O_{sym} | \psi^{hd}_{\vec{k},1} \rangle|^2$ at a fixed center-of-mass momentum $\vec{k}$ from the lowest eigenstate $\psi^{hd}_{\vec{k},1}$ to the excited states $\psi^{hd}_{\vec{k},m}$ with respect

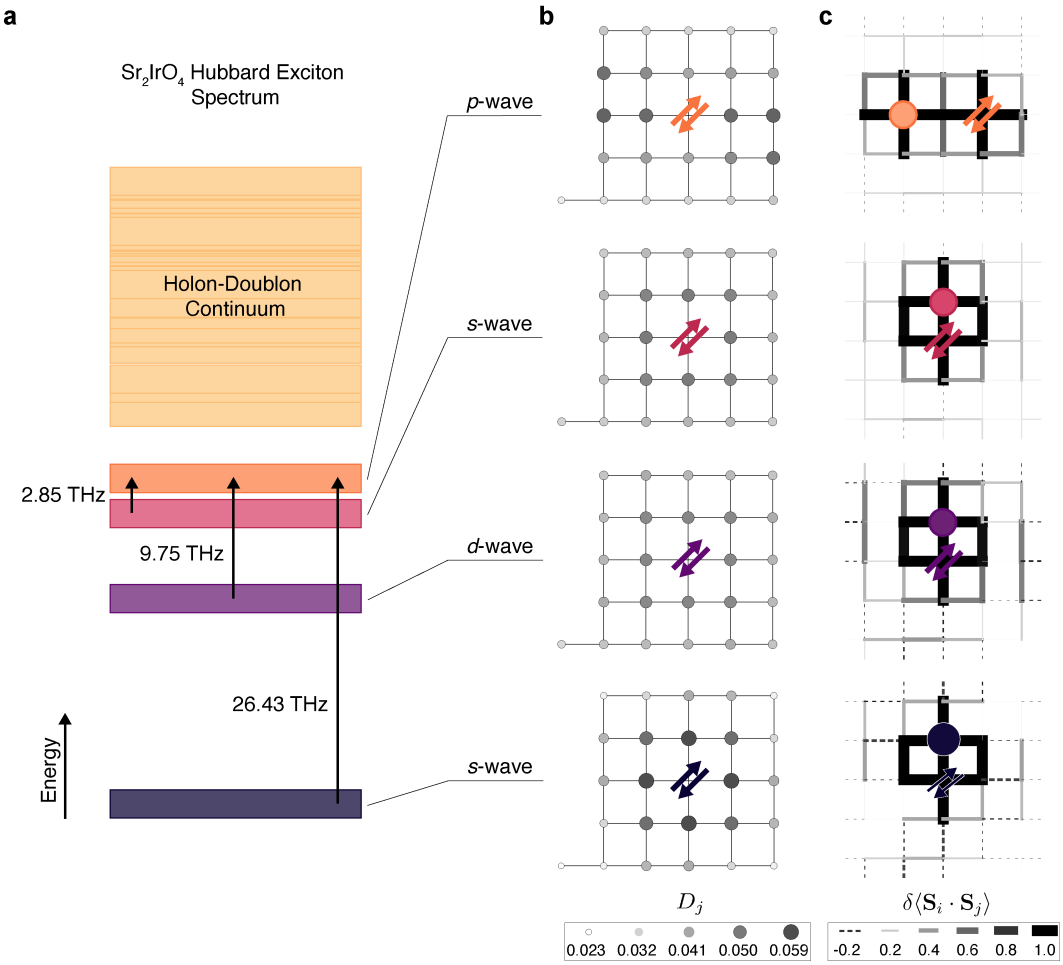

Figure 3.13: HE spectrum and characteristics obtained from effective model numerics. **a** Eigenstates of H_{tJV} in the sector of a single HD pair at zero center-of-mass momentum calculated via exact diagonalization (see main text). Vertical arrows mark the optically-allowed internal HE transitions. **b** The real space HD distribution on a square lattice represented through the density correlator $D_j = \langle \psi_m^{hd} | n_{hj} n_{d0} | \psi_m^{hd} \rangle$ for each of the four excitonic states labeled by m. The doublon is fixed at the center. The size and shade of each point indicate the strength of D_j, and therefore the probability of finding the holon at site j. **c** Relative deviation of the spin correlator from the Heisenberg ground-state with the holon and doublon fixed at their most probable locations. The size and shade of each bond indicate the deviation normalized by the AFM ground state value, with dashed lines representing negative changes.

to operators with a different (sym=$\{s, p, d\}$) symmetry, for example,

$$O_s = \sum_i d^\dagger_{i\rightarrow} d_i + d^\dagger_{i\leftarrow} d_i + d^\dagger_{i\uparrow} d_i + d^\dagger_{i\downarrow} d_i, \tag{3.6}$$

$$O_d = \sum_i d^\dagger_{i\rightarrow} d_i + d^\dagger_{i\leftarrow} d_i - d^\dagger_{i\uparrow} d_i - d^\dagger_{i\downarrow} d_i, \tag{3.7}$$

$$O_p = \sum_i d^\dagger_{i\rightarrow} d_i - d^\dagger_{i\leftarrow} d_i \tag{3.8}$$

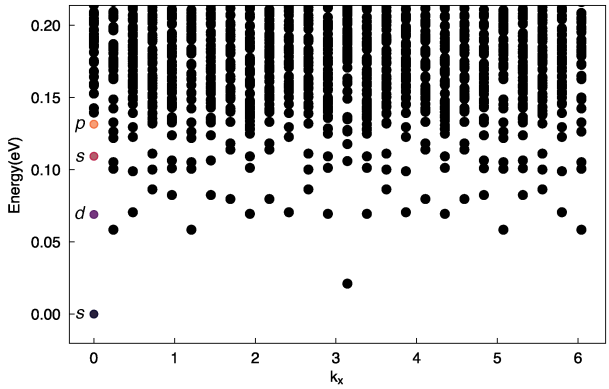

Figure 3.14: Eigenenergies of H_{tJV} in the sector of a single HD pair projected onto the k_x axis throughout the entire reciprocal space of the 26 site lattice. At zero center-of-mass momentum, $\vec{k} = [0, 0]$, the four lowest states are colored to indicate which excitonic states are depicted in Figure 3.13.

where $d_i = \sum_s d_{is}$ and $i \rightarrow /i \leftarrow /i \uparrow /i \downarrow$ are right/left/top/bottom neighboring sites of site i. Depending on the symmetry of both states, the matrix element will be zero or finite. The lowest excitonic state at $\vec{k} = [0, 0]$ has s-wave symmetry [129, 221, 223]. From the above procedure, we can determine that the other excitonic states at $\vec{k} = [0, 0]$ also have a definite symmetry: d-, s-, and p-wave, listed from lowest to highest energy, respectively (Figure 3.13a, Figure 3.14). This excitation spectrum clearly departing from the hydrogenic series as previously predicted [94, 130, 223, 242].

These symmetries can be directly visualized in real space through the density correlator $D_j = \langle \psi_m^{hd} | n_{hj} n_{d0} | \psi_m^{hd} \rangle$, where $|\psi_m^{hd}\rangle$ is the HD pair wave function, which describes the probability of measuring a holon at site j given a doublon at the origin for the four different excitonic states $m = 1 \rightarrow 4$ (Figure 3.13b). Whereas D_j for the s- and d-states is 4-fold rotational symmetric, that for the p-state is only 2-fold symmetric.

Our numerical simulations confirm that the observed 1.5 THz peak lies within the predicted frequency scale of low-lying intra-excitonic excitations in Sr_2IrO_4, which is an order of magnitude smaller than J. A leading candidate is the dipole-allowed s- to p-state transition appearing at 2.85 THz in our calculations (Figure 3.13a). Since HEs are generated by excitation across the Mott gap in our experiments, a finite initial population of excited HE states is expected. Moreover, the proximity of the p-state to the HD continuum (Figure 3.13a, Figure 3.14) implies a shortened

p-state lifetime, which may explain the broad linewidth of the observed 1.5 THz mode. Magnon emission could also contribute to the broadness of the peak. For any momentum, there are a few excitonic states, with energies that depend on the momentum (Figure 3.14). While the symmetry of excitonic states is definite for $\vec{k} = [0, 0]$ and $\vec{k} = [\pi, \pi]$, this is not the case for other $\vec{k}$. An intra-excitonic transition accompanied by a magnon emission is allowed by symmetry and would imply that the final exciton would be at a different momentum, which spreads the possible energy range for the final state and makes the peak broader. We note that while the experimental detection of a single mode is not sufficient to pin down the excitonic spectrum, our theoretical results show that its energy scale is consistent with an intra-HE transition.

To verify that J, in addition to V, contributes to binding the HEs identified in our simulations, we evaluated the relative deviation of the spin correlator relative to the AFM ground state for each HE state, defined as $\delta\langle \mathbf{S}_i \cdot \mathbf{S}_j \rangle = \frac{\langle \mathbf{S}_i \cdot \mathbf{S}_j \rangle_{\mathrm{HD}} - \langle \mathbf{S}_i \cdot \mathbf{S}_j \rangle_{\mathrm{AFM}}}{\langle \mathbf{S}_i \cdot \mathbf{S}_{i+1} \rangle_{\mathrm{AFM}}}$. For this calculation, we fix the holon and doublon to their most probable locations as determined by the value of D_j. As seen in Figure 3.13c, it is clear that the presence of the HD pair disrupts the AFM motif, and that the extent of this disruption becomes larger for the higher-energy excitonic states. This behavior supports the notion of a spin binding mechanism.

3.5.1 System size dependence

We now consider the effect of the system size N on the results of the simulation. In Figure 3.15, the results for $N = 20$ and $N = 26$ are shown. We find the existence of several excitonic states below a densely spaced continuum for both system sizes. These excitons have definite symmetries at high symmetry points $\vec{k} = [0, 0]$, $\vec{k} = [0, \pi]$, $\vec{k} = [\pi, 0]$, and $\vec{k} = [\pi, \pi]$ and mixed symmetries at other $\vec{k}$. However, a few details change depending on the values of N. Most importantly, the binding energies of the excitons, the number of excitonic states, and the order in which different symmetries of excitons appear at the high symmetry points of the spectrum can change. The latter two can be particularly sensitive to N, since the shapes of the lattices, which feature periodic boundary conditions, can favor different symmetries. We believe that this is a clear finite size effect that would eventually diminish with larger system sizes.

We believe that our conclusions remain qualitatively robust despite these finite size effects, since there are always optically-allowed intra-excitonic transitions that

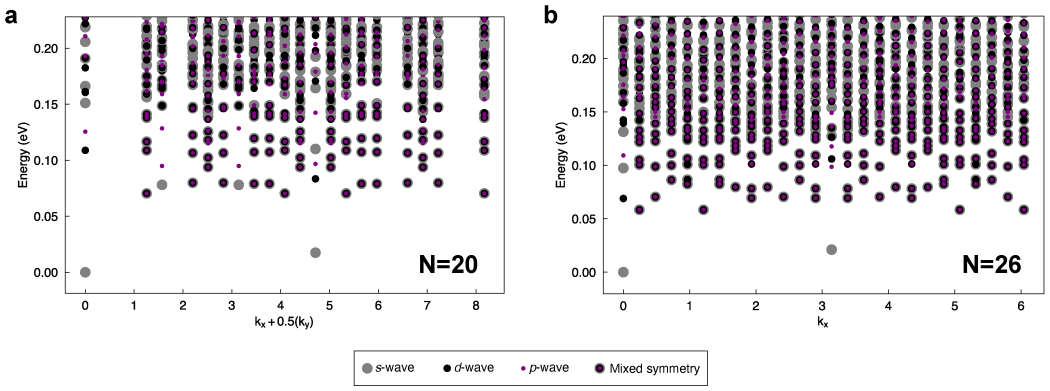

Figure 3.15: System size dependence of the spectra calculated with H_{tJV}. **a,b** Spectra obtained from the exact diagonalization procedure performed for two system sizes, $N = 20$ (a) and $N = 26$ (b). The latter is projected onto the k_x axis. Due to the symmetry of the $N = 20$ lattice, the spectrum is projected onto the $k_x + 0.5(k_y)$ axis to prevent the overlap of different states from different momenta. Large gray markers are states with s-wave symmetry, medium black markers are states with d-wave symmetry, and small violet markers are states with p-wave symmetry. Mixed symmetry states have multiple markers overlapped with one another. We define 0 eV to be the energy of the lowest-energy state.

appear at a fraction of J, in agreement with the peak observed in experiment, regardless of these choices. Also, we find that the excitons appear to be more stable (more clearly below the continuum) as the system size is increased.

3.6 Ruling out alternative explanations

While the data strongly points towards the presence of a Hubbard excitonic fluid in photo-doped Sr_2IrO_4, it is important to rule out alternative explanations for our transient spectra and dynamics. In this section, we list several mechanisms that can be ruled out using our experimental observations and the reported literature.

3.6.1 Transient phase separation

In this section, we show that our photo-induced optical spectra cannot be explained by the formation of a phase-separated state following the photo-doping process. To do this, we rely on the effective medium approximation to simulate the response of a heterogeneous photo-excited medium. We start by solving the Bruggeman formula to determine a model for the effective dielectric response of the phase-separated material. Since we are considering a mixture of metallic and insulating phases, we included two terms giving [212]:

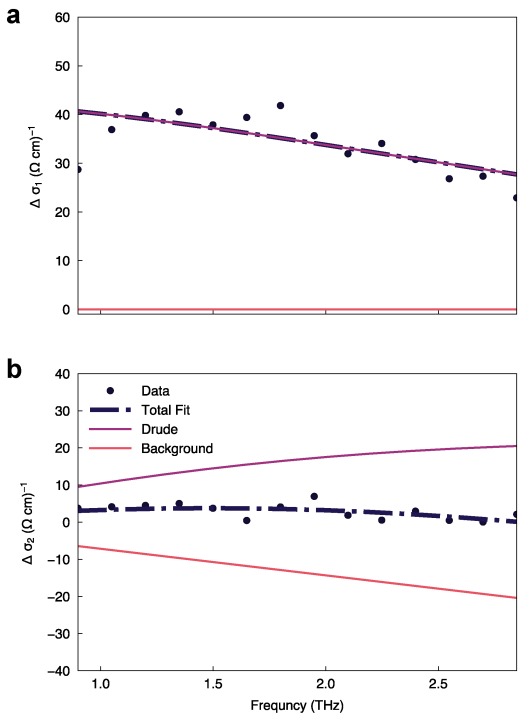

Figure 3.16: Drude-Lorentz Fitting of the transient changes to the optical conductivity at t = 0.3 ps. **a**,**b** Photo-induced changes to the real (a) and imaginary (b) parts of the optical conductivity. The solid lines represent various parts of the Drude-Lorentz fit (Section 3.2), while the dot-dashed line indicates the total fit.

$$p_1 \frac{\varepsilon_1 - \varepsilon_{eff}}{\varepsilon_1 + (d-1)\varepsilon_{eff}} + p_2 \frac{\varepsilon_2 - \varepsilon_{eff}}{\varepsilon_2 + (d-1)\varepsilon_{eff}} = 0 \tag{3.9}$$

where p_1 is the metallic area fraction, p_2 is the insulating area fraction, d is the dimension, ε_1 is the dielectric function of the metallic areas, ε_2 is the dielectric function of the insulating areas, and ε_{eff} is the effective response of the total area. Solving for ε_{eff} gives:

$$\varepsilon_{eff} = \frac{1}{2(d-1)} \left[d\varepsilon_{avg} - \varepsilon_1 - \varepsilon_2 \pm \sqrt{(d\varepsilon_{avg} - \varepsilon_1 - \varepsilon_2)^2 + 4(d-1)\varepsilon_1\varepsilon_2} \right] \tag{3.10}$$

where $\varepsilon_{avg} = p_1\varepsilon_1 + p_2\varepsilon_2$ and p_i sum to unity. From this expression, we can retrieve the effective light-induced changes to the conductivity of the heterogeneous film:

$$\Delta\sigma_{eff} = -i(\varepsilon_{eff} - \varepsilon_2)\omega\varepsilon_0 \tag{3.11}$$

where ω is frequency.

To define ε_1, we note that the system only contains metallic puddles after it is photo-excited. Indeed, the dataset at the early time delay of $t = 0.3$ ps can only be fit using a Drude term and a broad background term that primarily affects the imaginary part of the optical conductivity and is likely caused by higher energy changes to the conductivity (Figure 3.16). This result implies that the photo-induced layer is completely metallic at this time delay, suggesting that $p_1 = 1$ and $p_2 = 0$. Accordingly, we can define the response of the metallic portions using this fitted Drude response at this early time delay (see Chapter 3.2):

$$\Delta\sigma_{Drude} = \frac{D}{2}\left[\frac{1}{\gamma - i\omega}\right] \tag{3.12}$$

where the fitting constants D and γ and are the Drude strength and width, respectively. At $t = 0.3$ ps, these values are $330 \pm 7\ \Omega^{-1}\text{cm}^{-1}\text{ps}^{-1}$ and 3.9 ± 0.1 THz, respectively. Thus, we get the following result for ε_1:

$$\varepsilon_1 = \varepsilon_2 + \frac{i\Delta\sigma_{Drude}}{\omega\varepsilon_0} \tag{3.13}$$

ε_2 can be defined using the measured equilibrium response of the material:

$$\varepsilon_2 = (n + ik)^2 \tag{3.14}$$

where n and k are the real and imaginary parts of the index of refraction, respectively (Figure 3.4). However, our results do not change significantly with or without this condition.

With these considerations in mind, we can obtain a series of curves showing the expected response for the phase-separated material with different volume fractions of metallic and insulating puddles (Figure 3.17). Here, we enforce charge conservation by keeping $\Delta\sigma_{Drude}(\omega = 0) \cdot p_1$ to be constant. There are several important features that contrast starkly with our measured data on both a qualitative and quantitative level, ultimately ruling out phase-separation and heterogeneity as a possible explanation of our results:

- **Spectral discrepancies:** While a finite energy peak does emerge (Figure 3.17) as the volume fraction of the insulating phase grows, its characteristics

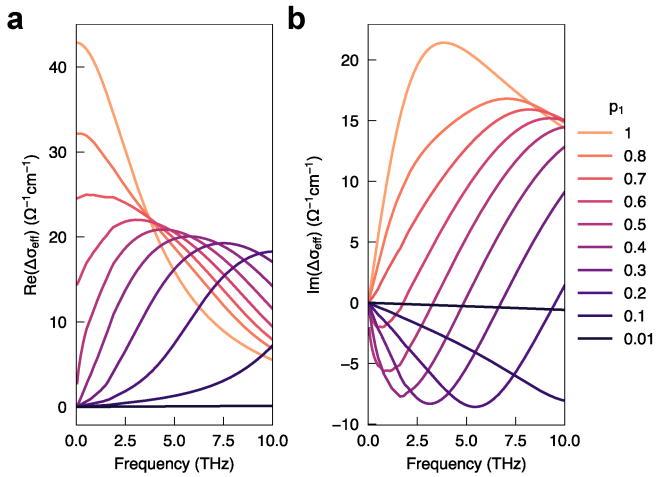

Figure 3.17: Results of the Bruggeman effective medium approximation analysis. **a**,**b** Simulated effective light-induced changes to the real (a) and imaginary (b) parts of the optical conductivity of the heterogeneous film. These curves were generated by using experimental inputs into the Bruggeman formula and varying the volume fraction of the metallic and insulating portions of the sample.

are qualitatively and quantitatively different from the experimentally observed finite energy peak. First, the peak that emerges from the effective medium analysis is significantly broader, spanning a frequency window of larger than 10 THz . On the other hand, the width of our observed resonance is always less than 2 THz (Figure 3.5). Moreover, the central frequencies of the finite energy peak that emerge from the Bruggeman analysis range from right above 0 THz to beyond 10 THz, as it is extremely sensitive to the volume fraction. In contrast, the central frequency of the measured mode is always between 1.5 and 2 THz.

- **Temporal dependence:** In our experimental data, we observe that the Drude spectral weight at early time delays evolves into a finite energy peak. For this to be explained by the heterogeneity hypothesis, the area fraction of the metallic regions p_1 would have to decrease as time evolves. However, as shown in Figure 3.17, as p_1 is decreased the finite energy peak will strongly blue-shift. It is clear from Figure 3.5 that our experimentally measured finite energy peak does not blue-shift, thereby ruling out this scenario.

- **Fluence dependence:** As mentioned above, the central frequency of the finite energy peak in the Bruggeman analysis is highly dependent on the ratio of metallic and insulating areas. We also found that it is highly sensitive

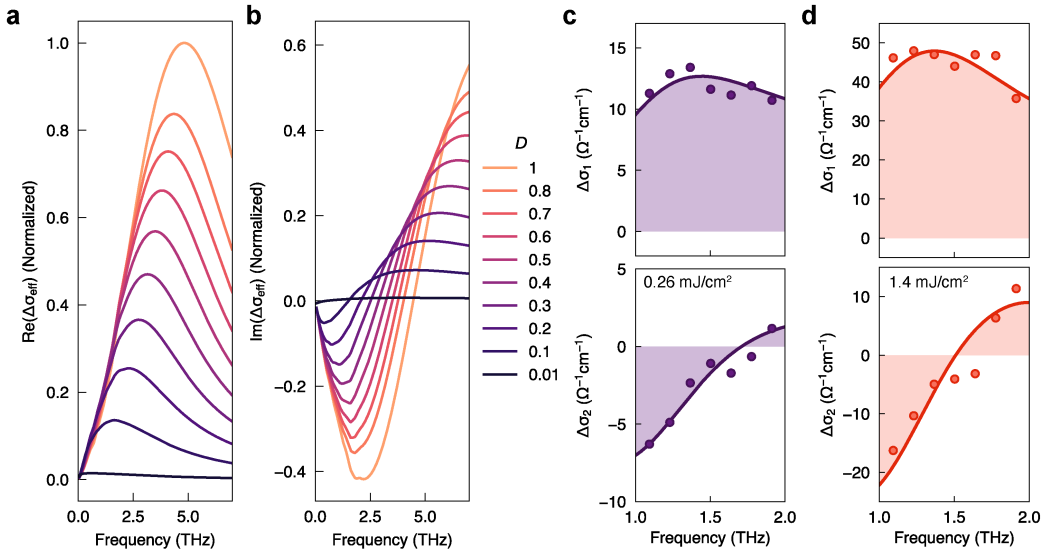

Figure 3.18: Dependence of the experimental and simulated finite energy peaks on photo-carrier density. **a**,**b** Simulated effective light-induced changes to the real (a) and imaginary (b) parts of the optical conductivity of the heterogeneous film extracted from the Bruggeman formalism. These curves were generated by using experimental inputs into the Bruggeman formula and varying the value of the Drude strength (D, see Equation 3.1). The values shown in the legend are normalized to the maximum D used, and the curves in the plots are normalized to the $D = 1$ curve. The value of p_1 was fixed to a representative value of 0.2. **c**,**d** Real (top) and imaginary (bottom) parts of the experimental optical conductivity obtained with pump fluences of 0.26 mJ/cm^2 (c) and 1.4 mJ/cm^2 (d). This data was taken at t = 2.55 ps and at 80 K.

to the Drude spectral weight within the metallic regions as well (Figures 3.18a,b). This behavior possibly stems from the fact that this feature has been attributed to the formation of a plasmon [212, 248], and is accordingly highly sensitive to the carrier density. Experimentally, we can control the carrier density by varying the pumping fluence. Thus, if the phase separation hypothesis were to correctly explain our observations, the central frequency of our observed resonance should vary drastically with the fluence of the driving pulse, strongly blue-shifting as the fluence is increased. To test this hypothesis, we performed spectrally-resolved experiments as a function of pump fluence. As seen in Figures 3.18c,d, we do not observe such behavior. Instead, we observe that the central frequency of the measured peak remains largely unchanged as the fluence is changed by more than 5 times, in contrast to the result predicted by the Bruggeman analysis. This result again rules out

the inhomogeneity hypothesis.

For these reasons, we believe that our data cannot be explained by the heterogeneity hypothesis and that the Drude-Lorentz model used in our manuscript is the most accurate representation of our data. Moreover, these results are consistent with our expectations based on physical reasoning. The metallic patches in chemically doped Sr_2IrO_4 samples nucleate from the sites of the chemical dopants [177], which tend to not be distributed evenly across the sample. The insulating patches appear in regions that are away from any chemical dopants. This sort of phase separation should not appear in our experiment, which is photo-doped as opposed to chemically doped. Unlike chemical dopants, we expect that photo-dopants will initially be distributed evenly across the sample because the pump beam is homogeneous, creating a uniform response. This assumption is supported by the fact that the system is well-described by the Drude model at early time delays.

3.6.2 Defect capture and charge trapping

In the following, we provide arguments and data to rule out defect capture as a possible explanation of our observed dynamical and spectral responses.

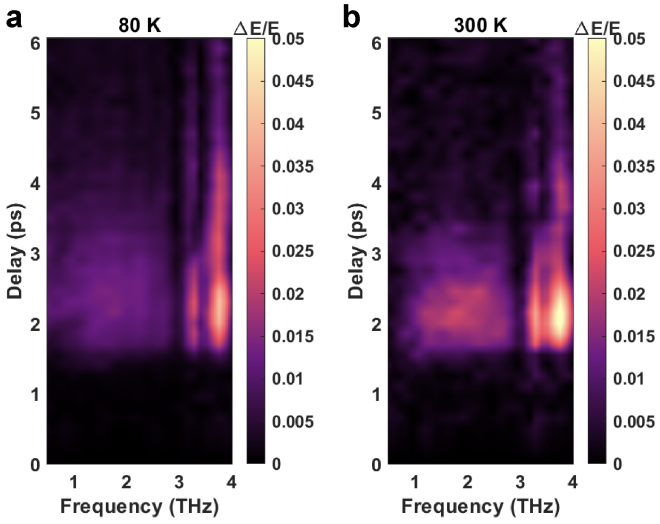

Figure 3.19: Temperature dependence of the tr-TDTS spectrum of Sr_2IrO_4. **a**,**b** tr-TDTS spectra obtained at temperatures of 80 K (a) and 300 K (b). Data were taken with a pump fluence of 2 mJ/cm^2.

Dynamics

Our picosecond-scale recombination dynamics cannot be mediated by defect capture. In this scenario, self-trapped excitons, either of intrinsic (through polaron formation) or extrinsic (through trapping by defects) origin, should show different intra-excitonic transition energies compared to free excitons due to the local trapping potential. Assuming that such behavior is at play, there are two options: (1) excitons are trapped within our accessible time and energy windows but the frequency shift is small; or (2) the peak frequency of trapped excitons is so different that it lies outside of our bandwidth.

To rule out case (1), we first note that because the trapped excitons would have a different intra-excitonic transition energy than the free excitons, we should observe two distinct Lorentzian peaks within our bandwidth. However, as can be seen in Figure 3.6, our data is well-fit by a single finite energy Lorentzian. We can further rule out scenario (1) by considering the fact that free excitons and trapped excitons typically have very different recombination times (usually much slower in the case of trapped excitons [137]). If there were contributions from both free and trapped excitons within our bandwidth, our decay dynamics would show at least two exponential components. In contrast, our decay dynamics remain well described by a single exponential throughout our temperature, energy, and fluence range (Figure 3.7, Figure 3.10, Figure 3.11). Thus, by considering both the spectral characteristics of our data as well as the temporal dynamics, we believe that we can safely rule out scenario (1).

For case (2), the spectral weight decay observed within our bandwidth would correspond to a spectral weight transfer to a separate peak corresponding to trapped excitons that lies outside our bandwidth. The percentage of excitons that is transferred into the trapped state should decrease upon heating because thermal energy in general works against exciton trapping. Moreover, the excitons should stay free for longer times for the same reason, extending the lifetime of our observed peak. However, this contradicts our observation that the decay becomes faster at higher temperatures (Figure 3.10b), and that the strength of the excitonic peak does not decrease at higher temperatures (Figure 3.19). Both of these experimental observations contradict the expected behavior for the trapping hypothesis, thereby ruling out scenario (2).

Spectral Response

Charge trapping is not a possible explanation for the existence of the 1.5 THz peak in the photo-induced change to the optical conductivity. If our data were to be explained by charge trapping into an impurity level, it would have to be extremely shallow, as we observe the peak frequency to be around 1.5 THz. This frequency corresponds to a temperature of 72 K. As such, we would expect that these impurity states should thermally dissociate in our experimental temperature range of 80 K to 300 K. However, we observe that the exciton remains stable across this entire temperature range, ruling out this scenario (Figure 3.19).

3.6.3 Strong bosonic coupling

For the following reasons, the 1.5 THz peak observed in our transient optical conductivity spectra cannot be attributed to a sideband arising from strong coupling to bosonic modes. First, the peak should be separated from the Drude peak by around the bosonic mode energy [18]. However, as seen in Figure 1c, there are no optically active bosonic modes in our measured energy region. Although sideband formation does not necessarily require the boson to be optically active, we note that previous inelastic x-ray scattering experiments [51, 197] on Sr_2IrO_4 measured no optical phonon modes at all (optically active or inactive) in the energy range of interest over the full Brillouin zone. While there are acoustic modes spanning the energy range of 0 to 5 meV [51, 197], their density of states is vanishingly small [51, 181]. Moreover, the formation of a sideband arises from the coupling of electrons to a bosonic mode with well-defined energy, often modeled as a dispersionless Einstein phonon mode exhibiting a large phonon density of states at one particular energy. In contrast, a highly dispersive acoustic phonon (or magnon) mode has a featureless density of states, which is incompatible with our observation of a Lorentzian peak with well-defined energy in the optical conductivity spectrum.

Second, the dynamics of the sideband should be similar to the dynamics of the main Drude peak (with a possible time delay in formation) as the spectral weight of the sideband is being redistributed from the Drude spectral weight [18]. It is clear from Figure 3.7 that the Drude and Lorentzian components of our data show completely different dynamics. Crucially, at later time delays ($t > 1$ ps), the Drude spectral weight is vanishing while the Lorentzian spectral weight is still near its peak (Figure 3.7). Moreover, between 0.5 and 1 ps, the two show opposite trends, with the Drude spectral weight decreasing and the Lorentzian spectral weight increasing.

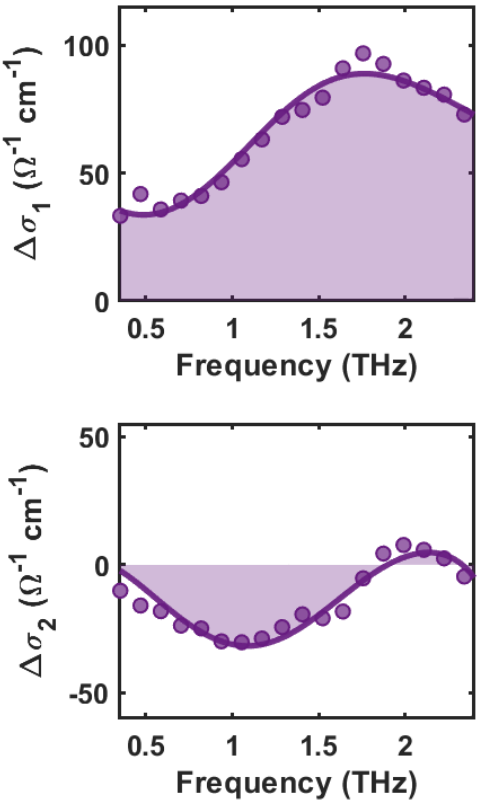

Figure 3.20: Real (top panel) and imaginary (bottom panel) parts of the pump-induced change of optical conductivity extracted from differential THz spectra measured using a ZnTe-based spectrometer. The pump was tuned to 0.6 eV (resonant with the α transition) and a fluence of 2.0 mJ/cm^2. The data was taken at 80 K. Fits to the Drude-Lorentz model (Equation 3.1) are displayed as solid lines.

We believe that these dynamics rule out the possibility of electron-boson coupling as an explanation of the observed 1.5 THz mode.

Third, if the observed Lorentzian peak were a sideband of a Drude peak, this would imply a Drude peak width below our lowest measured frequency of 0.35 THz (Figure 3.20). However, chemically-doped samples show a Drude peak that is much broader than 0.35 THz [244], and our THz data at short time delays show that photo-doped samples exhibit a Drude peak that is much broader than 0.35 THz (See Figure 3.5 and Figure 3.16). The temporal evolution of our THz data also shows that the Drude peak does not suddenly sharpen to below 0.35 THz after the onset of the Lorentzian component. We are not aware of any physical mechanism that would cause such a drastic change of the photo-induced Drude response. Such a scenario would be

rather exotic, as Drude peaks sharper than 0.35 THz (1.45 meV) are usually only resolved in the rare cases of heavy fermion systems [194] and nearly-perfect or highly-mobile conductors [8]. Neither of these scenarios apply to Sr_2IrO_4.

Finally, electron-boson coupling should generate a unique spectral response that can be detected through an extended Drude model analysis of the optical conductivity data. The effective mass $m^*(\omega)$ should be enhanced below the bosonic mode frequency, while the scattering rate $1/\tau(\omega)$ should begin to increase above the bosonic mode frequency. These quantities can be experimentally extracted using the following relations [8]:

$$\begin{aligned} m^*(\omega) &\propto -\frac{1}{\omega}\mathrm{Im}\left[\frac{1}{\tilde{\sigma}(\omega)}\right] \\ \frac{1}{\tau(\omega)} &\propto \mathrm{Re}\left[\frac{1}{\tilde{\sigma}(\omega)}\right] \end{aligned}. \tag{3.15}$$

We calculated the frequency dependent effective mass and scattering rate using Equation 3.15 for a characteristic dataset showing the Lorentzian peak. The results are shown in Figure 3.21. Within our resolution $1/\tau(\omega)$ is not enhanced above some characteristic energy and remains rather constant. More importantly, m^* is mostly below 0, indicating a breakdown of the model. These results further rule out the electron-boson coupling scenario.

3.6.4 Pseudogap formation

In chemically doped Sr_2IrO_4 samples, the characteristics of the pseudogap are highly dependent on both the number of charge carriers that are doped into the system as well as the temperature of the sample [52, 118, 119]. Thus, to determine whether a photo-induced pseudogap might explain our data, we can compare the temperature and pump fluence dependence of our photo-induced spectra with the spectra of chemically doped Sr_2IrO_4.

We find that both the temperature and fluence dependencies are not consistent with the expected behavior of the pseudogap. At a fixed temperature below the onset of the pseudogap, previous works found that the energy scale of the pseudogap can vary drastically with the doping level, reaching up to 80 meV [118]. On the other hand, as shown in Figure 3.18c and Figure 3.18d, the energy scale of our observed finite energy peak does not change as the fluence—and thus the photo-dopant density—is varied.

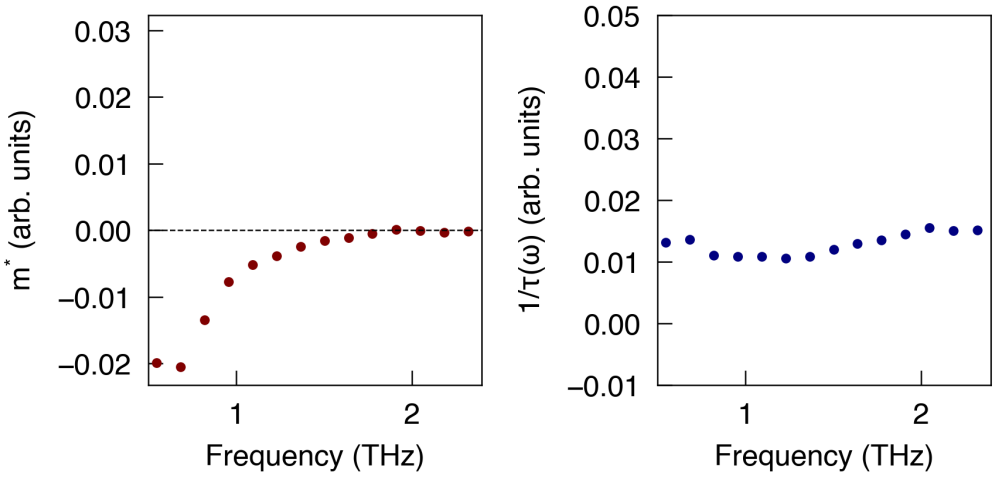

Figure 3.21: Results of the extended Drude model analysis. $m^*(\omega)$ (left) and $1/\tau(\omega)$ (right) calculated using Equation S7. This data was collected with an α-resonant pump at a fluence of 2.0 mJ/cm^2 and t = 1.2 ps. The temperature was 80 K.

Similarly, the pseudogap energy scale is highly dependent on the temperature of the sample, forming below a critical temperature around 110 K for a reported electron concentration of ~3 % [118] and enhancing as the temperature is reduced [118, 119]. On the other hand, in our case we observe that the energy scale of the finite energy peak remains unchanged as the temperature is varied (Figure 3.19). This observation is at odds with the physics of pseudogap formation.

Moreover, we find that the spectral characteristics of our finite energy peak are not compatible with pseudogap physics. First, the energy scale of our feature is roughly 6 meV, which is much smaller than the value of the pseudogap observed by photoemission spectroscopy (50-80 meV are typical maximum values over the reported doping and temperature ranges). Second, as shown in Figure 3.6, our finite energy peak is perfectly consistent with the Lorentzian lineshape, indicating that it originates from a dipole-active optical transition as opposed to a pseudogap feature. This can be confirmed by comparing against the optical response in the pseudogap phase, for example in the cuprates [228] or in Sr_2IrO_4 [199, 244]. In both cases, the low-energy response in the pseudogap phase is marked by a finite but spectrally flat optical response.

Given these reasons, we believe that the simplest explanation for our transient optical conductivity spectra would be the formation of excitons, which is consistent not only with our spectral properties as a function of energy, temperature, and photo-dopant

density, but also is the more likely scenario given the simultaneous presence of both holes and electrons.

3.7 Conclusions and outlook

Our tr-TDTS and theoretical results together establish that HEs can exist as metastable neutral quasiparticle excitations in a 2D AFM Mott insulator. Moreover, they demonstrate a pathway to prepare a HE fluid through photo-excitation resonant with the Mott gap. The energetic and dynamical properties of the HEs can in principle be controlled *in situ* by tuning J using mechanical or optical perturbations [153], serving new technological applications while also further confirming their exchange-bound nature. More generally, these results suggest that 2D magnetic Mott insulators, which host myriad ordered and quantum disordered phases, are a promising platform for discovering novel excitonic states.

Chapter 4

EVIDENCE FOR SPIN-MEDIATED EXCITONIC BINDING

Chapter temporarily redacted

Chapter 5

DYNAMICS OF ANTIFERROMAGNETIC ORDER IN A PHOTO-DOPED MOTT INSULATOR

Chapter temporarily redacted

Chapter 6

BEYOND RESONANT EXCITATION: KELDYSH-SPACE TUNING IN A MOTT INSULATOR

Xinwei Li, Honglie Ning, Omar Mehio, Hengdi Zhao, Min-Cheol Lee, Kyung-wan Kim, Fumihiko Nakamura, Yoshiteru Maeno, Gang Cao, and David Hsieh. Keldysh Space Control of Charge Dynamics in a Strongly Driven Mott Insulator. *Physical Review Letters*, 128(18):187402, May 2022. doi: 10.1103/PhysRevLett.128.187402.
O.M. contributed to the experimental effort and analyzed the data.

In each of the preceding chapters, we described experiments designed to characterize the charge and magnetic properties of Mott insulators as they are photo-doped with charge carriers. As such, the focus of these results was on the dynamics that follow the arrival of the pump pulse. In this chapter, we shift gears to instead study the photo-doping mechanism itself. Unlike the resonant drives used previously, here we explore the effects of driving the material with photons at energies that lie inside the Mott gap. We will find that doing so not only enables momentum-space control over the resulting charge distribution, but creates opportunities to produce non-thermal phenomena that are inaccessible with a resonant drive.

6.1 Non-resonant driving protocols in a Mott insulator

The response of a Mott insulator to a strong electric field is a fundamental question in the study of non-equilibrium correlated many-body systems [9, 44, 58, 60, 63, 127–129, 134, 157, 176, 178, 198, 211, 230]. In the DC limit, a breakdown of the insulating state occurs when the field strength exceeds the threshold for producing pairs of doubly-occupied (doublon) and empty (holon) sites by quantum tunneling, in analogy to the Schwinger mechanism for electron-positron pair production out of the vacuum [196]. Recently, the application of strong low frequency AC electric fields has emerged as a potential pathway to induce insulator-to-metal transitions [73, 149, 167, 245], realize efficient high-harmonic generation [100, 203], and coherently manipulate band structure and magnetic exchange interactions in Mott insulators [20, 45, 90, 153, 155, 235]. Therefore, there is growing interest to understand doublon-holon (HD) pair production and their non-thermal dynamics in the strong field AC regime.

Strong AC field induced HD pair production has been theoretically studied using Landau-Dykhne adiabatic perturbation theory [175] along with a suite of non-equilibrium numerical techniques [100, 167, 175, 203, 216, 219, 226]. Notably, HD pairs are primarily produced through two nonlinear mechanisms: multi-photon absorption and quantum tunneling [122, 175]. The two regimes are characterized by distinct electric field scaling laws and momentum space distributions of HD pairs. By tuning the Keldysh adiabaticity parameter $\gamma_K = \hbar\omega_{pump}/(eE_{pump}\xi)$ through unity, where ω_{pump} is the pump frequency, E_{pump} is the pump electric field, e is electron charge, and ξ is the HD correlation length, a cross-over from a multi-photon dominated ($\gamma_K > 1$) to a tunneling dominated ($\gamma_K < 1$) regime can in principle be induced. However, direct experimental tests are lacking owing to the challenging need to combine strong tunable low frequency pumping fields with sensitive ultrafast probes of non-equilibrium distribution functions.

We devise a protocol to study these predicted phenomena using ultrafast broad-band optical spectroscopy. As a testbed, we selected the multiband Mott insulator Ca_2RuO_4. Below a metal-to-insulator transition temperature T_{MIT} = 357 K, a Mott gap (Δ = 0.6 eV) opens within its 2/3-filled Ru 4d t_{2g} manifold [66, 79, 87, 104], with a concomitant distortion of the lattice [31]. Upon further cooling, the material undergoes an antiferromagnetic transition at T_N = 113 K into a Néel ordered state. It has recently been shown that for temperatures below T_{MIT}, re-entry into a metallic phase can be induced by a remarkably weak DC electric field of order 100 V/cm [171], making Ca_2RuO_4 a promising candidate for exhibiting efficient nonlinear pair production.

6.2 Demonstration of the Keldysh crossover in Ca_2RuO_4

To estimate the response of Ca_2RuO_4 to a low frequency AC electric field, we calculated the HD pair production rate (Γ) over the Keldysh parameter space using a Landau-Dykhne method developed by Oka [175]. Experimentally determined values of the Hubbard model parameters for Ca_2RuO_4 were used as inputs (Appendix A). As shown in Figure 6.1(a), Γ is a generally increasing function of E_{pump} and $\hbar\omega_{pump}$. For a fixed ω_{pump}, the predicted scaling of Γ with E_{pump} is clearly different on either side of the Keldysh cross-over line (γ_K = 1), evolving from power law behavior $\Gamma \propto (E_{pump})^a$ in the multi-photon regime to threshold behavior $\Gamma \propto \exp(-b/E_{pump})$ in the tunneling regime [Figure 6.1(b)].

At time delays where coherent nonlinear processes are absent, the transient pump-

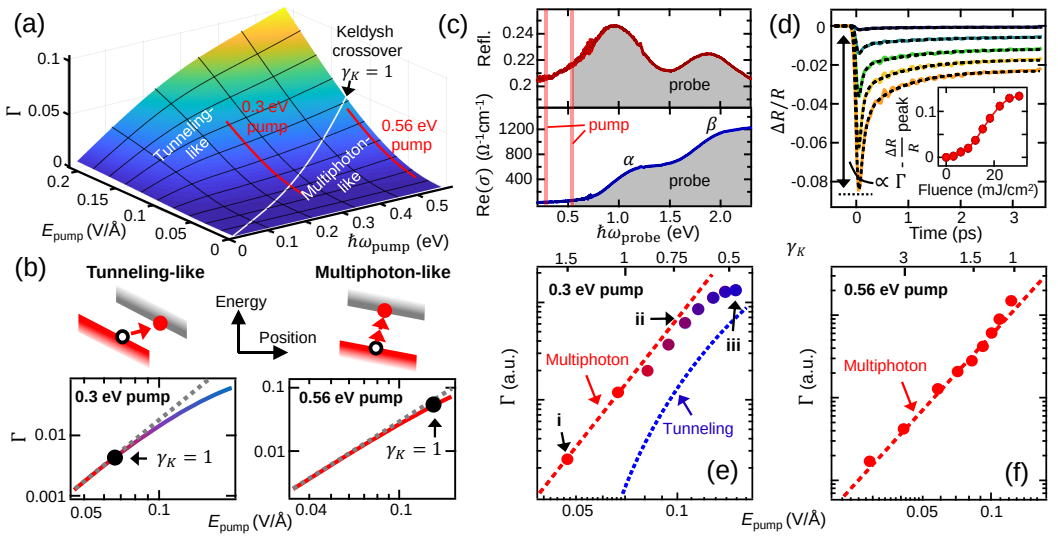

Figure 6.1: Resolving Keldysh tuning using pump-probe spectroscopy. (a) Γ calculated across Keldysh space using the Landau-Dykhne method. (b) Constant energy cuts along the red lines shown in (a) plotted on a logarithmic scale. Black dots mark the Keldysh cross-over. Gray dashed lines: scaling relation in the multi-photon regime. Schematics of the multi-photon and tunneling processes are shown above. (c) Equilibrium reflectivity (top) and conductivity (bottom) spectra of Ca_2RuO_4 at 20 K. The 0.3 eV and 0.56 eV pump energies are marked by vertical red lines. The probe energy range is shaded grey. (d) Select 0.3 eV pump 1.77 eV probe $\Delta R/R$ traces at fluences of 3, 9, 15, 22, and 30 mJ/cm^2 (top to bottom). Dashed lines are fits detailed in (Appendix A). Inset: Peak $\Delta R/R$ versus fluence showing nonlinearity. (e, f) Experimental cuts through the same regions of parameter space as in (b). Error bars are smaller than data markers. Scaling relations for multi-photon and tunneling behavior are overlaid as red and blue dashed lines, respectively.

induced change in reflectivity of a general gapped material is proportional to the density of photo-excited quasi-particles [42, 56, 72], which, upon dividing by a constant pump pulse duration (~100 fs), yields Γ. Differential reflectivity ($\Delta R/R$) transients from Ca_2RuO_4 single crystals were measured at T = 80 K using several different subgap pump photon energies ($\hbar\omega_{\text{pump}} < \Delta$) in the mid-infrared region, and across an extensive range of probe photon energies ($\hbar\omega_{\text{probe}}$) in the near-infrared region spanning both the α and β absorption peaks [Figure 6.1(c)]. These two band edge features can be assigned to optical transitions within the Ru t_{2g} manifold [50, 104]. Figure 6.1(d) shows reflectivity transients at various fluences measured using $\hbar\omega_{\text{pump}}$ = 0.3 eV and $\hbar\omega_{\text{probe}}$ = 1.77 eV. Upon pump excitation, we observe a rapid resolution-limited drop in $\Delta R/R$. With increasing fluence, the minimum value of $\Delta R/R$ becomes larger, indicating a higher value of Γ within the pump pulse

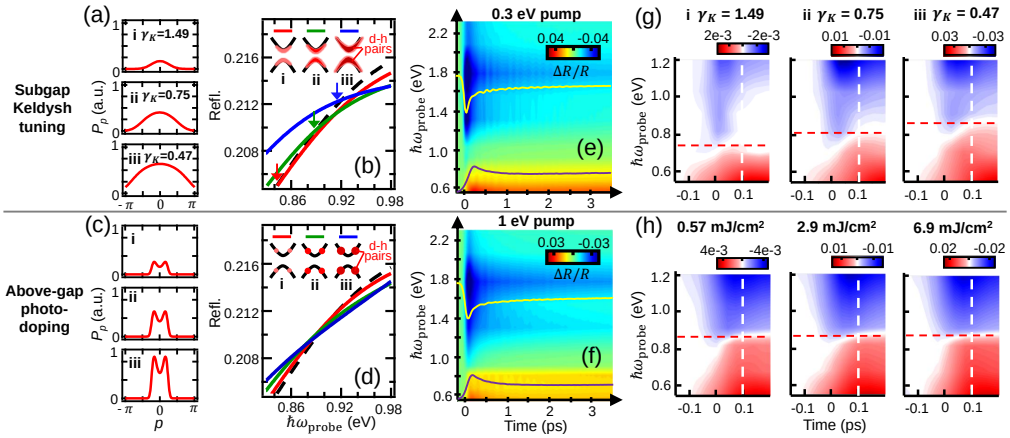

Figure 6.2: Non-thermal pair distribution through the Keldysh crossover. (a) Calculated P_p for conditions **i** to **iii** using the Landau-Dykhne method. (b) Simulated non-equilibrium reflectivity spectra for subgap pumping. (c, d) Analogues of (a) and (b) but simulated for above-gap pumping. Fluence increases from **i** to **iii**. Black curves in (b) and (d) are the equilibrium spectra. Arrows in (b) mark the crossing points between the non-equilibrium and equilibrium curves. Experimental $\Delta R/R$ maps of Ca_2RuO_4 for (e) 0.3 eV pump (fluence: 30 mJ/cm^2) and (f) 1 eV pump (fluence: 7 mJ/cm^2). Two representative constant energy cuts (yellow: 1.77 eV, purple: 0.56 eV) are overlaid. (g) Enlargement of $\Delta R/R$ maps for 0.3 eV pump using three pump fluences [marked in Figure 6.1(e)] corresponding to conditions (i) to (iii) in (a). (h) Enlargement of $\Delta R/R$ maps for 1 eV pump using three pump fluences indicated above. White dashed lines mark $t = 0.1$ ps. Red dashed lines: guides to the eye for the $\hbar\omega_{\text{probe}}$ where $\Delta R/R$ changes sign at $t = 0.1$ ps.

duration. This is followed by exponential recovery as the HD pairs thermalize and recombine (Appendix A). By plotting Γ against the peak value of E_{pump} (measured in vacuum), we observe a change from power law scaling to threshold behavior when $E_{\text{pump}} > 0.07$ V/Å [Figure 6.1(e)], in remarkable agreement with our calculated Keldysh cross-over [Figures 6.1(a),(b)]. In contrast, measurements performed using 0.56 eV pumping exhibit exclusively power law scaling over the same E_{pump} range [Figure 6.1(f)], again consistent with our model.

6.3 Momentum-space control of the photo-carrier distribution

A predicted hallmark of the Keldysh cross-over is a change in width of the non-thermal distribution of HD pairs in momentum space [175]. In the multi-photon regime, doublons and holons primarily occupy the conduction and valence band edges, respectively, resulting in a pair distribution function (P_p) sharply peaked about zero momentum ($p = 0$). In the tunneling regime, the peak drastically broadens, reflecting the increased spatial localization of HD pairs. Using the Landau-

Dykhne method (Appendix A), we calculated the evolution of P_p for Ca_2RuO_4 as a function of E_{pump} through the Keldysh cross-over. Figure 6.2(a) displays P_p curves at three successively larger E_{pump} values corresponding to (i) $\gamma_K = 1.49$, (ii) $\gamma_K = 0.75$ and (iii) $\gamma_K = 0.47$, which show a clearly broadening width along with increasing amplitude.

To demonstrate how signatures of a changing P_p width are borne out in experiments, we simulate the effects of different non-thermal electronic distribution functions on the broadband optical response of a model insulator. Assuming a direct-gap quasi-two-dimensional insulator with cosine band dispersion in the momentum plane (p_x, p_y), the optical susceptibility computed using the density matrix formalism can be expressed as [192] (Appendix A):

$$\chi = \sum_{p_x, p_y} C\mathcal{L}[\hbar\omega_{\text{probe}} - \Delta(p_x, p_y)][N_v(p_x, p_y) - N_c(p_x, p_y)]$$

where C is a constant incorporating the transition matrix element, $\mathcal{L}$ represents a Lorentzian oscillator centered at the gap energy $\Delta(p_x, p_y)$, and N_v and N_c are the occupations of the valence and conduction bands, respectively. As will be shown later [Figure 6.3(a)], it is valid to assume that $\Delta(p_x, p_y)$ decreases in proportion to the number of excitations (Appendix A). Figure 6.2(b) shows simulated reflectivity spectra around the band edge—converted from χ via the Fresnel equations—using Gaussian functions for N_v and N_c of variable width to approximate the P_p line-shapes [Figure 6.2(a)] (Appendix A). As P_p evolves from condition (i) to (iii), we find that the intersection between the non-equilibrium and equilibrium reflectivity spectra shifts to progressively higher energy. For comparison, we also performed simulations under resonant photo-doping conditions using the direct-gap insulator model. Figure 6.2(c) displays three P_p curves at successively larger E_{pump} values, which were chosen such that the total number of excitations match those in Figure 6.2(a). Each curve exhibits maxima at non-zero momenta where $\hbar\omega_{\text{pump}} = \Delta(|p|)$ is satisfied. In stark contrast to the subgap pumping case, the amplitude of P_p increases with E_{pump} but the width remains unchanged. This results in the non-equilibrium reflectivity spectra all intersecting the equilibrium spectrum at the same energy, forming an isosbestic point [Figure 6.2(d)]. The presence or absence of an isosbestic point is therefore a key distinguishing feature between Keldysh space tuning and photo-doping. This criterion can be derived from a more general analytical model (Appendix A), which shows that a key condition for identifying a Keldysh

crossover is that $\Delta R/R$ spectra at different fluences do not scale.

Probe photon energy-resolved $\Delta R/R$ maps of Ca_2RuO_4 were measured in both the Keldysh tuning ($\hbar\omega_{\text{pump}}$ = 0.3 eV) and photo-doping ($\hbar\omega_{\text{pump}}$ = 1 eV) regimes. As shown in Figures 6.2(e) & (f), the extremum in $\Delta R/R$, denoting the peak HD density, occurs near a time t = 0.1 ps measured with respect to when the pump and probe pulses are exactly overlapped ($t = 0$). This is followed by a rapid thermalization of HD pairs as indicated by the fast exponential relaxation in $\Delta R/R$, which will be discussed later (Appendix A). Figure 6.2(g) shows $\Delta R/R$ maps acquired in the subgap pumping regime for three different pump fluences corresponding to conditions (i) to (iii) in Figure 6.2(a) and 6.1(e). Focusing on the narrow time window around t = 0.1 ps where the HD distribution is highly non-thermal, we observe that $\Delta R/R$ changes sign across a well-defined probe energy (dashed red line), marking a crossing point of the transient and equilibrium reflectivity spectra. As γ_K decreases, the crossing energy increases, evidencing an absence of an isosbestic point. Analogous maps acquired in the photo-doping regime [Figure 6.2(h)] also exhibit a sign change. However, the crossing energy remains constant over an order of magnitude change in fluence, consistent with an isosbestic point. These measurements corroborate our simulations and highlight the unique distribution control afforded by Keldysh tuning.

6.4 Coherent bandwidth renormalization

To study the HD thermalization dynamics in more detail, we used a Kramers-Kronig transformation to convert our differential reflectivity spectra into differential conductivity ($\Delta\sigma$) spectra (Appendix A). Figure 6.3(a) shows the real part of the transient conductivity measured in the thermalized state (t = 0.5 ps) following an 0.3 eV pump pulse of fluence 26 mJ/cm^2 (γ_K = 0.5), overlaid with the equilibrium conductivity. Subgap pumping induces a spectral weight transfer from the β to α peak and a slight red-shift of the band edge, likely due to free carrier screening of the Coulomb interactions [76]. Unlike in the DC limit, there is no sign of Mott gap collapse despite E_{pump} exceeding 10^9 V/m. To verify that the electronic subsystem indeed thermalizes by t = 0.5 ps, we compare the real parts of $\Delta\sigma_{0.3\text{ eV}}$ (fluence: 26 mJ/cm^2) and $\Delta\sigma_{1\text{ eV}}$ (fluence: 4 mJ/cm^2), the change in conductivity induced by subgap and above-gap pumping respectively, at both t = 0.1 ps and 0.5 ps. A scaling factor A is applied to $\Delta\sigma_{1\text{ eV}}$ to account for any differences in excitation density. As shown in Figure 6.3(b), the t = 0.1 ps curves do not agree within any scale factor. This is expected because the linear and nonlinear pair production processes initially

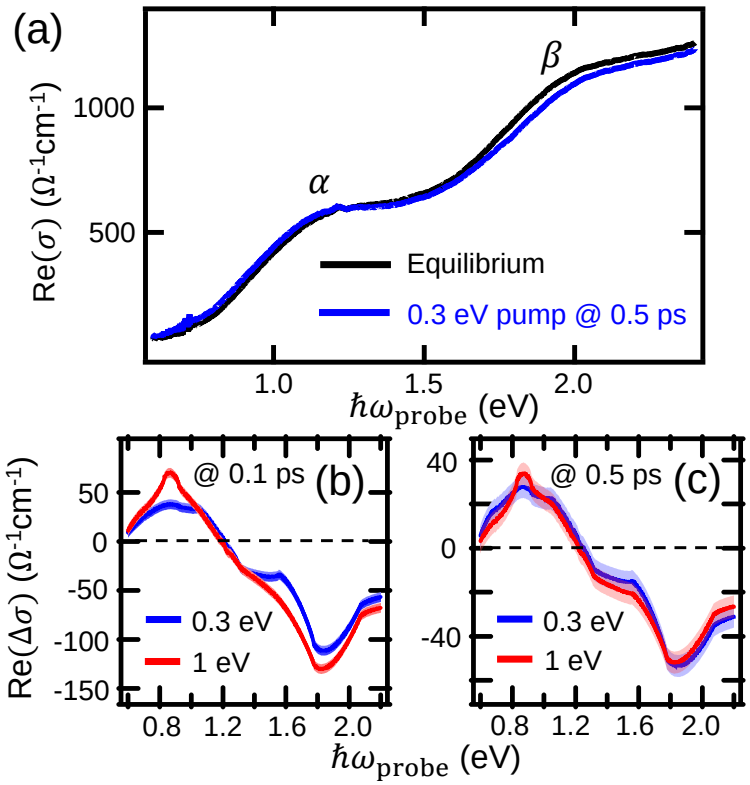

Figure 6.3: Non-equilibrium conductivity transients. (a) Conductivity spectra of Ca_2RuO_4 in the un-pumped equilibrium state at 80 K and the 0.3 eV pumped non-equilibrium state at t = 0.5 ps (fluence: 26 mJ/cm^2). (b) Comparison of differential conductivity spectra between 0.3 eV pump ($\Delta\sigma_{0.3\text{ eV}}$) and scaled 1 eV pump ($A\Delta\sigma_{1\text{ eV}}$) cases at t = 0.1 ps and (c) t = 0.5 ps. Red and blue shades indicate error estimated from the ω_{probe}-dependent fluctuations of the experimental $\Delta\sigma$ spectra.

give rise to very different non-thermal distributions (Figure 6.2). Conversely, by t = 0.5 ps, the curves overlap very well [Figure 6.3(c)], indicating that the system has lost memory of how the HD pairs were produced and is thus completely thermalized.

Based on the observations in Figures 6.3(b) and (c), the non-thermal window can be directly resolved by evaluating the time interval over which the quantity $\Delta(\Delta\sigma) = \Delta\sigma_{0.3\text{ eV}} - A \times \Delta\sigma_{1\text{ eV}}$ is non-zero (Appendix A). Figure 6.4(a) shows the complete temporal mapping of $\Delta(\Delta\sigma)$ spectra. The signal is finite only around t = 0 ps and is close to zero otherwise, supporting the validity our subtraction protocol. By taking a constant energy cut, we can extract a thermalization time constant of around 0.2 ps [Figure 6.4(b)]. Interestingly, $\Delta R/R$ and $\Delta\sigma_{0.3\text{ eV}}$, which both track the HD pair density, peak near 0.1 ps whereas $\Delta(\Delta\sigma)$ peaks earlier at t = 0 when the HD pair density is still quite low. This implies the existence of an additional coherent

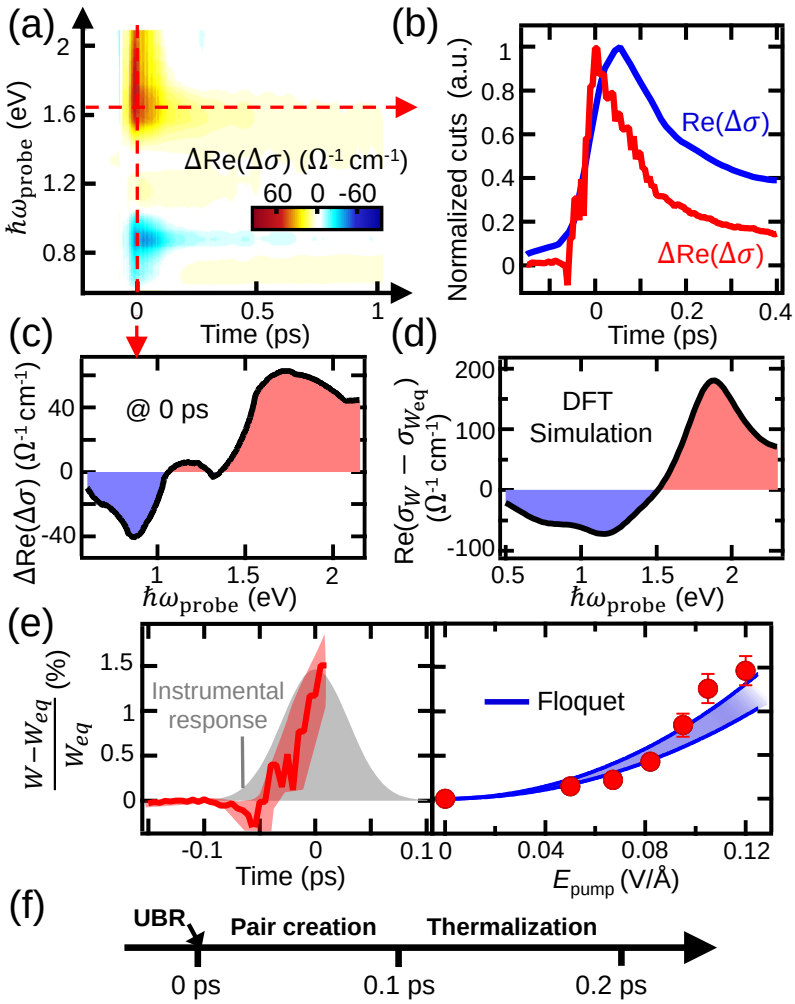

Figure 6.4: Ultrafast coherent bandwidth renormalization. (a) $\Delta(\Delta\sigma)$ map obtained by subtracting scaled $\Delta\sigma_{1\text{ eV}}$ from $\Delta\sigma_{0.3\text{ eV}}$ spectra. (b) A constant probe energy cut at 1.65 eV [dashed horizontal line in (a)] plotted together with $\Delta\sigma_{0.3\text{ eV}}$. (c) A constant time cut at $t = 0$ [dashed vertical line in (a)]. (d) DFT simulation of the spectrum change induced by bandwidth broadening. σ_W ($\sigma_{W_{\text{eq}}}$): conductivity with (without) bandwidth broadening. (e) (left) Quantitative extraction of pump-induced bandwidth modification versus t (with $E_{\text{pump}} = 0.12$ V/Å) and (right) versus E_{pump} (with $t = 0$ ps) based on fitting to DFT calculations. Red shaded region: error bar. Blue shaded region: Floquet theory prediction based on a periodically driven two-site cluster Hubbard model. Upper and lower bounds assume $U = 3$ eV [104] and $U = 3.5$ eV [79], respectively, where U is the on-site Coulomb energy, with no other adjustable parameters. (f) Chronology of non-thermal processes following an impulsive subgap drive.

non-thermal process that scales with E_{pump}, which peaks at $t = 0$, rather than with the HD density.

To identify the physical process responsible for the $t = 0$ signal, we examined how the electronic structure of Ca_2RuO_4 would need to change in order to produce the $\Delta(\Delta\sigma)$ profile observed at $t = 0$ [Figure 6.4(c)]. Using density functional theory (DFT), we performed an *ab initio* calculation of the optical conductivity of Ca_2RuO_4 based on its reported lattice and magnetic structures below T_N. The tilt angle of the RuO_6 octahedra was then systematically varied in our calculation as a means to simulate a changing electronic bandwidth (Appendix A). We find that both the real and imaginary parts of the measured $\Delta(\Delta\sigma)$ spectrum at $t = 0$ are reasonably well reproduced by our calculations if we assume the bandwidth of the driven system (W) to exceed that in equilibrium W_{eq} [Figure 6.4(d)] (Appendix A). This points to the coherent non-thermal process being a unidirectional ultrafast bandwidth renormalization (UBR) process that predominantly occurs under subgap pumping conditions [Figure 6.4(f)].

Coherent UBR can in principle occur via photo-assisted virtual hopping between lattice sites, which has recently been proposed as a pathway to dynamically engineer the electronic and magnetic properties of Mott insulators [20, 45, 90, 153, 155, 235]. To quantitatively extract the time- and E_{pump}-dependence of the fractional bandwidth change $(W - W_{eq})/W_{eq}$, we collected $\Delta(\Delta\sigma)$ spectra as a function of both time delay and pump fluence and fit them to DFT simulations (Appendix A). As shown in Figure 4(e), the bandwidth change exhibits a pulse-width limited rise with a maximum $t = 0$ value that increases monotonically with the peak pump field, reaching up to a relatively large amplitude of 1.5 % at $E_{pump} = 0.12$ V/Å, comparable to the bandwidth increases induced by doping [66] and pressure [170]. Independently, we also calculated the field dependence of $(W - W_{eq})/W_{eq}$ expected from photo-assisted virtual hopping by solving a periodically driven two-site Hubbard model in the Floquet formalism [153] (Appendix A), using the same model parameters for Ca_2RuO_4 as in our Landau-Dykhne calculations [Figure 6.1(a)]. We find a remarkable match to the data without any adjustable parameters [Figure 6.4(e)]. Since bandwidth renormalization increases with the Floquet parameter $(eaE_{pump})/\hbar\omega_{pump}$ in the case of photo-assisted virtual hopping, where a is the inter-site distance, this naturally explains why subgap pumping induces the much larger UBR effect compared to above-gap pumping.

Chapter 7

CONCLUSIONS AND OUTLOOK

In the past decade, light-based engineering of quantum materials has emerged as a central pillar of modern condensed matter physics. Mott insulators have been a primary target of these efforts because the myriad quantum many-body interactions that they host create a fertile playground to explore out-of-equilibrium phenomena. A primarily tool used in this endeavor is photo-doping. Though it is a conceptually simple technique, the transient states it induces are quite complicated owing to the strong interaction between charge and spin degrees of freedom in these materials.

The goal of this thesis was to address many of these complications by simultaneously tracking the ultrafast magnetic and charge dynamics of photo-doped Mott insulators. The first experimental result that was presented was the observation of a Hubbard excitonic fluid. This finding had several important ramifications. First, it established that not only are Hubbard excitons (HEs) metastable neutral excitations of the two-dimensional Mott antiferromagnet (AFM), but that they are critical to the out-of-equilibrium dynamics of the material. From the perspective of the charge degrees of freedom, HEs facilitate the formation of a photo-induced insulating state that lies between the photo-excitation process and the return to equilibrium. This previously overlooked phenomenon is vitally important to the spin degrees of freedom, since HEs have a unique relationship with the AFM order. Since HEs are much less destructive to the AFM motif than their free carrier counterparts, we found that their presence greatly diminishes the efficiency of photo-doping-induced demagnetization.

We built upon these efforts by also exploring the properties of HEs themselves. We demonstrated that short-range correlations are critical for the stability of bound HEs in Mott AFMs. While an attractive Coulombic interaction is in principle present between a holon and doublon, our experimental evidence suggests that the magnetic binding mechanism is the dominant factor that leads to the formation of a bound state. We identified a consequence of this spin-binding by examining the ultrafast (~1 ps) Hubbard excitonic recombination pathway. We found that the HEs recombine through a multi-magnon emission process, reflecting the intimate connection between the spin and charge degrees of freedom.

Finally, our work on subgap driving provides a novel method to rationally tune a Mott insulator *in situ* over Keldysh space, enabling targeted searches for exotic out-of-equilibrium phenomena such as strong correlation assisted high harmonic generation [100, 203], coherent dressing of quasiparticles [173], Wannier-Stark localization [127], AC dielectric breakdown [175] and dynamical Franz-Keldysh effects [207, 219], which are predicted to manifest in separate regions of Keldysh space. It also provides control over the nonlinear holon-doublon pair production rate—the primary source of heating and decoherence under subgap pumping conditions—in Mott systems, which is crucial for experimentally realizing coherent Floquet engineering of strongly correlated electronic phases. Moreover, the control over the carrier distribution in momentum space promised by Keldysh tuning can be an important tool for the engineering of novel photo-doped phases.

These results establish many important directions of future work. From the perspective of excitonics, HEs present an opportunity to develop devices that cannot exist in conventional semiconducting systems. Mott insulators host a myriad of magnetic interactions that have the potential to enable an entire ecosystem of magnetically-bound excitons. By devising experimental protocols to tune exchange interactions—through Floquet engineering, heterostructuring, or material growth, for example—HE properties can be engineered on-demand to facilitate novel excitonic technologies. More generally, these results provide a new perspective on the rich non-equilibrium phase diagrams that photo-doped Mott insulators can host. The Hubbard excitonic instability must be carefully considered when characterizing photo-induced phenomena in these materials and when analyzing their transient spectra. Finally, it is interesting to consider whether ensembles of HEs can serve as a platform for simulating quantum many-body dynamics, potentially hosting phenomena that are borne out of the strong interactions that are unique to these systems.

Appendix A

APPENDIX TO CHAPTER 6

A.1 Density functional theory simulations

The electronic structure of Ca_2RuO_4 was calculated from first principles with density functional theory implemented in the QUANTUM ESPRESSO package. The calculation used a plane-wave basis set and scalar relativistic norm-conserving Vanderbilt pseudopotentials. The energy cutoff was set to 60 Ry. A self-consistent calculation using a 4×4×4 Monkhorst-Pack grid was run at first, followed by a non-self-consistent calculation with a denser user defined grid. Convergence was tested for the energy cutoff and the grid density. The calculation was set to the spin-polarized mode to take into account the low-temperature antiferromagnetic structure of Ca_2RuO_4, and to the DFT+U mode to take into account the Coulomb correlation. The real and imaginary parts of the optical conductivity were calculated by the epsilon.x package after the non-self-consistent calculation. Finite interband and intraband smearings were used to avoid sharp spikes in the spectra caused by numerical issues.

To unambiguously confirm the modification of the electronic structure made by the pump field, we performed calculations using different input material parameters of Ca_2RuO_4 to account for different scenarios. The UBR scenario was implemented by changing the crystal structural input by tuning the tilting angles of the RuO_6 octahedra; the tilting angle changes the Ru-O-Ru bond angle, and thereby modifies the bandwidth. The case of Hubbard-U modification was simulated by directly tuning the U value in the DFT+U input. Details of the simulation results and how we chose different input parameters of Ca_2RuO_4 to simulate different cases are discussed in detail in the Section A.6.

A.2 Differential reflectivity spectra

A.2.1 Fitting analysis

Here we discuss the analysis procedure for the differential reflectivity data reported in this paper. $[\Delta R/R](t)$ transients at ten consecutive probe photon energies were measured within the range of 0.55 - 2.2 eV, forming the three-dimensional colormaps in Figure 6.2(e), (f) in the main text. Figure A.1(a) shows another example of a colormap of similar type for 0.3 eV pump at a fluence (F) of 15.2 mJ/cm^2.

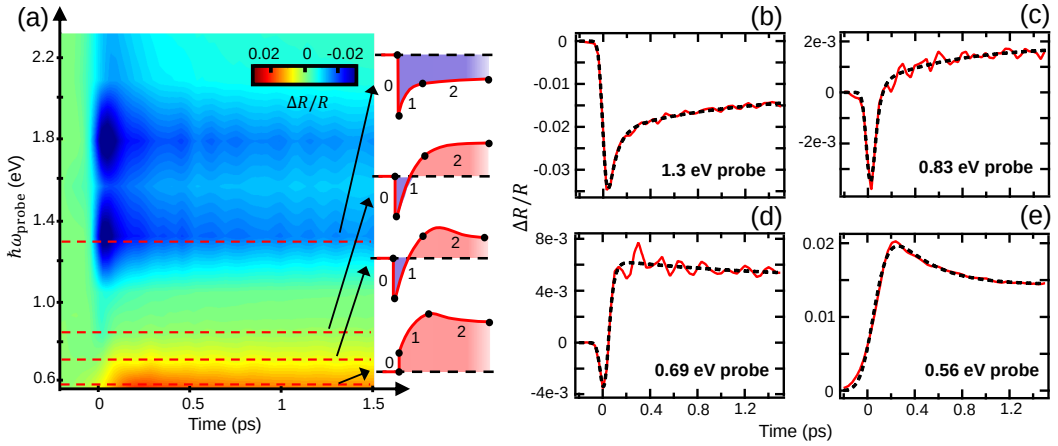

Figure A.1: Fitting of the transient reflectivity in Ca_2RuO_4. (a) $[\Delta R/R](t)$ map for 0.3 eV pump and F =15.2 mJ/cm^2. Transients of four types are schematically shown to the right. (b)-(e) Four constant probe photon energy cuts marked by red dashed lines in (a). Red lines are data. Black dashed lines are fittings from the convolution.

For all probe energies, the dynamics of $[\Delta R/R](t)$ transients can be described by three consecutive steps as expressed in the double exponential function

$$f(t) = \begin{cases} 0, & \text{for } t < 0 \text{ ps} \\ A_1 e^{-t/t_1} + A_2 e^{-t/t_2} + C, & \text{for } t \geq 0 \text{ ps}, \end{cases} \tag{A.1}$$

namely, the initial excitation upon pump arrival at $t = 0$ ps (Step 0), followed by a fast exponential process with $t_1 \sim 0.1$ ps (Step 1), and a slow exponential process with $t_2 \sim 1$ ps (Step 2) which settles the signal down to a constant plateau that decays on much longer time scales. However, depending on the probe photon energy, the signs and magnitudes of A_1, A_2, and C can change, leading to four types of traces as schematically summarized in Figure A.1(a). The signs of the coefficients for different probe energies are summarized in Table A.1. Four horizontal cuts to the experimental data marked by red dashed lines in Figure A.1(a) are shown in Figure A.1(b)-(e) to represent these four types of transients.

	$A_1 + A_2 + C$	A_1	A_2	C
1.2 - 2.2 eV	< 0	< 0	< 0	< 0
0.8 - 1.1 eV	< 0	< 0	< 0	> 0
0.7 eV	< 0	< 0	> 0	> 0
0.55 - 0.7 eV	> 0	< 0	> 0	> 0

Table A.1: Signs of coefficients for different probe energies.

Then, we fit the experimental $[\Delta R/R](t)$ with a convolution $[f \otimes IRF](t)$, where $f(t)$ is the intrinsic dynamics (Equation A.1), and the instrumental response function (IRF) takes the form of a Gaussian

$$IRF(t) = \frac{1}{\sigma\sqrt{2\pi}}\exp[-\frac{-(t-t_0)^2}{2\sigma^2}], \tag{A.2}$$

where σ is the instrumental time resolution and t_0 is the time zero of the measurement at which the pump and probe pulses reach temporal overlap. Fitting parameters are A_1, t_1, A_2, t_2, C, t_0, and σ.

The black dashed lines in Figure A.1(b)-(e) are the fitted curves, which are in close agreement with the experimental transients. There is a slight change in σ depending on pump and probe photon energies, ranging from 50 fs to 120 fs. The fitted σ values are used to infer the pump pulse widths. The pulse duration for 0.3 eV pump is around $\Delta t = 100$ fs, which is used for estimating the pump electric field strength E_{pump} through the expression for the energy density $u = \frac{1}{2}\varepsilon_0(E_{\text{pump}})^2 = F/(c\Delta t)$, where F is the fluence in vacuum and c is the speed of light. Determination of t_0 allows us to align transients at different probe energies temporally with a common time zero. Robustness of the fitted t_0 can be seen in the coherent phonon oscillation map in Figure A.2. The map is obtained by subtracting the $[\Delta R/R](t)$ map (temporally aligned with t_0) with the fitted electronic backgrounds. Good alignment of the oscillation phase of the coherent phonon across the entire probe energy range suggests that the fitting procedure for t_0 is reliable.

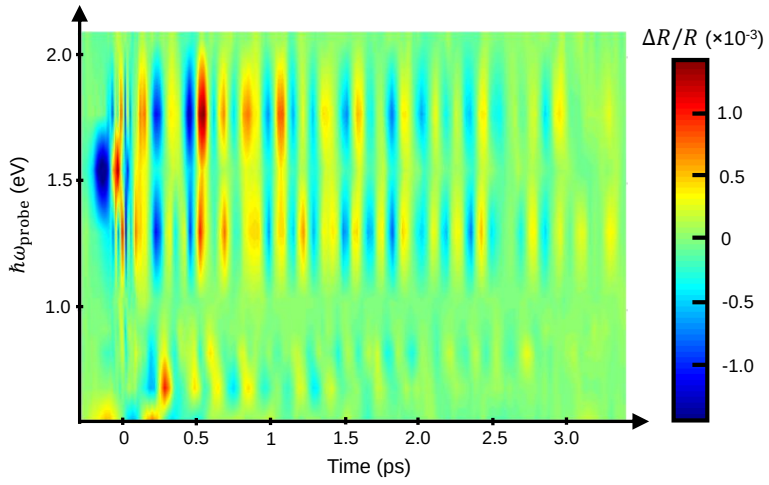

Figure A.2: Coherent phonon oscillation map obtained by subtracting the $[\Delta R/R](t)$ map in Figure A.1(a) with the fitted electronic background.

A.2.2 Time dynamics of zero-crossing feature

In Figure 6.2 of the main text, the evolution of the zero-crossing feature of the $[\Delta R/R](t)$ spectra versus pump fluence is used as a metric to distinguish the subgap Keldysh tuning scenario and the above-gap photodoping scenario. What is visually unclear when showing colormaps as in Figures 6.2(e)-(h) is the evolution of the energy of the zero crossing features after $t = 0.1$ ps, the time delay we identified to have the highest HD pair density and most nonthermal distribution. Here, we show the time dynamics of the zero-crossing feature a lot more clearly by plotting $|[\Delta R/R]|(t)$, the absolute value of $[\Delta R/R](t)$ on a logarithmic scale.

Figure A.3 shows three representative maps of $|[\Delta R/R]|(t)$ with different pumping conditions. The zero crossing feature is where $|[\Delta R/R]|(t)$ is smallest, corresponding to the valleys marked by blue lines in the graphs. The feature clearly continues to shift in energy after $t = 0.1$ ps (red vertical cuts), indicating that the optical response of the sample undergoes subsequent stages of evolution, including pair thermalization, interband recombination, and heating, each with a characteristic timescale. A notable example is at $t = 3$ ps, where pairs have mostly recombined and the electronic and the lattice systems have equilibrated at a higher transient temperature; the energy of the zero-crossing is an indicator of sample heating [124]. The fluence of Figure A.3(b) is higher, and creates more heat than that in Figure A.3(a), which naturally explains why its zero-crossing is at higher energy at $t = 3$ ps.

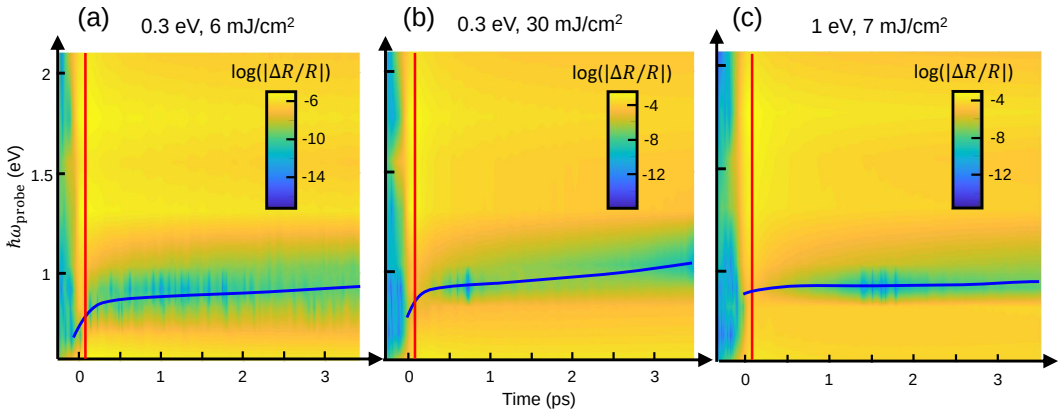

Figure A.3: Time dynamics of the zero-crossing feature highlighted in the logarithmic plot of $|[\Delta R/R]|(t)$ map. (a) and (b), Two fluences for the 0.3 eV pump scenario. (c) Highest fluence for the 1 eV pump scenario. Blue lines are guides to the eye for the minimum of $|[\Delta R/R]|(t)$, highlighting the shift of zero-crossing versus time. Red lines mark the cuts at $t = 0.1$ ps, where the pair distribution is nonthermal.

A.3 Calculation of the Keldysh parameter space

The Keldysh parameter space is formed by the subgap pump field strength and pump photon energy. In Figures 6.1 and 6.2 of the main text, we plot the total HD pair production rate Γ in the Keldysh space as well as the momentum dependent transition probability P_p. These calculations were obtained by using the Landau-Dykhne method combined with the Bethe Ansatz, as reported in Ref. [175].

A.3.1 The Landau-Dykhne method

The Landau-Dykhne method combined with the Bethe Ansatz has been used to model the nonlinear HD pair production process in Mott insulators across the entire Keldysh parameter space, from the multiphoton regime to the tunneling regime. We closely followed the procedure developed by Oka [175]; the theory was applied to a 1-dimensional (1D) Hubbard model in the original paper, but results and equations therein have been widely referenced by dielectric breakdown experiments on materials with higher dimensions [149, 245]. Therefore, we anticipate that the model can provide important qualitative guidance to our experiments, even though the 1D Hubbard model cannot fully reflect the realistic electronic structure or multiband Mott nature of Ca_2RuO_4.

For a 1D Hubbard model in a time-dependent electric field, the adiabatic perturbative theory expands the time-dependent state into the linear combination of adiabatic eigenstates

$$\Psi(t) = a(t)0;\Phi(t) + b(t)p;\Phi(t)_{dh}, \tag{A.3}$$

where p is momentum, $\Phi(t)$ is the Peierls phase, and $a(t)$ and $b(t)$ are the probability amplitudes for the channel at p to be in the ground state (no pair) or in the excited state (with a pair). The p-dependent transition probability $P_p = [b(t)]^2$ can be calculated as

$$P_p = \exp(-2\mathrm{Im}\mathcal{D}_p), \tag{A.4}$$

where $\mathcal{D}_p$ is the difference between the dynamical phase of the ground state and the excited state. After more treatments, Ref. [175] gives

$$\mathrm{Im}\mathcal{D}_p = \mathrm{Im}\mathcal{D}_{p1} + \mathrm{Im}\mathcal{D}_{p2}, \tag{A.5}$$

and

$$\mathrm{Im}\mathcal{D}_{p1} = \int_p^0 \Delta E(l)\mathrm{Im}\left(\frac{1}{F(p-l)}\right)dl, \tag{A.6}$$

$$\mathrm{Im}\mathcal{D}_{p2} = \int_0^{1/\xi} \Delta E(il)\mathrm{Im}\left(\frac{i}{F(p-il)}\right)dl. \tag{A.7}$$

Here, ΔE is the gap function, $F(\Phi) = \pm\sqrt{F_0^2 - \Omega^2\Phi^2}$ is the time-dependent field with sinusoidal oscillations, ξ is the HD correlation length, Ω is the pump frequency, and F_0 is the amplitude of F. After P_p is calculated, the total HD pair production rate can be obtained by an integral

$$\Gamma = \frac{\Omega}{2\pi}\int_{-\pi}^{\pi}\frac{dp}{2\pi}P_p. \tag{A.8}$$

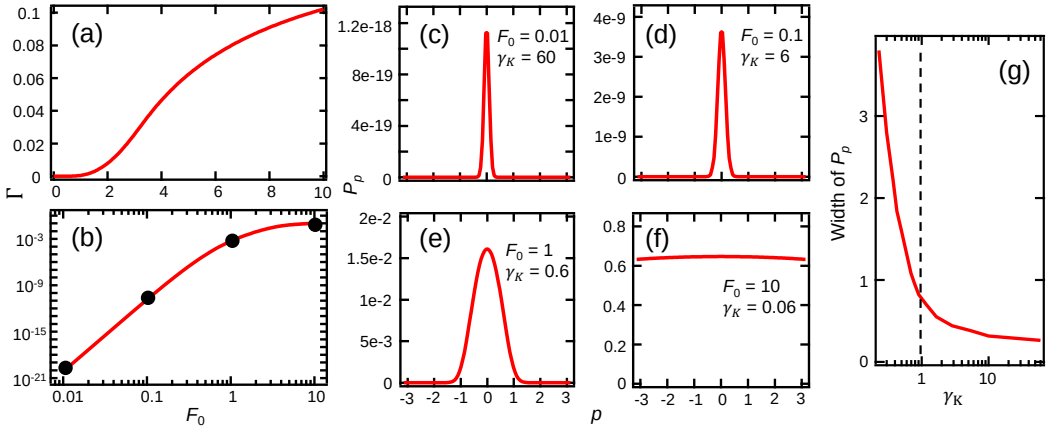

Figure A.4: Field-dependent nonlinear excitation for $U = 8$, $\Delta = 4.6$, $\Omega = 1$. (a) Total HD production rate Γ versus field strength F_0. (b) Same as (a) but on a logarithmic scale. (c)-(f) Momentum dependent transition probability P_p at the four different field strengths marked with black circles in (b). The corresponding Keldysh parameters are also labeled. (g) Width of P_p versus γ_K.

Figure A.4 shows a validating calculation using Hubbard $U = 8$, Mott gap $\Delta = 4.6$, pump frequency $\Omega = 1$, at various field strengths F_0. The energy unit is the hopping energy t_{hop}, F_0 is in the unit of t_{hop}/a, where a is the lattice parameter. The nonlinear production rate Γ versus F_0 is shown in Figures A.4(a) and (b) on linear and logarithmic scales, respectively; in (b), the Keldysh crossover is observed as the line deviates from the power law scaling of the multiphoton process as F_0 increases. P_p's at the four representative F_0's marked by black circles in Figure A.4(b) are shown in Figures A.4(c)-(f). Drastic broadening of P_p is clearly seen in the vicinity of the Keldysh crossover $\gamma_K \sim 1$, while in the deep multiphoton regime ($\gamma_K \gg 1$) the broadening effect is minimal; see Figure A.4(g), and the comparison between Figures A.4(c) and (d). These results all well reproduce findings in Reference [175].

A.3.2 Band parameters of Ca_2RuO_4 used in the calculation

Band parameters of Ca_2RuO_4 and realistic subgap pumping conditions were plugged in the equations above to calculate the Keldysh map and the P_p curves in Figures

6.1 and 6.2 of the main text. We used the parameters reported in the dynamical mean-field theory calculations for Ca_2RuO_4 [79], with U = 3.5 eV, Δ = 0.6 eV (from optical measurements in [104]), a = 5.6 Å (in-plane lattice parameter), and t_{hop} = 0.23 eV (the hopping integral between xy orbitals, since joint density of states near the Mott gap is mostly contributed by $d_{xy} \rightarrow d_{xz/yz}$ transitions). The correlation length [208] can be calculated with $\xi = [\ln(U/4.377t_{\text{hop}})]^{-1}a$ in the strong-coupling limit (which holds for Ca_2RuO_4 since U/t_{hop} = 15 [208]). We estimate ξ = 4.45 Å. This value is the same order of magnitude as ξ = 2.1 Å estimated for VO_2 [149], which is another Mott insulator showing a cooperative charge-lattice response across a temperature-driven metal-to-insulator transition.

A.4 Simulation of optical properties of a photoexcited insulator

To understand how photo-induced band filling affects the $\Delta R/R$ spectrum, we performed simulations assuming a simplified insulator model. Figure A.5(a) shows the band structure of the simulated insulator. Due to the quasi-2D nature of the electronic structure of Ca_2RuO_4, we considered a cosine-type dispersion in the 2D momentum plane formed by p_x and p_y. Conduction and valence bands are symmetric about zero energy, each with a bandwidth of 0.8 eV, and separated by a direct gap of 0.9 eV (which, upon considering the band edge smearing effect due to dephasing, gives an optical gap of 0.6 eV). These parameters were chosen to produce similar band-edge optical properties as Ca_2RuO_4. The optical susceptibility spectrum resulting from interband transitions can be obtained by [192]

$$\chi(\omega) = \sum_{p_x,p_y} \frac{e^2 x_{vc}(p_x,p_y)T_2}{\epsilon_0\hbar} \frac{[\omega_{\text{probe}} - \frac{\Delta(p_x,p_y)}{\hbar}]T_2 - i}{[\omega_{\text{probe}} - \frac{\Delta(p_x,p_y)}{\hbar}]^2 T_2^2 + 1} [N_v(p_x,p_y) - N_c(p_x,p_y)], \tag{A.9}$$

where e is the electron charge, ϵ_0 is vacuum permittivity, $\hbar$ is Planck's constant divided by 2π, x_{vc} is the matrix element of the vertical interband transition at a particular momentum (assumed to be a constant for all momenta for simplification), T_2 (assume to be constant) is the band dephasing time, ω_{probe} represents probe frequency, $\Delta(p_x, p_y)$ represents the gap energy, and N_v and N_c are the electron occupations of the valence and conduction bands, respectively. The physical picture of the equation is that the bands are viewed as an ensemble of vertical two-level systems (TLSs) in the p_x- p_y plane with level separations $\Delta(p_x, p_y) = \hbar(\omega_c - \omega_v)$; each TLS contributes a Lorentzian oscillator, weighted by its corresponding occupation factor, to the total susceptibility.

In equilibrium (N_v = 1, N_c = 0 for all p_x and p_y), we calculated the susceptibility

by Equation A.9 and converted it into static real and imaginary parts of conductivity σ and reflectivity, as shown in Figures A.5(c)-(e). The values and trends of the curves are similar to those of Ca_2RuO_4 measured around its α peak onset energy (Mott band edge), but the higher energy transitions that involve multiple orbitals in Ca_2RuO_4, such as the β and γ peaks, are not accounted for by the model.

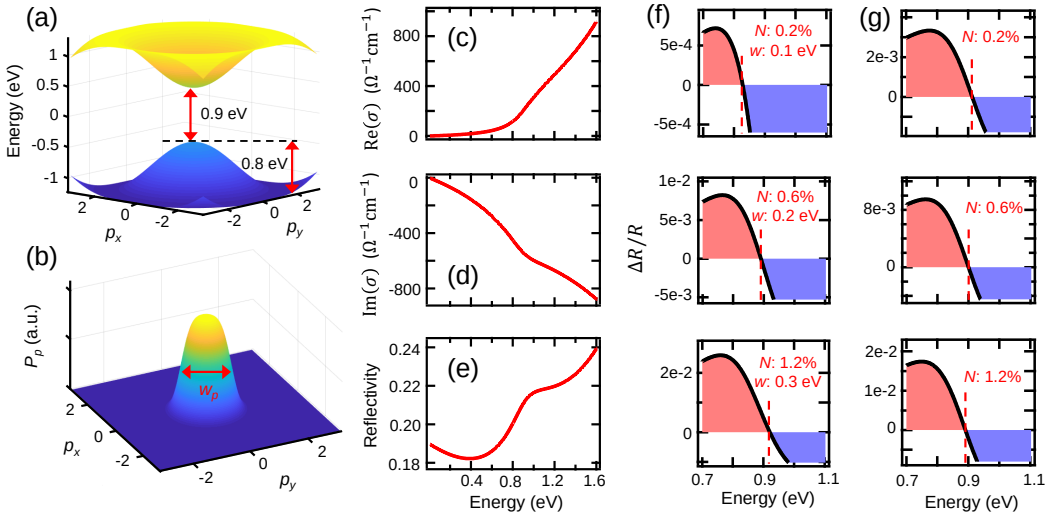

Figure A.5: Simulation of optical properties of a photoexcited insulator. (a) Band structure. (b) Momentum dependent photocarrier distribution. w_p (w) represents the width of the distribution in the momentum (energy) space. (c)-(e) Equilibrium optical properties calculated from the band structure in (a) with no photocarriers. (f) Differential reflectivity spectrum (spectrum with photocarriers subtracted by that without photocarriers) at various carrier densities (N) and width of distribution w. (g) Same as (f) except that the P_p is adjusted to the 1-eV-pump nonthermal distribution. N changes consistently, while the width of distribution stays constant for the three panels.

Next, we consider the laser-driven case. We used the Gaussian distribution to account for a total of N photoexcited nonthermal carriers

$$N = \sum_{p_x,p_y} N_c(p_x,p_y) = \sum_{p_x,p_y} \frac{A}{w\sqrt{2\pi}} \exp \frac{-[\omega_c(p_x,p_y)-\omega_0]^2}{2w^2}, \tag{A.10}$$

where we specified width w, peak center ω_0, and N to determine A and $N_c(p_x,p_y)$; for 0.3 eV pump experiments, we set ω_0 to be half of the direct gap (assuming zero energy centers the gap), and w progressively increases with N to mimic the width evolution of the γ_K-dependent P_p distribution obtained from the Landau-Dykhne theory, while for 1 eV pumping, we set $\omega_0 = 0.5$ eV, and w remains constant with increasing N. A representative Gaussian distribution landscape is shown in Figure

A.5(b), mimicking the situation for subgap pumping at a relatively low fluence, where the states at the band edge (where the gap is smallest) are mostly occupied. The nonthermal photocarrier distribution affects $N_c(p_x, p_y)$ and $N_v(p_x, p_y) = 1 - N_c(p_x, p_y)$, and therefore, modifies the nonequilibrium σ and reflectivity. By applying the Fresnel equations, we simulated $\Delta R/R$ spectra for various photocarrier densities N and distribution widths w, and plotted three scenarios in Figure A.5(f); N is expressed as the percentage of the pair density within the maximum allowed number of pairs in the bands. One detail we noticed was that simply considering the filling-induced optical bleaching will only lead to negative $\Delta R/R$ for all probe energies. This is because the equilibrium reflectivity develops a peak structure around the energy where the gap onsets (see Figure A.5(c) and (e)), and filling will only bleach the gap feature, and therefore, lead to a suppression of the reflectivity peak. We found that, to match the experimental fact that positive $\Delta R/R$ regions are present in the experimental data, a term considering the photocarrier-induced band edge redshift has to be included. Therefore, we assumed the photoinduced change in Δ to be proportional to N (If the change is small, only the linear term in the Taylor expansion is retained.). This assumption is reasonable because quantitative extraction of band edge energy shift versus fluence in the 1 eV pump experiments indeed recovers linearity; see Figure A.6.

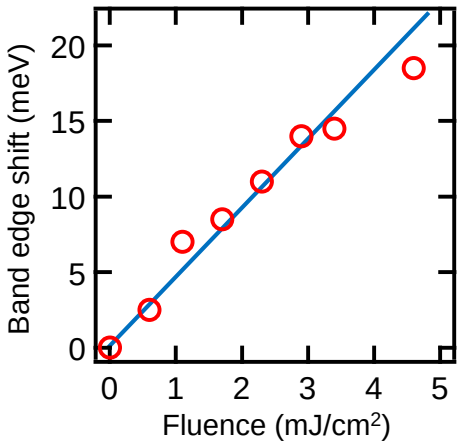

Figure A.6: Band edge energy redshift versus fluence for 1 eV pump experiments. This graph is obtained by performing a Kramers-Kronig transform detailed in the next section.

For the three scenarios plotted in Figure A.5(f), we included both the filling effect through $N_v(p_x, p_y)$ and $N_c(p_x, p_y)$ and the band edge redshift through Δ. For the three rows in Figure A.5(f), the simultaneous increase of N and w is for simulating

the fluence dependence of our subgap pumping experiment, where pair density increases with fluence, and w increases as γ_K decreases (predicted by the Landau-Dykhne theory). An apparent expansion of the $\Delta R/R > 0$ region is observed from the top panel to the bottom panel. This key feature is present in the simulations and experimental data in Figure 6.2 of the main text, because this type of evolution of $\Delta R/R$ prohibits an isosbestic point in the nonequilibrium reflectivity spectra in the subgap pumping scenario. On the other hand, the simulations shown in Figure A.5(g), which are adapted to the experimental 1 eV pumping condition, and accounts for both the increase of N and the band edge redshift ($\propto N$) but not the increase of w or any change in the nonthermal probability distribution function, fails to reproduce the expansion of the $\Delta R/R > 0$ region. The fact that the entire $\Delta R/R$ spectrum seems to scale with N for a constant distribution function in Figure A.5(g) leads to the appearance of an isosbestic point in the nonequilibrium reflectivity spectra for the 1 eV pumping case; which was exactly observed in experiments.

A.5 Kramers-Kronig transform and differential optical conductivity

Figures 6.3 and 6.4 of the main text shows differential optical conductivity spectra ($\Delta\sigma$), which were obtained by a Kramers-Kronig (KK) analysis of the $\Delta R/R$ spectra. In this section, we first discuss our KK algorithm, which converts experimental $\Delta R/R$ spectra within a limited probe energy range to $\Delta\sigma$, provided that the static broadband optical conductivity σ is known. Second, we will discuss details of identifying modifications to differential conductivity for 0.3 eV pumping ($\Delta\sigma_{0.3\text{ eV}}$) by Floquet bandwidth renormalization.

A.5.1 The regional KK transform algorithm

KK transform is a powerful technique that enables calculation of intrinsic complex-valued optical constants of a material from the reflectivity data alone. If the reflectivity spectrum $R(\omega)$ is known, the reflection phase $\theta(\omega)$ can be calculated as

$$\theta(\omega) = \frac{1}{\pi}\int_0^\infty \ln\frac{\omega' + \omega}{\omega' - \omega}\frac{d\ln\sqrt{R(\omega')}}{d\omega'}d\omega' \tag{A.11}$$

without directly measuring it in experiments, and the real and imaginary parts of refractive index can be calculated by

$$\mathrm{Re}(n) = \frac{1 - R}{1 + R - 2\cos\theta\sqrt{R}} \tag{A.12}$$

$$\mathrm{Im}(n) = \frac{-2\sin\theta\sqrt{R}}{1 + R - 2\cos\theta\sqrt{R}}. \tag{A.13}$$

The optical conductivity σ can be obtained by $\sigma = (n^2 - 1)\omega\epsilon_0/i$. However, to use Equation A.11, $R(\omega)$ must be known from zero to infinite frequencies, which is impractical for experiments. Various methods exist that extrapolate $R(\omega)$ within a limited measurement range to high and low frequencies to complete the calculation.

Our situation is the following. The static optical constants of Ca_2RuO_4 without optical pumping have already been determined by measuring broadband $R(\omega)$ from 80 meV to 6.5 eV, followed by data extrapolation and KK transform. However, the key issue is that our pump-probe measurement that gives $\Delta R/R$ covers a smaller frequency range (0.5 eV to 2.2 eV), and we hope to obtain $\Delta\sigma$ in the same range. Equation A.11 cannot be directly applied because no model exists to extrapolate $\Delta R/R$. But Equation A.11 shows a strong resonance at $\omega \sim \omega'$, suggesting that frequencies that are away from the range of interest contribute less to θ. And when $\Delta R/R \ll 1$, it is possible that, numerically, simply considering the $\Delta R/R$ only in the measurement range is accurate enough to give $\Delta\sigma$ in the same range. We followed the discussions in Ref. [191] to perform such a regional KK analysis.

The θ integral can be written as the sum of three frequency ranges, namely, the low-frequency range, the measurement range, and the high-frequency range:

$$\theta(\omega) = -\frac{1}{\pi}\int_0^{0.5\text{ eV}} f(R,\omega)d\omega' - \frac{1}{\pi}\int_{0.5\text{ eV}}^{2.2\text{ eV}} f(R,\omega)d\omega' - \frac{1}{\pi}\int_{2.2\text{ eV}}^{\infty} f(R,\omega)d\omega', \tag{A.14}$$

where

$$f(R,\omega) = \ln\sqrt{R(\omega')}\frac{d}{d\omega'}\left(\ln\frac{\omega'+\omega}{\omega'-\omega}\right). \tag{A.15}$$

Applying the generalized mean value theorem to first and third integrals in Equation A.14, and defining the second term as ϕ gives

$$\theta(\omega) = A\,\ln\frac{0.5\text{ eV}+\omega}{0.5\text{ eV}-\omega} + \phi(\omega) + B\,\ln\frac{2.2\text{ eV}+\omega}{2.2\text{ eV}-\omega}, \tag{A.16}$$

where A and B are coefficients.

We fitted A and B from the known static σ data at 20 K. In the nonequilibrium scenario, $\Delta R/R$ due to the optical pump will enter $\phi(\omega)$ to affect $\theta(\omega)$. A and B are also expected to change slightly due to nonzero $\Delta R/R$ in these unmeasured ranges. However, we found that when $\Delta R/R \ll 1$, it is still numerically accurate to keep the nonequilibrium A and B constants to be the same as their equilibrium values, because the first and third terms in Equation A.16 are off resonant in frequency.

We did a benchmark test to prove the validity of this protocol. Figure A.7(a) shows the static σ at various temperatures. In Figure A.7(b), the 20 K curve is still the static

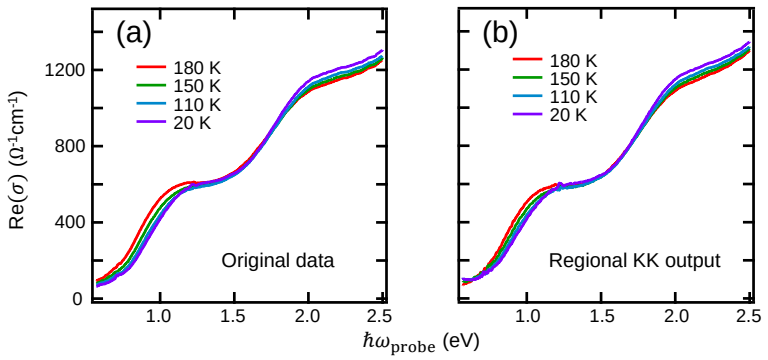

Figure A.7: Benchmark test for the regional KK algorithm using the temperature dependent data set. (a) Temperature dependent optical conductivity spectra directly from experiment used as the benchmark. (b) Regional KK output, where the known 20 K conductivity spectrum is used to fit the A and B coefficients, and the reflectivity spectra for the rest of the temperatures are input into regional KK to output their respective conductivity spectra. Close agreement of conductivity spectra for all temperatures with (a) is observed.

one, while the 110 K, 150 K, 180 K curves are outputs from Equation A.16, where A and B coefficients are results from fitting to the 20 K data, and the differences of reflectivity, $\Delta R_x = R_x - R_{20\text{ K}}$ (x =110 K, 150 K, 180 K), were input to the ϕ term. The close agreement between regional KK output at 110 K, 150 K, and 180 K in Figure A.7(b) and the experimental data in Figure A.7(a) suggests that the regional KK algorithm is accurate enough to give $\Delta\sigma$ when $\Delta R/R$ is small. None of our pump induced $\Delta R/R$ exceeds that induced by temperature (difference between 180 K and 20 K), and therefore, the method is expected to work well for our entire measurement.

Empirically speaking, we found that the most critical factor impacting the robustness of the algorithm is the probe energy width of the experiment. For wider measurement ranges, the definite integral term for calculating the reflection phase (the middle term of Equation A.14) becomes more dominant, and the algorithm appears more robust. This is because the equation used for fitting the reflection phase in Equation A.16 contains two poles that are located exactly at the energy boundaries of the measurement. The KK transformed signals are inevitably subject to numerical artifacts at the poles and energies around the poles, but empirically we found that the artifact can be mitigated when the energy boundaries get further and further apart, that is, the range within which $\Delta R/R$ is experimentally measured gets wider. In our case, we did find artifacts associated with the poles (see the slight upturns

of a few curves in Figure A.7(b) at the low-energy boundary for example), but our measurement range (0.55 eV to 2.2 eV) is large enough so that the artifacts are contained within a manageable extent.

A.5.2 Subtracting the differential optical conductivity

The regional KK transform outputs pump-induced differential conductivity spectra $\Delta\sigma$ for both the 0.3 eV pump ($\Delta\sigma_{0.3\text{ eV}}$) and the 1 eV pump ($\Delta\sigma_{1\text{ eV}}$) cases at various fluences and time delays. In Figure 6.4 of the main text, we report analysis of difference spectra $\Delta(\Delta\sigma) = \Delta\sigma_{0.3\text{ eV}} - A \times \Delta\sigma_{1\text{ eV}}$, where A is the scale factor, to account for the unique spectral signatures of the coherent non-thermal regime that are exclusively related to the subgap strong-field drive but not the photocarrier doping effect. Here, we describe how this subtraction was performed, and our way to determine the proper scaling factor multiplying $\Delta\sigma_{1\text{ eV}}$ in the subtraction.

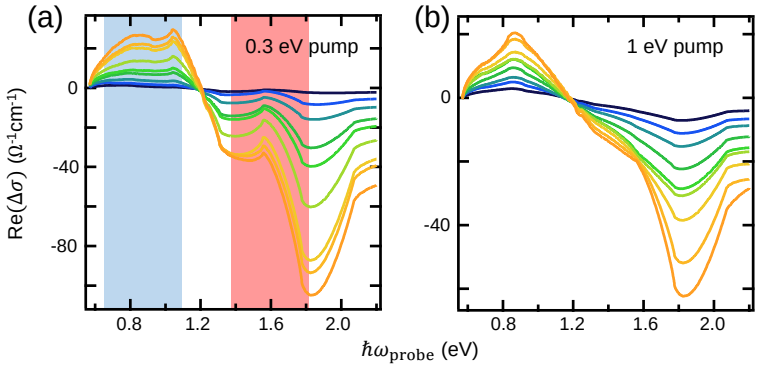

Figure A.8: Comparison of $\Delta\sigma$ spectra for 0.3 eV pump (a) and 1 eV pump (b) at $t = 0$ ps. Curves from blue to orange represent low to high fluences. 0.3 eV pump fluences range from 3 mJ/cm^2 to 30.4 mJ/cm^2. 1 eV pump fluences range from 0.57 mJ/cm^2 to 6.9 mJ/cm^2. Blue and red shaded regions in (a) highlight spectral ranges where additional modifications develop on the 0.3 eV pump data compared to the 1 eV pump data.

Figures A.8(a) and (b) show a comparison between $\Delta\sigma_{0.3\text{ eV}}$ and $\Delta\sigma_{1\text{ eV}}$ across all fluences at time zero ($t = 0$ ps). The probe energy ranges that show apparent modifications in $\Delta\sigma_{0.3\text{ eV}}$ data compared to $\Delta\sigma_{1\text{ eV}}$ are marked by the blue shade, where the positive peak looks flattened out, and the red shade, where a bump appears in the negative portion of the signal. In addition, a robust isosbestic point can be identified in both data sets at the same probe energy (1.2 eV) for all fluences. Generally speaking, for spectroscopic studies, an isosbestic point represents a frequency where measurement is most accurate, and is usually used as

a reference point [65]. In our case, the fact that it lies outside the blue and red shades (where spectral modifications obviously take place) strongly suggests that the probe energy of 1.2 eV, and energies that are right in the vicinity of it, are not influenced by the strong-field modification effect. Therefore, we chose the probe energy range between 1.1 eV to 1.3 eV as the reference, scaled $\Delta\sigma_{1\text{ eV}}$ to obtain the best matching with $\Delta\sigma_{0.3\text{ eV}}$ data in this range, and calculated $\Delta(\Delta\sigma) = \Delta\sigma_{0.3\text{ eV}} - A \times \Delta\sigma_{1\text{ eV}}$. This procedure was repeated for all time delays, producing the colormap in Figure 6.4(a) of the main text.

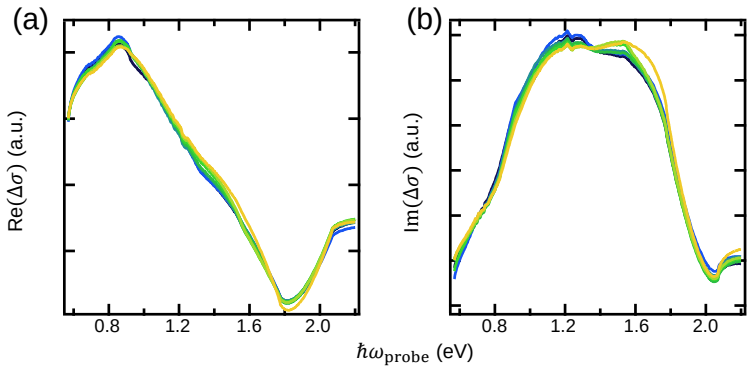

Figure A.9: Scaling analysis for the real (a) and imaginary (b) parts of $\Delta\sigma$ for 1 eV pump at $t = 0$ ps. Curves from blue to orange represent low to high fluences, and are multiplied by their respective scaling factors to make the traces overlap to the largest extent. Nice overlap is seen after scaling for both the real and the imaginary parts.

As shown in Figure A.9, both the real and the imaginary parts of $\Delta\sigma_{1\text{ eV}}$ at $t = 0$ ps scale well for all fluences, so the scaling factor in the $\Delta(\Delta\sigma)$ equation can simply account for the amplitude difference, and it is not important which fluence of $\Delta\sigma_{1\text{ eV}}$ is selected for the subtraction.

A.6 Density functional theory simulations for bandwidth broadening

In Figures 6.4(d) and (e) of the main text, we report the expected change to optical conductivity by considering a bandwidth broadening process. The simulation outcomes were used to fit experimental $\Delta(\Delta\sigma)$ spectra to quantify the amount of bandwidth modification $(W - W_{\text{eq}})/W_{\text{eq}}$ as a function of fluence and time delay. Here we present details of the density functional theory (DFT) simulation and the way to fit data.

We used the structural parameters in Ref. [31], considered the collinear antiferromagnetic (AFM) structure along the b axis, and applied the DFT+U (static

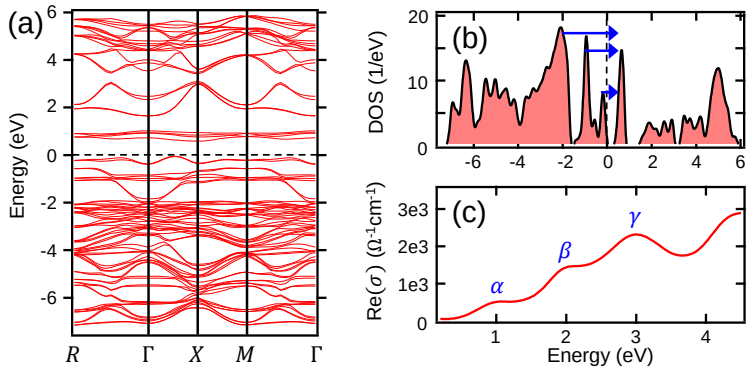

Figure A.10: Static electronic properties of Ca_2RuO_4 calculated by DFT. (a) Band structure. (b) Total density of states (DOS). Blue arrows indicate the α, β, and γ transition peaks in (c). (c) Optical conductivity spectrum. Dashed lines show Fermi levels.

U = 3.5 eV) method to simulate the static electronic properties of Ca_2RuO_4. Figures A.10(a), (b), and (c) show the calculated band structure, total density of states (DOS), and conductivity spectrum, respectively. The Mott gap clearly opens up around the Fermi level when both the AFM structure and the Coulomb correlation are considered. Flat bands near the Fermi level are mostly contributed by d orbitals of Ru, leading to concentrated DOS peaks. Three optical transitions across the DOS peaks clearly manifest in the optical conductivity spectrum as α, β, and γ transition peaks. This is in agreement with previous DFT and experimental studies on Ca_2RuO_4 [66, 104].

To simulate the effect of bandwidth broadening, we changed the structural input parameters. In Ca_2RuO_4, each RuO_6 octahedron undergoes two types of distortions compared to the K_2NiO_4 structure (I4/mmm), leading to significant modifications to the in-plane hopping amplitudes, and therefore, the bandwidth. Figure A.11(a) summarizes the two types of distortions, the rigid rotation of the octahedron around the c axis by the angle ϕ, and the rigid tilting of the octahedron around an in-plane (ab plane) axis by the angle θ. In the static low temperature AFM state, $\phi = 12°$ and $\theta = 12°$, and the Ru-O-Ru bond angle $\angle$(Ru-O-Ru) = 150.1°.

We broadened the bandwidth W in the simulation by reducing the tilting angle θ of the structure (blue arrows in Figure A.11(a) bottom panel), while keeping all other structural parameters the same; this will make $\angle$(Ru-O-Ru) approach 180°, and broaden the bandwidth according to the empirical formula $W \propto [\cos\angle(\text{Ru-O-Ru})]^2$ [241]. It is worth noting that the logic of choosing θ to change while keeping ϕ a

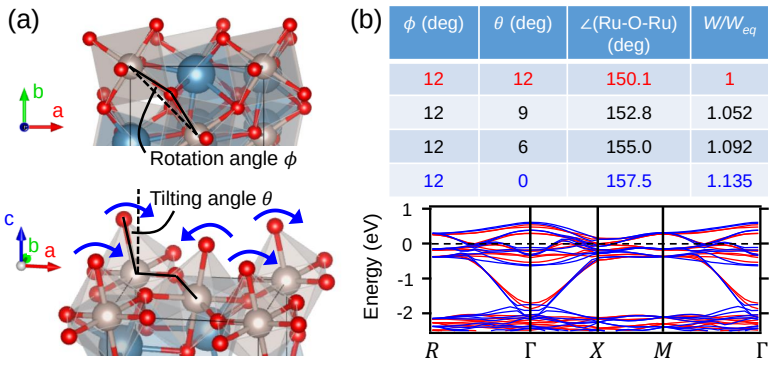

ϕ (deg)	θ (deg)	∠(Ru-O-Ru) (deg)	W/W_{eq}
12	12	150.1	1
12	9	152.8	1.052
12	6	155.0	1.092
12	0	157.5	1.135

Figure A.11: Method to simulate the effect of bandwidth broadening. (a) There are two angles related to the lattice distortion in Ca_2RuO_4. Top: the rotation angle ϕ about the c axis. Bottom: the tilting angle θ about an in-plane axis. (b) Examples of how tuning θ affects the Ru-O-Ru bond angle and therefore, the bandwidth. Top: table displaying combinations of angles and the resulting modification to the bandwidth W from the equilibrium W_{eq}. Bottom: band structures using the red and blue parameter conditions from the top table with a nonmagnetic structure and $U = 0$ eV. Red (blue) bands correspond to the red (blue) parameter set.

constant is based on the well-known fact that θ responds much more sensitively to Sr doping [66], temperature [31], and applied current [22] than ϕ. In addition, the coherent A_g phonon mode at 3.8 THz, which consists majorly of the tilting motion of RuO_6 octahedra, shows robust anomalies across the AFM ordering [125] and orbital ordering [124] temperatures. These all suggest that the tilting distortion is a crucial structural parameter in Ca_2RuO_4 which responds sensitively to magnetic and electronic ground states. This justifies us adjusting θ for simulating the bandwidth renormalization induced by the strong-field drive, even though the drive does not directly modify θ. The table in Figure A.11(b) shows examples of combinations of structure parameters, and the resulting ratio of the modified bandwidth to the static equilibrium bandwidth, W/W_{eq}, estimated from $W \propto [\cos\angle(\text{Ru-O-Ru})]^2$. To make sure that W is actually modified, we simulated the nonmagnetic crystal with $U = 0$ eV using the red and blue parameter sets in the table; the calculated bands are shown in the bottom panel of Figure A.11(b). The nonmagnetic setting with $U = 0$ eV fully collapses the Mott gap, making it easier for us to identify a bandwidth change. As clearly observed in the bottom panel of Figure A.11(b), the blue parameter set indeed leads to a broadened bandwidth compared to the red parameter set.

Figures A.12(a) and (b) show calculated modifications to conductivity by changing the bandwidth by various amounts; W/W_{eq} are labeled on each curve. Both the real

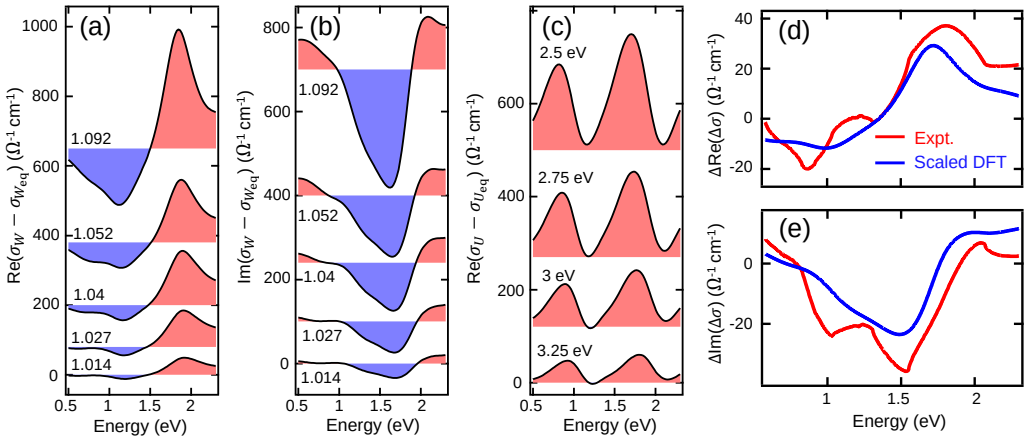

Figure A.12: DFT simulation outcomes of bandwidth modification. Calculated change in the real (a) and imaginary (b) parts of conductivity due to bandwidth broadening. Bandwidth narrowing would give spectra off from these traces by a minus sign. W/W_{eq} values are labeled. (c) Calculated change in conductivity due to dynamical U modification. Values of U are labeled. (d) and (e) show an example of scaling the simulated DFT spectra to fit the experimental $\Delta(\Delta\sigma)$ data to quantify W/W_{eq}. Real and imaginary parts are scaled by a common factor. Curves are offset for clarity from (a) to (c).

and the imaginary part show agreement with the experimental $\Delta(\Delta\sigma) = \Delta\sigma_{0.3\,\mathrm{eV}} - A \times \Delta\sigma_{1\,\mathrm{eV}}$. In contrast, if we consider another scenario where modification to Coulomb correlation U occurs [218], the change in conductivity would look very different, and would not match $\Delta(\Delta\sigma)$; see Figure A.12(c). Finally, given the simulation results of bandwidth modification, the method we used to quantitatively determine experimental W/W_{eq} is scaling the $W/W_{\mathrm{eq}} = 1.052$ curve (Since the difference in σ roughly grows in proportion with $(W - W_{\mathrm{eq}})/W_{\mathrm{eq}}$, it does not matter which curve to pick here.) in Figures A.12(a) and (b) by a common factor to fit experimental data, as shown in Figures A.12(d) and (e). The same factor is then multiplied to the $(W - W_{\mathrm{eq}})/W_{\mathrm{eq}}$ ratio set for the simulation to give the actual experimental $(W - W_{\mathrm{eq}})/W_{\mathrm{eq}}$, assuming linear proportionality when the fractional modification is small. Error bars in the main text are quantified by the standard deviation between the calculation and experiment.

A.7 Floquet calculation of bandwidth renormalization

In the main text, we discussed that the ultrafast bandwidth renormalization (UBR) observed in the subgap strong-field pump data at exactly time zero originates from a Floquet engineering mechanism. To give a quantitative estimate of the UBR due to

the Floquet mechanism and compare with our experiment, we followed Reference [153] and used the Floquet-driven two-site cluster model therein. The two-site cluster model takes the periodic-field-dependent electronic hopping into account, but significantly simplifies the problem. Dynamical mean-field theory for systems with extended dimensions also show good agreement with the two-site model. According to Reference [153], when the Mott insulator is strongly coupled ($U \gg t$), the ratio between the light-modified bandwidth and the static bandwidth is

$$\frac{W}{W_{\mathrm{eq}}} = \sqrt{\sum_{n=-\infty}^{\infty} \frac{J_n(\mathcal{E})^2}{1 + n\omega/U}}, \tag{A.17}$$

where $\mathcal{E} = eaE_0/(\hbar\omega)$ is the Floquet parameter, a is the lattice constant, E_0 is the field amplitude, ω is the pump frequency, and $J_n(x)$ is the nth Bessel function.

We input our experimental pumping conditions into the equation, $a = 5.6$ Å, and a range of U from 3 eV to 3.5 eV, with no other adjustable parameter. Since hopping $t = 0.23$ eV, the $t/U \ll 1$ condition holds. The result of this calculation using Equation A.17 is reported in Figure 6.4(e) of the main text.

A.8 Relation between differential reflectivity and HD pair density

In this section, we present additional clarifications of the relation between the differential reflectivity and the HD pair density. Two specific problems will be addressed. One is the proof of proportionality between differential reflectivity and the pair generation rate. We will then expand the model to take into account pair distribution functions, and show that the pair distribution function must undergo a crossover in the fluence scaling whenever the differential reflectivity spectra at different fluences cannot scale.

First, we identify that any pump-induced spectral modification at 0.1 ps (time delay at which $\Delta R/R$ peaks) should originate from the photo-excited pairs. The coherent Floquet modification and heating is expected to provide negligible contribution since these processes are separated in time from 0.1 ps. For photo-excited HD pairs with a density of n, their impact on the reflectivity spectrum can be expanded as

$$\Delta R(\omega) = R(n,\omega) - R(n=0,\omega) \approx n \left.\frac{\partial R(n,\omega)}{\partial n}\right|_{n=0} \tag{A.18}$$

where we retain only the linear term in the Taylor series (given the condition of $\Delta R/R \ll 1$, which holds for our entire fluence range), and assume that the coefficient $\left.\frac{\partial R(n,\omega)}{\partial n}\right|_{n=0}$ is nonzero in general. Note that the expression remains valid for all types

of photo-induced spectral modifications, including peak shift and broadening, and the resulting relation of $\Delta R(\omega) \propto n$ has been frequently used by the ultrafast optical community to describe quasiparticle dynamics in various photo-excited gapped systems [42, 56, 72]. Assuming a simplified scenario where pair generation is uniform in rate within the pump pulse duration Δt, one can write the rate $\Gamma = n/\Delta t$. This relation, combined with Equation A.18, establishes $\Delta R(\omega) \propto n \propto \Gamma$. The reason we leave Γ in arbitrary units is because the coefficient relating $\Delta R(\omega)$ with Γ is not determined quantitatively. But establishing the proportionality is sufficient for us to perform the scaling analysis in this work.

We then consider an expanded model where ΔR is influenced by, not one, but multiple species of HD pairs distinguished by the pair energies. For the nonequilibrium situation where photo-excited HD pairs are occupying the upper and lower Hubbard bands, the pairs can be labeled in the joint density of states spectrum by their energies (doublon and holon energies combined for each pair) ω_i. If we represent the number of pairs with energy ω_i as n_{ω_i}, and divide the energy window within which pairs populate into a total of N bins, the pair distribution function can then be represented by a collection of $\{n_{\omega_i}\}$ for $i \in \{1, 2, ..., N\}$; see Figure A.13 for a schematic.

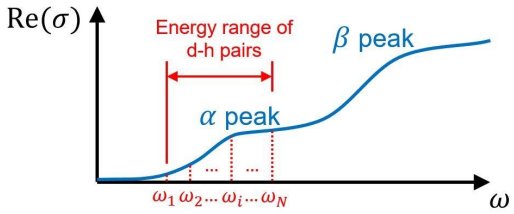

Figure A.13: Schematic showing the HD pair population on the optical conductivity (joint density of states) spectrum that can be distinguished by the pair energy.

We are interested in finding the influence of $\{n_{\omega_i}\}$ on the reflectivity spectrum. Consider the general case where pairs with different energies impact the spectrum differently, the photo-carrier induced reflectivity change can be expanded into the Taylor series as

$$\Delta R(F, \omega) = R(n_{\omega_1}, n_{\omega_2}, ..., n_{\omega_N}, \omega) - R(n_{\omega_1} = n_{\omega_2} = ... = n_{\omega_N} = 0, \omega) \quad \text{(A.19)}$$

$$\approx \sum_{i=1}^{N} n_{\omega_i}(F) \left. \frac{\partial R(n_{\omega_1}, n_{\omega_2}, ..., n_{\omega_N}, \omega)}{\partial n_{\omega_i}} \right|_{n_{\omega_1}=n_{\omega_2}=...=n_{\omega_N}=0} \quad \text{(A.20)}$$

where again only the linear terms are retained, and n_{ω_i} depends on pump fluence F as $n_{\omega_i}(F)$. For two fluence values F_1 and F_2, the ratio of the reflectivity spectra

$$\frac{\Delta R(F_1,\omega)}{\Delta R(F_2,\omega)} = \frac{\sum_{i=1}^{N} n_{\omega_i}(F_1)\left.\frac{\partial R(n_{\omega_1},n_{\omega_2},...,n_{\omega_N},\omega)}{\partial n_{\omega_i}}\right|_{n_{\omega_1}=n_{\omega_2}=...=n_{\omega_N}=0}}{\sum_{i=1}^{N} n_{\omega_i}(F_2)\left.\frac{\partial R(n_{\omega_1},n_{\omega_2},...,n_{\omega_N},\omega)}{\partial n_{\omega_i}}\right|_{n_{\omega_1}=n_{\omega_2}=...=n_{\omega_N}=0}} \tag{A.21}$$

should be ω-dependent in general. However, in certain regimes of photo-excitation, the pair distribution follows well-defined scaling functions, that is, for $\forall i, j \in \{1, 2, ...N\}$, there always exists a constant C, that makes $C \cdot n_{\omega_i}(F)/n_{\omega_j}(F) = 1$. This is equivalent to writing $n_{\omega_i}(F) = C_i f(F)$, where C_i is F-independent and $f(F)$ is a universal scaling function.

We give three concrete cases where such scaling functions exist:
(1) For above-gap photo-doping pump, $f(F) = F$.
(2) Within the deep multi-photon regime [175] ($\gamma_K \gg 1$), $f(F) = F^{a/2}$ ($a > 2$).
(3) Within the deep tunneling regime [175] ($\gamma_K \ll 1$), $f(F) = e^{-b/\sqrt{F}}$.

The fluence dependence can then be factored out as

$$\Delta R(F,\omega) = f(F)\sum_{i=1}^{N} C_i \cdot \left.\frac{\partial R(n_{\omega_1}, n_{\omega_2}, ..., n_{\omega_N}, \omega)}{\partial n_{\omega_i}}\right|_{n_{\omega_1}=n_{\omega_2}=...=n_{\omega_N}=0} \tag{A.22}$$

so that the ratio $\frac{\Delta R(F_1,\omega)}{\Delta R(F_2,\omega)} = \frac{f(F_1)}{f(F_2)}$ becomes ω-independent. The $\Delta R(\omega)$ spectrum therefore "scales" for various pump fluences, and we refer to this scenario as successful scaling. For the specific case of insulating systems, photo-excitation typically causes spectral weight transfers, which manifest as zero crossing features in $\Delta R(\omega)$. For this type of spectra, a successful scaling ensures that the zero-crossing energy does not shift with fluence (as observed in Figure 6.2(h) of the main text), leading to an isosbestic point in the reflectivity spectrum, $R(\omega) = \Delta R(\omega) + R_{\text{eq}}(\omega)$, where $R_{\text{eq}}(\omega)$ represents the spectrum in equilibrium.

On the other hand, according to Eq. A.21, unsuccessful scaling, defined as $\frac{\Delta R(F_1,\omega)}{\Delta R(F_2,\omega)}$ being ω-dependent, occurs for the Keldysh crossover [175] during which there is no universal scaling function $f(F)$ that can be factored out from n_{ω_i}; pair distribution change during the Keldysh crossover causes n_{ω_i} at different ω_i to scale differently with F. Absence of an isosbestic point in $R(\omega) = \Delta R(\omega) + R_{\text{eq}}(\omega)$, which is equivalent to the statement that the zero-crossing energy in $\Delta R(\omega)$ shifts with fluence, should be a manifestation of unsuccessful scaling, and therefore, can serve as evidence for the Keldysh crossover.

A.9 Lorentz model fitting of transient conductivity

Here we examine if the UBR due to Floquet engineering can be directly identified from the conductivity spectra. The idea is to fit α and β peaks with Lorentzians, and see if UBR manifests in their peak widths as a function of pump electric field strength E_{pump}.

We set up a fitting equation that expresses conductivity σ versus probe photon energy E as

$$\text{Re}(\sigma) = p_0 + p_1 E + p_2 E^2 + \frac{A_\alpha \Delta E_\alpha}{(E - E_\alpha)^2 + (\Delta E_\alpha)^2} + \frac{A_\beta \Delta E_\beta}{(E - E_\beta)^2 + (\Delta E_\beta)^2}, \quad \text{(A.23)}$$

which contains polynomial terms up to quadratic order to account for the background spectral weight, and two Lorentzians to account for the α and β peaks. A_α (A_β), E_α (E_β), ΔE_α (ΔE_β) represent spectral weight, center energy, and peak width of the α (β) peak, respectively. Figure A.14(a) shows the agreement between the fit and the equilibrium conductivity spectrum using Equation A.23.

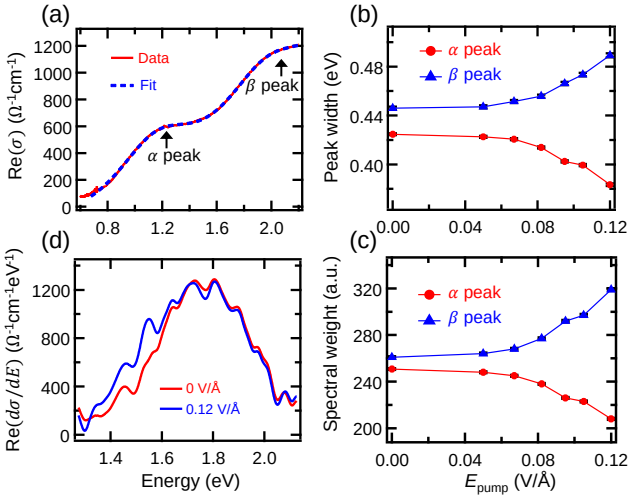

Figure A.14: Lorentz model fitting of optical conductivity. (a) Equilibrium conductivity at 20 K fitted by Equation A.23. (b) Peak widths and (c) amplitudes for the α and β bands versus pump field. (d) First order derivative of conductivity to show earlier onset of β peak conductivity in the laser-driven sample (blue) than the sample in equilibrium (red).

The similar fitting procedure is carried out for nonequilibrium $\text{Re}(\sigma)$ at various E_{pump} values. In order to only take the Floquet effect into account, we express $\sigma = \sigma_{\text{eq}} + \Delta(\Delta\sigma(t = 0))$, where σ_{eq} is the equilibrium conductivity, and $\Delta(\Delta\sigma(t = 0))$ is the time-zero nonthermal signal identified using the subtraction process (explained

in Section A.5.2). Figure A.14(b) shows the extracted peak widths versus E_{pump}. Although the α peak narrows with E_{pump}, the β peak clearly shows a broadening with E_{pump} whose trend matches closely with that in Figure 6.4(e) of the main text. In addition, the α peak spectral weight transfers to the β peak with increasing E_{pump} (Figure A.14(c)). The β peak broadening can be directly identified in the conductivity spectra by performing an energy derivative; see Figure A.14(d) for a comparison of $d\sigma/dE$ between the equilibrium and the laser-driven scenarios. The fact that the driven scenario shows an earlier onset of the beta peak in the 1.4 eV - 1.8 eV range corroborates the conclusion from our fitting.

The broadening of the β peak suggests a bandwidth increase of the d_{xz} and d_{yz} orbitals, which agrees with the conclusion from the DFT simulations reported in the main text. The observation of the α peak narrowing, however, requires more interpretations by future work. At a qualitative level, the α peak is expected to closely correlate with the hole population within the d_{xy} orbital (which arises from orbital mixing of d_{xy} into $d_{xz/yz}$ due to crystal field distortions), the appearance of the peak can thus respond sensitively to conditions other than a pure d_{xy} bandwidth broadening effect. Indeed, the spectral weight decrease of the α peak suggests a decrease of the d_{xy} hole population versus E_{pump}, which should be expected when DFT simulates a less distorted, bandwidth-broadened crystal by "straightening" the Ru-O-Ru bonds [104]. Therefore, a narrowing of the α peak can still be consistent with bandwidth broadening provided microscopic details are fully considered as in our first-principles calculations.

Bibliography

[1] A. Abragam and B. Bleaney. *Electron Paramagnetic Resonance of Transition Ions*. Oxford Classic Texts in the Physical Sciences. Oxford University Press, Oxford, New York, July 2012. ISBN 978-0-19-965152-8.

[2] D. Afanasiev, A. Gatilova, D.J. Groenendijk, B.A. Ivanov, M. Gibert, S. Gariglio, J. Mentink, J. Li, N. Dasari, M. Eckstein, Th. Rasing, A.D. Caviglia, and A.V. Kimel. Ultrafast Spin Dynamics in Photodoped Spin-Orbit Mott Insulator Sr_2IrO_4. *Physical Review X*, 9(2):021020, April 2019.

[3] Gihyeon Ahn, S. J. Song, T. Hogan, S. D. Wilson, and S. J. Moon. Infrared Spectroscopic Evidences of Strong Electronic Correlations in $(Sr_{1-x}La_x)_3Ir_2O_7$. *Scientific Reports*, 6(1):32632, September 2016.

[4] Zhanybek Alpichshev, Fahad Mahmood, Gang Cao, and Nuh Gedik. Confinement-Deconfinement Transition as an Indication of Spin-Liquid-Type Behavior in Na_2IrO_3. *Physical Review Letters*, 114(1):017203, January 2015.

[5] Philip W. Anderson. Is There Glue in Cuprate Superconductors? *Science*, 316(5832):1705–1707, June 2007.

[6] Andrew M. Weiner. *Ultrafast Optics*. John Wiley & Sons, Inc., first edition, 2008. ISBN 978-0-471-41539-8.

[7] Hideo Aoki, Naoto Tsuji, Martin Eckstein, Marcus Kollar, Takashi Oka, and Philipp Werner. Nonequilibrium dynamical mean-field theory and its applications. *Reviews of Modern Physics*, 86(2):779–837, June 2014.

[8] N. P. Armitage. Electrodynamics of correlated electron systems, August 2018. arXiv:0908.1126v3 [cond-mat.str-el].

[9] A. Asamitsu, Y. Tomioka, H. Kuwahara, and Y. Tokura. Current switching of resistive states in magnetoresistive manganites. *Nature*, 388(6637):50–52, July 1997.

[10] Kenichi Asano and Takuya Yoshioka. Exciton–Mott Physics in Two-Dimensional Electron–Hole Systems: Phase Diagram and Single-Particle Spectra. *Journal of the Physical Society of Japan*, 83(8):084702, August 2014.

[11] Seongkwang Bae and Sangwan Sim. Anisotropic excitons in 2D rhenium dichalcogenides: a mini-review. *Journal of the Korean Physical Society*, 81 (6):532–548, September 2022.

[12] Youn Jue Bae, Jue Wang, Allen Scheie, Junwen Xu, Daniel G. Chica, Geoffrey M. Diederich, John Cenker, Michael E. Ziebel, Yusong Bai, Haowen Ren, Cory R. Dean, Milan Delor, Xiaodong Xu, Xavier Roy, Andrew D. Kent, and

Xiaoyang Zhu. Exciton-coupled coherent magnons in a 2D semiconductor. *Nature*, 609(7926):282–286, September 2022.

[13] S. Bahr, A. Alfonsov, G. Jackeli, G. Khaliullin, A. Matsumoto, T. Takayama, H. Takagi, B. Büchner, and V. Kataev. Low-energy magnetic excitations in the spin-orbital Mott insulator Sr_2IrO_4. *Physical Review B*, 89(18):180401, May 2014.

[14] Edoardo Baldini, Michael A. Sentef, Swagata Acharya, Thomas Brumme, Evgeniia Sheveleva, Fryderyk Lyzwa, Ekaterina Pomjakushina, Christian Bernhard, Mark van Schilfgaarde, Fabrizio Carbone, Angel Rubio, and Cédric Weber. Electron–phonon-driven three-dimensional metallicity in an insulating cuprate. *Proceedings of the National Academy of Sciences*, 117 (12):6409–6416, March 2020.

[15] Karsten Balzer, F. Alexander Wolf, Ian P. McCulloch, Philipp Werner, and Martin Eckstein. Nonthermal Melting of Néel Order in the Hubbard Model. *Physical Review X*, 5(3):031039, September 2015.

[16] Michal Baranowski and Paulina Plochocka. Excitons in Metal-Halide Perovskites. *Advanced Energy Materials*, 10(26):1903659, 2020.

[17] Christopher J. Bardeen. The Structure and Dynamics of Molecular Excitons. *Annual Review of Physical Chemistry*, 65(1):127–148, 2014.

[18] D. N. Basov, Richard D. Averitt, Dirk van der Marel, Martin Dressel, and Kristjan Haule. Electrodynamics of correlated electron materials. *Reviews of Modern Physics*, 83(2):471–541, June 2011.

[19] D. N. Basov, R. D. Averitt, and D. Hsieh. Towards properties on demand in quantum materials. *Nature Materials*, 16(11):1077–1088, November 2017.

[20] G. Batignani, D. Bossini, N. Di Palo, C. Ferrante, E. Pontecorvo, G. Cerullo, A. Kimel, and T. Scopigno. Probing ultrafast photo-induced dynamics of the exchange energy in a Heisenberg antiferromagnet. *Nature Photonics*, 9(8): 506–510, August 2015.

[21] J. G. Bednorz and K. A. Müller. Possible highTc superconductivity in the BaLaCuO system. *Zeitschrift für Physik B Condensed Matter*, 64(2):189–193, June 1986.

[22] J. Bertinshaw, N. Gurung, P. Jorba, H. Liu, M. Schmid, D.T. Mantadakis, M. Daghofer, M. Krautloher, A. Jain, G.H. Ryu, O. Fabelo, P. Hansmann, G. Khaliullin, C. Pfleiderer, B. Keimer, and B.J. Kim. Unique Crystal Structure of Ca_2RuO_4 in the Current Stabilized Semimetallic State. *Physical Review Letters*, 123(13):137204, September 2019.

[23] Joel Bertinshaw, Y.K. Kim, Giniyat Khaliullin, and B.J. Kim. Square Lattice Iridates. *Annual Review of Condensed Matter Physics*, 10(1):315–336, 2019.

[24] Churna Bhandari, Zoran S. Popović, and S. Satpathy. Electronic structure and optical properties of Sr_2IrO_4 under epitaxial strain. *New Journal of Physics*, 21(1):013036, January 2019.

[25] Nikolaj Bittner, Takami Tohyama, Stefan Kaiser, and Dirk Manske. Possible Light-Induced Superconductivity in a Strongly Correlated Electron System. *Journal of the Physical Society of Japan*, 88(4):044704, April 2019.

[26] Nikolaj Bittner, Denis Golež, Martin Eckstein, and Philipp Werner. Photoenhanced excitonic correlations in a Mott insulator with nonlocal interactions. *Physical Review B*, 101(8):085127, February 2020.

[27] Jacqueline Bloch, Andrea Cavalleri, Victor Galitski, Mohammad Hafezi, and Angel Rubio. Strongly correlated electron–photon systems. *Nature*, 606 (7912):41–48, June 2022.

[28] Annabelle Bohrdt, Lukas Homeier, Immanuel Bloch, Eugene Demler, and Fabian Grusdt. Strong pairing in mixed-dimensional bilayer antiferromagnetic Mott insulators. *Nature Physics*, 18(6):651–656, June 2022.

[29] J. Bonča, P. Prelovšek, and I. Sega. Exact-diagonalization study of the effective model for holes in the planar antiferromagnet. *Physical Review B*, 39(10):7074–7080, April 1989.

[30] Max Born and Emil Wolf. *Principles of Optics: Electromagnetic Theory of Propagation, Interference and Diffraction of Light*. Cambridge University Press, Cambridge, 7 edition, 1999.

[31] M. Braden, G. André, S. Nakatsuji, and Y. Maeno. Crystal and magnetic structure of Ca_2RuO_4: Magnetoelastic coupling and the metal-insulator transition. *Physical Review B*, 58(2):847–861, July 1998.

[32] M. Budden, T. Gebert, M. Buzzi, G. Jotzu, E. Wang, T. Matsuyama, G. Meier, Y. Laplace, D. Pontiroli, M. Riccò, F. Schlawin, D. Jaksch, and A. Cavalleri. Evidence for metastable photo-induced superconductivity in K_3C_{60}. *Nature Physics*, 17(5):611–618, May 2021.

[33] L. V. Butov, A. L. Ivanov, A. Imamoglu, P. B. Littlewood, A. A. Shashkin, V. T. Dolgopolov, K. L. Campman, and A. C. Gossard. Stimulated Scattering of Indirect Excitons in Coupled Quantum Wells: Signature of a Degenerate Bose-Gas of Excitons. *Physical Review Letters*, 86(24):5608–5611, June 2001.

[34] L. V. Butov, A. C. Gossard, and D. S. Chemla. Macroscopically ordered state in an exciton system. *Nature*, 418(6899):751–754, Aug 2002.

[35] L. V. Butov, C. W. Lai, A. L. Ivanov, A. C. Gossard, and D. S. Chemla. Towards Bose–Einstein condensation of excitons in potential traps. *Nature*, 417(6884):47–52, May 2002.

[36] M. Buzzi, D. Nicoletti, M. Fechner, N. Tancogne-Dejean, M.A. Sentef, A. Georges, T. Biesner, E. Uykur, M. Dressel, A. Henderson, T. Siegrist, J.A. Schlueter, K. Miyagawa, K. Kanoda, M.-S. Nam, A. Ardavan, J. Coulthard, J. Tindall, F. Schlawin, D. Jaksch, and A. Cavalleri. Photomolecular High-Temperature Superconductivity. *Physical Review X*, 10(3):031028, August 2020.

[37] G. Cao, J. Bolivar, S. McCall, J. E. Crow, and R. P. Guertin. Weak ferromagnetism, metal-to-nonmetal transition, and negative differential resistivity in single-crystal Sr_2IrO_4. *Physical Review B*, 57(18):R11039–R11042, May 1998.

[38] Samuel George Carter, Susan L. Dexheimer, Robert A. Kaindl, Jie Shan, R. Alan Cheville, Jason B. Baxter, Ingrid Wilke, Suranjana Sengupta, Richard Douglas Averitt, Charles A. Shmuttenmaer, John Cerne, Mark S. Sherwin, Edwin J. Heilweil, David F. Plusquellic, J. Axel Zeitler, Thomas Rades, and Phillip F. Taday. *Terahertz Spectroscopy: Principles and Applications*. CRC Press, Boca Raton, January 2017. ISBN 978-1-315-22176-2.

[39] A. Cavalleri, Th. Dekorsy, H. H. W. Chong, J. C. Kieffer, and R. W. Schoenlein. Evidence for a structurally-driven insulator-to-metal transition in VO_2: A view from the ultrafast timescale. *Physical Review B*, 70(16):161102, October 2004.

[40] Sambuddha Chattopadhyay, Christian J. Eckhardt, Dante M. Kennes, Michael A. Sentef, Dongbin Shin, Angel Rubio, Andrea Cavalleri, Eugene A. Demler, and Marios H. Michael. Mechanisms for Long-Lived, Photo-Induced Superconductivity, March 2023. arXiv:2303.15355 [cond-mat, physics:physics].

[41] D. S. Chemla and Jagdeep Shah. Many-body and correlation effects in semiconductors. *Nature*, 411(6837):549–557, May 2001.

[42] Elbert E. M. Chia, Jian-Xin Zhu, H. J. Lee, Namjung Hur, N. O. Moreno, E. D. Bauer, T. Durakiewicz, R. D. Averitt, J. L. Sarrao, and A. J. Taylor. Quasiparticle relaxation across the spin-density-wave gap in the itinerant antiferromagnet $UNiGa_5$. *Physical Review B*, 74(14):140409, October 2006.

[43] Christie S. Chiu, Geoffrey Ji, Annabelle Bohrdt, Muqing Xu, Michael Knap, Eugene Demler, Fabian Grusdt, Markus Greiner, and Daniel Greif. String patterns in the doped Hubbard model. *Science*, 365(6450):251–256, July 2019.

[44] Hao Chu, Min-Jae Kim, Kota Katsumi, Sergey Kovalev, Robert David Dawson, Lukas Schwarz, Naotaka Yoshikawa, Gideok Kim, Daniel Putzky, Zhi Zhong Li, Hélène Raffy, Semyon Germanskiy, Jan-Christoph Deinert, Nilesh Awari, Igor Ilyakov, Bertram Green, Min Chen, Mohammed Bawatna,

Georg Cristiani, Gennady Logvenov, Yann Gallais, Alexander V. Boris, Bernhard Keimer, Andreas P. Schnyder, Dirk Manske, Michael Gensch, Zhe Wang, Ryo Shimano, and Stefan Kaiser. Phase-resolved Higgs response in superconducting cuprates. *Nature Communications*, 11(1):1–6, April 2020.

[45] Martin Claassen, Hong-Chen Jiang, Brian Moritz, and Thomas P. Devereaux. Dynamical time-reversal symmetry breaking and photo-induced chiral spin liquids in frustrated Mott insulators. *Nature Communications*, 8(1):1–9, October 2017.

[46] David G. Clarke. Particle-hole bound states in Mott-Hubbard insulators. *Physical Review B*, 48(10):7520–7525, September 1993.

[47] Giacomo Coslovich, Alexander F. Kemper, Sascha Behl, Bernhard Huber, Hans A. Bechtel, Takao Sasagawa, Michael C. Martin, Alessandra Lanzara, and Robert A. Kaindl. Ultrafast dynamics of vibrational symmetry breaking in a charge-ordered nickelate. *Science Advances*, 3(11):e1600735, November 2017.

[48] S. Dal Conte, L. Vidmar, D. Golež, M. Mierzejewski, G. Soavi, S. Peli, F. Banfi, G. Ferrini, R. Comin, B. M. Ludbrook, L. Chauviere, N. D. Zhigadlo, H. Eisaki, M. Greven, S. Lupi, A. Damascelli, D. Brida, M. Capone, J. Bonča, G. Cerullo, and C. Giannetti. Snapshots of the retarded interaction of charge carriers with ultrafast fluctuations in cuprates. *Nature Physics*, 11(5):421–426, May 2015.

[49] Andrea Damascelli, Zahid Hussain, and Zhi-Xun Shen. Angle-resolved photoemission studies of the cuprate superconductors. *Reviews of Modern Physics*, 75(2):473–541, April 2003.

[50] L. Das, F. Forte, R. Fittipaldi, C.G. Fatuzzo, V. Granata, O. Ivashko, M. Horio, F. Schindler, M. Dantz, Yi Tseng, D.E. McNally, H.M. Rønnow, W. Wan, N.B. Christensen, J. Pelliciari, P. Olalde-Velasco, N. Kikugawa, T. Neupert, A. Vecchione, T. Schmitt, M. Cuoco, and J. Chang. Spin-Orbital Excitations in Ca_2RuO_4 Revealed by Resonant Inelastic X-Ray Scattering. *Physical Review X*, 8(1):011048, March 2018.

[51] C. D. Dashwood, H. Miao, J. G. Vale, D. Ishikawa, D. A. Prishchenko, V. V. Mazurenko, V. G. Mazurenko, R. S. Perry, G. Cao, A. de la Torre, F. Baumberger, A. Q. R. Baron, D. F. McMorrow, and M. P. M. Dean. Momentum-resolved lattice dynamics of parent and electron-doped Sr_2IrO_4. *Physical Review B*, 100(8):085131, August 2019.

[52] A. de la Torre, S. McKeown Walker, F.Y. Bruno, S. Riccó, Z. Wang, I. Gutierrez Lezama, G. Scheerer, G. Giriat, D. Jaccard, C. Berthod, T.K. Kim, M. Hoesch, E.C. Hunter, R.S. Perry, A. Tamai, and F. Baumberger. Collapse of the Mott Gap and Emergence of a Nodal Liquid in Lightly Doped Sr_2IrO_4. *Physical Review Letters*, 115(17):176402, October 2015.

[53] Alberto de la Torre, Dante M. Kennes, Martin Claassen, Simon Gerber, James W. McIver, and Michael A. Sentef. Colloquium: Nonthermal pathways to ultrafast control in quantum materials. *Reviews of Modern Physics*, 93(4): 041002, October 2021.

[54] Alberto de la Torre, Kyle L. Seyler, Michael Buchhold, Yuval Baum, Gufeng Zhang, Nicholas J. Laurita, John W. Harter, Liuyan Zhao, Isabelle Phinney, Xiang Chen, Stephen D. Wilson, Gang Cao, Richard D. Averitt, Gil Refael, and David Hsieh. Decoupling of static and dynamic criticality in a driven Mott insulator. *Communications Physics*, 5(1):1–8, February 2022.

[55] M. P. M. Dean, Y. Cao, X. Liu, S. Wall, D. Zhu, R. Mankowsky, V. Thampy, X. M. Chen, J. G. Vale, D. Casa, Jungho Kim, A. H. Said, P. Juhas, R. Alonso-Mori, J. M. Glownia, A. Robert, J. Robinson, M. Sikorski, S. Song, M. Kozina, H. Lemke, L. Patthey, S. Owada, T. Katayama, M. Yabashi, Yoshikazu Tanaka, T. Togashi, J. Liu, C. Rayan Serrao, B. J. Kim, L. Huber, C.-L. Chang, D. F. McMorrow, M. Först, and J. P. Hill. Ultrafast energy- and momentum-resolved dynamics of magnetic correlations in the photo-doped Mott insulator Sr_2IrO_4. *Nature Materials*, 15(6):601–605, June 2016.

[56] J. Demsar, K. Biljaković, and D. Mihailovic. Single Particle and Collective Excitations in the One-Dimensional Charge Density Wave Solid $K_{0.3}MoO_3$ Probed in Real Time by Femtosecond Spectroscopy. *Physical Review Letters*, 83(4):800–803, July 1999.

[57] S. Di Matteo and M. R. Norman. Magnetic ground state of Sr_2IrO_4 and implications for second-harmonic generation. *Physical Review B*, 94(7): 075148, August 2016.

[58] P. Diener, E. Janod, B. Corraze, M. Querré, C. Adda, M. Guilloux-Viry, S. Cordier, A. Camjayi, M. Rozenberg, M.P. Besland, and L. Cario. How a dc Electric Field Drives Mott Insulators Out of Equilibrium. *Physical Review Letters*, 121(1):016601, July 2018.

[59] Oleg P. Dimitriev. Dynamics of Excitons in Conjugated Molecules and Organic Semiconductor Systems. *Chemical Reviews*, 122(9):8487–8593, May 2022.

[60] Martin Eckstein and Philipp Werner. Thermalization of a pump-excited Mott insulator. *Physical Review B*, 84(3):035122, July 2011.

[61] Martin Eckstein and Philipp Werner. Photoinduced States in a Mott Insulator. *Physical Review Letters*, 110(12):126401, March 2013.

[62] Martin Eckstein and Philipp Werner. Ultra-fast photo-carrier relaxation in Mott insulators with short-range spin correlations. *Scientific Reports*, 6(1): 21235, February 2016.

[63] Martin Eckstein, Takashi Oka, and Philipp Werner. Dielectric Breakdown of Mott Insulators in Dynamical Mean-Field Theory. *Physical Review Letters*, 105(14):146404, September 2010.

[64] Satoshi Ejima, Tatsuya Kaneko, Florian Lange, Seiji Yunoki, and Holger Fehske. Photoinduced η-pairing at finite temperatures. *Physical Review Research*, 2(3):032008, July 2020.

[65] Albert Eschenmoser and Claude E. Wintner. Natural Product Synthesis and Vitamin B12. *Science*, 196(4297):1410–1420, June 1977.

[66] Zhong Fang, Naoto Nagaosa, and Kiyoyuki Terakura. Orbital-dependent phase control in $Ca_{2-x}Sr_xRuO_4$ ($x < 0.5$). *Physical Review B*, 69(4):045116, January 2004.

[67] D. Fausti, R. I. Tobey, N. Dean, S. Kaiser, A. Dienst, M. C. Hoffmann, S. Pyon, T. Takayama, H. Takagi, and A. Cavalleri. Light-Induced Superconductivity in a Stripe-Ordered Cuprate. *Science*, 331(6014):189–191, January 2011.

[68] Eduardo Fradkin. *Field Theories of Condensed Matter Physics*. Cambridge University Press, Cambridge, second edition, 2013. ISBN 978-0-521-76444-5.

[69] Cesare Franchini, Michele Reticcioli, Martin Setvin, and Ulrike Diebold. Polarons in materials. *Nature Reviews Materials*, 6(7):560–586, July 2021.

[70] S. Fujiyama, H. Ohsumi, T. Komesu, J. Matsuno, B. J. Kim, M. Takata, T. Arima, and H. Takagi. Two-Dimensional Heisenberg Behavior of J_{eff} = 1/2 Isospins in the Paramagnetic State of the Spin-Orbital Mott Insulator Sr_2IrO_4. *Physical Review Letters*, 108(24):247212, June 2012.

[71] Florian Gebhard. *The Mott Metal-Insulator Transition: Models and Methods*, volume 137 of *Springer Tracts in Modern Physics*. Springer, Berlin, Heidelberg, 1997. ISBN 978-3-642-08263-4.

[72] N. Gedik, P. Blake, R. C. Spitzer, J. Orenstein, Ruixing Liang, D. A. Bonn, and W. N. Hardy. Single-quasiparticle stability and quasiparticle-pair decay in $YBa_2Cu_3O_{6.5}$. *Physical Review B*, 70(1):014504, July 2004.

[73] Flavio Giorgianni, Joe Sakai, and Stefano Lupi. Overcoming the thermal regime for the electric-field driven Mott transition in vanadium sesquioxide. *Nature Communications*, 10(1):1–6, March 2019.

[74] S. L. Gnatchenko, I. S. Kachur, V. G. Piryatinskaya, Yu. M. Vysochanskii, and M. I. Gurzan. Exciton-magnon structure of the optical absorption spectrum of antiferromagnetic $MnPS_3$. *Low Temperature Physics*, 37(2):144–148, February 2011.

[75] Denis Golež, Janez Bonča, Marcin Mierzejewski, and Lev Vidmar. Mechanism of ultrafast relaxation of a photo-carrier in antiferromagnetic spin background. *Physical Review B*, 89(16):165118, April 2014.

[76] Denis Golež, Martin Eckstein, and Philipp Werner. Dynamics of screening in photodoped Mott insulators. *Physical Review B*, 92(19):195123, November 2015.

[77] Denis Golež, Lewin Boehnke, Martin Eckstein, and Philipp Werner. Dynamics of photodoped charge transfer insulators. *Physical Review B*, 100(4): 041111, July 2019.

[78] Hiroki Gomi, Akira Takahashi, Toshihiro Ueda, Hisashi Itoh, and Masaki Aihara. Photogenerated holon-doublon cluster states in strongly correlated low-dimensional electron systems. *Physical Review B*, 71(4):045129, January 2005.

[79] E. Gorelov, M. Karolak, T. O. Wehling, F. Lechermann, A. I. Lichtenstein, and E. Pavarini. Nature of the Mott Transition in Ca_2RuO_4. *Physical Review Letters*, 104(22):226401, June 2010.

[80] H. Gretarsson, J. P. Clancy, X. Liu, J. P. Hill, Emil Bozin, Yogesh Singh, S. Manni, P. Gegenwart, Jungho Kim, A. H. Said, D. Casa, T. Gog, M. H. Upton, Heung-Sik Kim, J. Yu, Vamshi M. Katukuri, L. Hozoi, Jeroen van den Brink, and Young-June Kim. Crystal-Field Splitting and Correlation Effect on the Electronic Structure of A_2IrO_3. *Physical Review Letters*, 110(7):076402, February 2013.

[81] H. Gretarsson, N.H. Sung, M. Höppner, B.J. Kim, B. Keimer, and M. Le Tacon. Two-Magnon Raman Scattering and Pseudospin-Lattice Interactions in Sr_2IrO_4 and $Sr_3Ir_2O_7$. *Physical Review Letters*, 116(13):136401, March 2016.

[82] H. Gretarsson, N.H. Sung, J. Porras, J. Bertinshaw, C. Dietl, Jan A.N. Bruin, A.F. Bangura, Y.K. Kim, R. Dinnebier, Jungho Kim, A. Al-Zein, M. Moretti Sala, M. Krisch, M. Le Tacon, B. Keimer, and B.J. Kim. Persistent Paramagnons Deep in the Metallic Phase of $Sr_{2-x}La_xIrO_4$. *Physical Review Letters*, 117(10):107001, September 2016.

[83] Christian Gross and Immanuel Bloch. Quantum simulations with ultracold atoms in optical lattices. *Science*, 357(6355):995–1001, September 2017.

[84] Fabian Grusdt, Eugene Demler, and Annabelle Bohrdt. Pairing of holes by confining strings in antiferromagnets, October 2022. arXiv:2210.02321v1 [cond-mat.str-el].

[85] Martin C. Gutzwiller. Effect of Correlation on the Ferromagnetism of Transition Metals. *Physical Review Letters*, 10(5):159–162, March 1963.

[86] A. Gössling, R. Schmitz, H. Roth, M. W. Haverkort, T. Lorenz, J. A. Mydosh, E. Müller-Hartmann, and M. Grüninger. Mott-Hubbard exciton in the optical conductivity of $YTiO_3$ and $SmTiO_3$. *Physical Review B*, 78(7):075122, August 2008.

[87] Qiang Han and Andrew Millis. Lattice Energetics and Correlation-Driven Metal-Insulator Transitions: The Case of Ca_2RuO_4. *Physical Review Letters*, 121(6):067601, August 2018.

[88] J. W. Harter, L. Niu, A. J. Woss, and D. Hsieh. High-speed measurement of rotational anisotropy nonlinear optical harmonic generation using position-sensitive detection. *Optics Letters*, 40(20):4671–4674, October 2015.

[89] Hartmut Haug and Stephan W Koch. *Quantum Theory of the Optical and Electronic Properties of Semiconductors*. WORLD SCIENTIFIC, 5 edition, January 2009. ISBN 978-981-283-883-4.

[90] Kasra Hejazi, Jianpeng Liu, and Leon Balents. Floquet spin and spin-orbital Hamiltonians and doublon-holon generations in periodically driven Mott insulators. *Physical Review B*, 99(20):205111, May 2019.

[91] Sarah Hirthe, Thomas Chalopin, Dominik Bourgund, Petar Bojović, Annabelle Bohrdt, Eugene Demler, Fabian Grusdt, Immanuel Bloch, and Timon A. Hilker. Magnetically mediated hole pairing in fermionic ladders of ultracold atoms. *Nature*, 613(7944):463–467, January 2023.

[92] D. Hsieh, F. Mahmood, D. H. Torchinsky, G. Cao, and N. Gedik. Observation of a metal-to-insulator transition with both Mott-Hubbard and Slater characteristics in Sr_2IrO_4 from time-resolved photocarrier dynamics. *Physical Review B*, 86(3):035128, July 2012.

[93] Yong Hu, Xiang Chen, S.-T. Peng, C. Lane, M. Matzelle, Z.-L. Sun, M. Hashimoto, D.-H. Lu, E.F. Schwier, M. Arita, T. Wu, R.S. Markiewicz, K. Shimada, X.-H. Chen, Z.-X. Shen, A. Bansil, S.D. Wilson, and J.-F. He. Spectroscopic Evidence for Electron-Boson Coupling in Electron-Doped Sr_2IrO_4. *Physical Review Letters*, 123(21):216402, November 2019.

[94] T.-S. Huang, C. L. Baldwin, M. Hafezi, and V. Galitski. Spin-Mediated Mott Excitons. April 2020.

[95] J. Hubbard. Electron correlations in narrow energy bands. II. The degenerate band case. *Proceedings of the Royal Society of London. Series A. Mathematical and Physical Sciences*, 277(1369):237–259, 1963.

[96] J. Hubbard. Electron correlations in narrow energy bands. *Proceedings of the Royal Society of London. Series A. Mathematical and Physical Sciences*, 276(1365):238–257, 1963.

[97] J. Hubbard. Electron correlations in narrow energy bands III. An improved solution. *Proceedings of the Royal Society of London. Series A. Mathematical and Physical Sciences*, 281(1386):401–419, 1964.

[98] R. Huber, F. Tauser, A. Brodschelm, M. Bichler, G. Abstreiter, and A. Leitenstorfer. How many-particle interactions develop after ultrafast excitation of an electron–hole plasma. *Nature*, 414(6861):286–289, November 2001.

[99] Cassandra Renee Hunt. *Manipulating superconductivity in cuprates with selective ultrafast excitation*. PhD thesis, University of Illinois at Urbana-Champaign, Urbana, April 2015.

[100] Shohei Imai, Atsushi Ono, and Sumio Ishihara. High Harmonic Generation in a Correlated Electron System. *Physical Review Letters*, 124(15):157404, April 2020.

[101] G. Jackeli and G. Khaliullin. Mott Insulators in the Strong Spin-Orbit Coupling Limit: From Heisenberg to a Quantum Compass and Kitaev Models. *Physical Review Letters*, 102(1):017205, January 2009.

[102] Geoffrey Ji, Muqing Xu, Lev Haldar Kendrick, Christie S. Chiu, Justus C. Brüggenjürgen, Daniel Greif, Annabelle Bohrdt, Fabian Grusdt, Eugene Demler, Martin Lebrat, and Markus Greiner. Coupling a Mobile Hole to an Antiferromagnetic Spin Background: Transient Dynamics of a Magnetic Polaron. *Physical Review X*, 11(2):021022, April 2021.

[103] Ying Jiang, Shula Chen, Weihao Zheng, Biyuan Zheng, and Anlian Pan. Interlayer exciton formation, relaxation, and transport in TMD van der Waals heterostructures. *Light: Science & Applications*, 10(1):72, April 2021.

[104] J. H. Jung, Z. Fang, J. P. He, Y. Kaneko, Y. Okimoto, and Y. Tokura. Change of Electronic Structure in Ca_2RuO_4 Induced by Orbital Ordering. *Physical Review Letters*, 91(5):056403, July 2003.

[105] R. A. Kaindl, M. A. Carnahan, D. Hägele, R. Lövenich, and D. S. Chemla. Ultrafast terahertz probes of transient conducting and insulating phases in an electron–hole gas. *Nature*, 423(6941):734–738, June 2003.

[106] R. A. Kaindl, D. Hägele, M. A. Carnahan, and D. S. Chemla. Transient terahertz spectroscopy of excitons and unbound carriers in quasi-two-dimensional electron-hole gases. *Physical Review B*, 79(4):045320, January 2009.

[107] Junjiro Kanamori. Electron Correlation and Ferromagnetism of Transition Metals. *Progress of Theoretical Physics*, 30(3):275–289, September 1963.

[108] Y. Kanamori, H. Matsueda, and S. Ishihara. Photoinduced Change in the Spin State of Itinerant Correlated Electron Systems. *Physical Review Letters*, 107(16):167403, October 2011.

[109] C. L. Kane, P. A. Lee, and N. Read. Motion of a single hole in a quantum antiferromagnet. *Physical Review B*, 39(10):6880–6897, April 1989.

[110] Tatsuya Kaneko, Tomonori Shirakawa, Sandro Sorella, and Seiji Yunoki. Photoinduced η Pairing in the Hubbard Model. *Physical Review Letters*, 122 (7):077002, February 2019.

[111] Tatsuya Kaneko, Seiji Yunoki, and Andrew J. Millis. Charge stiffness and long-range correlation in the optically induced η-pairing state of the one-dimensional Hubbard model. *Physical Review Research*, 2(3):032027, July 2020.

[112] Soonmin Kang, Kangwon Kim, Beom Hyun Kim, Jonghyeon Kim, Kyung Ik Sim, Jae-Ung Lee, Sungmin Lee, Kisoo Park, Seokhwan Yun, Taehun Kim, Abhishek Nag, Andrew Walters, Mirian Garcia-Fernandez, Jiemin Li, Laurent Chapon, Ke-Jin Zhou, Young-Woo Son, Jae Hoon Kim, Hyeonsik Cheong, and Je-Geun Park. Coherent many-body exciton in van der Waals antiferromagnet $NiPS_3$. *Nature*, 583(7818):785–789, July 2020.

[113] T. Kazimierczuk, D. Fröhlich, S. Scheel, H. Stolz, and M. Bayer. Giant Rydberg excitons in the copper oxide Cu_2O. *Nature*, 514(7522):343–347, October 2014.

[114] L. V. Keldysh. The electron-hole liquid in semiconductors. *Contemporary Physics*, 27(5), September 1986.

[115] B. J. Kim, Hosub Jin, S. J. Moon, J.-Y. Kim, B.-G. Park, C. S. Leem, Jaejun Yu, T. W. Noh, C. Kim, S.-J. Oh, J.-H. Park, V. Durairaj, G. Cao, and E. Rotenberg. Novel $J_{\text{eff}} = 1/2$ Mott State Induced by Relativistic Spin-Orbit Coupling in Sr_2IrO_4. *Physical Review Letters*, 101(7):076402, August 2008.

[116] B. J. Kim, H. Ohsumi, T. Komesu, S. Sakai, T. Morita, H. Takagi, and T. Arima. Phase-Sensitive Observation of a Spin-Orbital Mott State in Sr_2IrO_4. *Science*, 323(5919):1329–1332, March 2009.

[117] Jungho Kim, D. Casa, M. H. Upton, T. Gog, Young-June Kim, J. F. Mitchell, M. van Veenendaal, M. Daghofer, J. van den Brink, G. Khaliullin, and B. J. Kim. Magnetic Excitation Spectra of Sr_2IrO_4 Probed by Resonant Inelastic X-Ray Scattering: Establishing Links to Cuprate Superconductors. *Physical Review Letters*, 108(17):177003, April 2012.

[118] Y. K. Kim, O. Krupin, J. D. Denlinger, A. Bostwick, E. Rotenberg, Q. Zhao, J. F. Mitchell, J. W. Allen, and B. J. Kim. Fermi arcs in a doped pseudospin-1/2 Heisenberg antiferromagnet. *Science*, 345(6193):187–190, July 2014.

[119] Y. K. Kim, N. H. Sung, J. D. Denlinger, and B. J. Kim. Observation of a d-wave gap in electron-doped Sr_2IrO_4. *Nature Physics*, 12(1):37–41, January 2016.

[120] Robert Seiple Knox. *Theory of Excitons*. Academic Press, 1963. ISBN 978-0-12-607765-0.

[121] Joannis Koepsell, Jayadev Vijayan, Pimonpan Sompet, Fabian Grusdt, Timon A. Hilker, Eugene Demler, Guillaume Salomon, Immanuel Bloch, and Christian Gross. Imaging magnetic polarons in the doped Fermi–Hubbard model. *Nature*, 572(7769):358–362, August 2019.

[122] Stanislav Yu. Kruchinin, Ferenc Krausz, and Vladislav S. Yakovlev. Colloquium: Strong-field phenomena in periodic systems. *Reviews of Modern Physics*, 90(2):021002, April 2018.

[123] O. Krupin, G. L. Dakovski, B. J. Kim, J. W. Kim, Jungho Kim, S. Mishra, Yi-De Chuang, C. R. Serrao, W.-S. Lee, W. F. Schlotter, M. P. Minitti, D. Zhu, D. Fritz, M. Chollet, R. Ramesh, S. L. Molodtsov, and J. J. Turner. Ultrafast dynamics of localized magnetic moments in the unconventional Mott insulator Sr2IrO4. *Journal of Physics: Condensed Matter*, 28(32): 32LT01, June 2016.

[124] Min-Cheol Lee, Choong H. Kim, Inho Kwak, J. Kim, S. Yoon, Byung Cheol Park, Bumjoo Lee, F. Nakamura, C. Sow, Y. Maeno, T. W. Noh, and K. W. Kim. Abnormal phase flip in the coherent phonon oscillations of Ca_2RuO_4. *Physical Review B*, 98(16):161115, October 2018.

[125] Min-Cheol Lee, Choong H. Kim, Inho Kwak, C. W. Seo, Changhee Sohn, F. Nakamura, C. Sow, Y. Maeno, E.-A. Kim, T. W. Noh, and K. W. Kim. Strong spin-phonon coupling unveiled by coherent phonon oscillations in Ca_2RuO_4. *Physical Review B*, 99(14):144306, April 2019.

[126] Patrick A. Lee, Naoto Nagaosa, and Xiao-Gang Wen. Doping a Mott insulator: Physics of high-temperature superconductivity. *Reviews of Modern Physics*, 78(1):17–85, January 2006.

[127] Woo-Ram Lee and Kwon Park. Dielectric breakdown via emergent nonequilibrium steady states of the electric-field-driven Mott insulator. *Physical Review B*, 89(20):205126, May 2014.

[128] Zala Lenarčič and Peter Prelovšek. Dielectric Breakdown in Spin-Polarized Mott Insulator. *Physical Review Letters*, 108(19):196401, May 2012.

[129] Zala Lenarčič and Peter Prelovšek. Ultrafast Charge Recombination in a Photoexcited Mott-Hubbard Insulator. *Physical Review Letters*, 111(1):016401, July 2013.

[130] Zala Lenarčič and Peter Prelovšek. Charge recombination in undoped cuprates. *Physical Review B*, 90(23):235136, December 2014.

[131] Zala Lenarčič, Martin Eckstein, and Peter Prelovšek. Exciton recombination in one-dimensional organic Mott insulators. *Physical Review B*, 92(20): 201104, November 2015.

[132] J. Li, D. Golez, P. Werner, and M. Eckstein. Superconducting optical response of photodoped Mott insulators. *Modern Physics Letters B*, 34(19n20): 2040054, July 2020.

[133] Jiajun Li and Martin Eckstein. Nonequilibrium steady-state theory of photodoped Mott insulators. *Physical Review B*, 103(4):045133, January 2021.

[134] Jiajun Li, Camille Aron, Gabriel Kotliar, and Jong E. Han. Electric-Field-Driven Resistive Switching in the Dissipative Hubbard Model. *Physical Review Letters*, 114(22):226403, June 2015.

[135] Jiajun Li, Hugo U. R. Strand, Philipp Werner, and Martin Eckstein. Theory of photoinduced ultrafast switching to a spin-orbital ordered hidden phase. *Nature Communications*, 9(1):1–7, November 2018.

[136] Jiajun Li, Denis Golez, Philipp Werner, and Martin Eckstein. η-paired superconducting hidden phase in photodoped Mott insulators. *Physical Review B*, 102(16):165136, October 2020.

[137] Junze Li, Haizhen Wang, and Dehui Li. Self-trapped excitons in two-dimensional perovskites. *Frontiers of Optoelectronics*, 13(3):225–234, September 2020.

[138] Yuelin Li, Richard D. Schaller, Mengze Zhu, Donald A. Walko, Jungho Kim, Xianglin Ke, Ludi Miao, and Z. Q. Mao. Strong lattice correlation of non-equilibrium quasiparticles in a pseudospin-1/2 Mott insulator Sr_2IrO_4. *Scientific Reports*, 6(1):19302, January 2016.

[139] B. Liu, M. Först, M. Fechner, D. Nicoletti, J. Porras, T. Loew, B. Keimer, and A. Cavalleri. Pump Frequency Resonances for Light-Induced Incipient Superconductivity in $YBa_2Cu_3O_{6.5}$. *Physical Review X*, 10(1):011053, March 2020.

[140] M. K. Liu, B. Pardo, J. Zhang, M. M. Qazilbash, Sun Jin Yun, Z. Fei, Jun-Hwan Shin, Hyun-Tak Kim, D. N. Basov, and R. D. Averitt. Photoinduced Phase Transitions by Time-Resolved Far-Infrared Spectroscopy in V_2O_3. *Physical Review Letters*, 107(6):066403, August 2011.

[141] James Lourembam, Amar Srivastava, Chan La-o vorakiat, Liang Cheng, T. Venkatesan, and Elbert E. M. Chia. Evidence for Photoinduced Insulator-to-Metal transition in B-phase vanadium dioxide. *Scientific Reports*, 6(1): 1–7, May 2016.

[142] D. J. Lovinger, M. Brahlek, P. Kissin, D. M. Kennes, A. J. Millis, R. Engel-Herbert, and R. D. Averitt. Influence of spin and orbital fluctuations on Mott-Hubbard exciton dynamics in $LaVO_3$ thin films. *Physical Review B*, 102(11):115143, September 2020.

[143] Hantao Lu, Shigetoshi Sota, Hiroaki Matsueda, Janez Bonča, and Takami Tohyama. Enhanced Charge Order in a Photoexcited One-Dimensional Strongly Correlated System. *Physical Review Letters*, 109(19):197401, November 2012.

[144] Kin Fai Mak and Jie Shan. Photonics and optoelectronics of 2D semiconductor transition metal dichalcogenides. *Nature Photonics*, 10(4):216–226, April 2016.

[145] Gerardo Martinez and Peter Horsch. Spin polarons in the t-J model. *Physical Review B*, 44(1):317–331, July 1991.

[146] M. Matsubara, Y. Okimoto, T. Ogasawara, Y. Tomioka, H. Okamoto, and Y. Tokura. Ultrafast Photoinduced Insulator-Ferromagnet Transition in the Perovskite Manganite $Gd_{0.55}Sr_{0.45}MnO_3$. *Physical Review Letters*, 99(20): 207401, November 2007.

[147] Masakazu Matsubara, Alexander Schroer, Andreas Schmehl, Alexander Melville, Carsten Becher, Mauricio Trujillo-Martinez, Darrell G. Schlom, Jochen Mannhart, Johann Kroha, and Manfred Fiebig. Ultrafast optical tuning of ferromagnetism via the carrier density. *Nature Communications*, 6(1): 1–7, April 2015.

[148] K. Matsuda, I. Hirabayashi, K. Kawamoto, T. Nabatame, T. Tokizaki, and A. Nakamura. Femtosecond spectroscopic studies of the ultrafast relaxation process in the charge-transfer state of insulating cuprates. *Physical Review B*, 50(6):4097–4101, August 1994.

[149] B. Mayer, C. Schmidt, A. Grupp, J. Bühler, J. Oelmann, R. E. Marvel, R. F. Haglund, T. Oka, D. Brida, A. Leitenstorfer, and A. Pashkin. Tunneling breakdown of a strongly correlated insulating state in VO_2 induced by intense multiterahertz excitation. *Physical Review B*, 91(23):235113, June 2015.

[150] Daniel G. Mazzone, Derek Meyers, Yue Cao, James G. Vale, Cameron D. Dashwood, Youguo Shi, Andrew J. A. James, Neil J. Robinson, Jiaqi Lin, Vivek Thampy, Yoshikazu Tanaka, Allan S. Johnson, Hu Miao, Ruitang Wang, Tadesse A. Assefa, Jungho Kim, Diego Casa, Roman Mankowsky, Diling Zhu, Roberto Alonso-Mori, Sanghoon Song, Hasan Yavas, Tetsuo Katayama, Makina Yabashi, Yuya Kubota, Shigeki Owada, Jian Liu, Junji Yang, Robert M. Konik, Ian K. Robinson, John P. Hill, Desmond F. McMorrow, Michael Först, Simon Wall, Xuerong Liu, and Mark P. M. Dean. Laser-induced transient magnons in $Sr_3Ir_2O_7$ throughout the Brillouin zone.

Proceedings of the National Academy of Sciences, 118(22):e2103696118, June 2021.

[151] J. W. McIver, B. Schulte, F.-U. Stein, T. Matsuyama, G. Jotzu, G. Meier, and A. Cavalleri. Light-induced anomalous Hall effect in graphene. *Nature Physics*, 16(1):38–41, January 2020.

[152] Richard S. Meltzer, Ming Y. Chen, Donald S. McClure, and Marian Lowe-Pariseau. Exciton-Magnon Bound State in MnF_2 and the Exciton Dispersion in MnF_2 and $RbMnF_3$. *Physical Review Letters*, 21(13):913–916, September 1968.

[153] J. H. Mentink, K. Balzer, and M. Eckstein. Ultrafast and reversible control of the exchange interaction in Mott insulators. *Nature Communications*, 6(1): 1–8, March 2015.

[154] J.H. Mentink and M. Eckstein. Ultrafast Quenching of the Exchange Interaction in a Mott Insulator. *Physical Review Letters*, 113(5):057201, July 2014.

[155] R. V. Mikhaylovskiy, E. Hendry, A. Secchi, J. H. Mentink, M. Eckstein, A. Wu, R. V. Pisarev, V. V. Kruglyak, M. I. Katsnelson, Th Rasing, and A. V. Kimel. Ultrafast optical modification of exchange interactions in iron oxides. *Nature Communications*, 6(1):1–9, September 2015.

[156] R. C. Miller and D. A. Kleinman. Excitons in GaAs quantum wells. *Journal of Luminescence*, 30(1):520–540, February 1985.

[157] M. Mitrano, G. Cotugno, S.R. Clark, R. Singla, S. Kaiser, J. Stähler, R. Beyer, M. Dressel, L. Baldassarre, D. Nicoletti, A. Perucchi, T. Hasegawa, H. Okamoto, D. Jaksch, and A. Cavalleri. Pressure-Dependent Relaxation in the Photoexcited Mott Insulator ET-F_2TCNQ: Influence of Hopping and Correlations on Quasiparticle Recombination Rates. *Physical Review Letters*, 112(11):117801, March 2014.

[158] M. Mitrano, A. Cantaluppi, D. Nicoletti, S. Kaiser, A. Perucchi, S. Lupi, P. Di Pietro, D. Pontiroli, M. Riccò, S. R. Clark, D. Jaksch, and A. Cavalleri. Possible light-induced superconductivity in K_3C_60 at high temperature. *Nature*, 530(7591):461–464, February 2016.

[159] T. Miyamoto, Y. Matsui, T. Terashige, T. Morimoto, N. Sono, H. Yada, S. Ishihara, Y. Watanabe, S. Adachi, T. Ito, K. Oka, A. Sawa, and H. Okamoto. Probing ultrafast spin-relaxation and precession dynamics in a cuprate Mott insulator with seven-femtosecond optical pulses. *Nature Communications*, 9 (1):1–7, September 2018.

[160] T. Miyamoto, T. Kakizaki, T. Terashige, D. Hata, H. Yamakawa, T. Morimoto, N. Takamura, H. Yada, Y. Takahashi, T. Hasegawa, H. Matsuzaki,

T. Tohyama, and H. Okamoto. Biexciton in one-dimensional Mott insulators. *Communications Physics*, 2(1):1–9, October 2019.

[161] S. J. Moon, Hosub Jin, W. S. Choi, J. S. Lee, S. S. A. Seo, J. Yu, G. Cao, T. W. Noh, and Y. S. Lee. Temperature dependence of the electronic structure of the $J_{\mathrm{eff}} = 1/2$ Mott insulator Sr_2IrO_4 studied by optical spectroscopy. *Physical Review B*, 80(19):195110, November 2009.

[162] S. A. Moskalenko and D. W. Snoke. *Bose-Einstein Condensation of Excitons and Biexcitons: And Coherent Nonlinear Optics with Excitons*. Cambridge University Press, Cambridge, UK ; New York, 1st edition edition, February 2000. ISBN 978-0-521-58099-1.

[163] N. F. Mott. The Basis of the Electron Theory of Metals, with Special Reference to the Transition Metals. *Proceedings of the Physical Society. Section A*, 62(7):416, July 1949.

[164] N. F. Mott. The transition to the metallic state. *The Philosophical Magazine: A Journal of Theoretical Experimental and Applied Physics*, 6(62), February 1961.

[165] N. F. Mott and R. Peierls. Discussion of the paper by de Boer and Verwey. *Proceedings of the Physical Society*, 49(4S):72, August 1937.

[166] Nevill Mott. *Metal-Insulator Transitions*. CRC Press, London, August 1990. ISBN 978-0-429-09488-0.

[167] Yuta Murakami and Philipp Werner. Nonequilibrium steady states of electric field driven Mott insulators. *Physical Review B*, 98(7):075102, August 2018.

[168] Yuta Murakami, Shintaro Takayoshi, Tatsuya Kaneko, Zhiyuan Sun, Denis Golež, Andrew J. Millis, and Philipp Werner. Exploring nonequilibrium phases of photo-doped Mott insulators with generalized Gibbs ensembles. *Communications Physics*, 5(1):1–8, January 2022.

[169] Ajay Nahata, Aniruddha S. Weling, and Tony F. Heinz. A wideband coherent terahertz spectroscopy system using optical rectification and electro-optic sampling. *Applied Physics Letters*, 69(16):2321–2323, October 1996.

[170] Fumihiko Nakamura, Tatsuo Goko, Masakazu Ito, Toshizo Fujita, Satoru Nakatsuji, Hideto Fukazawa, Yoshiteru Maeno, Patricia Alireza, Dominic Forsythe, and Stephen R. Julian. From Mott insulator to ferromagnetic metal: A pressure study of Ca_2RuO_4. *Physical Review B*, 65(22):220402, May 2002.

[171] Fumihiko Nakamura, Mariko Sakaki, Yuya Yamanaka, Sho Tamaru, Takashi Suzuki, and Yoshiteru Maeno. Electric-field-induced metal maintained by current of the Mott insulator Ca_2RuO_4. *Scientific Reports*, 3(1):1–6, August 2013.

[172] Fabio Novelli, Daniele Fausti, Julia Reul, Federico Cilento, Paul H. M. van Loosdrecht, Agung A. Nugroho, Thomas T. M. Palstra, Markus Grüninger, and Fulvio Parmigiani. Ultrafast optical spectroscopy of the lowest energy excitations in the Mott insulator compound YVO_3: Evidence for Hubbard-type excitons. *Physical Review B*, 86(16):165135, October 2012.

[173] Fabio Novelli, Giulio De Filippis, Vittorio Cataudella, Martina Esposito, Ignacio Vergara, Federico Cilento, Enrico Sindici, Adriano Amaricci, Claudio Giannetti, Dharmalingam Prabhakaran, Simon Wall, Andrea Perucchi, Stefano Dal Conte, Giulio Cerullo, Massimo Capone, Andrey Mishchenko, Markus Grüninger, Naoto Nagaosa, Fulvio Parmigiani, and Daniele Fausti. Witnessing the formation and relaxation of dressed quasi-particles in a strongly correlated electron system. *Nature Communications*, 5(1):1–8, October 2014.

[174] Martin C. Nuss and Joseph Orenstein. Terahertz time-domain spectroscopy. In George Grüner, editor, *Millimeter and Submillimeter Wave Spectroscopy of Solids*, Topics in Applied Physics, pages 7–50. Springer, Berlin, Heidelberg, 1998. ISBN 978-3-540-68710-8.

[175] Takashi Oka. Nonlinear doublon production in a Mott insulator: Landau-Dykhne method applied to an integrable model. *Physical Review B*, 86(7): 075148, August 2012.

[176] Takashi Oka and Hideo Aoki. Ground-State Decay Rate for the Zener Breakdown in Band and Mott Insulators. *Physical Review Letters*, 95(13):137601, September 2005.

[177] Yoshinori Okada, Daniel Walkup, Hsin Lin, Chetan Dhital, Tay-Rong Chang, Sovit Khadka, Wenwen Zhou, Horng-Tay Jeng, Mandar Paranjape, Arun Bansil, Ziqiang Wang, Stephen D. Wilson, and Vidya Madhavan. Imaging the evolution of metallic states in a correlated iridate. *Nature Materials*, 12 (8):707–713, August 2013.

[178] H. Okamoto, H. Matsuzaki, T. Wakabayashi, Y. Takahashi, and T. Hasegawa. Photoinduced Metallic State Mediated by Spin-Charge Separation in a One-Dimensional Organic Mott Insulator. *Physical Review Letters*, 98(3):037401, January 2007.

[179] H. Okamoto, T. Miyagoe, K. Kobayashi, H. Uemura, H. Nishioka, H. Matsuzaki, A. Sawa, and Y. Tokura. Ultrafast charge dynamics in photoexcited Nd_2CuO_4 and La_2CuO_4 cuprate compounds investigated by femtosecond absorption spectroscopy. *Physical Review B*, 82(6):060513, August 2010.

[180] H. Okamoto, T. Miyagoe, K. Kobayashi, H. Uemura, H. Nishioka, H. Matsuzaki, A. Sawa, and Y. Tokura. Photoinduced transition from Mott insulator to metal in the undoped cuprates Nd_2CuO_4 and La_2CuO_4. *Physical Review B*, 83(12):125102, March 2011.

[181] K. Parlinski. Lattice Dynamics: Vibrational Modes. In Franco Bassani, Gerald L. Liedl, and Peter Wyder, editors, *Encyclopedia of Condensed Matter Physics*, pages 98–102. Elsevier, Oxford, January 2005. ISBN 978-0-12-369401-0.

[182] Ernest Pastor, David Moreno-Mencía, Maurizio Monti, Allan S. Johnson, Nina Fleischmann, Cuixiang Wang, Youguo Shi, Xuerong Liu, Daniel G. Mazzone, Mark P. M. Dean, and Simon Wall. Nonthermal breaking of magnetic order via photogenerated spin defects in the spin-orbit coupled insulator $Sr_3Ir_2O_7$. *Physical Review B*, 105(6):064409, February 2022.

[183] S. Peli, S. Dal Conte, R. Comin, N. Nembrini, A. Ronchi, P. Abrami, F. Banfi, G. Ferrini, D. Brida, S. Lupi, M. Fabrizio, A. Damascelli, M. Capone, G. Cerullo, and C. Giannetti. Mottness at finite doping and charge instabilities in cuprates. *Nature Physics*, 13(8):806–811, August 2017.

[184] Ilias E. Perakis. Exciton developments. *Nature*, 417(6884):33–35, May 2002.

[185] J. C. Petersen, A. Farahani, D. G. Sahota, Ruixing Liang, and J. S. Dodge. Transient terahertz photoconductivity of insulating cuprates. *Physical Review B*, 96(11):115133, September 2017.

[186] C. Piovera, V. Brouet, E. Papalazarou, M. Caputo, M. Marsi, A. Taleb-Ibrahimi, B. J. Kim, and L. Perfetti. Time-resolved photoemission of Sr_2IrO_4. *Physical Review B*, 93(24):241114, June 2016.

[187] Paul C. M. Planken, Han-Kwang Nienhuys, Huib J. Bakker, and Tom Wenckebach. Measurement and calculation of the orientation dependence of terahertz pulse detection in ZnTe. *JOSA B*, 18(3):313–317, March 2001.

[188] C. Poellmann, P. Steinleitner, U. Leierseder, P. Nagler, G. Plechinger, M. Porer, R. Bratschitsch, C. Schüller, T. Korn, and R. Huber. Resonant internal quantum transitions and femtosecond radiative decay of excitons in monolayer WSe_2. *Nature Materials*, 14(9):889–893, September 2015.

[189] J. Porras, J. Bertinshaw, H. Liu, G. Khaliullin, N. H. Sung, J.-W. Kim, S. Francoual, P. Steffens, G. Deng, M. Moretti Sala, A. Efimenko, A. Said, D. Casa, X. Huang, T. Gog, J. Kim, B. Keimer, and B. J. Kim. Pseudospin-lattice coupling in the spin-orbit Mott insulator Sr_2IrO_4. *Physical Review B*, 99(8):085125, February 2019.

[190] Emma C. Regan, Danqing Wang, Eunice Y. Paik, Yongxin Zeng, Long Zhang, Jihang Zhu, Allan H. MacDonald, Hui Deng, and Feng Wang. Emerging exciton physics in transition metal dichalcogenide heterobilayers. *Nature Reviews Materials*, 7(10):778–795, October 2022.

[191] D. M. Roessler. Kramers-Kronig analysis of reflection data. *British Journal of Applied Physics*, 16(8):1119, August 1965.

[192] Emmanuel Rosencher and Borge Vinter. *Optoelectronics*. Cambridge University Press, 2002.

[193] Matteo Sandri and Michele Fabrizio. Nonequilibrium gap collapse near a first-order Mott transition. *Physical Review B*, 91(11):115102, March 2015.

[194] Marc Scheffler, Martin Dressel, Martin Jourdan, and Hermann Adrian. Extremely slow Drude relaxation of correlated electrons. *Nature*, 438(7071): 1135–1137, December 2005.

[195] S. Schmitt-Rink, C. M. Varma, and A. E. Ruckenstein. Spectral Function of Holes in a Quantum Antiferromagnet. *Physical Review Letters*, 60(26): 2793–2796, June 1988.

[196] Julian Schwinger. On Gauge Invariance and Vacuum Polarization. *Physical Review*, 82(5):664–679, June 1951.

[197] K. Sen, R. Heid, S. M. Souliou, D. Boll, A. Bosak, N. H. Sung, J. Bertinshaw, H. Gretarsson, B. J. Kim, F. Weber, and M. Le Tacon. Absence of temperature-dependent phonon anomalies in Sr_2IrO_4 and $Sr_3Ir_2O_7$. *Physical Review B*, 105(4):045142, January 2022.

[198] Rajdeep Sensarma, David Pekker, Ehud Altman, Eugene Demler, Niels Strohmaier, Daniel Greif, Robert Jördens, Leticia Tarruell, Henning Moritz, and Tilman Esslinger. Lifetime of double occupancies in the Fermi-Hubbard model. *Physical Review B*, 82(22):224302, December 2010.

[199] J. H. Seo, G. H. Ahn, S. J. Song, X. Chen, S. D. Wilson, and S. J. Moon. Infrared probe of pseudogap in electron-doped Sr_2IrO_4. *Scientific Reports*, 7 (1):10494, September 2017.

[200] K. L. Seyler, A. de la Torre, Z. Porter, E. Zoghlin, R. Polski, M. Nguyen, S. Nadj-Perge, S. D. Wilson, and D. Hsieh. Spin-orbit-enhanced magnetic surface second-harmonic generation in Sr_2IrO_4. *Physical Review B*, 102(20): 201113, November 2020.

[201] A. Shekhter and C. M. Varma. Considerations on the symmetry of loop order in cuprates. *Physical Review B*, 80(21):214501, December 2009.

[202] Kazuya Shinjo, Yoshiki Tamaki, Shigetoshi Sota, and Takami Tohyama. Density-matrix renormalization group study of optical conductivity of the Mott insulator for two-dimensional clusters. *Physical Review B*, 104(20): 205123, November 2021.

[203] R. E. F. Silva, Igor V. Blinov, Alexey N. Rubtsov, O. Smirnova, and M. Ivanov. High-harmonic spectroscopy of ultrafast many-body dynamics in strongly correlated systems. *Nature Photonics*, 12(5):266–270, May 2018.

[204] Jai Singh. *Theory of Excitons*. Physics of Solids and Liquids. Springer US, Boston, MA, 1994. ISBN 978-1-4899-0996-1.

[205] David Snoke. Spontaneous Bose Coherence of Excitons and Polaritons. *Science*, 298(5597):1368–1372, November 2002.

[206] Jonathan A. Sobota, Yu He, and Zhi-Xun Shen. Angle-resolved photoemission studies of quantum materials. *Reviews of Modern Physics*, 93(2): 025006, May 2021.

[207] Ajit Srivastava, Rahul Srivastava, Jigang Wang, and Junichiro Kono. Laser-Induced Above-Band-Gap Transparency in GaAs. *Physical Review Letters*, 93(15):157401, October 2004.

[208] C. A. Stafford and A. J. Millis. Scaling theory of the Mott-Hubbard metal-insulator transition in one dimension. *Physical Review B*, 48(3):1409–1425, July 1993.

[209] Georgios L. Stamokostas and Gregory A. Fiete. Mixing of t_{2g}-e_g orbitals in $4d$ and $5d$ transition metal oxides. *Physical Review B*, 97(8):085150, February 2018.

[210] Philipp Steinleitner, Philipp Merkl, Philipp Nagler, Joshua Mornhinweg, Christian Schüller, Tobias Korn, Alexey Chernikov, and Rupert Huber. Direct Observation of Ultrafast Exciton Formation in a Monolayer of WSe_2. *Nano Letters*, 17(3):1455–1460, March 2017.

[211] Niels Strohmaier, Daniel Greif, Robert Jördens, Leticia Tarruell, Henning Moritz, Tilman Esslinger, Rajdeep Sensarma, David Pekker, Ehud Altman, and Eugene Demler. Observation of Elastic Doublon Decay in the Fermi-Hubbard Model. *Physical Review Letters*, 104(8):080401, February 2010.

[212] D. Stroud. The effective medium approximations: Some recent developments. *Superlattices and Microstructures*, 23(3):567–573, March 1998.

[213] A. Stupakiewicz, C. S. Davies, K. Szerenos, D. Afanasiev, K. S. Rabinovich, A. V. Boris, A. Caviglia, A. V. Kimel, and A. Kirilyuk. Ultrafast phononic switching of magnetization. *Nature Physics*, 17(4):489–492, April 2021.

[214] Zhiyuan Sun and Andrew J. Millis. Transient Trapping into Metastable States in Systems with Competing Orders. *Physical Review X*, 10(2):021028, May 2020.

[215] Akira Takahashi, Hiroki Gomi, and Masaki Aihara. Photoinduced superconducting states in strongly correlated electron systems. *Physical Review B*, 66 (11):115103, September 2002.

[216] Akira Takahashi, Hisashi Itoh, and Masaki Aihara. Photoinduced insulator-metal transition in one-dimensional Mott insulators. *Physical Review B*, 77 (20):205105, May 2008.

[217] N. Takubo, I. Onishi, K. Takubo, T. Mizokawa, and K. Miyano. Photoinduced Metal-to-Insulator Transition in a Manganite Thin Film. *Physical Review Letters*, 101(17):177403, October 2008.

[218] Nicolas Tancogne-Dejean, Michael A. Sentef, and Angel Rubio. Ultrafast modification of Hubbard U in a strongly correlated material: Ab initio high-harmonic generation in NiO. *Phys. Rev. Lett.*, 121:097402, Aug 2018.

[219] Nicolas Tancogne-Dejean, Michael A. Sentef, and Angel Rubio. Ultrafast transient absorption spectroscopy of the charge-transfer insulator NiO: Beyond the dynamical Franz-Keldysh effect. *Phys. Rev. B*, 102:115106, Sep 2020.

[220] Alexander Tartakovskii. Excitons in 2D heterostructures. *Nature Reviews Physics*, 2(1):8–9, January 2020.

[221] T. Terashige, T. Ono, T. Miyamoto, T. Morimoto, H. Yamakawa, N. Kida, T. Ito, T. Sasagawa, T. Tohyama, and H. Okamoto. Doublon-holon pairing mechanism via exchange interaction in two-dimensional cuprate Mott insulators. *Science Advances*, 5(6):eaav2187, June 2019.

[222] J. Tindall, B. Buča, J.R. Coulthard, and D. Jaksch. Heating-Induced Long-Range η Pairing in the Hubbard Model. *Physical Review Letters*, 123(3): 030603, July 2019.

[223] T. Tohyama. Symmetry of Photoexcited States and Large-Shift Raman Scattering in Two-Dimensional Mott Insulators. *Journal of the Physical Society of Japan*, 75(3):034713, March 2006.

[224] T. Tohyama, Y. Inoue, K. Tsutsui, and S. Maekawa. Exact diagonalization study of optical conductivity in the two-dimensional Hubbard model. *Physical Review B*, 72(4):045113, July 2005.

[225] Darius H. Torchinsky and David Hsieh. Rotational Anisotropy Nonlinear Harmonic Generation. In Challa S.S.R. Kumar, editor, *Magnetic Characterization Techniques for Nanomaterials*, pages 1–49. Springer, Berlin, Heidelberg, 2017. ISBN 978-3-662-52780-1.

[226] Naoto Tsuji, Takashi Oka, Philipp Werner, and Hideo Aoki. Dynamical Band Flipping in Fermionic Lattice Systems: An ac-Field-Driven Change of the Interaction from Repulsive to Attractive. *Physical Review Letters*, 106(23): 236401, June 2011.

[227] Kenji Tsutsui, Kazuya Shinjo, Shigetoshi Sota, and Takami Tohyama. Exciton-assisted low-energy magnetic excitations in a photoexcited Mott insulator on a square lattice. *Communications Physics*, 6(1):1–7, March 2023.

[228] S. Uchida, T. Ido, H. Takagi, T. Arima, Y. Tokura, and S. Tajima. Optical spectra of $La_{2-x}Sr_xCuO_4$: Effect of carrier doping on the electronic structure of the CuO_2 plane. *Physical Review B*, 43(10):7942–7954, April .

[229] J. G. Vale, S. Boseggia, H. C. Walker, R. Springell, Z. Feng, E. C. Hunter, R. S. Perry, D. Prabhakaran, A. T. Boothroyd, S. P. Collins, H. M. Rønnow, and D. F. McMorrow. Importance of XY anisotropy in Sr_2IrO_4 revealed by magnetic critical scattering experiments. *Physical Review B*, 92(2):020406, July 2015.

[230] S. Wall, D. Brida, S. R. Clark, H. P. Ehrke, D. Jaksch, A. Ardavan, S. Bonora, H. Uemura, Y. Takahashi, T. Hasegawa, H. Okamoto, G. Cerullo, and A. Cavalleri. Quantum interference between charge excitation paths in a solid-state Mott insulator. *Nature Physics*, 7(2):114–118, February 2011.

[231] Fa Wang and T. Senthil. Twisted Hubbard Model for Sr_2IrO_4: Magnetism and Possible High Temperature Superconductivity. *Physical Review Letters*, 106(13):136402, March 2011.

[232] Gang Wang, Alexey Chernikov, Mikhail M. Glazov, Tony F. Heinz, Xavier Marie, Thierry Amand, and Bernhard Urbaszek. Colloquium: Excitons in atomically thin transition metal dichalcogenides. *Reviews of Modern Physics*, 90(2):021001, April 2018.

[233] Y. Y. Wang, F. C. Zhang, V. P. Dravid, K. K. Ng, M. V. Klein, S. E. Schnatterly, and L. L. Miller. Momentum-Dependent Charge Transfer Excitations in $Sr_2CuO_2Cl_2$ Angle-Resolved Electron Energy Loss Spectroscopy. *Physical Review Letters*, 77(9):1809–1812, August 1996.

[234] Yao Wang, Cheng-Chien Chen, B. Moritz, and T.P. Devereaux. Light-Enhanced Spin Fluctuations and d-Wave Superconductivity at a Phase Boundary. *Physical Review Letters*, 120(24):246402, June 2018.

[235] Yao Wang, Thomas P. Devereaux, and Cheng-Chien Chen. Theory of time-resolved Raman scattering in correlated systems: Ultrafast engineering of spin dynamics and detection of thermalization. *Physical Review B*, 98(24): 245106, December 2018.

[236] Hiroshi Watanabe, Tomonori Shirakawa, and Seiji Yunoki. Microscopic Study of a Spin-Orbit-Induced Mott Insulator in Ir Oxides. *Physical Review Letters*, 105(21):216410, November 2010.

[237] Philipp Werner and Martin Eckstein. Field-induced polaron formation in the Holstein-Hubbard model. *Europhysics Letters*, 109(3):37002, February 2015.

[238] Philipp Werner, Naoto Tsuji, and Martin Eckstein. Nonthermal symmetry-broken states in the strongly interacting Hubbard model. *Physical Review B*, 86(20):205101, November 2012.

[239] Philipp Werner, Karsten Held, and Martin Eckstein. Role of impact ionization in the thermalization of photoexcited Mott insulators. *Physical Review B*, 90 (23):235102, December 2014.

[240] Philipp Werner, Hugo U. R. Strand, Shintaro Hoshino, Yuta Murakami, and Martin Eckstein. Enhanced pairing susceptibility in a photodoped two-orbital Hubbard model. *Physical Review B*, 97(16):165119, April 2018.

[241] L. M. Woods. Electronic structure of Ca_2RuO_4:$ A comparison with the electronic structures of other ruthenates. *Physical Review B*, 62(12):7833–7838, September 2000.

[242] P. Wróbel and R. Eder. Excitons in Mott insulators. *Physical Review B*, 66 (3):035111, July 2002.

[243] M. K. Wu, J. R. Ashburn, C. J. Torng, P. H. Hor, R. L. Meng, L. Gao, Z. J. Huang, Y. Q. Wang, and C. W. Chu. Superconductivity at 93 K in a new mixed-phase Y-Ba-Cu-O compound system at ambient pressure. *Physical Review Letters*, 58(9):908–910, March 1987.

[244] B. Xu, P. Marsik, E. Sheveleva, F. Lyzwa, A. Louat, V. Brouet, D. Munzar, and C. Bernhard. Optical Signature of a Crossover from Mott- to Slater-Type Gap in Sr_2IrO_4. *Physical Review Letters*, 124(2):027402, January 2020.

[245] H. Yamakawa, T. Miyamoto, T. Morimoto, T. Terashige, H. Yada, N. Kida, M. Suda, H. M. Yamamoto, R. Kato, K. Miyagawa, K. Kanoda, and H. Okamoto. Mott transition by an impulsive dielectric breakdown. *Nature Materials*, 16(11):1100–1105, November 2017.

[246] Ziliang Ye, Ting Cao, Kevin O'Brien, Hanyu Zhu, Xiaobo Yin, Yuan Wang, Steven G. Louie, and Xiang Zhang. Probing excitonic dark states in single-layer tungsten disulphide. *Nature*, 513(7517):214–218, September 2014.

[247] G. Yu, C. H. Lee, A. J. Heeger, S. W. Cheong, and Z. Fisk. Photo-excitation of single crystals of $La_2CuO_4+\delta$ near the metal-insulator transition. *Physica C: Superconductivity*, 190(4):563–568, January 1992.

[248] X. C. Zeng, P. M. Hui, and D. Stroud. Numerical study of optical absorption in two-dimensional metal-insulator and normal-superconductor composites. *Physical Review B*, 39(2):1063–1067, January 1989.

[249] Qi Zhang, Yongrui Wang, Weilu Gao, Zhongqu Long, John D. Watson, Michael J. Manfra, Alexey Belyanin, and Junichiro Kono. Stability of High-Density Two-Dimensional Excitons against a Mott Transition in High Magnetic Fields Probed by Coherent Terahertz Spectroscopy. *Physical Review Letters*, 117(20):207402, November 2016.

[250] Xi-Cheng Zhang and Jingzhou Xu. *Introduction to THz Wave Photonics*. Springer US, Boston, MA, 2010. ISBN 978-1-4419-0977-0.

[251] L. Zhao, D. H. Torchinsky, H. Chu, V. Ivanov, R. Lifshitz, R. Flint, T. Qi, G. Cao, and D. Hsieh. Evidence of an odd-parity hidden order in a spin–orbit coupled correlated iridate. *Nature Physics*, 12(1):32–36, January 2016.

[252] Liuyan Zhao, Darius Torchinsky, John Harter, Alberto de la Torre, and David Hsieh. Second Harmonic Generation Spectroscopy of Hidden Phases. In Bob D. Guenther and Duncan G. Steel, editors, *Encyclopedia of Modern Optics (Second Edition)*, pages 207–226. Elsevier, Oxford, January 2018. ISBN 978-0-12-814982-9.

[253] Alfred Zong, Pavel E. Dolgirev, Anshul Kogar, Emre Ergeçen, Mehmet B. Yilmaz, Ya-Qing Bie, Timm Rohwer, I-Cheng Tung, Joshua Straquadine, Xirui Wang, Yafang Yang, Xiaozhe Shen, Renkai Li, Jie Yang, Suji Park, Matthias C. Hoffmann, Benjamin K. Ofori-Okai, Michael E. Kozina, Haidan Wen, Xijie Wang, Ian R. Fisher, Pablo Jarillo-Herrero, and Nuh Gedik. Dynamical Slowing-Down in an Ultrafast Photoinduced Phase Transition. *Physical Review Letters*, 123(9):097601, August 2019.

[254] C. Benoit à la Guillaume. Electron-hole droplets in semiconductors. In Baldassare Di Bartolo, editor, *Collective Excitations in Solids*, pages 633–642. Springer US, Boston, MA, 1983. ISBN 978-1-4684-8878-4.